uc3m | Universidad Carlos III de Madrid

DOCTORAL THESIS

Classification and Localization of Electromagnetic and Ultrasonic Pulsed Emitters

Author:
José Manuel FRESNO DE MARCOS

Supervisor:
Dr. Guillermo ROBLES MUÑOZ

A thesis submitted in fulfilment of the requirements for the degree of Doctor of Electrical Engineering, Electronics and Automation

in the

Department of Electrical Engineering at the University Carlos III of Madrid

Leganés
17th December, 2017

DOCTORAL THESIS

Classification and Localization of Electromagnetic and Ultrasonic Pulsed Emitters

Author:
José Manuel FRESNO DE MARCOS

Supervisor:
Dr. Guillermo ROBLES MUÑOZ

The evaluation panel for this PhD Thesis will be formed for the following professionals:

Signature

President: PhD. Andrea Cavallini

Secretary: PhD. José Antonio García Souto

Vocal: PhD. Iliana Portugues

This panel has granted qualification:

Leganés (Madrid), December 2017

Abstract

The localization of radiative sources is very important in many fields of work such as: sonar, radar and underwater radar, indoor localization in wireless networks, earthquake epicenter localization, defective assets localization in electrical facilities and so forth. In the process of locating radiative sources exist many issues which can provoke errors in the localization. The signals acquired may belong to different sources or they can be mixed with environmental noise, then, their separation before using localization algorithms is of great interest to be efficient and accurate in the computational process. Furthermore, the geometry and radiation characteristics of the receivers, the nature of the signal or their measuring process may cause deviations in the signal onset calculus and therefore the source localization could be displaced from the actual position.

In this thesis, there are three kinds of algorithms to undertake three steps in the emitter localization: signal separation, onset and time delay estimation of the signals and source localization. For each step, in order to reduce the error in the localization, several algorithms are analyzed and compared in each application, to choose the most reliable.

As the first step, to separate different kinds of signals is of interest to facilitate further processing. In this thesis, different optimization techniques are presented over the power ratio (PR) maps method. The PR uses a selective spectral signal characterization to extract the features of the analyzed signals. The technique identifies automatically the most representative frequency bands which report a great separation of the different kinds of signals in the PR map.

After separating and selecting the signals, it is of interest to compare the algorithms to calculate the onset and time delay of the pulsed signals to know their performance because the time variables are inputs to the most common triangulation algorithms to locate radiative and ultrasonic sources. An overview of the algorithms used to estimate the time of flight (ToF) and time differences of arrival (TDoA) of pulsed signals is done in this thesis. In the comparison, there is also a new algorithm based on statics of high order, which is proposed in this thesis. The survey of their performance is done applied to muscle deep estimation, localization in one dimension (1D), and for the localization of emitters in three dimensions (3D). The results show how the presented algorithm yields great results.

As the last step in the radiative source localization, the formulation and principle of work of both iterative and non-iterative triangulation algorithms are presented. A new algorithm is presented as a combination of two already existing improving their performance when working alone. All the algorithms, the proposed and the previous which already exist, are compared in terms of accuracy and computational time. The proposed algorithm reports good results in terms of accuracy and it is one of the fastest in computational time.

Once the localization is achieved, it is of great interest to understand how the errors in the determination of the onset of the signals are propagated in the emitter localization. The triangulation algorithms estimate the radiative source position using time variables as inputs: ToF, TDoA or pseudo time of flight (pToF) and the receiver positions. The propagation of the errors in the time variables to the radiative source localization is done in two dimensions (2D) and 3D. New spherical diagrams have been created to represent the directions where the localization is more or less sensible to the errors. This study and their sphere diagrams are presented for several antenna layouts.

Finally, how the errors in the positioning of the receivers are propagated to the emitter localization is analyzed. In this study, the effect in the propagation of both the relative distance from the receivers to the emitter and the direction between them has been characterized. The propagation of the error considering the direction is also represented in spherical diagrams. For a preferred direction identified in the spheres, the propagated error in the source localization has been quantified regarding both the source distance and the magnitude of the errors in the receivers positioning.

A mis padres

"Las malas hierbas han de quitarse de pequeñas, de otro modo, tendrás que trabajar más para quitarlas cuando sean grandes y se hayan reproducido".

Manuel Fresno Angulo

"Cuesta lo mismo hacer las cosas bien que hacerlas mal. Hazlas bien a la primera y no tendras que trabajar dos veces".

Pilar De Marcos Gómez

Acknowledgements

Gracias a todas las personas que de uno u otro modo, me han enseñado algo a lo largo de mi vida.

En primer lugar, dentro el ámbito académico, la persona a quien más agradecido estoy es Guillermo Robles Muñoz, eternamente le estaré agradecido por cómo me ha guiado en mi carrera académica. Con una amistad que se remonta 10 años atrás, nunca ha dejado de enseñarme, siempre tiene una respuesta acertada a cualquier pregunta. He tenido la suerte de recibir de él grandes consejos muy útiles para mí. Por otro lado, estoy muy agradecido a Brian G. Stewart que me ha ayudado desde la estancia. También estoy muy agradecido a Juan Manuel Martínez Tarifa, Ángel Gómez Solanilla, Mónica Victoria Rojas Moreno, Carlos Álvarez y al resto del profesorado del Departamento de Ingeniería Eléctrica en la UC3M. Agradecido a los compañeros de doctorado, en especial a Miguel, acentuando la i, juntos desde el primer día, avanzando brazada a brazada hasta la consecución de nuestros objetivos.

En el ámbito personal, mis principales maestros han sido mis padres, estoy tremendamente orgulloso de ellos. Lo han dado todo por mí, soy consciente de su sacrificio. Mis hermanas María Pilar e Isabel, compañeras de juegos y peleas, que cuando salí fuera de San Esteban de Gormaz, me enseñaron a ser independiente, siempre han hecho todo lo posible por mí. A mi cuñado, mis tíos, a mis primos y a mis abuelas que de todos ellos he aprendido.

Continuando en el ámbito personal, estoy muy agradecido a los amigos que más batallas han compartido conmigo, los integrantes de La Adicción. También tengo gran afecto por las peñas hermanadas con nosotros, Las Más Buscadas y La Cogorza. Agradecido a los compañeros de universidad con los que he pasado y seguimos pasando muy buenos momentos.

Cambiando al ámbito profesional, quiero agradecer a mis compañeros de Circe, allí decidí que quería ser doctor. También quiero mencionar a mis nuevos compañeros de Pamplona.

Por último quiero dar las gracias al amor de mi vida, Carolina. Esa persona con la que no importa donde vayas porque si estás a su lado, estás en el paraíso, siempre hay espacio para la risa aunque sea para reírse de los contratiempos, capaz de escucharme y aconsejarme siempre que le hablo de la tesis o de cualquier otro tema. Gracias a Jesús y Almudena, sus padres, por cómo me quieren y gracias a sus amigos por cómo me acogen.

En general, agradecido a la vida.

Contents

List of Figures

List of Tables

Chapter 1

Introduction

1.1 Motivation for the dissertation

The radiometric localization of emitters with an array of sensors or antennas is a paramount issue approached in several applications [1]. The emissions, depending on the application, are produced in different frequency bands. Then, the receivers can be inductive, capacitive, acoustic or ultrasonic tuned at different frequencies depending on the characteristics of the acquired signals. Some examples of localization through pulsed signals are location with seismic signals [2], the detection of failures in pipes and mechanical structures [3], the localization of damaged electrical insulator materials [4, 5], in vivo bone localization [6], tumor localization [7].

There are different location techniques in the literature [8, 9] that could be classified in triangulation, received signal strength (RSS) and proximity. The algorithms used in this thesis are based on multilateration techniques whose principle of work is that the distance traveled by an emission is equal to the time spent by the wave in the trip, multiplied by the speed propagation. The localization algorithms use different time variables as the time of flight (ToF) of the emission from the emitter to the sensor [10], other use the time differences of arrival (TDoA) of the emissions between sensors [11, 12, 13] and others work with the pseudo time of flight (pToF) of the emission to the sensors [14]. All the algorithms are commonly used indistinctly in different applications.

The performance of the localization algorithms depends on the calculation of the time variables with high accuracy since small errors on these variables can give large errors in the localization and therefore the estimated position of the source will be shifted far from the actual position. The main causes of error are due to wavefronts that can be hidden in noise or contaminated with interferences. In addition, obstacles in the

direct path to the sensors can also attenuate and hinder the wavefront and the reflected waves can create positive interferences that give peaks long past the first front. In general, three categories of source of errors can be defined: the nature of the signal, their measuring process and the geometry and radiation characteristics of the receivers. In the thesis, several algorithms are analyzed to identify their influence in the localization to reduce the uncertainties in the localization. It is also studied how the errors in the input of the algorithms are propagated in the error in the localization.

As a first step, it is important to be efficient in the computing process so a signal classification to separate noise or different types of pulses from pulses of interest before the processing of the onset of the pulse is very useful. In some cases the calculation of the propagation times of the emissions can take high computational time, the same problem applies in the localization algorithms. Usually, the acquired signals can be mixed with noise or can coexist several kinds of signals. Then, a separation before the processing can reduce the time spent in the analysis of the signals. The separation undertaken in this thesis is based on the information contained in the power spectral density of the signals [15, 16].

Usually, in two dimensions (2D) and three dimensions (3D) source localization are used four receivers or sensors. The geometry of the array has to be correctly deployed to have minimal errors in the localization [17]. The antenna layouts have great influence in the sensibility to the systematic errors in the time variables calculation. Even if the reciver array is carefully deployed, unknown and undesired errors will affect the propagation times. The consequence is that, when the acquired data are analyzed, the location is found to be shifted with respect the actual position.

The inputs of the localization algorithms are the receiver positions and the time variables and them have to be measured. When a variable is measured there is an error associated to the magnitude. Thus, it is of interest to evaluate how the errors in the position of the receivers and in the time variables are propagated to the localization. In the bibliography, several receiver layouts have been used to locate radio frequency (RF) emitters such as square, pyramidal [17], cartesian [4] and trapezoidal [18] deployments. To find the best configuration and its best direction is of great interest to mitigate the effect of the errors.

Although the previous knowledge can be applied in many fields of work, the results of this thesis are applied to the localization of partial discharges (PD) and in vivo bone depth measurement. The PD measurements can reveal multiple ageing mechanisms in high voltage (HV) infrastructures [19, 20, 21]. In addition, these techniques allow to locate PD sources using arrays of at least four sensors, which is especially useful inside oil-insulated power transformers, gas-insulated substations and in air-insulated substations [22]. The second application would be very useful, for example, to measure the position of the pelvis bones of subjects forced to stay in wheelchairs in real time, to optimize the stance and avoid or minimize injuries [6].

In the thesis, several types of RF signals are analyzed. During the classification and analysis of the signals, the frequency modulation (FM), very high frequency (VHF) and ultra high frequency (UHF) ranges are separated. The algorithms to estimate the time variables have been tested over signals in the ultrasound (US) and UHF ranges. Finally, the localization algorithms are used with UHF signals. The analysis of sensitivity to errors are applied to UHF although the knowledge can be applied to any kind of signal.

1.2 Objectives of the dissertation

The main objectives addressed in this thesis are the following:

- To find new contributions to the state of the art in localization techniques and signal processing.
- To localize emitters using their electromagnetic emission acquired with antennas.
- To compare the algorithms used in the bibliography to locate emitters with the aim of proposing new ones to improve the performance of the previous ones in terms of accuracy and computation time.
- To compare the algorithms used in bibliography to calculate the ToF and TDoA of pulsed signals with the propose of developing a new method to improve the exactness of the previous ones.
- To automatize and optimize the selections of the bands of frequencies of interest to separate signals through the power ratio (PR) technique. To compare the performance of metaheuristic techniques with the technique already used in this application.
- To evaluate the behaviour of different antenna layouts to locate emitters in presence of TDoA errors. To find the preferred directions for each layout where the localizations are less sensible to the TDoA errors.
- To quantify the antenna error positioning propagation in the source localization. The error propagation is evaluated in terms of distance and direction estimation individually.

1.3 Structure of the dissertation

This thesis is based on the published and submitted articles during the thesis enumerated in Subsection 7.3. The chapters are extensions of these papers and in some cases, the chapters are based on more than one paper. This is the reason why some

concepts are recapitulated in the introductions of the different chapters. The first paper published, item 1 in Subsection 7.3.1, is a paper which englobe the three steps in localization: to separate different signals, to calculate their time variables and finally, to localize the RF. Then, the structure of this paper has defined the thesis structure. The following publications are derived from this work trying to improve the results in each step and trying to improve the understanding of the propagation of the errors in localization.

The dissertation structure is summarized in the diagram shown in Figure 1.1 and it is organized as follows: Chapter 2 shows the selective spectral characterization technique named PR maps to separate different kinds of signals. This technique requires the conversion of the signals from the time domain to the frequency domain. After that, selecting two frequency intervals, the power in each interval is represented in a 2D map, the PR map, for every signal,yielding different clouds of points in the PR map. Each cluster represent one kind of signal which have the similar spectral characteristics in the intervals of frequency selected. In this chapter some techniques to automatize and maximize the signals separation are detailed and compared. This is done maximizing the distance between clusters in PR maps using different optimization techniques as particle swarm optimization (PSO) and genetic algorithms (GA). The PR maps technique allows the user to select n intervals to achieve better separation but, for simplicity, in this thesis only two intervals are used. The results of each optimization technique is evaluated in different groups of signals with different origins.

After separating the different kinds of signals, the next step in the localization is to estimate the onset of the pulsed signal and hence, any of the time variables defined before (ToF, TDoA and pToF). With this propose, Chapter 3 describes and evaluates several algorithms to calculate the ToF and TDoA of pulsed signals and propose a new one which improves the exactness of others in the bibliography. The algorithms are based on different criteria to estimate the onset of pulsed signals or the time delay between two signals. The different algorithms are based on the maximum value of the signal, thresholding, the biggest increment of the cumulated energy of the signal, the Akaike information criterion (AIC), the maximum derivative of the time series cumulative kurtosis, the cross correlation and fourth-order cumulants. The proposed algorithm is derived from the one based on the time series cumulative kurtosis. The performance of all of these algorithms are tested with pulsed signals which come from two applications; in vivo bone depth estimation and in PD source localization.

After estimating the time variables, the next step in the localization is to calculate the position of the source. Then, Chapter 4 presents and compares the most commonly used triangulation algorithms to locate the emitting sources. Both standard least squares (SLS) and hyperbolic least squares (HLS) are iterative and based on Newton-Raphson. Other two iterative algorithms are metaheuristic techniques GA and PSO,

which are also studied due to the fact that they are used to find emitters by defining an objective function (OF) based on HLS. A few non-iterative algorithms based on global positioning systems (GPS) are also presented as hyperbolic positioning algorithms (HPA), maximum likelihood estimator (MLE) and Bancroft. In the thesis, a new combined algorithm (MLE-HLS) based on MLE and HLS is presented yielding better results than the previous ones. The algorithms are tested in multiple conditions to evaluate their performance and their time of execution.

When the localization is achieved, to know how the error in the time variables are propagated in the source location is of great interest. Chapter 5 presents a study where the sensibility to TDoA errors of several antenna layout with the PD source outside the polygon defined by the array in 2D and 3D localization is compared. In 2D localization both a realistic modelling of different antenna deployments that takes into account errors in the measurement of the TDoA and experimental measurements are shown. Since the simulations in 2D localization are validated with experimental measurements, the analysis in 3D localization is only undertaken by simulation due the complexity and quantity of the experimental measurements required.

The position of the receivers has uncertainties so quantifying the propagation of these errors in the emitter localization is also useful. With this aim, Chapter 6 presents a Montecarlo-analysis on how the systematic errors in the antennas positioning are propagated in emitter localization. This effect is analyzed over three parameters: the direction and distance between the source and the antenna array and the magnitude of the positioning error of the receivers. This study is carried out for the most widely used antenna layouts.

Finally, Chapter 7 draws the main conclusions, details the original contributions and the publications yielded from the thesis.

1.4 Bibliography

[1] J. H. Kurz. "New approaches for automatic threedimensional source localization of acoustic emissions Applications to concrete specimens". In: *Ultrasonics* 63 (Dec. 2015), pp. 155–162. ISSN: 0041-624X. DOI: 10.1016/j.ultras.2015.07.003. URL: http://www.sciencedirect.com/science/article/pii/S0041624X15001717 (cit. on p. 1).

[2] H. Zhang, C. Thurber, and C. Rowe. "Automatic P-Wave Arrival Detection and Picking with Multiscale Wavelet Analysis for Single-Component Recordings". en. In: *Bulletin of the Seismological Society of America* 93.5 (Oct. 2003), pp. 1904–1912. ISSN: 0037-1106, 1943-3573. DOI: 10.1785/0120020241. URL: http://www.geology.wisc.edu/~hjzhang/Reviewed/Zhang.autopick.BSSA.03.pdf (cit. on p. 1).

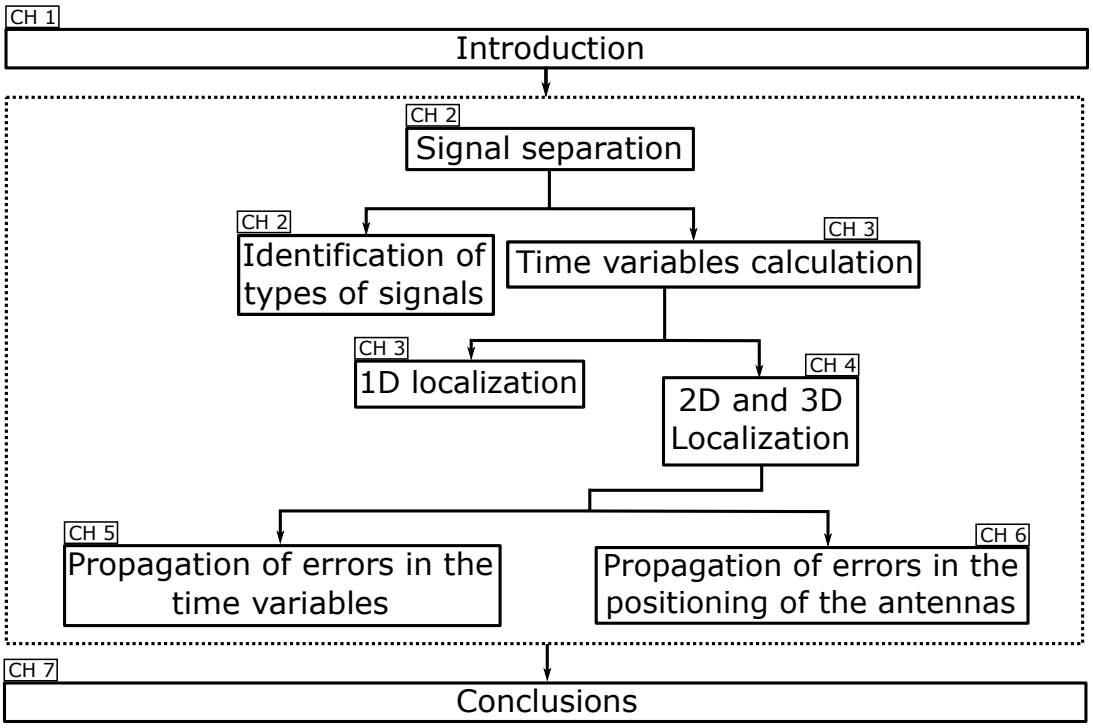

Figure 1.1: Flow chart of the structure of the dissertation. The labels CHi denote the chapter where the topic is addressed.

[3] J. H. Kurz, C. U. Grosse, and H.-W. Reinhardt. "Strategies for reliable automatic onset time picking of acoustic emissions and of ultrasound signals in concrete". In: *Ultrasonics* 43.7 (June 2005), pp. 538–546. ISSN: 0041-624X. DOI: 10.1016/j.ultras.2004.12.005. URL: http://www.sciencedirect.com/science/article/pii/S0041624X04003166 (cit. on p. 1).

[4] G. Robles, J. M. Fresno, and J. M. Martínez-Tarifa. "Separation of Radio-Frequency Sources and Localization of Partial Discharges in Noisy Environments". en. In: *Sensors* 15.5 (Apr. 2015), pp. 9882–9898. DOI: 10.3390/s150509882. URL: http://www.mdpi.com/1424-8220/15/5/9882 (cit. on pp. 1, 2).

[5] P. Wagenaars, P. Wouters, P. van der Wielen, et al. "Accurate estimation of the time-of-arrival of partial discharge pulses in cable systems in service". In: *IEEE Transactions on Dielectrics and Electrical Insulation* 15.4 (Aug. 2008), pp. 1190–1199. ISSN: 1070-9878. DOI: 10.1109/TDEI.2008.4591242 (cit. on p. 1).

[6] R. Giannetti, A. Petrella, J. Bach, et al. "Feasibility study of in vivo bone depth measurement using high frequency ultrasound". In: *Instrumentation and Measurement Technology Conference (I2MTC), 2015 IEEE International*. May 2015, pp. 762–766. DOI: 10.1109/I2MTC.2015.7151364 (cit. on pp. 1, 2).

[7] A. Lazaro, D. Girbau, and R. Villarino. "WAVELET-BASED BREAST TUMOR LOCALIZATION TECHNIQUE USING A UWB RADAR". en. In: *Progress In Electromagnetics Research* 98 (2009), pp. 75–95. ISSN: 1559-8985. DOI: 10.2528/

PIER09100705. URL: http://www.jpier.org/PIER/pier.php?paper=09100705 (cit. on p. 1).

[8] L. Brás, N. B. Carvalho, P. Pinho, et al. "A Review of Antennas for Indoor Positioning Systems". en. In: *International Journal of Antennas and Propagation* 2012 (Dec. 2012), e953269. ISSN: 1687-5869. DOI: 10.1155/2012/953269. URL: https://www.hindawi.com/journals/ijap/2012/953269/abs/ (cit. on p. 1).

[9] K. Fujiwara and M. Kano. "Efficient input variable selection for soft-senor design based on nearest correlation spectral clustering and group Lasso". In: *ISA Transactions* 58 (Sept. 2015), pp. 367–379. ISSN: 0019-0578. DOI: 10.1016/j.isatra.2015.04.007. URL: http://www.sciencedirect.com/science/article/pii/S0019057815001044 (cit. on p. 1).

[10] Y. Lu, X. Tan, and X. Hu. "PD detection and localisation by acoustic measurements in an oil-filled transformer". In: *IEE Proceedings - Science, Measurement and Technology* 147.2 (Mar. 2000), pp. 81–85. ISSN: 1350-2344. DOI: 10.1049/ip-smt:20000223 (cit. on p. 1).

[11] R. M. Harris and M. D. Judd. "Locating Partial Discharge Using Particle Swarm Optimisation". In: *Universities' Power Engineering Conference (UPEC), Proceedings of 2011 46th International*. Sept. 2011, pp. 1–6 (cit. on p. 1).

[12] Y. T. Chan and K. C. Ho. "A simple and efficient estimator for hyperbolic location". In: *IEEE Transactions on Signal Processing* 42.8 (Aug. 1994), pp. 1905–1915. ISSN: 1053-587X. DOI: 10.1109/78.301830 (cit. on p. 1).

[13] R. Bucher and D. Misra. "A Synthesizable VHDL Model of the Exact Solution for Three-dimensional Hyperbolic Positioning System". In: *VLSI Design* 15.2 (2002), pp. 507–520. DOI: 10.1080/1065514021000012129. URL: http://dx.doi.org/10.1080/1065514021000012129 (cit. on p. 1).

[14] S. Bancroft. "An Algebraic Solution of the GPS Equations". In: *IEEE Transactions on Aerospace and Electronic Systems* AES-21.1 (Jan. 1985), pp. 56–59. ISSN: 0018-9251. DOI: 10.1109/TAES.1985.310538 (cit. on p. 1).

[15] J. Ardila-Rey, J. Martínez-Tarifa, G. Robles, et al. "Partial discharge and noise separation by means of spectral-power clustering techniques". In: *IEEE Transactions on Dielectrics and Electrical Insulation* 20.4 (Aug. 2013), pp. 1436–1443. ISSN: 1070-9878. DOI: 10.1109/TDEI.2013.6571466 (cit. on p. 2).

[16] J. M. Martínez-Tarifa, J. A. Ardila-Rey, and G. Robles. "Partial discharge source recognition by means of clustering of spectral power ratios". en. In: *Measurement Science and Technology* 24.12 (2013), p. 125605. ISSN: 0957-0233. DOI: 10.1088/0957-0233/24/12/125605. URL: http://stacks.iop.org/0957-0233/24/i=12/a=125605 (cit. on p. 2).

[17] P. J. Moore, I. E. Portugues, and I. A. Glover. "Radiometric location of partial discharge sources on energized high-Voltage plant". In: *IEEE Transactions on Power Delivery* 20.3 (July 2005), pp. 2264–2272. ISSN: 0885-8977. DOI: 10.1109/TPWRD.2004.843397 (cit. on p. 2).

[18] G. Robles, J. M. Fresno, M. Sánchez-Fernández, et al. "Antenna Deployment for the Localization of Partial Discharges in Open-Air Substations". en. In: *Sensors* 16.4 (Apr. 2016), p. 541. DOI: 10.3390/s16040541. URL: http://www.mdpi.com/1424-8220/16/4/541 (cit. on p. 2).

[19] "IEEE Guide for Partial Discharge Testing of Shielded Power Cable Systems in a Field Environment". In: *IEEE Std 400.3-2006* (Feb. 2007), pp. 1–44. DOI: 10.1109/IEEESTD.2007.305045 (cit. on p. 2).

[20] "IEEE Guide for the Measurement of Partial Discharges in AC Electric Machinery". In: *IEEE Std 1434-2014 (Revision of IEEE Std 1434-2000)* (Dec. 2014), pp. 1–89. DOI: 10.1109/IEEESTD.2014.6973042 (cit. on p. 2).

[21] R.-j. Liao, L.-j. Yang, J. Li, et al. "Aging condition assessment of transformer oil-paper insulation model based on partial discharge analysis". In: *IEEE Transactions on Dielectrics and Electrical Insulation* 18.1 (Feb. 2011), pp. 303–311. ISSN: 1070-9878. DOI: 10.1109/TDEI.2011.5704522 (cit. on p. 2).

[22] I. Portugues, P. Moore, I. Glover, et al. "RF-Based Partial Discharge Early Warning System for Air-Insulated Substations". In: *IEEE Transactions on Power Delivery* 24.1 (Jan. 2009), pp. 20–29. ISSN: 0885-8977. DOI: 10.1109/TPWRD.2008.2005464 (cit. on p. 2).

Chapter 2

Separating different types of signals through spectral characterization

2.1 Abstract

The identification and separation of different types of signals is a task of great interest to classify and to process them efficiently. A spectral analysis can unveil information about the origin and nature of signals. Unfortunately, in most of the cases, the data of interest are hidden by noise and coupled interferences that hinders their interpretation and render them useless. This chapter is focused on a method, named PR separation, that uses a selective spectral signal characterization to feature each signal with

the energy contained in the most representative frequency bands. The technique can be considered as a dimensionality reduction problem where all the energy information contained in the frequency components is condensed in a reduced number of bands. In general, dimensionality reduction methods make the interpretation of results a difficult task because the inherent physical nature of the signal is lost in the process. The proposed selective spectral characterization is a preprocessing tool that facilitates further main processing. Therefore, the dimensionality reduction technique should find out the best frequency bands to enhance the affinity between signals in the same cluster and the differences between signals in different clusters. This is done maximizing the distance between clusters in PR maps using different optimization techniques. The tool is tested with four sets of experimental signals to demonstrate its capabilities in separating noise and signals with low signal-to-noise ratio (SNR) and separating two or three different types of events.

2.2 Introduction

In this chapter are merged and extended two publications "Partial discharges and noise separation using spectral power ratios and genetic algorithms" and "Selective spectral characterization using particle swarm optimization". Their full citation are detailed in Subsection 7.3.1 in items 4 and 6 respectively.

Signal representation in terms of frequency is key in the solution of most signal processing problems due to the fact that the spectrum of signals is strongly related to their source and nature. Signal characterization, [1], facilitates the processing greatly reducing computational burden (the representation of the acquired signals as a sequence of frequency or time samples is replaced by a few scalars) and simplifies the interpretation and analysis of the results by humans. The focus of this work is on the identification of signals through a selective spectral characterization representing each signal with the energy contained in b frequency bands. In this thesis specifically, $b = 2$, since we are interested in the design of visualization tools based on scatter plots in 2D. Such simple signal characterization will certainly increase the usability of the corresponding systems. Our starting point for the design of the procedure is a set of training signals represented in terms of their sampled spectrum. Each sampled spectrum can be regarded as a datum, formed by m features: the value of the power spectral density in the corresponding frequency. The selective spectral characterization can thus be considered as a dimensionality reduction problem: transform each m dimensional spectrum in a b dimensional array in which each component is the energy contained in one of the frequency bands of interest.

Dimensionality reduction techniques, [2, 3], have been long used in machine learning. These techniques can lead to improvements in the performance of general purpose machine learning algorithms along three axes:

- improvements in accuracy due to the removal of noisy or irrelevant information from the observations,
- improvements in the numerical stability of algorithms due to the removal of redundant features, and
- facilitating the visualization and interpretation of the results.

Dimensionality reduction methods are grouped into two main families: feature selection and feature extraction. On the one hand, feature selection methods remove redundant and irrelevant features to yield the minimal subset of the original features that contains the information necessary for solving the problem at hand. Broadly used feature selection methods are Lasso [4, 5] or Recursive Feature Selection [6]. On the other hand, feature extraction techniques transform the initial set of variables in a new, reduced set in a way that the new variables contain only relevant information. Principal Component Analysis [7, 8], Orthogonal Partial Least Squares [9] or t-Stochastic Neighbors Embedding [10] are widely used examples of feature extraction techniques.

A big problem with these dimensionality reduction methods is that they would obscure the interpretation of the results of the processing. Feature selection techniques would come up with sets of scattered frequencies, not necessarily forming meaningful bands since in most scenarios adjacent frequencies will be highly correlated, and the feature selection method would filter out correlated features.

In the case of feature extraction, each resulting new feature comes from a transformation that merges and melts the original frequencies. This greatly hampers the determination, the relevance and influence of each frequency band in the final result.

The dimensionality reduction technique should find out the best frequency bands to enhance the similarities between types of signals and the differences between the different kinds of signals. As introduced before, selective spectral characterization is a preprocessing tool that facilitates the main processing. This chapter is focused on a clustering of signals that could form the core of a visual monitoring system or part of a data exploratory analysis. In the thesis, this technique is used to separate environmental noise from useful emissions which allow to locate the emitter through further processing as the follow chapters show. Additionally, the technique has also been used to separate signals from different emitters opening the possibility to detect several sources at the same time.

This chapter shows the approach that interleaves the selective spectral characterization with the clustering in a same optimization without an a priori knowledge of the spectral power distribution in the signals. The different optimization techniques refine the frequency bands that support the signal characterization and the optimization of the clustering criterion using the signals characterized with these bands as dataset. The performance of the optimization techniques is evaluated in terms of separation

distance of the clusters and time of execution. The capabilities of the method are extensively illustrated in several experiments.

The remainder of the chapter is organized as follows: Section 2.3 explains the process to extract the spectral information from signals reducing the information of separability to clusters in two dimensions for the sake of clearness in the interpretation of the results. Section 2.4 justifies the criterion defined to maximize the minimum distance between clusters considering the scattering in the clouds and the number of clusters. Section 2.5 describes the methods to maximize the distance function proposed in Section 2.4 and sets the constraints to be accomplished in the clustering process. Afterwards, Section 2.6 shows the performance of the method in four experiments involving separation of two types of signals from similar events, signal and noise separation and separation of three signals from different types of events. Finally, Section 2.7 draws the main conclusions of the work.

2.3 PR Maps

The PR technique is applied to separate signals corresponding to different events characterizing them through their spectral power and finding those bands of frequency where their spectra are different. The study done in this thesis is based on two bands of frequency because the representation in a two dimensional map is very intuitive; however, the extension of the algorithm to $b > 2$ dimensions is straightforward.

Let f_{1L} and f_{2L} be the start and end frequencies, respectively, for the first band, whereas f_{1H} and f_{2H} are the extremes of the second band. The subindex L states that the interval is placed at lower frequencies than the second band which has the subindex H for higher frequencies. The significant parameters of the signals are the spectral powers calculated in those frequency bands referred to the total power of the signal. With this consideration the power ratio at low frequencies (PRL) and power ratio at high frequencies (PRH) variables are in per unit so low-energy signals have the same importance as high-energy ones. Then, every signal would be parameterized with a PRL, and PRH:

$$PRL = \frac{\sum_{f=f_{1L}}^{f_{2L}} |G(f)|^2}{\sum_{f=0}^{f_t} |G(f)|^2} \tag{2.1}$$

$$PRH = \frac{\sum_{f=f_{1H}}^{f_{2H}} |G(f)|^2}{\sum_{f=0}^{f_t} |G(f)|^2} \tag{2.2}$$

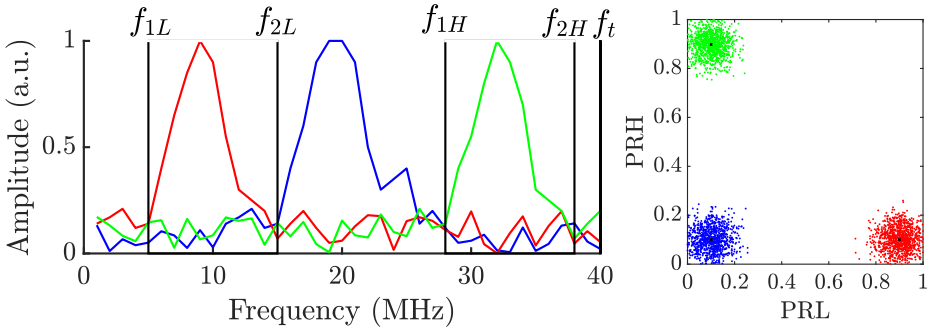

(a) Frequency spectra. *(b)* PR map.

Figure 2.1: Example to visualize how the PR maps works.

where $G(f)$ is the Fourier transform of signal $g(t)$ and f_t is the highest frequency of interest of $g(t)$.

Signals derived from the same event would have similar spectra and then, similar PRL and PRH parameters so, when plotted in a two dimensional map all points would form a packed cluster. Other events may present differences in these parameters, so the clusters would be plotted separately from the first one. Any incoming signal would be analyzed and plotted in the spectral power map. If they are close to any of the existing clusters they can be classified as events of that type.

The selection of the frequency limits for the intervals is paramount to have separated clusters. This can be done by visual inspection of the spectra of the signals if the differences are notable and there are very few types of events, [11, 12]. Otherwise, the classification has to be automatized selecting the intervals according to some criteria and this is precisely what this chapter presents. It seems appropriate that the best set of frequencies would be that which gives the largest separation between clusters.

As an example of how the classification works, Figure 2.1 (left) shows the mean spectra of sets of three kinds of signals (blue, red and green), and the parameters f_{1L}, f_{2L}, f_{1H}, f_{2H} and f_t. Almost all the energy of the red signals is inside the PRL interval, so when they are plotted in the PR map, Figure 2.1, they will placed at the right bottom side. On the other hand, the green spectrum has all the energy in the PRH interval so the green cluster would be at the top left side in the PR map. Finally, the blue signal has all the energy out of the intervals so the blue cluster will be placed at the bottom left side of the map.

2.4 Cluster separation

Once the signals have been parameterized in a PR map, it is necessary to gather them in groups and maximize the distances between clusters to distinguish clearly the type of signal.

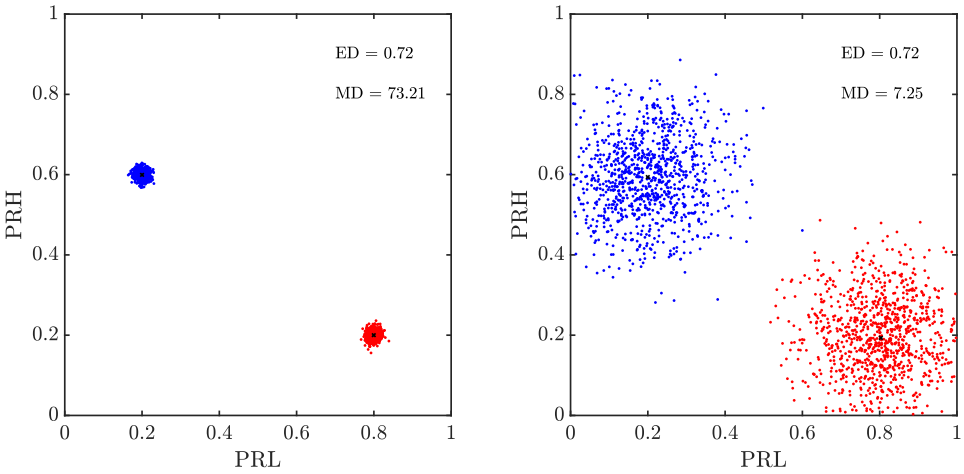

Figure 2.2: Euclidean distance (ED) and Mahalanobis distance (MD) comparison for two cases with two clusters formed by 1000 points with the same mean but different dispersion.

There are several methods to undertake the cluster definition as k-means [13], k-medoids, hierarchical clustering, etc. These algorithms define the clouds of the scattered points using as input the number of clusters, Nc, and the values of the 2D variables PRL and PRH for each signal. k-means has been implemented during the tests because it requires low execution times and yields a good performance in the separation.

After plotting the signals in the PR maps and defining the Nc clusters, it is necessary to evaluate the aptitude of the separation that gather every type of signal. The separation can be evaluated through both euclidean distance (ED) and mahalanobis distance (MD). In Figure 2.2, two examples with two clusters in the PR maps are shown to compare the aptitude of ED and MD. The clusters are positioned in the same coordinates in both cases but in the left one the dispersion of the clouds are smaller than in the right one. In the Figure 2.2, it can be seen how the two cases yield the same ED but very different MD values, this is why the MD considers the dispersion of the clusters. When the MD is maximized, it is expected to obtain less-dispersive clusters and well separated. Therefore, the distance among clusters, d_{ij}, is defined as the MD instead of the ED:

$$d_{ij} = \sqrt{(\mathbf{C}_i - \mathbf{C}_j)^T \left(\frac{1}{\mathbf{S}_i} - \frac{1}{\mathbf{S}_j}\right)(\mathbf{C}_i - \mathbf{C}_j)} \tag{2.3}$$

being

$$\mathbf{S}_{i(j)} = \frac{1}{N_{i(j)}} \sum_{k=1}^{N_{i(j)}} (\mathbf{p}_n - \mathbf{C}_{i(j)})(\mathbf{p}_n - \mathbf{C}_{i(j)})^T \tag{2.4}$$

where $\mathbf{C}_{i(j)}$ is the centroid of the cluster $i(j)$, $\mathbf{S}_{i(j)}$ the covariance matrix of element $\mathbf{p}_n$ in cluster $i(j)$. $N_{i(j)}$ is the number of elements in cluster $i(j)$. Every combination of

frequency intervals will create a different location of points in the PR map; thus, every set of frequencies will yield a different MD value.

When there are three clusters in the PR there would be three MDs, (MD_{12}, MD_{13} and MD_{23}) and an OF to maximize the separation between clusters has to be defined. During the thesis three OFs have been evaluated:

- The sum or the mean of the MD between clusters.
- The minimum MD of all the MDs between clusters.
- The area delimited by the triangle defined by the centroid of the clusters.

The second option is the criterion selected for the results presented, to maximize the minimum distance among clusters, with Equation (2.5). This choice is justified because it avoids a wrong separation when two of the clusters are very close but the other is far.

$$OF(f_{1L}, f_{2L}, f_{1H}, f_{2H}, f_t) = \max \min_{i=1;j=1;i\neq j}^{k} d_{ij} \tag{2.5}$$

This OF is maximized with the unsupervised algorithms presented in Section 2.5. These algorithms are run several times to find the set of frequencies that defines the best separation.

2.5 Maximizing distances between clusters in PR maps

This section describes the different methods to estimate the PRL and PRH frequency intervals which maximize the distance between clusters in the PR maps, through Equation (2.5). Before the study done in this thesis, the separation was first made manually and then with the algorithm presented in [14] which is explained in Subsection 2.5.1. Further in this section, two different metaheuristic techniques are also presented to address this task.

2.5.1 Maximization through the algorithm based on the standard deviation of the PR magnitude

The algorithm presented in this subsection undertakes an exhaustive search to maximize the distance among clusters in PR maps selecting the frequency intervals where the power of all signals have more statistical dispersion. The initial consideration is that different kinds of signals have different power spectra in the frequency domain. The frequency bands where more power fluctuations exist for the analyzed signals, should imply more statistic dispersion in the PR. Then, the PRL and PRH are defined

as the frequency bands where the standard deviation of the PR take the maxima values. This algorithm, detailed below, was presented in [14] and applied successfully to several experiments in [15].

The algorithm defines a frequency window, Δf_n, used to delimit the width of the intervals.

$$\Delta f_n = \frac{BW}{n} \tag{2.6}$$

$$BW = f_t - \frac{1}{T_W} \tag{2.7}$$

where f_t is the maximum frequency of the spectra under analysis and T_W represents the time window of the acquired signals. In the main loop of the algorithm, the integer parameter n ranges from 2 to $BW \cdot T_W$ so the interval width Δf_n explore different values starting in the widest interval with $\Delta f_2 = BW/2$ to the most narrow with a minimum width of $\Delta f_{BW \cdot T_W} = 1/T_W$.

In the secondary loop, for each n, the frequency window Δf_n is shifted from the lowest frequency $f_{1n,1} = 1/T_W$ to the highest at f_t. Frequency 0 is omitted to avoid problems with the average value. Then, in the secondary loop, the boundaries of the intervals are:

$$f_{1n,i} = \frac{i}{T_W} \tag{2.8}$$

$$f_{2n,i} = f_{1n,i} + \Delta f_n \tag{2.9}$$

where i is the index of the interval. The frequencies of the intervals $[f_{1n,i}, f_{2n,i}]$ are shifted from $[1/T_W, 1/T_W + \Delta f_n]$ to $[f_t - \Delta f_n, f_t]$ in i steps of $1/T_W$, see Figure 2.3. In each i-interval a central frequency $f_{cn,i} = (f_{1n,i} + f_{2n,i})/2$ is designated and the PR is determined for every signal as follows:

$$PR_i = \frac{\sum_{f=f_{in,i}}^{f_{2n,i}} |G(f)|^2}{\sum_{f=\frac{1}{T_W}}^{f_t} |G(f)|^2} \tag{2.10}$$

The next step inside of the main loop, is to calculate the standard deviation of the PR obtaining the variable σ_{PR}, see the top plot in Figure 2.4. Later, the position where the two maxima of the σ_{PR} take place has to be identified to designate the two central frequencies $f_{cn,i} = (f_{2n,i} + f_{1n,i})/2$ of each maximum, see Figure 2.4. Then the selected intervals for the frequency window Δf_n in the n iteration to calculate PRL and PRH are:

$$[f_{1L}, f_{2L}] = f_{cn,i=arg(max(\sigma_{PR})),1} \pm \frac{\Delta f_n}{2} \tag{2.11}$$

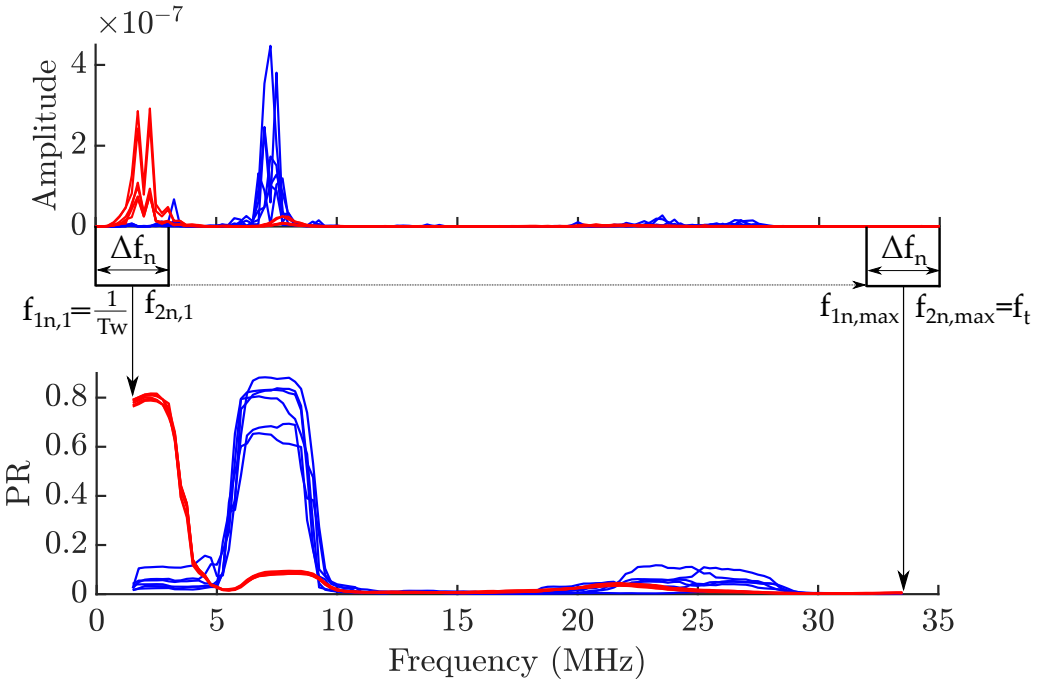

Figure 2.3: Frequency bands movement along the spectrum to calculate PR_i (top) and example of PR_i (botton).

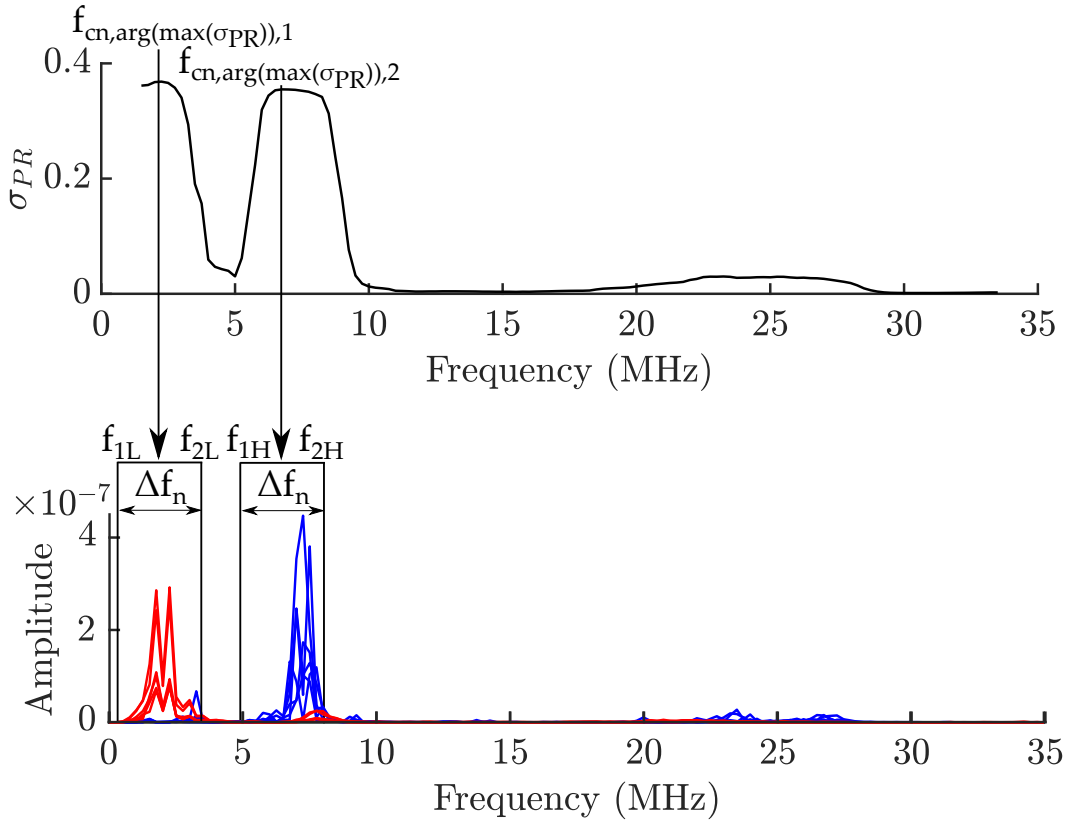

Figure 2.4: Standard deviation of the PR signals, maxima of σ_{PR} selection (top) and intervals definition (botton).

$$[f_{1H}, f_{2H}] = f_{cn,i=arg(max(\sigma_{PR})),2} \pm \frac{\Delta f_n}{2} \tag{2.12}$$

To avoid overlapped intervals, the difference $f_{n,max,1} - f_{n,max,2}$ has to be greater or equal than Δf_n. The next step in the main loop is to calculate the temporary value of the OF for the intervals PRL and PRH in the n iteration. If the temporary OF is greater than the maximum OF, the temporary intervals and the temporary OF are saved as the maximum. Figure 2.5 shows the flow diagram of the algorithm.

2.5.2 Maximization through GA

The maximization of the OF shown in Equation (2.5) to obtain the PRL and PRH can be addressed with genetic algorithms (GA). This meta-heuristic technique is based on the Darwinian principle of evolution and uses concepts as selection, reproduction, crossover and mutation in the improvement of the elements that constitute the possible solutions to the OF [16].

The GA works modifying a population of Mp members which evolves through G generations. Every member of every generation has a chromosome formed by a boolean string containing information about how they fit with the OF. The chromosome has to be constructed with the five frequencies $f_{1L}, f_{2L}, f_{1H}, f_{2H}$ and f_t which represents the limits of the intervals that define the PR.

Every member of the population has its own chromosome in the boolean domain forming a string of 1 and 0. The minimum number of elements of the string, Ng also named gens, of each variable $f_{1L}, f_{2L}, f_{1H}, f_{2H}$ and f_t has to be calculated through Equation (2.13).

$$NG \geq \frac{\log\left(\frac{f_{max}-f_{min}}{\Delta f} + 1\right)}{\log(2)} \tag{2.13}$$

where f_{max} is the maximum frequency under study, f_{min} is the minimum frequency equal to $\frac{1}{T_W}$ is the inverse of the time window, the DC is omitted to avoid problems with the mean and finally Δf is the minimum frequency step $\frac{1}{T_W}$.

To evaluate the fitness of the members, their chromosomes have to be converted to decimal domain to obtain $f_{1L}, f_{2L}, f_{1H}, f_{2H}$ and f_t which represents one feasible solution of the problem. An example of the chromosome of one member of the population in the boolean and decimal domains is shown below. In this simple example $f_{max} = 32$ MHz, $f_{min} = 1$ MHz, $\Delta f = 1$ MHz and furthermore $NG = 5$ gens. The starting point is the boolean domain:

$$(00000,\ 01100,\ 01110,\ 11011,\ 11111) = (f_{1L}, f_{2L}, f_{1H}, f_{2H}, f_t)$$

the chromosome is converted to the decimal domain in the range of 0 to $2^5 - 1$. Afterwards, the variables are fitted to the range under study. In this case, the 0 corresponds

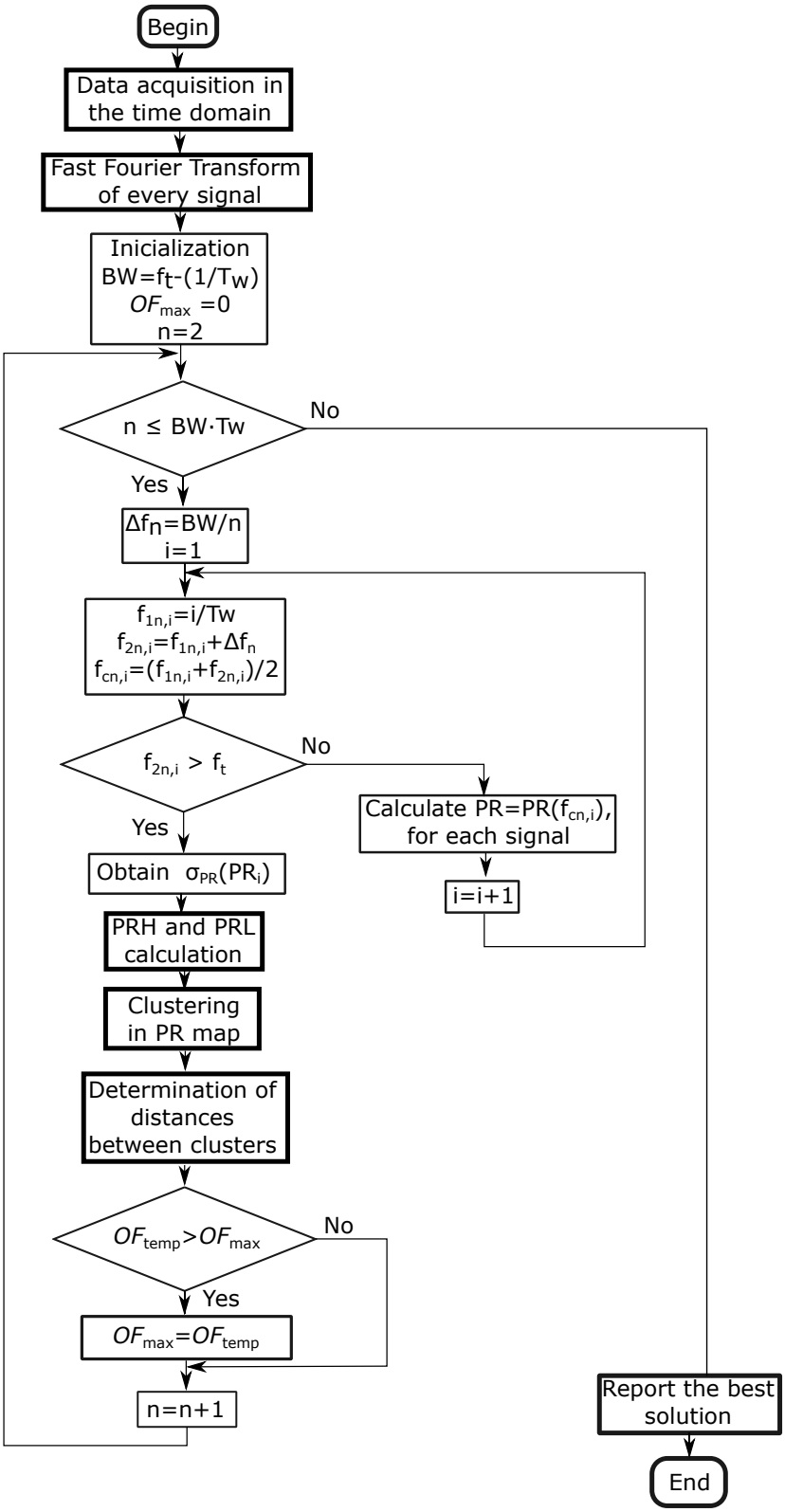

Figure 2.5: Flow diagram of the algorithm based on the standard deviation of the PR magnitude.

with 1 MHz and the 31 corresponds with 32 MHz. In the example, the final result is:

$$(1,\ 7,\ 15,\ 28,\ 32) = (f_{1L}, f_{2L}, f_{1H}, f_{2H}, f_t)$$

To initialize the algorithm it is needed to define the number of generations, to generate randomly the chromosome of the members of the population and to define the percentage of crossover and mutation.

A detailed flow diagram of the algorithm is shown in Figure 2.6. The steps inside the algorithm are as follows:

- To select the new population for the next generation according to their fitness values.
- To apply crossover between the selected members and the rest of the population.
- To apply mutation to the resulting individuals from the crossover.
- To convert the boolean string to frequency values and evaluate the fitness of the OF in Equation (2.5).
- The process is repeated when the number of generations g does not reach a specific value G. Otherwise, the solution is defined as the member who has the interval which reports the best fitness.

The algorithm has the following constraints to avoid overlapped intervals, empty intervals and to restrict the maximum frequency:

$$\begin{aligned} f_{1L} &< f_{2L} \leq f_t \\ f_{2L} &< f_{2H} \leq f_t \\ f_{1L} &< f_{2L} \\ f_{1H} &< f_{2H} \end{aligned} \tag{2.14}$$

When the mutations or crossovers send the frequencies out of the bounds defined by the constraints, the fitness value is set to 0 so in the next generation this member will be ignored.

2.5.3 Maximization through standard PSO

This method, particle swarm optimization (PSO), maximizes the OF by placing a flock or swarm of entities in the solution space [17] which, in the studied case, has five dimensions $f_{1L}, f_{2L}, f_{1H}, f_{2H}$ and f_t. A set of K particles are deployed randomly and then, moved around changing their position by the addition of a frequency step, Δf, to all their components in every l iteration. Then, the parameters PRL and PRH in Equations (2.1) and (2.2) and the distance in Equation (2.5) are computed for the

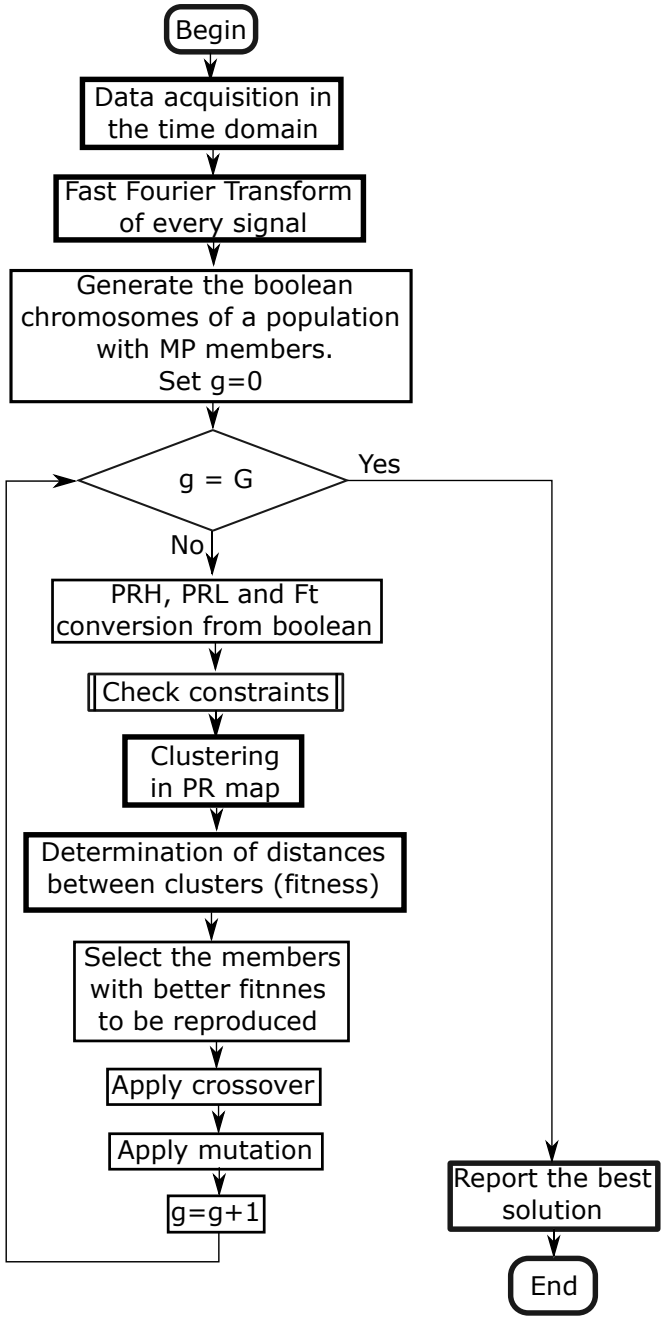

Figure 2.6: Flow diagram of the separation algorithm based on GA.

new intervals. The movement of the particles is modified by a weighted component that moves the particle along its own direction, its own best and another weighted component that pulls the particle to the global best, [18]. The following set of Equations represents the original algorithm introduced in [17] and defines the position $\mathbf{P_k}$ and the speed $\mathbf{v_k}$ of the k^{th} particle in every iteration:

$$\mathbf{v_k}(l) = \mathbf{v_k}(l-1)+C_1\mathbf{U_1}\otimes(\mathbf{P_{k,b}}(l-1)-\mathbf{P_k}(l-1))+C_2\mathbf{U_2}\otimes(\mathbf{P_b}(l-1)-\mathbf{P_k}(l-1)) \quad (2.15)$$

$$\mathbf{P_k}(l) = \mathbf{P_k}(l-1) + \mathbf{v_k}(l) \quad (2.16)$$

$\mathbf{U_1}(0,1)$ and $\mathbf{U_2}(0,1)$ are line matrices with five elements randomly distributed between 0 and 1 that randomizes the movement of the particles towards their own best $\mathbf{P_{k,b}}$ and the swarm best $\mathbf{P_b}$, respectively. These two parameters together with the particle inertia $\mathbf{v_k}(l-1)$, the particle speed in the previous iteration, are part of the swarm intelligence so every particle knows its own speed, its own best fitness and the particle with the best fitness. The operator $\otimes$ multiplies the random numbers by the five coordinates, component by component. The parameters C_1 and C_2 describe the balance between the personal influence of the particle and the social influence on the solution.

When the iteration l is finished and all particles have moved, the position of the particle with the overall best OF is stored as the global best. In the same way, if the new position of any particle improves its fitness, the new position is stored as the best personal solution for that particle. The algorithm stops when the maximum iteration L is reached or when all the particles are placed at the same position.

During the process some constraints have to be supervised during the movement of particles:

- $f_{1L} < f_{2L} \leq f_{1H} < f_{2H} < f_t$
- Δf has to be multiple of $1/T_W$ being T_W the sampling window to have exact steps in frequency.
- If any of the frequencies is rendered negative, the particle position is not updated and the speed of the particle is set to naught in order to reduce its inertia.
- If $f_{1L} \geq f_{2L}$ or $f_{2L} \geq f_{1H}$, f_{1L} and f_{2L} are regenerated randomly considering the first restriction.
- If $f_{1H} \geq f_{2H}$, f_{1H} is regenerated randomly considering the first restriction.

This approach is the original PSO algorithm, its flow diagram is shown in Figure 2.7. It has been modified in many ways to control the convergence towards a global optimum instead of falling in local maxima or minima. Thus, many variants have

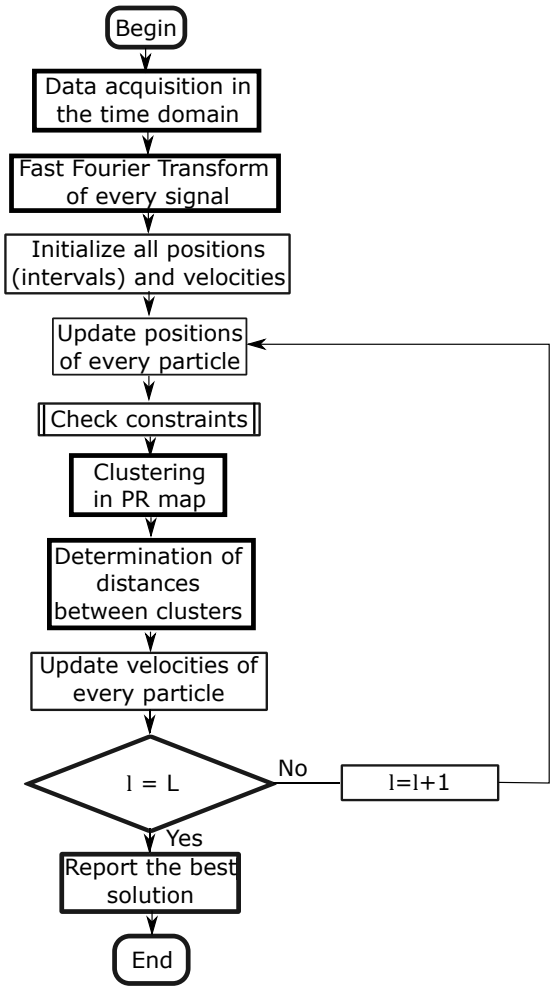

Figure 2.7: Flow diagram of the original PSO algorithm.

been proposed to give solutions to different types of problems [19, 20, 21]. The next algorithms are three different approaches to improve the convergence of PSO.

2.5.4 Maximization through Canonical PSO

In this variation of the standard PSO, the convergence is controlled by a constriction factor, χ, with the idea of exploring in detail the area where a good fitting has been found, [19]. This parameter depends on the constants that update the velocity of the particles, C_1 and C_2. Then,

$$\chi = \frac{2a}{2 - \varphi - \sqrt{\varphi^2 - 4\varphi}}, \quad \varphi = C_1 + C_2 \tag{2.17}$$

where a is a random number between 0 and 1 though it is usually set to 1. The velocity equation is rewritten as:

$$\begin{aligned} \mathbf{v_k}(l) = &\chi\big(\mathbf{v_k}(l-1) + C_1\mathbf{U_1} \otimes (\mathbf{P_{k,b}}(l-1) - \mathbf{P_k}(l-1)) \\ &+ C_2\mathbf{U_2} \otimes (\mathbf{P_b}(l-1) - \mathbf{P_k}(l-1))\big) \end{aligned} \tag{2.18}$$

When $\chi < 4$ the swarm would attempt to reach the best found solution moving slowly around it while for $\chi > 4$ the convergence would be faster [22]. It is possible to modify the behavior of the swarm choosing different values for C_1 and C_2, but, usually, for the sake of simplicity, both parameters are set with the same value. It is a common practice to assume $\varphi = 4.1$ to ensure convergence with $C_1 = C_2 = 2.05$ so, the value for $\chi = 0.72984$. The flow diagram of this algorithm is the same than the initial PSO, see Figure 2.7 the unique variation is the velocity update with Equation (2.18).

2.5.5 Maximization through PSO with time varying inertia

This algorithm is a modification of the standard PSO presented in Subsection 2.5.3. This modification varies the inertia $\mathbf{v_k}(l-1)$ of the particles imprinting different velocities to the swarm in certain moments when searching for the optimum solution. It is possible to set high velocities when the swarm has to explore large areas of the space of solutions and reduce the speed when some particles had reached their best fittings. This idea was introduced in [20] reducing the coefficient of the inertia from a maximum value ω_{max} to a minimum value ω_{min} using a linear function, (2.19)

$$\omega(m) = \omega_{max} - (\omega_{max} - \omega_{min})\frac{m}{M} \tag{2.19}$$

where $\omega(m)$ is the coefficient in iteration m and M is the maximum number of iterations in which the inertia changes its value. The velocity equation is changed into:

$$\begin{aligned}\mathbf{v_k}(l) =& \omega(m)\mathbf{v_k}(l-1) + C_1\mathbf{U_1} \otimes (\mathbf{P_{k,b}}(l-1) - \mathbf{P_k}(l-1)) \\ &+ C_2\mathbf{U_2} \otimes (\mathbf{P_b}(l-1) - \mathbf{P_k}(l-1))\end{aligned} \tag{2.20}$$

with $M \leq L$, being L the total number of iterations, in the presented study $M = L$. The flow diagram of this algorithm is also the same than the initial PSO, Figure 2.7.

2.5.6 Maximization through PSO with aging leader and challengers

Another technique that tries to avoid falling in local maxima or minima is based on giving opportunities to particles different from the best one that could improve the behavior of the swarm, [21]. Then, the global best particle $\mathbf{P_b}$ is the leader of the swarm, $\mathbf{P_{leader}}$, as long as its lifespan is not depleted. The velocity equation is changed into (2.21).

$$\begin{aligned}\mathbf{v_k}(l) =& \omega(m)\mathbf{v_k}(l-1) + C_1\mathbf{U_1} \otimes (\mathbf{P_{k,b}}(l-1) - \mathbf{P_k}(l-1)) \\ &+ C_2\mathbf{U_2} \otimes (\mathbf{P_{leader}}(l-1) - \mathbf{P_k}(l-1))\end{aligned} \tag{2.21}$$

When the leader reaches certain age, a challenger appears to seize the leadership. This challenger is evaluated during a number of iterations and is accepted as leader if the

behavior of the swarm is improved, otherwise, the former leader remains unchanged. The algorithm can be summarized into these steps [21, 23]:

1. Initialization. All particles are randomly deployed in the solution space. The global best particle is selected as the leader, the age, θ is set to 0 and the lifespan Θ to an initial value Θ_0.

2. Velocity and position update. All particles are moved according to Equation (2.21) and $\mathbf{P_k}(l+1) = \mathbf{P_k}(l) + \mathbf{v_k}(l+1)$.

3. Personal best positions and leader $\mathbf{P_{leader}}$ update. If $\mathbf{P_{k,b}}(l)$ is better than $\mathbf{P_{k,b}}(l-1)$ the personal best for particle k is updated. If any of the new positions give a new best solution, the leader is also updated.

4. Lifespan control. Once the positions of all particles have been updated, the age of the leader is increased $\theta \leftarrow \theta + 1$ and its lifespan is modified according certain rules. If the life of the leader is depleted, $\theta \geq \Theta$, the algorithm continues in step 5, otherwise, resumes in step 7.

5. Challenger uprise. A new particle is generated inheriting some coordinates of the leader randomly.

6. Challenger evaluation. The algorithm tests whether the challenger would improve or not the swarm behaviour during a predefined number of cycles. If the test is positive, the challenger becomes the new leader with an age $\theta = 0$ and a lifespan $\Theta = \Theta_0$.

7. Check performance. The termination of the algorithm is based on the number of iterations, so this condition checks if $l > L$. If it is false, the new iteration starts again in step 2.

Figure 2.8 shows the flow diagram of the algorithm with calls to two subroutines to check the constraints of the frequencies in the intervals and to control the lifespan of the leader.

2.5.6.1 Lifespan control

The rules that define the modification of the lifespan are based on three parameters during the life of the leader: related to the evolution of the global best, $\delta_{P_b}(\theta)$; the change of the personal best solutions accumulated into the parameter $\delta_{P_{k,b}}(\theta)$ and the

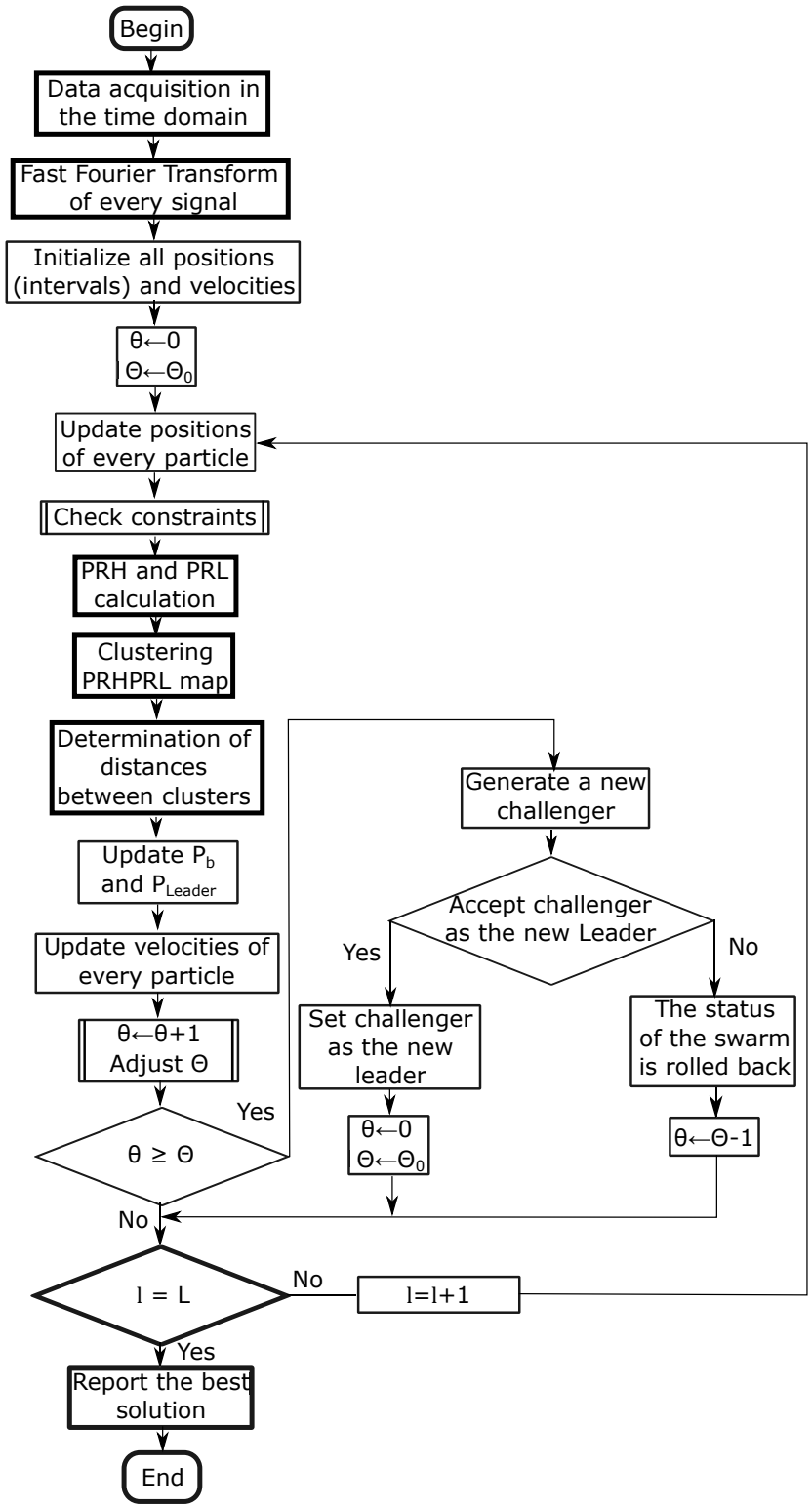

Figure 2.8: Flow diagram of the particle swarm optimization with aging leader and challengers.

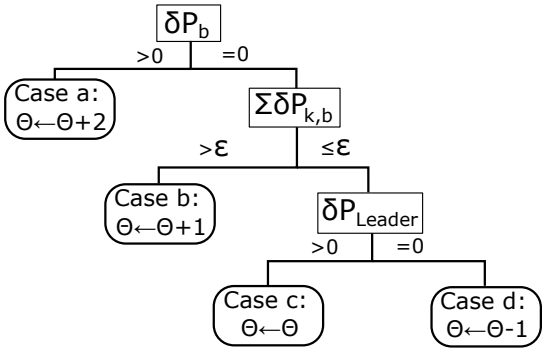

Figure 2.9: Flow diagram of the lifespan control based on the behavior of the global best, the swarm and the leader.

evolution of the OF for the selected leader, $\delta_{P_{leader}}(\theta)$, Equations (2.22).

$$\begin{aligned} \delta_{P_b}(\theta) &= OF\left(\mathbf{P_b}(\theta)\right) - OF\left(\mathbf{P_b}(\theta-1)\right) \\ \sum_{k=1}^{K}\delta_{P_{n,b}}(\theta) &= \sum_{k=1}^{K} OF\left(\mathbf{P_{n,b}}(\theta)\right) - \sum_{k=1}^{K} OF\left(\mathbf{P_{n,b}}(\theta-1)\right) \\ \delta_{P_{leader}}(\theta) &= OF\left(\mathbf{P_{leader}}(\theta)\right) - OF\left(\mathbf{P_{leader}}(\theta-1)\right) \\ \theta &= 1, 2, ...\Theta. \end{aligned} \tag{2.22}$$

All these sequences represent the evolution of the leader and the swarm and evaluate the capability of command of that particle. There are several categories of leadership described below and represented in Figure 2.9.

- Case a, implies that the leader is capable of improving the global best $\delta_{P_b}(\theta) > 0$ guiding the swarm to a better solution so its lifespan is increased in 2.
- Case b, the global best is not improved but the personal bests of the swarm, $\sum_{k=1}^{K}\delta_{P_b}(\theta) > 0$ are increased in at least a 10%, then, the lifespan of the leader is incremented in 1.
- Case c, the only particle that improves is the leader itself $\delta_{P_{leader}}(\theta) > 0$, the decision tree still has confidence in the leader but the lifespan is not modified.
- Case d, means that the leader is incapable of improving the former situation and should be changed soon, the lifespan is reduced in 1.

2.5.6.2 Challenger uprise

A challenger appears when the leader is no longer capable of improving the optimization function and its lifespan is exhausted. The challenger inherits some of the coordinates of the leader after a random decision. In our case there is the possibility of changing the PRL interval, $[f_{1L}, f_{2L}]$ or the PRH interval $[f_{1H}, f_{2H}]$ plus f_t. When

the decision is taken, another random process generates the frequencies of the chosen interval and the other one remains unchanged.

2.6 Applications and results

The optimization algorithms presented in Section 2.5 that estimate the intervals which maximize the distance between clusters are tested for four experiments with different frequency ranges. Since the optimization function has many possible local maxima the choice of the intervals is not always the same every time the algorithm is run. For each experiment all algorithms have been run 20 times and the worst results have been compared in order to analyze their performance in the worst case scenario because, even in that case, the performance of the separation algorithm is good enough to have the clusters clearly separated.

The algorithm based on the standard deviation of the PR magnitude does not require to set any initialization parameters due to the fact that its setup depends on the variables of the acquired signals as: time window, bandwidth and maximum frequency.

In the GA algorithm a population of 40 members and 200 generations are defined. As the problem under study has 5 variables, each variable is represented by 8 gens, then the size of the boolean chromosome is set to 40 gens. Then, every parameter in the string of 8 bits would assign 256 possible values of frequency in constant steps from $1/T_W$ to the maximum frequency f_t. The crossover probability is set to 75 % and the mutation probability is set to 20 %. These parameters are higher than those taken in other applications [16] because this OF has many local maxima that should be avoided.

Concerning the PSO algorithms, the number of particles deployed to the search for the solution is set to 20 and the maximum number of iterations to 500 for all four PSO methods. The initial position of the particles is set randomly, for the 5 variables $f_{1L}, f_{2L}, f_{1H}, f_{2H}$ and f_t. The parameters C_1 and C_2 have been set considering that the individual maxima and global maxima are balanced and, $C_1 = C_2 = 2.05$, for the sake of simplicity. Additionally, in the time varying inertia PSO and in the aging leader and challengers PSO, the maximum and minimum inertia are $\omega_{max} = 0.9$ and $\omega_{min} = 0.4$, respectively. Furthermore, the leader lifespan Θ is set to 3.

2.6.1 UHF signals

In this experiment, HV is applied to a 20 kV cable that has two separated sections with high divergence electric fields created on purpose for these measurements. Electrical discharges are activated on the surface of the dielectric of the cable and captured with two antennas, [24]. The sampling frequency is 5 GS/s and the time window is 1 μs, so the frequency step is 1 MHz. The TDoA between antennas of the RF emission

Table 2.1: Minima of the maxima distances achieved with every algorithm and their mean time of execution in seconds for case of the UHF signals .

Algorithm	Minimum distance	Execution time
σ_{PR} based	19.7	32.6
GA	21.4	4.4
PSO standard	20.1	4.3
PSO canonical	17.9	3.1
PSO time varying inertia	14.5	**2.2**
PSO aging leader	**22.3**	38.3

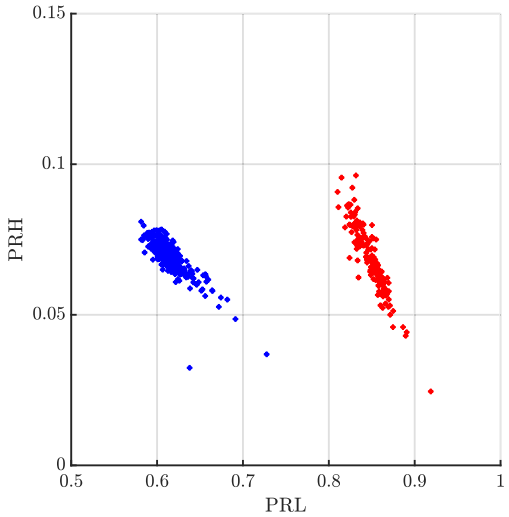

Figure 2.10: PR map with the clusters of discharges from the two sections of the cable received by one of the antennas in the UHF range.

of the discharges to the antennas are different, so it is possible to know beforehand which pulse corresponds to which section of the cable, [25]. This is necessary to check whether the classification is correct or not though the information is not used to help the algorithm. In fact, the classification algorithm is only run with the pulses arriving from the two sources to one of the antennas.

The results of the worst case scenario, minima OF throughout the 20 simulated cases, are summarized in Table 2.1 where the ageing leader and challengers algorithm shows the best behaviour in terms of the minima of the maximized distance using Equation (2.5). The time varying inertia PSO is the algorithm which converges to the solution faster than the others in average.

In that case, the resulting clusters are plotted in the PR map in Figure 2.10 where they are clearly separated. The selected set of frequencies, $f_{1L} = 115$ MHz, $f_{2L} = 361$ MHz, $f_{1H} = 443$ MHz, $f_{2H} = 524$ MHz and $f_t = 607$ MHz, was found to be the best option considering all algorithms to maximize the distance between the two clusters obtaining a value of 22.3.

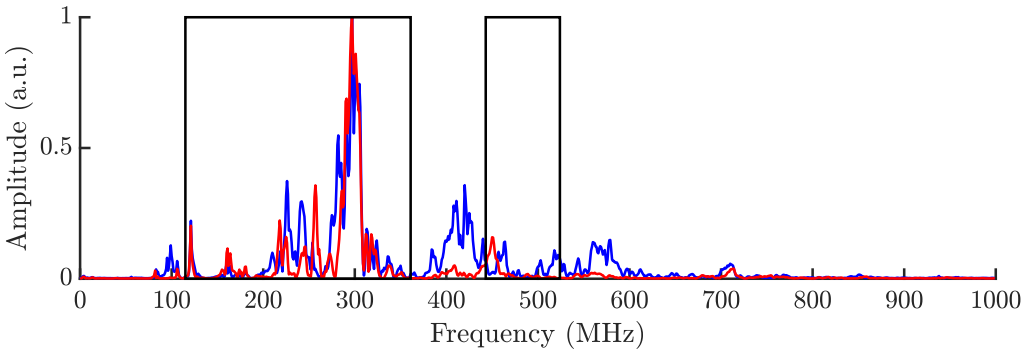

Figure 2.11: Average spectra of the pulses and the selected intervals that maximize the OF for the UHF signals case.

Figure 2.11 shows the average spectra of the signals in clusters 1 and 2. Notice that the algorithm does not waits to select the frequencies in the averaged spectra, on the contrary, it analyzes the spectral power of every signal even when the variance is larger. The spectra are plotted in arbitrary units (a.u.) because all components are referred to the peak amplitude. This is done because the algorithm calculates the PRL and PRH parameters referred to the total power of the signal and, eliminating the scale factor due to signals with different amplitudes, helps in the interpretation of what the algorithm is doing.

In this particular case, both clusters 1 and 2 have low values for the parameter PRH around 5-10 %. Most of the power is concentrated inside the PRL interval, the signals of cluster 1 have around 60 % of their energy in the PRL and the signals of cluster 2 have around 85 % in it. This is because the selected bands have kept out power of the signals of cluster 1 in the 380-440 MHz and 550-570 MHz bands so the relative power in $[f_{1L}, f_{2L}]$ is lower for this cluster.

Any new incoming signal from the cable would be plotted close to any of the clusters. At this stage, the algorithm is capable of separating two electromagnetic sources but there is not a correspondence between the clusters and the section of cable that emits the radiation. However, using the information of the TDoA between the antennas using the signals in the clusters, they can be labeled as coming from section 1 or section 2 of the cable. Figure 2.12 shows two examples of electromagnetic pulses generated when HV is applied to the cable. The upper plot corresponds to section 1 and the lower plot to section 2 of the cable. In summary, despite the fact that both signals are derived from the same pulsed ionization process, this procedure allows to identify the origin of the signals with an algorithm completely unsupervised and without any previous training.

To demonstrate the correct performance of the algorithm the emissions were acquired with two antennas located in different positions. The two antennas were placed in the left vertices of a square of one meter on each side and the section 1 and 2 of the

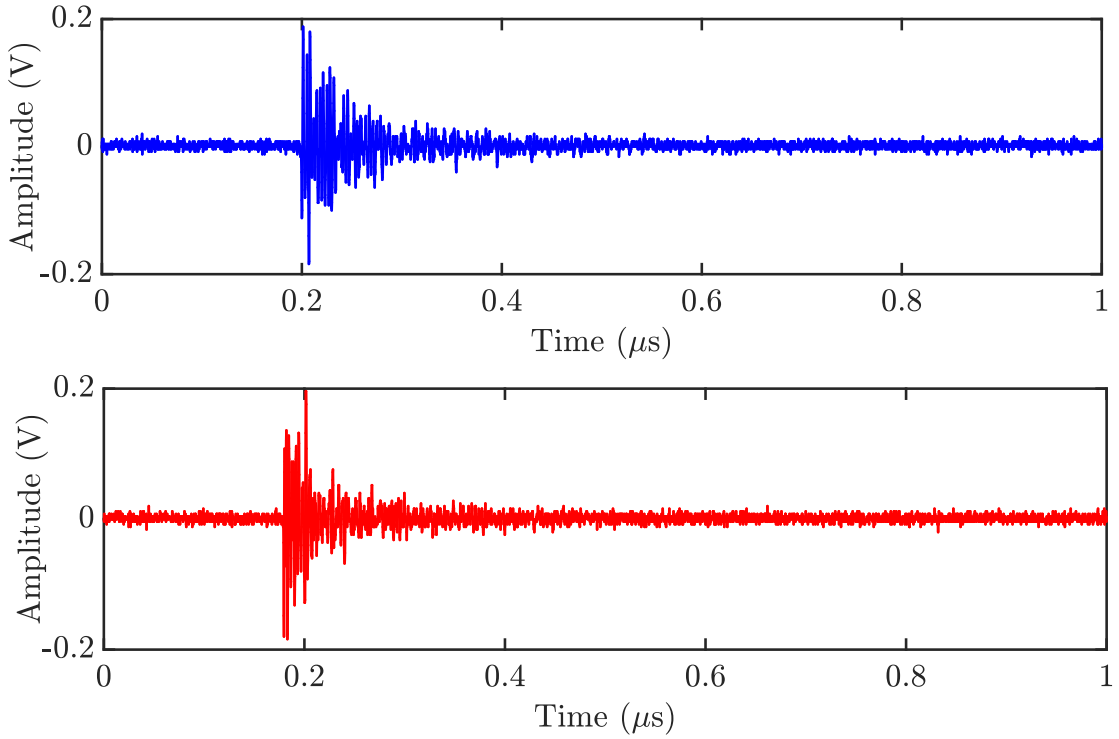

Figure 2.12: Simultaneous UHF signals from the same type of phenomenon in two different sections of a cable.

cable were placed in the right vertices of the square, see Figure 2.13. With this configuration, the emissions of each section provoke opposite TDoA between the antenna 1 and 2. Since the TDoA is defined as the difference of the ToF, then $t_{12} = t_1 - t_2$ where t_1 and t_2 are the ToF from the source to the antennas 1 and 2, respectively. These absolute times are unknown but the difference, t_{12}, can be measured from the data shown in Figure 2.12. When the section 1 emits, the radiation reaches the antenna 1 before the antenna 2 so $t_{12} < 0$. On the other hand, when the section 2 emits, the wave arrives to the antenna 2 before the antenna 1, so $t_{12} > 0$. Figure 2.14 shows the TDoA associated to each cluster demonstrating the correct performance of the separation and opening the possibility of labelling the clusters in Figure 2.10 as belonging to one section or the other depending on the sign of t_{12}.

2.6.2 FM radio and electrical interference

In this example, FM radio signals are disturbed by electromagnetic emissions provoked by electrical discharges. The target is to show the ability of the algorithm of discerning signals with similar levels of energy, [26]. These types of disturbances are very common in areas close to HV overhead lines and substations. Figure 2.15 shows an example of the acquired signals in the time domain with a SNR very close to unity, SNR = 1.15.

The results in Table 2.2 show that the best method would be again the ageing leader

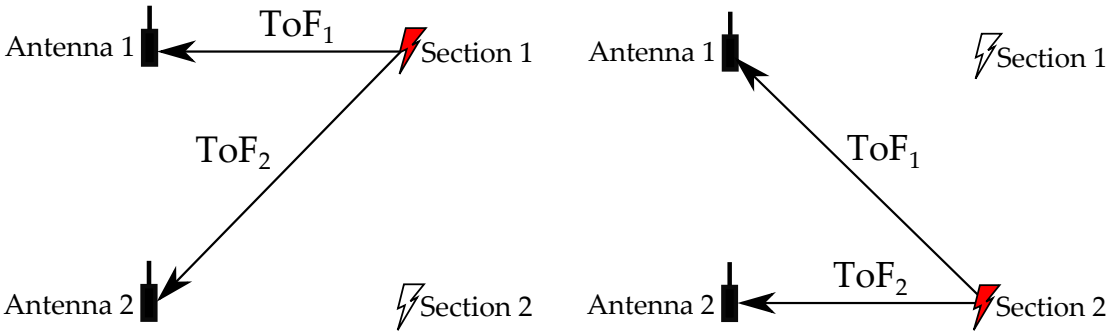

(a) ToF when emitter 1 is active. *(b)* ToF when emitter 2 is active.

Figure 2.13: Simultaneous UHF signals from the same type of phenomenon in two different sections of a cable.

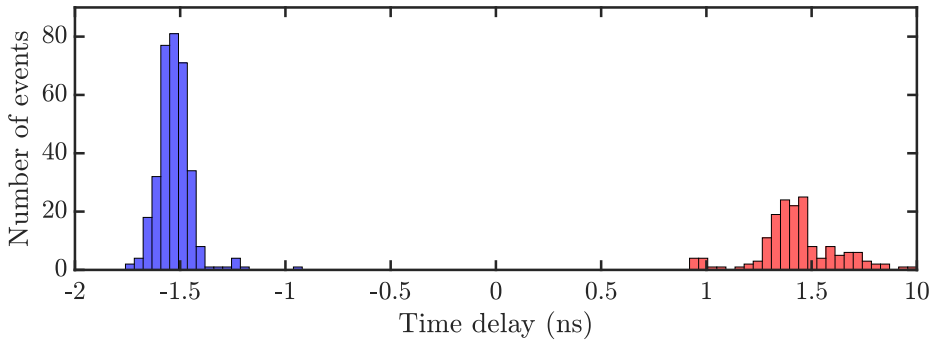

Figure 2.14: TDoA of the emissions to each antenna plotted by color for each cluster for the UHF signals case.

Table 2.2: Minima of the maxima distances achieved with every algorithm and their mean time of execution in seconds for the FM radio and electrical interference case.

Algorithm	Minimum distance	Execution time
σ_{PR} based	21.0	**0.6**
GA	22.2	3.6
PSO standard	31.4	2.9
PSO canonical	22.1	2.5
PSO time varying inertia	32.3	3.8
PSO aging leader	**33.6**	32.1

and challenger PSO. The selected intervals are f_{1L} = 5 MHz, f_{2L} = 15 MHz, f_{1H} = 82 MHz, f_{2H} = 98 and f_t = 98 MHz. In terms of execution time, the fastest algorithm is the σ_{PR} based algorithm. The resulting clusters of the ageing leader and challenger PSO are plotted in a PR map as shown Figure 2.16. The averaged spectra of the signals of each cluster are plotted in blue and red in Figure 2.17, the selected intervals are represented by black rectangles.

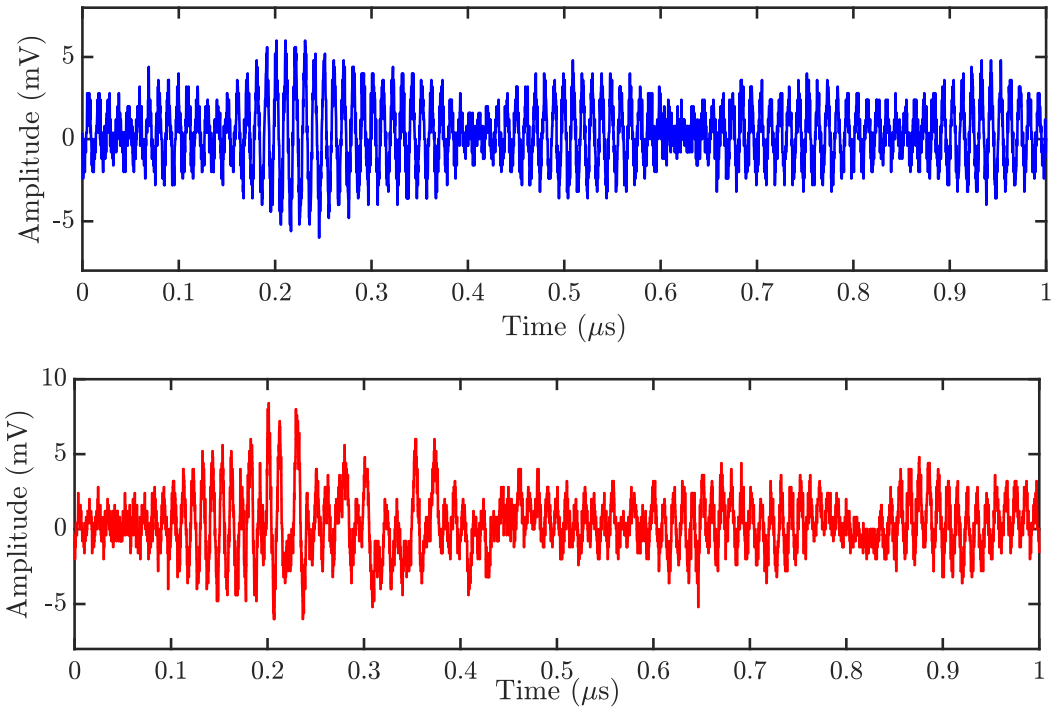

Figure 2.15: FM radio signals (blue) and electrical interference (red).

Notice that the algorithm has discarded almost all the common band with the highest power, so the considered interval would span from 1 to f_t = 98 MHz, see Figure 2.17. Then, it selects the PRL interval, $[f_{1L}, f_{2L}]$, where the power of the red signal is noticeable (15 %) and the power of the blue signal is very low. This places cluster 2 to the right of the map with higher PRL than cluster 1, in the left with low PRL, see Figure 2.16. Finally, the algorithm chooses the PRH interval where the blue signal has

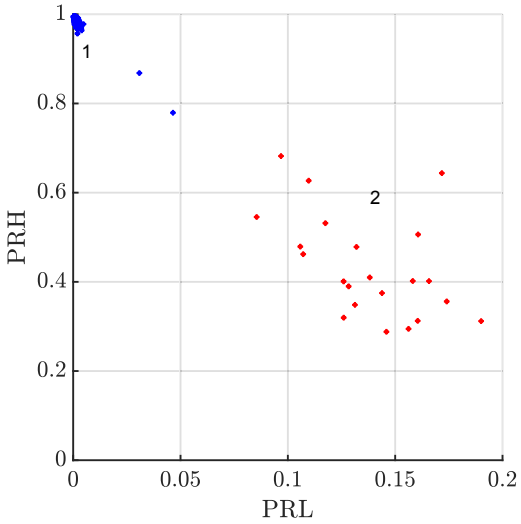

Figure 2.16: PR map with the clusters of the FM radio and electrical interference.

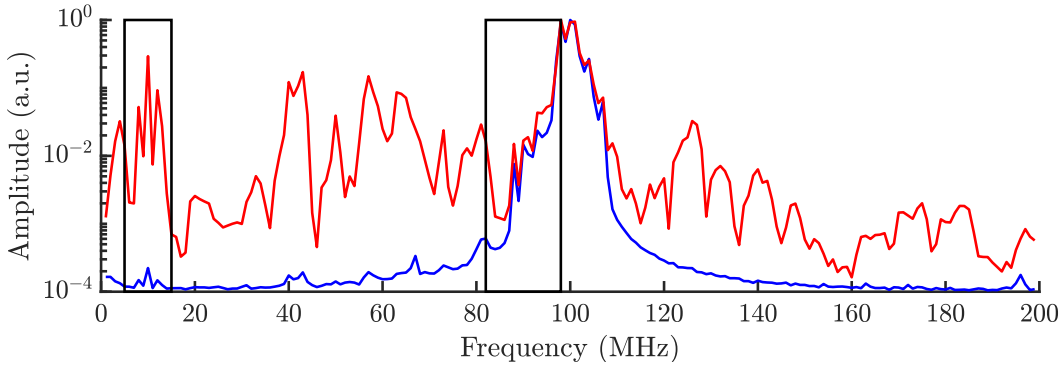

Figure 2.17: Average spectra of the pulses and the selected intervals that maximize the OF for the FM radio signals and electrical interference.

most of the power so pushes cluster 1 to the top of the map, highest PRH. Cluster 2 has less power in the PRH band (40 %) than cluster 1 (100 %) then cluster 1 is placed over cluster 2. The high dispersion in cluster 2 means that the energy of its signals have noticeable variations in the selected intervals.

The identification of the signals is easy because the disturbances have power in bands of frequency below the minimum FM radio frequency in 87.5 MHz, red line, whereas the FM radio spectrum is strictly confined in the 87.5 - 108 MHz band, blue line resulting in the smooth sinusoidal signals shown in blue in Figure 2.15. Moreover, signals in cluster 2 are very dispersive since disturbances have a stochastic nature and, hence, the spectral characteristics are not uniform. To assert these statements, taking a sample of a signal already classified in one of the clusters and analyzing its spectrum would label that cluster as FM radio or disturbance. In this case, the algorithm can help in cleaning FM radio or audio signals where the disturbances have low SNR.

2.6.3 Application of the PR maps to VHF signals generated by PD

PD measurement is a quite versatile technique for the detection of incipient ageing phenomena in the electrical insulation of electric machines and power cables [27]. However, the interpretation of results in presence of several type of signals is complex [28], and errors in this step may lead to unnecessary disconnections of the equipment or unexpected failures due to "false positive" or "negative" conclusions in the diagnosis, respectively. In this context, the identification of high-amplitude noise pulses and/or multiple simultaneously active PD sources is paramount for diagnosis. These situations are quite common in field measurements, making the well-known identification techniques based on the phase of the acquired signals like phase resolved partial discharge (PRPD) patterns almost useless [29]. However, there is a strong knowledge based on these patterns [27, 30, 31], that can be obtained with conventional detection systems using capacitive paths complying with the standards [32]. The PRPD pattern plots the amplitude of the pulses in phase with the fundamental sinusoid of the network signal [27]. Then, the amplitude and the phase of the PD signals are represented over one cycle of the alternating current (AC) signal. From the PRPD graphs different patterns can be identified and they can be associated to different kinds of PDs as internal, surface or corona. For all the aforementioned, there has been a strong research effort on pulse source identification by several means. Inductive sensors are used for this purpose, since they allow making measurements compatible with the international electrotechnical commission (IEC) standard and, in addition, they can measure and characterize pulse waveforms [29, 33]. One approach would be a direct identification of the pulse sources, but it requires the analysis of multiple parameters (related to PRPD patterns and pulse waveforms) that have to be statistically analyzed through complex machine learning techniques, and this requires a previous training [34]. A different focus tries to separate pulse sources to isolate each noise or PD source, whose PRPD could be easily diagnosed. This has been done in several works which used the successful time-frequency maps [29], wavelet analysis [35, 36] and S-transform [37] among others. With the same objective, the so-called spectral PR to separate PD and noise sources is proposed in previous works [11]. Despite the fact that PR maps have given good results for PD and noise separation in multiple experimental setups [11, 12], their capability for source separation is clearly dependent on the appropriate choice of the b frequency intervals, which could be difficult in certain experimental conditions where two clusters may be overlapped. The following experiments show the performance of the optimization techniques applied to the separation of different kinds of PD signals using PR maps which is an original work done during this thesis.

Figure 2.18: Point-plane electrode and winding coil.

Table 2.3: Minima of the maxima distances achieved with every algorithm and their mean time of execution in seconds for the VHF experiment with PD in winding coil, corona PD and noise.

Algorithm	Minimum distance	Execution time
σ_{PR} based	7.0	**1.2**
GA	7.5	4.7
PSO standard	**10.5**	2.3
PSO canonical	10.2	2.8
PSO time varying inertia	10.4	2.0
PSO aging leader	10.4	39.8

2.6.3.1 VHF signals: Winding coil, corona and noise

The signals used in this case are three different types of signals occurring simultaneously: pulses derived from PDs occurring inside a 300 kVA power transformer, corona discharges due to the ionization of a sharp point at HV and electrical noise. They are conducted pulses through a cable in the VHF range mixed with noise captured by the measuring system, [11]. An inductive sensor captures all signals together and the algorithm is capable of classifying them in three clusters maximizing the distance between them. Identifying these signals is interesting because it helps in detecting insulation problems in HV equipment, [38].

The elements of the setup are a point-plane electrode, to obtain corona PD, together with a coil of a power transformer, see Figure 2.18, to obtain surface PD and the electrical noise which comes from the environment. They are connected in parallel to obtain the three kinds of signals simultaneously. The trigger level is set so the noise could be captured during the acquisition.

The results of the worst case scenario, minima of the maximum OF throughout the 20 simulated cases, are summarized in Table 2.3 where the PSO algorithms report similar results in terms of minima OF. The algorithm based on σ_{PR} is again the one which converges to the solution faster than the others.

In this experiment, however slower than σ_{PR}, the best algorithm regarding the worst case scenario is the standard PSO. The resulting clusters are plotted in the PR map as shown in Figure 2.19. The selected set of frequencies, $f_{1L} = 0.25$ MHz, $f_{2L} =$

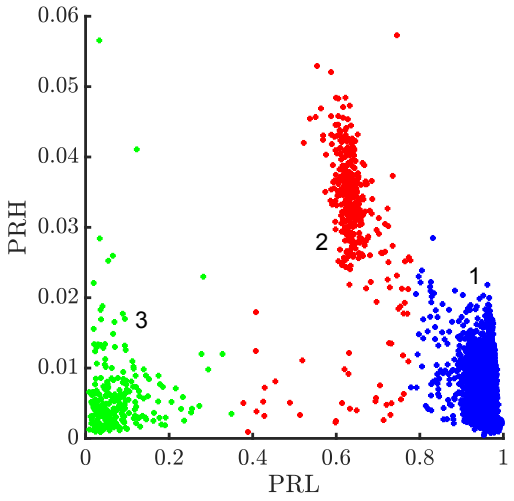

Figure 2.19: PR map with three clusters for the VHF experiment with PD in winding coil, corona PD and noise.

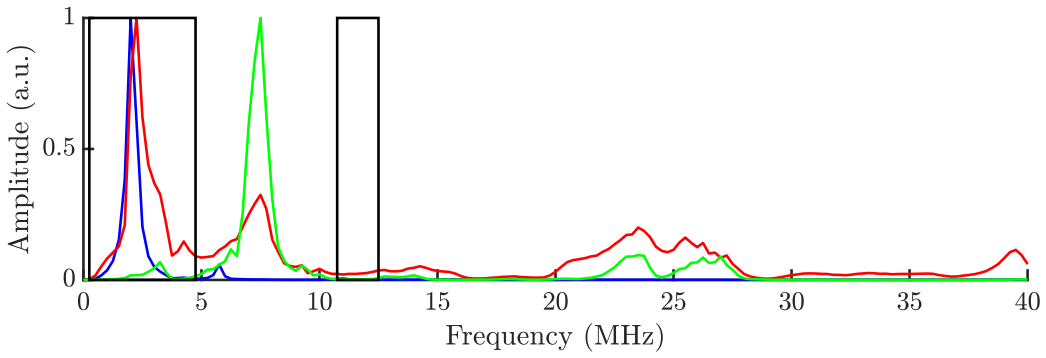

Figure 2.20: Average spectra of the pulses and the selected intervals that maximize the OF in the VHF experiment with PD in winding coil, corona PD and noise.

4.75 MHz, $f_{1H} = 10.75$ MHz, $f_{2H} = 12.5$ MHz and $f_t = 12.5$ MHz, was found to be the best option to maximize the OF obtaining a distance of 10.4. Figure 2.20 shows the average spectra of the signals in three clusters.

In this particular case, all clusters have low values for the parameter PRH. Most of the power is concentrated inside the PRL interval. The signals of cluster 1 have around $90 \sim 100$ % of their energy in the PRL and the signals of cluster 2 have around 60 % in it. Moreover, the selected bands have kept out power of the signals of cluster 3, then it is placed close to the origin in the PR map. The algorithms avoid to select the PRH in the interval $[7, 9]$ MHz, this selection would send cluster 3 to the top PRH but with high dispersion because of the fluctuations of the energy of the signals in these frequencies. The scattering of the clusters in the cluster reduces the MD and consequently the OF, this is the reason why the algorithm selects the PRH where the signals have low energy, low dispersion and results more compact clusters. There are dots in the PR map in

Figure 2.19 that are not close to any of the clouds and could be discarded. The k-means clustering algorithm used in these examples associates all points to a certain group so, even when those events can be considered outliers, they are assigned to a cluster.

The PR method does not identify the type of signal which should be done with additional information. Thus, at the moment, the only information we have is which signals and spectra correspond to which cluster but the origin of the signals is unknown. In this particular case, the nature of the electrical discharges can be known using the phase of the grid voltage in which the discharge occurs, explained at the beginning of Section 2.6.3. Then, selecting the elements of every cloud and plotting the PRPD patterns using the phase information, [31], it is possible to obtain the rest of plots in Figure 2.21. Particularly, the blue pattern in Figure 2.21 corresponds to cluster 1 in Figure 2.19 and it is identified as internal PD in the winding coil because they occur in both semi-cycles and close to the zero-crossings of the voltage. The red plot in Figure 2.21 corresponds to cluster 2 which is identified as corona PD because they occur only in one semi-cycle of sinusoidal voltage. Finally, the green plot in Figure 2.21 corresponds to cluster 3 which is noise because the pattern is not correlated with the voltage phase. Figure 2.22 shows an example of the three types of pulses. Notice that, though the SNR is pretty poor, the algorithm is again able to separate the different types of signals.

2.6.3.2 VHF signals: Conducting sphere on insulating sheet and point-plane electrode

For this case, the point-plane electrode arrangement used in the previous configuration, is connected in parallel to a conducting sphere (10 cm in diameter) placed over an insulating sheet of NOMEX paper (polyamide thick film). The separation in the point-plane electrode is adjusted to 5 cm. For this configuration, a stable PD activity is obtained at 8.6 kV. As in the previous experiment, the trigger level is set so the noise could be captured during the acquisition. Thus, three different sources and consequently three types of signals are simultaneously active again: two of them are PD and the other is noise.

Table 2.4 displays the results of the worst case scenario, minima of the maximum OF throughout the 20 simulated cases. The results of all PSO algorithms are close again but the best corresponds to the time varying inertia and the ageing leader and challenger. The algorithm based on σ_{PR} converges to the solution faster than the others in average.

The resulting clusters for the best among the results in Table 2.4 are plotted in the PR map shown in Figure 2.23. The selected set of frequencies, $f_{1L} = 2.75$ MHz, $f_{2L} = 11.5$ MHz, $f_{1H} = 14.5$ MHz, $f_{2H} = 20.5$ MHz and $f_t = 23.75$ MHz, were found to be the best option to maximize the OF obtaining a distance of 16.1. Figure 2.24 shows the average spectra of the signals of the three clusters.

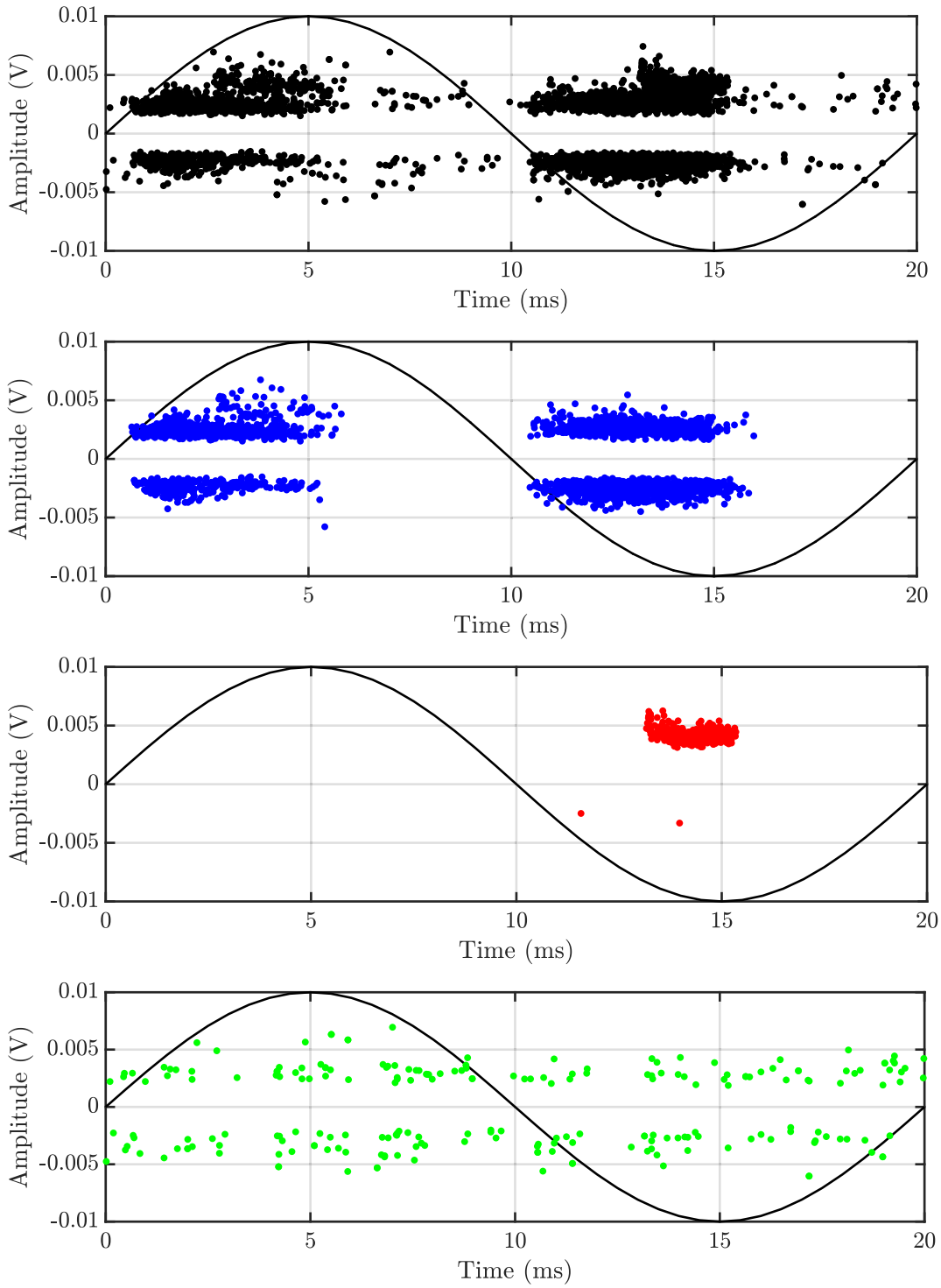

Figure 2.21: PRPD pattern in the third experiment. The black PRPD pattern represents the pattern of all the VHF signals together. The PD in winding coil PRPD pattern are represented in blue, corona PD in red and noise in green.

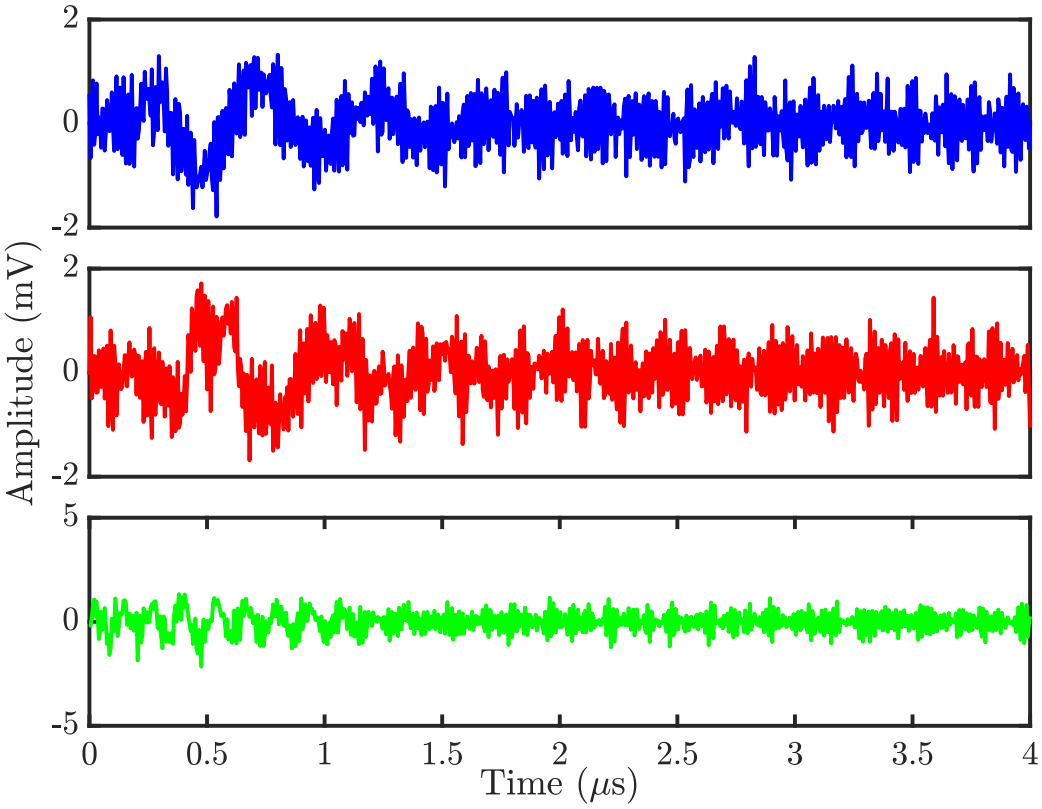

Figure 2.22: Signals in the time domain in the VHF experiment with PD in winding coil, corona PD and noise.

Table 2.4: Minima of the maxima distances achieved with every algorithm and their mean time of execution in seconds for the VHF signals: Conducting sphere on insulating sheet and point-plane electrode.

Algorithm	Minimum distance	Execution time
σ_{PR} based	9.2	**1.5**
GA	12.5	6.8
PSO standard	16.0	5.8
PSO canonical	15.7	2.5
PSO time varying inertia	**16.1**	5.0
PSO aging leader	**16.1**	58.9

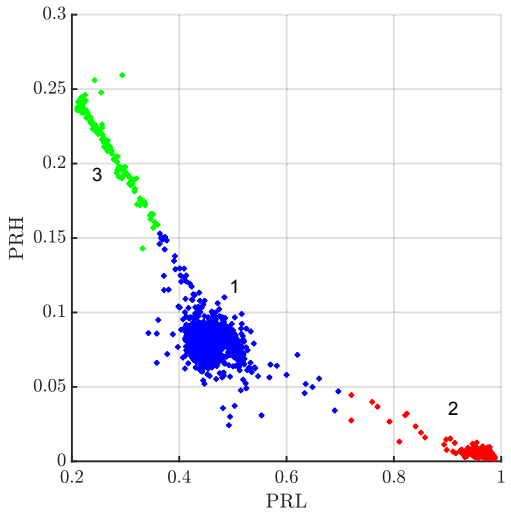

Figure 2.23: PR map with three clusters for the VHF experiment with PD in winding coil, corona PD and noise.

In this case, cluster 1 has 45 % of its energy in the PRL and around 5 $\sim$ 10 % in the PRH intervals, this result plots cluster 1 in the middle-bottom side in the PR map. Cluster 2 has all its energy in the PRL and almost nothing in the PRH interval. This fact places cluster 2 at the bottom right in the PR map. Cluster 3 has 20 % of its energy in PRH and 25 % in PRL interval. Since this cluster has the highest PRH and lowest PRL it is placed at the top left side of the PR map. Some scattered dots in the PR map in Figure 2.23 which are not clear what cluster they belong to could be discarded as in Subsection 2.6.3.1.

The signals can be identified using the phase information as in the previous example. The black PRPD pattern shown in Figure 2.25, where all the signals are displayed together, is difficult to analyze due to the agglomeration of points. The type of signal can be found applying the separation algorithm, selecting the clusters in the PR map, in Figure 2.23, and plotting the PRPD . The blue pattern in Figure 2.25 corresponds to cluster 1 and it is identified as corona PD because they occur only in one semi-cycle of the sinusoidal voltage. The red plot in Figure 2.25 corresponds to cluster 2 which is identified as noise because the pattern is not correlated with the voltage phase. Finally, the green plot in Figure 2.25, corresponds to cluster 3 which are PD in the conducting sphere because they occur in both semi-cycles and close to the zero-crossings of the voltage. Figure 2.26 shows an example of the three types of pulses.

2.7 Conclusions

The PR method can be applied to the classification of any type of signal as long as the information of interest is found in its spectral characteristics. Unlike other feature extraction techniques, the nature of the signal and the physical meaning of the outcome

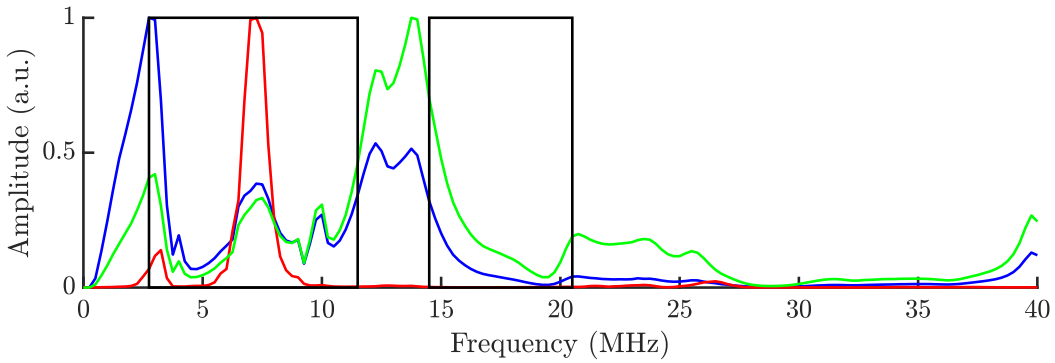

Figure 2.24: Average spectra of the pulses and the selected intervals that maximize the OF in the VHF signals: Conducting sphere on insulating sheet and point-plane electrode.

solution is preserved so further deductions on the results can be conducted. The spectral characterization has been limited to two bands of frequency to present clear and intuitive clusters in 2D plots. The algorithms produce a satisfactory classification without the supervision of any human operator and this fact has been demonstrate with the TDoA, spectra and with the PRPD patterns.

The k-means clustering technique has been found to be suitable in the tested cases though it can be further improved by including more sophisticated methods where it is not necessary to know the number of classes a priori or the borders of the clouds are better defined such as spectral clustering.

In the separation, other approaches can be followed such as to maximize the sum of the distances between clusters or maximize the area of a polygon whose vertices are the clusters centroid although the proposed as the minimum distance between clusters seems to be the best choice to define the OF. The distance is another variable in the method that can be tweaked. Currently, it is defined as the Mahalanobis distance to consider the dispersion of data inside the cluster. However, the method is open to the use of other similarity measures that capture prior knowledge about the problem.

During the process with the different algorithms, it has been found that the method is very sensitive to the selected components of the frequency intervals because the power spectra of the signals are usually very spiked. This means that changing one of the components of the frequency bands can move the positions of the clusters in the map from one place to another one far away. The result is that the separations achieved by any algorithm except σ_{PR} are not the same every time they are run. Nevertheless, after running all algorithms twenty times, all the frequency bands selected were those that gave the worst distances between clusters and, hence, the poorest separation of the signals. Even in this worst case scenario, those bands were sufficient to have the clusters clearly identified and separated.

The results of all algorithms in every experiment are shown in Table 2.5, where the minimum of the maximum OF is summarized throughout the 20 simulations. All PSO

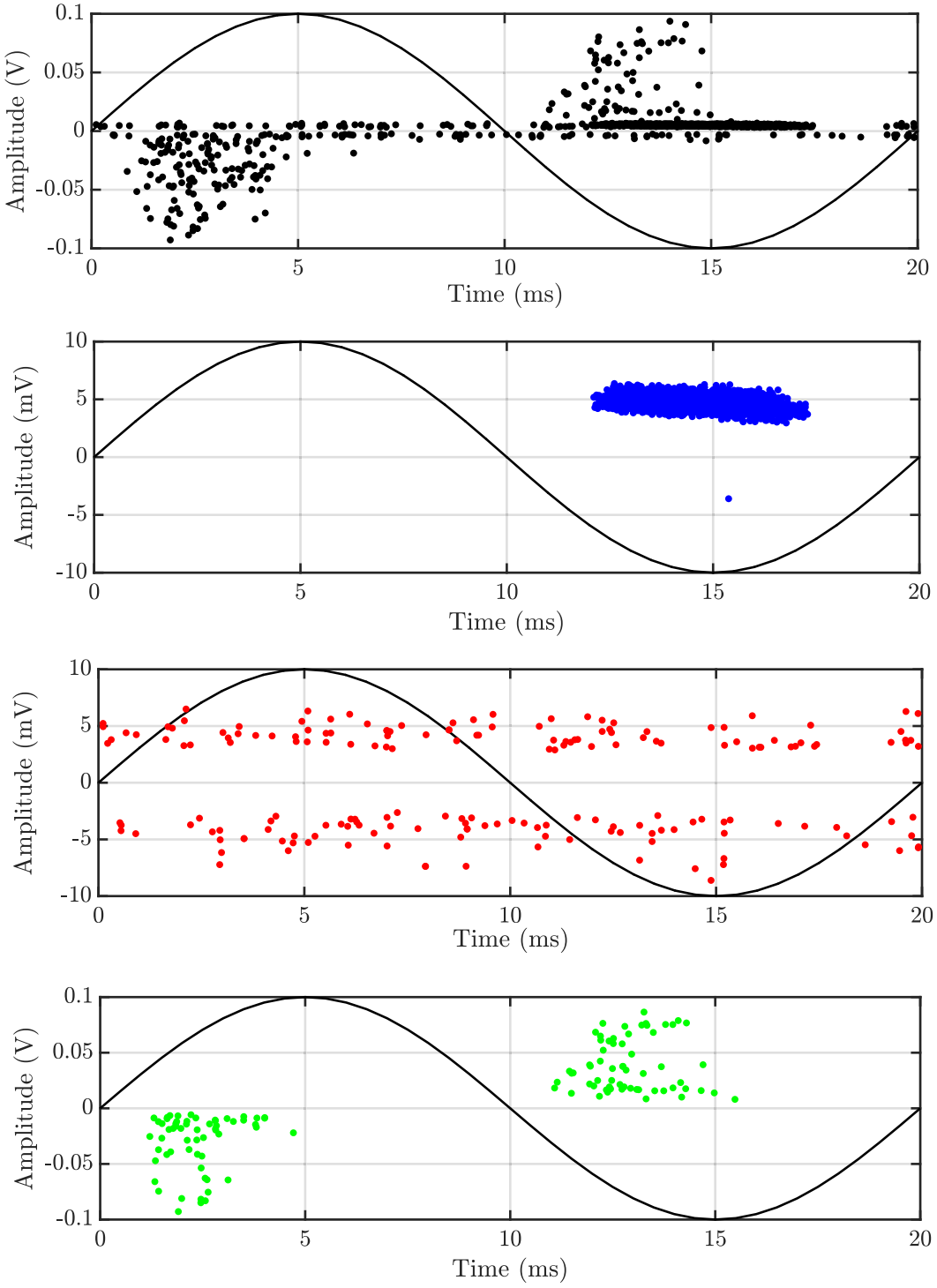

Figure 2.25: PRPD pattern in the fourth experiment. The black PRPD pattern represents the pattern of all the VHF signals together. The corona PD PRPD pattern is represented in blue, the noise in red and the PD generated in the sphere is represented in the green pattern.

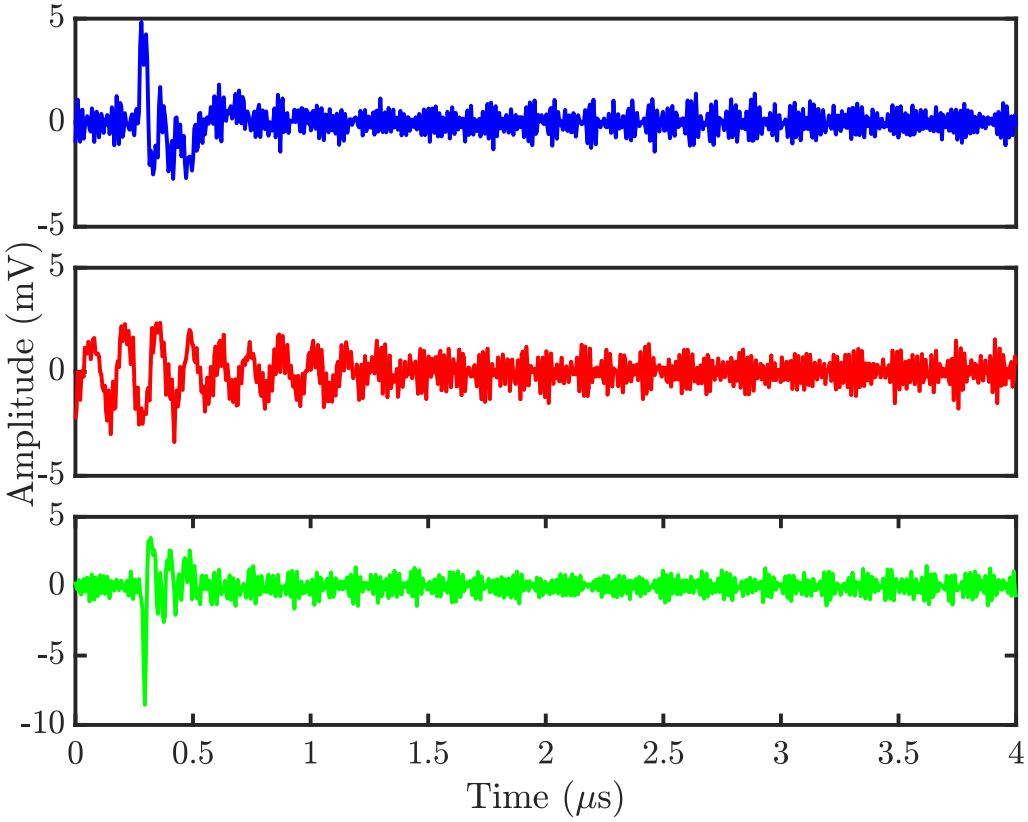

Figure 2.26: Signals in the time domain in the fourth experiment. The corona PD is plotted in blue, the noise in red and the PD example generated in the sphere is plotted in the green.

Table 2.5: Minima of the maxima distances achieved with every algorithm for all the cases.

Algorithm	Case UHF	Case FM	Case VHF 1	Case VHF 2
σ_{PR} based	19.7	21.0	7.0	9.2
GA	21.4	22.2	7.5	12.5
PSO standard	20.1	31.4	**10.5**	16.0
PSO canonical	17.9	22.1	10.2	15.7
PSO time varying inertia	14.5	32.3	10.4	**16.1**
PSO aging leader	**22.3**	**33.6**	10.4	**16.1**

Table 2.6: Time of execution in seconds for all the cases.

Algorithm	Case UHF	Case FM	Case VHF 1	Case VHF 2
σ_{PR} based	32.6	**0.6**	**1.2**	**1.5**
GA	4.4	3.6	4.7	6.8
PSO standard	4.3	2.9	2.3	5.8
PSO canonical	3.1	2.5	2.8	2.5
PSO time varying inertia	**2.2**	3.8	2.0	5.0
PSO aging leader	38.3	32.1	39.8	58.9

algorithms yield better results than σ_{PR} and GA algorithms but the ageing leader and challenger PSO method seems to achieve the best results. This algorithm is capable to explore larger areas of the solutions space, and escape from local maxima, thanks to the change of leader. However, the ageing leader and challenger PSO is slower than the others algorithms, see Table 2.6. If the computing time is an important constraint, other versions of PSO such as canonical or time varying inertia would be recommended.

The computational time in the σ_{PR} based algorithm varies depending on the spectrum bandwidth, BW, and the time window of the acquired signal, T_W. It might be worth noting that the execution time for the σ_{PR} method in the case of UHF signals is extremely high. The reason seems to be in the number of discrete frequencies in the spectra since in this case is 1000 while in the rest os experiments is 200 and below. Therefore, the number of cases to study by the algorithm is increased potentially. The σ_{PR} based algorithm works looking for the intervals where there is high dispersion in the energy of all kinds of signals together. This fact could provoke the selection of an interval which selects the frequency band where one kind of signal is highly dispersive. This will plot a high scattered cluster in the PR map and furthermore poor values in the OF since the MD decreases when decreases the dispersion of the clusters.

2.8 Bibliography

[1] A. V. Oppenheim, A. S. Willsky, and S. H. Nawab. *Signals & Systems (2nd Ed.)* Upper Saddle River, NJ, USA: Prentice-Hall, Inc., 1996. ISBN: 9780138147570 (cit. on p. 10).

[2] L. Van Der Maaten, E. Postma, and J. Van den Herik. "Dimensionality reduction: a comparative". In: *J Mach Learn Res* 10 (2009), pp. 66–71 (cit. on p. 10).

[3] N. Zhou, H. Cheng, W. Pedrycz, et al. "Discriminative sparse subspace learning and its application to unsupervised feature selection". In: *ISA Transactions* 61 (Mar. 2016), pp. 104–118. ISSN: 0019-0578. DOI: 10.1016/j.isatra.2015.12.011. URL: http://www.sciencedirect.com/science/article/pii/S0019057815003158 (cit. on p. 10).

[4] R. Tibshirani. "Regression Shrinkage and Selection via the Lasso". In: *Journal of the Royal Statistical Society. Series B (Methodological)* 58.1 (1996), pp. 267–288. ISSN: 0035-9246. URL: http://www.jstor.org/stable/2346178 (cit. on p. 11).

[5] K. Fujiwara and M. Kano. "Efficient input variable selection for soft-senor design based on nearest correlation spectral clustering and group Lasso". In: *ISA Transactions* 58 (Sept. 2015), pp. 367–379. ISSN: 0019-0578. DOI: 10.1016/j.isatra.2015.04.007. URL: http://www.sciencedirect.com/science/article/pii/S0019057815001044 (cit. on p. 11).

[6] I. Guyon, J. Weston, S. Barnhill, et al. "Gene Selection for Cancer Classification using Support Vector Machines". en. In: *Machine Learning* 46.1-3 (Jan. 2002), pp. 389–422. ISSN: 0885-6125, 1573-0565. DOI: 10.1023/A:1012487302797. URL: https://link.springer.com/article/10.1023/A:1012487302797 (cit. on p. 11).

[7] K Pearson. "On lines and planes of closest fit to systems of points in space". In: *Philosophical Magazine* 2.6 (1901), pp. 559–572 (cit. on p. 11).

[8] P. Ralston, G. DePuy, and J. H. Graham. "Graphical enhancement to support PCA-based process monitoring and fault diagnosis". In: *ISA Transactions* 43.4 (Oct. 2004), pp. 639–653. ISSN: 0019-0578. DOI: 10.1016/S0019-0578(07)60174-8. URL: http://www.sciencedirect.com/science/article/pii/S0019057807601748 (cit. on p. 11).

[9] G. C. Reinsel. *Multivariate reduced-rank regression : theory and applications /*. New York : Springer, 1998. ISBN: 9780387986012 (cit. on p. 11).

[10] L. v. d. Maaten and G. Hinton. "Visualizing Data using t-SNE". In: *Journal of Machine Learning Research* 9.Nov (2008), pp. 2579–2605. ISSN: ISSN 1533-7928. URL: http://www.jmlr.org/papers/v9/vandermaaten08a.html (cit. on p. 11).

[11] J. Ardila-Rey, J. Martínez-Tarifa, G. Robles, et al. "Partial discharge and noise separation by means of spectral-power clustering techniques". In: *IEEE Transactions on Dielectrics and Electrical Insulation* 20.4 (Aug. 2013), pp. 1436–1443. ISSN: 1070-9878. DOI: 10.1109/TDEI.2013.6571466 (cit. on pp. 13, 35, 36).

[12] J. M. Martínez-Tarifa, J. A. Ardila-Rey, and G. Robles. "Partial discharge source recognition by means of clustering of spectral power ratios". en. In: *Measurement Science and Technology* 24.12 (2013), p. 125605. ISSN: 0957-0233. DOI: 10.1088/0957-0233/24/12/125605. URL: http://stacks.iop.org/0957-0233/24/i=12/a=125605 (cit. on pp. 13, 35).

[13] D. Xu and Y. Tian. "A Comprehensive Survey of Clustering Algorithms". en. In: *Annals of Data Science* 2.2 (June 2015), pp. 165–193. ISSN: 2198-5804, 2198-5812. DOI: 10.1007/s40745-015-0040-1. URL: http://link.springer.com/article/10.1007/s40745-015-0040-1 (cit. on p. 14).

[14] J. M. Martinez-Tarifa, J. A. Ardila-Rey, and G. Robles. "Automatic selection of frequency bands for the power ratios separation technique in partial discharge measurements: part I, fundamentals and noise rejection in simple test objects". In: *IEEE Transactions on Dielectrics and Electrical Insulation* 22.4 (Aug. 2015), pp. 2284–2291. ISSN: 1070-9878. DOI: 10.1109/TDEI.2015.004821 (cit. on pp. 15, 16).

[15] J. A. Ardila-Rey, J. M. Martinez-Tarifa, and G. Robles. "Automatic selection of frequency bands for the power ratios separation technique in partial discharge measurements: part II, PD source recognition and applications". In: *IEEE Transactions on Dielectrics and Electrical Insulation* 22.4 (Aug. 2015), pp. 2293–2301. ISSN: 1070-9878. DOI: 10.1109/TDEI.2015.004822 (cit. on p. 16).

[16] D. E. Goldberg and J. H. Holland. "Genetic Algorithms and Machine Learning". en. In: *Machine Learning* 3.2-3 (Oct. 1988), pp. 95–99. ISSN: 0885-6125, 1573-0565. DOI: 10.1023/A:1022602019183. URL: http://link.springer.com/article/10.1023/A:1022602019183 (cit. on pp. 18, 28).

[17] J. Kennedy and R. Eberhart. "Particle swarm optimization". In: *, IEEE International Conference on Neural Networks, 1995. Proceedings*. Vol. 4. Nov. 1995, 1942–1948 vol.4. DOI: 10.1109/ICNN.1995.488968 (cit. on pp. 20, 22).

[18] R. Poli, J. Kennedy, and T. Blackwell. "Particle swarm optimization". en. In: *Swarm Intelligence* 1.1 (June 2007), pp. 33–57. ISSN: 1935-3812, 1935-3820. DOI: 10.1007/s11721-007-0002-0. URL: https://link.springer.com/article/10.1007/s11721-007-0002-0 (cit. on p. 22).

[19] M. Clerc and J. Kennedy. "The particle swarm - explosion, stability, and convergence in a multidimensional complex space". In: *IEEE Transactions on Evolutionary Computation* 6.1 (Feb. 2002), pp. 58–73. ISSN: 1089-778X. DOI: 10.1109/4235.985692 (cit. on p. 23).

[20] Y. Shi and R. C. Eberhart. "Parameter selection in particle swarm optimization". en. In: *Evolutionary Programming VII*. Springer, Berlin, Heidelberg, Mar. 1998, pp. 591–600. DOI: 10.1007/BFb0040810. URL: https://link.springer.com/chapter/10.1007/BFb0040810 (cit. on pp. 23, 24).

[21] R. P. Singh, V. Mukherjee, and S. P. Ghoshal. "Particle swarm optimization with an aging leader and challengers algorithm for the solution of optimal power flow problem". In: *Applied Soft Computing* 40 (Mar. 2016), pp. 161–177. ISSN: 1568-4946. DOI: 10.1016/j.asoc.2015.11.027. URL: http://www.sciencedirect.com/science/article/pii/S1568494615007450 (cit. on pp. 23–25).

[22] D. Bratton and J. Kennedy. "Defining a Standard for Particle Swarm Optimization". In: *2007 IEEE Swarm Intelligence Symposium*. Apr. 2007, pp. 120–127. DOI: 10.1109/SIS.2007.368035 (cit. on p. 24).

[23] W. N. Chen, J. Zhang, Y. Lin, et al. "Particle Swarm Optimization With an Aging Leader and Challengers". In: *IEEE Transactions on Evolutionary Computation* 17.2 (Apr. 2013), pp. 241–258. ISSN: 1089-778X. DOI: 10.1109/TEVC.2011.2173577 (cit. on p. 25).

[24] G. Robles, M. Sánchez-Fernández, R. A. Sánchez, et al. "Antenna Parametrization for the Detection of Partial Discharges". In: *IEEE Transactions on Instrumentation and Measurement* 62.5 (May 2013), pp. 932–941. ISSN: 0018-9456. DOI: 10.1109/TIM.2012.2223332 (cit. on p. 28).

[25] G. Robles, J. M. Fresno, and J. M. Martínez-Tarifa. "Separation of Radio-Frequency Sources and Localization of Partial Discharges in Noisy Environments". en. In: *Sensors* 15.5 (Apr. 2015), pp. 9882–9898. DOI: 10.3390/s150509882. URL: http://www.mdpi.com/1424-8220/15/5/9882 (cit. on p. 29).

[26] R. Albarracin, G. Robles, J. M. Martinez-Tarifa, et al. "Separation of sources in radiofrequency measurements of partial discharges using time–power ratio maps". In: *ISA Transactions* 58 (Sept. 2015), pp. 389–397. ISSN: 0019-0578. DOI: 10.1016/j.isatra.2015.04.006. URL: http://www.sciencedirect.com/science/article/pii/S0019057815001032 (cit. on p. 31).

[27] F. H. Kreuger. *Partial discharge detection in high-voltage equipment*. en. Google-Books-ID: GOdSAAAAMAAJ. Butterworths, 1989. ISBN: 9780408020633 (cit. on p. 35).

[28] G. C. Stone and V. Warren. "Effect of manufacturer, winding age and insulation type on stator winding partial discharge levels". In: *IEEE Electrical Insulation Magazine* 20.5 (Sept. 2004), pp. 13–17. ISSN: 0883-7554. DOI: 10.1109/MEI.2004.1342428 (cit. on p. 35).

[29] A. Cavallini, G. C. Montanari, A. Contin, et al. "A new approach to the diagnosis of solid insulation systems based on PD signal inference". In: *IEEE Electrical Insulation Magazine* 19.2 (Mar. 2003), pp. 23–30. ISSN: 0883-7554. DOI: 10.1109/MEI.2003.1192033 (cit. on p. 35).

[30] C. Hudon and M. Belec. "Partial discharge signal interpretation for generator diagnostics". In: *IEEE Transactions on Dielectrics and Electrical Insulation* 12.2 (Apr. 2005), pp. 297–319. ISSN: 1070-9878. DOI: 10.1109/TDEI.2005.1430399 (cit. on p. 35).

[31] CIGRE. "Recognition of Discharges". In: *Electra* (1969) (cit. on pp. 35, 38).

[32] I. 60270. "High Voltage Test Techniques. Partial Discharge Measurements". In: 3.0Ed (2000) (cit. on p. 35).

[33] J. M. Martínez-Tarifa, G. Robles, M. V. Rojas-Moreno, et al. "Partial discharge pulse shape recognition using an inductive loop sensor". en. In: *Measurement Science and Technology* 21.10 (2010), p. 105706. ISSN: 0957-0233. DOI: 10.1088/0957-0233/21/10/105706. URL: http://stacks.iop.org/0957-0233/21/i=10/a=105706 (cit. on p. 35).

[34] J. A. Hunter, P. L. Lewin, L. Hao, et al. "Autonomous classification of PD sources within three-phase 11 kV PILC cables". In: *IEEE Transactions on Dielectrics and Electrical Insulation* 20.6 (Dec. 2013), pp. 2117–2124. ISSN: 1070-9878. DOI: 10.1109/TDEI.2013.6678860 (cit. on p. 35).

[35] L. Hao, P. L. Lewin, and S. G. Swingler. "Improving detection sensitivity for partial discharge monitoring of high voltage equipment". en. In: *Measurement Science and Technology* 19.5 (2008), p. 055707. ISSN: 0957-0233. DOI: 10.1088/0957-0233/19/5/055707. URL: http://stacks.iop.org/0957-0233/19/i=5/a=055707 (cit. on p. 35).

[36] X. Ma, C. Zhou, and I. J. Kemp. "Interpretation of wavelet analysis and its application in partial discharge detection". In: *IEEE Transactions on Dielectrics and Electrical Insulation* 9.3 (June 2002), pp. 446–457. ISSN: 1070-9878. DOI: 10.1109/TDEI.2002.1007709 (cit. on p. 35).

[37] K. Wang, J. Li, S. Zhang, et al. "A hybrid algorithm based on s transform and affinity propagation clustering for separation of two simultaneously artificial partial discharge sources". In: *IEEE Transactions on Dielectrics and Electrical Insulation* 22.2 (Apr. 2015), pp. 1042–1060. ISSN: 1070-9878. DOI: 10.1109/TDEI.2015.7076806 (cit. on p. 35).

[38] R. E. James and Q. Su. *Condition Assessment of High Voltage Insulation in Power System Equipment*. IET Digital Library, Jan. 2008. ISBN: 9780863419898. URL: http://digital-library.theiet.org/content/books/po/pbpo053e (cit. on p. 36).

Chapter 3

Calculating the onset and time delay of pulsed signals

3.1 Abstract

As it will be shown in Chapters 4 and 5, it is of paramount importance the ability to measure the onset of the pulsed signals, also named relative ToF or time of arrival (ToA), of the signals from the emitter to the receiver with a high level of confidence. These variables and the TDoA, are used to locate emitting sources. Small errors in their estimation can give large errors in the localization, shifting the calculated emitter position far from the actual position. The main causes of error are due to unclear wavefronts that can be hidden in noise or contaminated with interferences by high frequency components. In addition, obstacles in the direct path to the sensors or antennas can attenuate or hinder the wavefront and reflections can create positive interferences that give peaks long past the first front.

In this thesis, the performance of seven methods to estimate the relative ToF and two to estimate the TDoA of the emissions have been analyzed and a new algorithm based on the cumulative kurtosis of the signals has been developed. In the study presented, the actual values of the relative ToF and TDoA are known because the geometry of the emitters and receivers has been arranged in a laboratory. So the estimated results of the algorithms are evaluated when compared with the real solution.

The algorithms are used in two applications: to measure the muscle depth to estimate the positions of bones (one dimension (1D) location) and in the localization of emitters in 3D. In the first application, the experiments are made using both simple setups used for calibration purposes and real human tissues to test the performance of the algorithms. In the second application, the experiments are done in a high-voltage laboratory to locate the origin of PD in insulations. In this case, four antennas or sensors are needed to carry out the localization in 3D. The performance of the algorithms is evaluated comparing the theoretical TDoA with the estimated one.

Finally, after testing several methods and processing the algorithms for both accuracy and repeatability, the Hinkley algorithm, presented in Subsection 3.3.5 and the proposed in this thesis, minimum time series cumulative kurtosis, presented in Subsection 3.5, were found to be the most appropriate in the case of measuring bone depths in-vivo and in the case of emitter localization in 3D. The results also show that the method used to process the data to evaluate the TDoA of the signals can significantly affect the outcome of the measurements.

3.2 Introduction

In many applications, it is of interest to localize emitters with antennas or sensors. Some examples of applications are earthquake epicenter location [1], detection, [2], electrical engineering [3, 4], tumor localization [5]. In this thesis, muscle depth estimation and RF emitter localization are the applications analyzed. In the first application there is no need to separate the acquired signals because the experimental setup only acquires signals of interest. On the other hand, in the second experiment, the RF emissions of interest are mixed with environmental noise, so it is necessary to apply previously the techniques shown in Chapter 2.

The localization bases its principle of work on the fact that the distance traveled by an emission D_i between the emitter and the i^{th} receiver, it is equal to the time spent by the emission in the trip, t_i, multiplied by the speed of propagation of the transmission medium, v, as represented in Equation (3.1).

$$D_i = v \cdot t_i \tag{3.1}$$

In some applications, as in PD source localization, the instant when the emission departs is unknown, so the ToF can not be calculated. Therefore, when the algorithm of ToF estimation are used over acquired signals, the results are referred as relative ToF. Using the TDoA variables, Equation (3.1) is modified to Equation (3.2).

$$D_{ij} = D_i - D_j = v \cdot t_{ij} \tag{3.2}$$

where:

$$\begin{aligned} D_i &= \|\mathbf{P_s} - \mathbf{P_i}\| = \sqrt{(x_s - x_i)^2 + (y_s - y_i)^2 + (z_s - z_i)^2} \\ D_j &= \|\mathbf{P_s} - \mathbf{P_j}\| = \sqrt{(x_s - x_j)^2 + (y_s - y_j)^2 + (z_s - z_j)^2} \end{aligned} \tag{3.3}$$

being $\mathbf{P_s} = (x_s, y_s, z_s)$ the source position, $\mathbf{P_i} = (x_i, y_i, z_i)$ the i antenna position and $\mathbf{P_j} = (x_j, y_j, z_j)$ the j antenna position. The t_{ij} is the difference of times spent by the emission in travel from the emitter to the i and j receivers. D_{ij} is the distance difference from the emitter to the i and j receivers. A graphic representation of the ToF and TDoA is shown in Figure 3.1.

The estimation of the ToF and TDoA is not always clear because many factors may provoke uncertainties and errors in the estimation of these time variables. Some causes are the own nature of the signal, the measuring process and the geometry and radiation characteristics of the receiver. Because of these issues, a special effort was put in this stage of the algorithm to obtain the most accurate solutions and several methods to obtain TDoA were tested. In Chapter 5, there is a deep analysis of the TDoA error and their propagation in the 3D source location. In this chapter, the results of the different algorithms are evaluated when compared with the real solution because the position of the sensors and the reflecting surface in 1D localization or the emitter position in

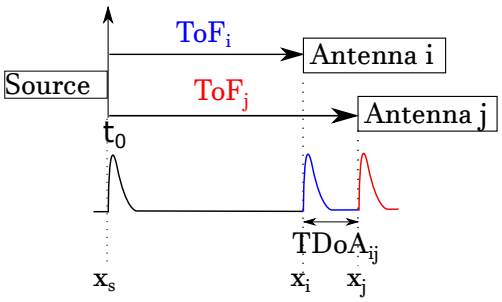

Figure 3.1: ToF and TDoA representation in 1D localization.

3D localization are known. This allows us to know which algorithms report the best accuracy in different applications with several kinds of signals.

The remainder of the chapter is organized as follows: Section 3.3 and 3.4 explain and detail the formulation of the most common algorithms used to calculate the ToF and TDoA, respectively, for pulsed signals. Section 3.5 presents a new algorithm derived from one of the algorithms which already exists, improving the accuracy of the TDoA calculus. Section 3.6 and 3.7 shows the performance of the algorithms presented in the previous sections in two applications; muscle depth estimation and RF emitter localization respectively. Finally, Section 3.8 draws the main conclusions of the work.

3.3 Time of flight (ToF)

In this section, several methods used in different applications to calculate the onset, relative ToF or ToA of pulsed signals are compiled and explained. The processed signals are in the discrete domain then the signal is denoted as $s(n)$ where n is, now, the sample in the discrete domain.

As explained before, instant when the acquired signals departs is not known and the acquisition system starts to capture the waves in a concrete instant different to the signal departure, the time variable estimated by the algorithms shown in this subsection is the relative ToF, and it is represented by t'.

3.3.1 Maximum value of the signal

This algorithm is the most straightforward method and can be easily implemented. The onset of the signal is defined as the sample where the maximum absolute value of the signal, positive or negative, is reached, see Equation (3.4) [6, 7].

$$t' = \arg\max(|s(n)|) \tag{3.4}$$

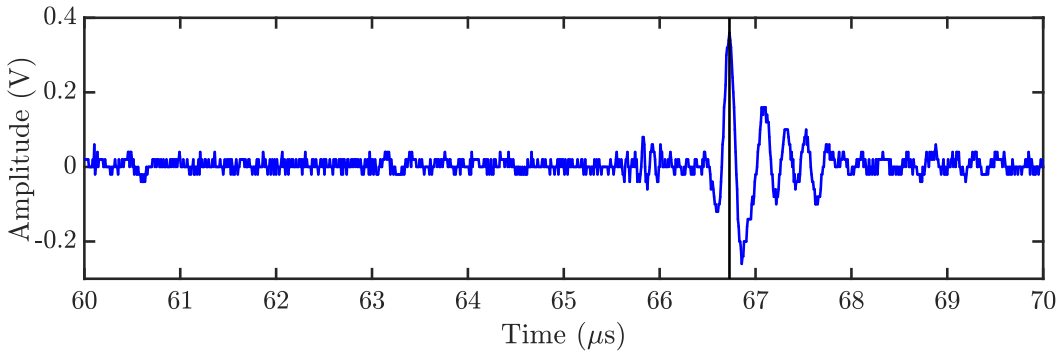

Figure 3.2: Detail of the time of occurrence of the maximum peak to determine the relative ToF. The vertical line represents the onset of the signal using the maximum peak algorithm.

This algorithm works properly under ideal conditions in which multipath reflections are strongly damped and the propagation media is homogeneous. Under these circumstances, the results would be repeatable and precise but not necessarily accurate, or close to the correct solution. The accuracy will depend on the rise time of the front wave of the emission and, consequently, on its attenuation, and change of slope, when the wave travels through more dispersive media. Any deviation from these conditions would induce systematic and random errors to the measurements jeopardizing the robustness of this method. Figure 3.2 shows an example of this algorithm for the relative ToF calculation.

3.3.2 Threshold

This algorithm can be implemented in different modalities. The simplest threshold algorithm defines the onset of the pulsed signal as the sample when the signal overpass the defined level of amplitude [7, 8]. Figure 3.3 shows an example of how this method works.

The threshold is usually defined as a percentage of the maximum amplitude of the signal. In the simulations carried out in this thesis, the threshold is defined as the 50% of the maximum value of the signal. This algorithm used in signals with low SNR can set the relative ToF erroneously in the noise previous to the pulsed signal. Other weakness of threshold algorithm is the rise time of the pulsed signal. It can introduce an undesired delay or advance in the relative ToF estimation if the analyzed signals have different onset slopes.

3.3.3 Threshold Slope

To avoid the possible source of error of the threshold algorithm, shown in Subsection 3.3.2, the slope of the pulsed signal is taken in to account at the point where the signal overpass the threshold [8].

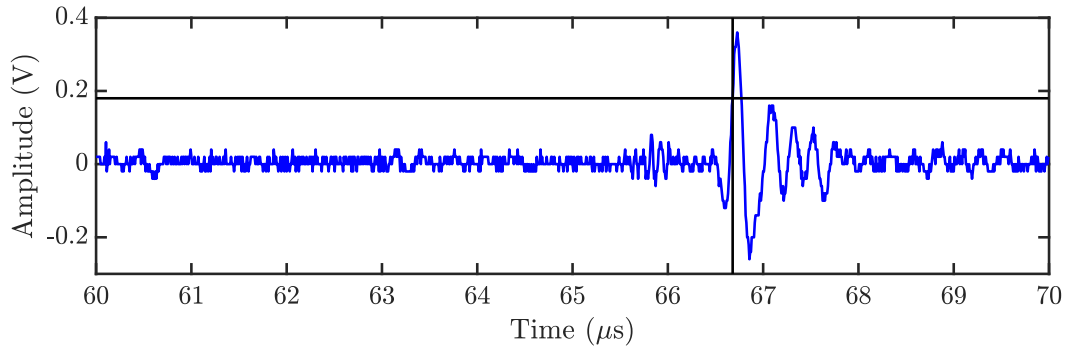

Figure 3.3: Relative ToF estimation through threshold algorithm. The horizontal black line is the threshold and the vertical black line is the onset of the signal calculated with threshold algorithm.

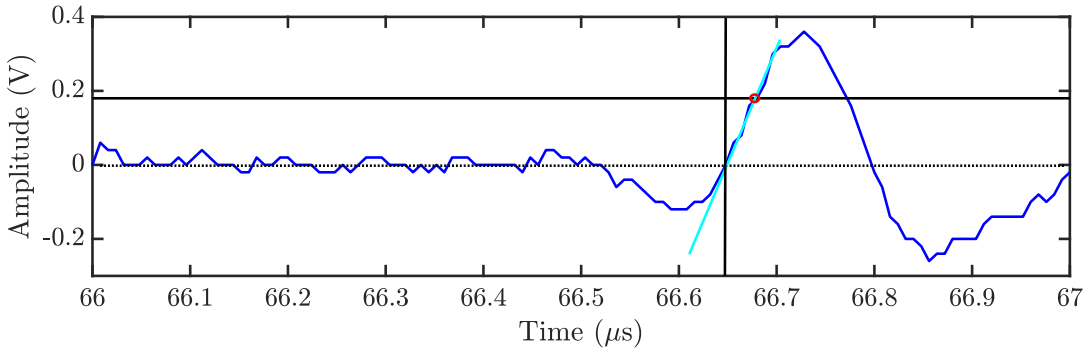

Figure 3.4: Relative ToF estimation through threshold algorithm corrected with the signal slope. The horizontal black line is the threshold, the red circle represents the onset of the signal estimated with the threshold algorithm. The cyan line is the slope of the signal at the onset and the vertical black line is the relative ToF with this algorithm.

This modification of the threshold algorithm defines the onset of the pulsed signal in three steps. The first step is to calculate the sample n where the signal overpass the threshold. The second step is to calculate the slope, p of the signal s at $s(n)$. In the last step, the relative ToF is calculated as the zero crossing of the straight line which passes through $s(n)$ with the slope calculated in the second step. The relative ToF is obtained through Equation (3.5). Figure 3.4 shows an example on how this method works. The horizontal black line is the threshold and its cross with the signal is the position $(n, s(n))$ defined as the onset of the signal, represented by a red circle. The cyan line is the slope of the signal s at $s(n)$ and the vertical black line is the relative ToF with this algorithm.

$$t' = n - \frac{2 \cdot s(n)}{s(n+1) - s(n-1)} \tag{3.5}$$

The algorithms based on threshold have some disadvantages, the main is the definition of the value of the threshold. It is not an easy task and it affects directly in the relative ToF estimation. Under real conditions, these algorithms can fall down in the

same problems than the algorithm shown in Subsection 3.3.1 decreasing the accuracy in the relative ToF estimation.

3.3.4 Maximum derivative of the cumulative energy of the signal (MDCE)

This algorithm bases its relative ToF estimation in the energy of the noise and the energy of the impulsive signal. Since the emissions are usually acquired with noise, the signal can be divided in two parts. The first one is the background noise and the second part is the impulsive signal overlapped to the noise. The amplitude of the pulse is larger than the amplitude of first part of the signal, then the energy is also greater in the second part of the wave. A proportional measure of the power of the acquired signal is calculated squaring the original signal. To obtain the energy in a concrete time interval, it is needed to sum the power in that interval. So calculating the cumulative sum of the power, the cumulative energy of the acquired emission is obtained, see Equation (3.6). The onset of the signal produces a knee where the cumulated energy increase suddenly [9]. Thus the onset of the signal is defined as the point where the cumulative signal has the largest derivative [10], see Equation (3.7).

$$E_c(n) = \sum_{m=1}^{N} s^2(m), \qquad n = 1, 2, \dots N \tag{3.6}$$

where N is the total number of samples

$$t' = \arg\max\left(\frac{\partial E_c(n)}{\partial n}\right) \tag{3.7}$$

Figure 3.5 shows an example of the acquired signals in blue represented in Volts and their cumulative energy in red, the units are proportional to $t \cdot V^2$ where V represents the amplitude of the signal in Volts. It can be clearly seen the boost in the cumulative energy when the onset of the pulse occurs. Figure 3.6 shows the cumulative energy in blue and its derivative in red, in units $\propto t \cdot V^2/\partial t$. Figure 3.7 merges the original signal in blue and the derivative of the cumulated signal in red. Finally, the relative ToF of the signal is represented in Figure 3.7 by the vertical black line, which corresponds with the maximum of the derivative.

In some cases, when there are noticeable oscillations before the sharp impulse, this method produces early onsets estimation. Subsection 3.3.5 shows an improvement on the calculus of the relative ToF which tries to avoid this drawback.

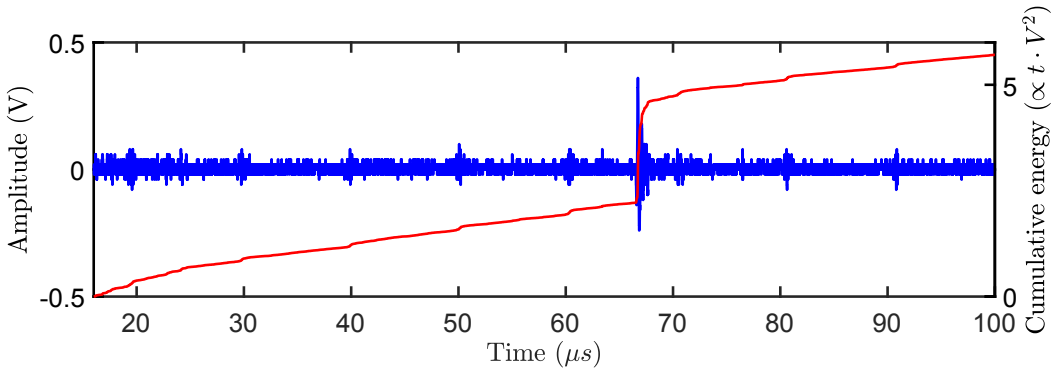

Figure 3.5: An acquired signal in blue and its cumulative energy in red.

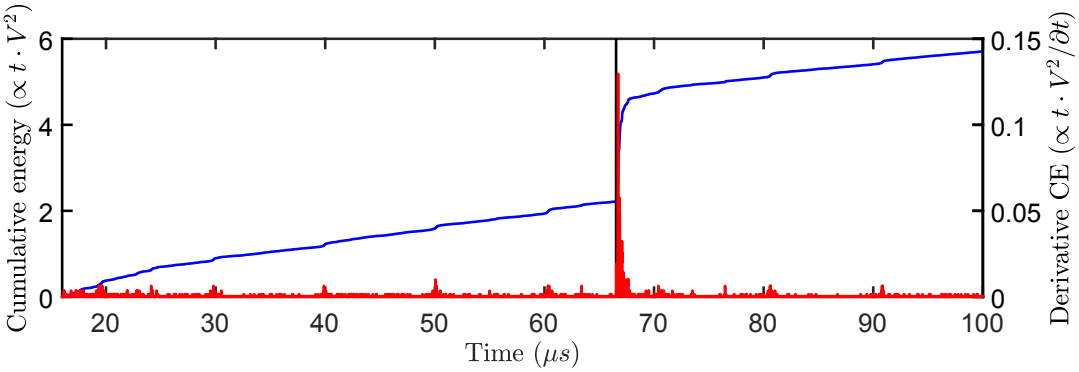

Figure 3.6: The cumulative energy, in blue, of the signal in the Figure 3.5. The red signal represents the derivative of the cumulative energy.

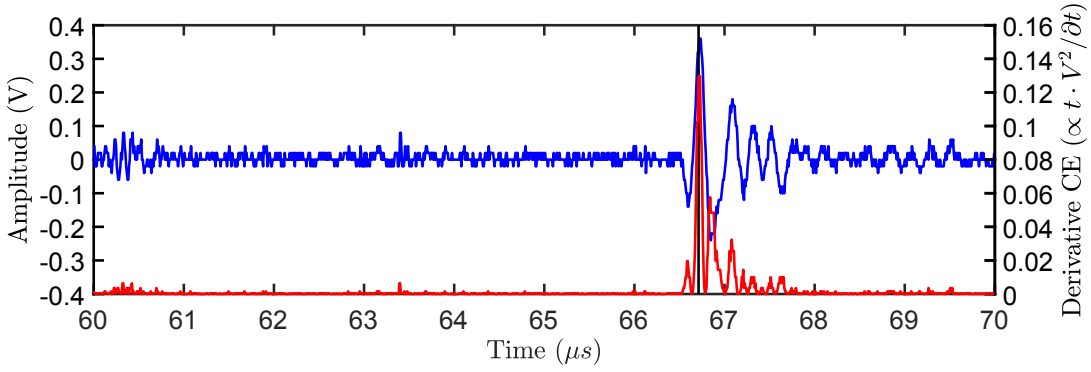

Figure 3.7: Relative ToF estimation through the maximum of the derivative of the cumulative energy, represented by the vertical black line. The blue line is the original signal and the derivative of its cumulated energy is represented by the red wave.

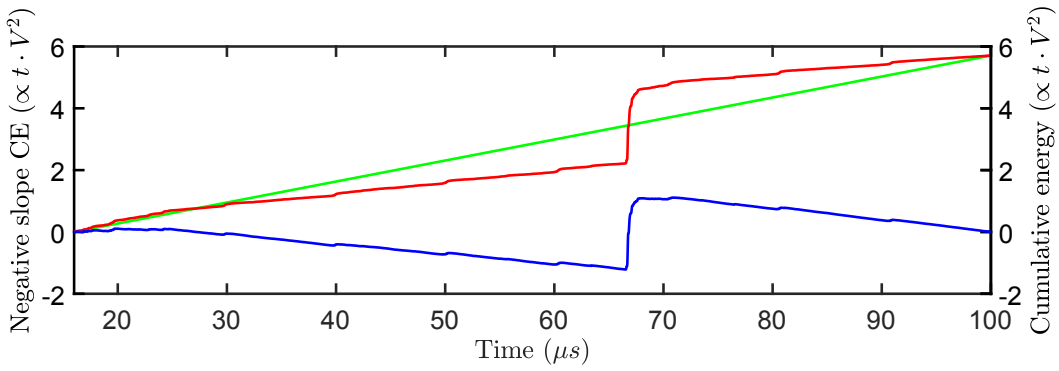

Figure 3.8: Shape of the cumulative energy in red. The green line represents the slope to fold the cumulative energy with $a = 1$. The blue signal is the folded cumulative energy.

3.3.5 Cumulative energy of the signal with negative slope. Hinkley criterion

This algorithm is derived from the one presented in Subsection 3.3.4 and it is based on the so called Hinkley criterion [11]. It considers the relative ToF of the signal as the knee point where the cumulative energy suddenly increases. This point is not the sample where the maximum derivative takes place. The main idea of this algorithm is to fold the cumulative energy curve in order to push down the knee point of the cumulative energy converting it in a minimum [2, 4]. This method is characterized through Equation (3.8) and defines the relative ToF as Equation (3.9).

$$E_{neg}(n) = \sum_{m=1}^{N} \left(s^2(m) - a \cdot n \cdot \frac{E_N}{N} \right), \qquad n = 1, 2, \ldots N \tag{3.8}$$

$$t' = \arg\min \left(E_{neg}(n) \right) \tag{3.9}$$

where E_N is the total energy of the signal, N is the total number of samples and a is a constant that pulls the absolute minimum further down in case that there are several minima close to the correct one.

Figure 3.8 shows an example of the cumulative energy in red. It also shows, the slope to fold the red signal considering the parameter $a = 1$ in green. The final result is the folded cumulative energy, represented in blue. Figure 3.9 shows the relative ToF calculus through this method denoted as a black vertical line over the original signal in blue.

3.3.6 Akaike Information Criterion (AIC)

This method assumes that the impulsive signals have two parts clearly defined and are two independent statistical models [12]. The first part is the noise previous to the

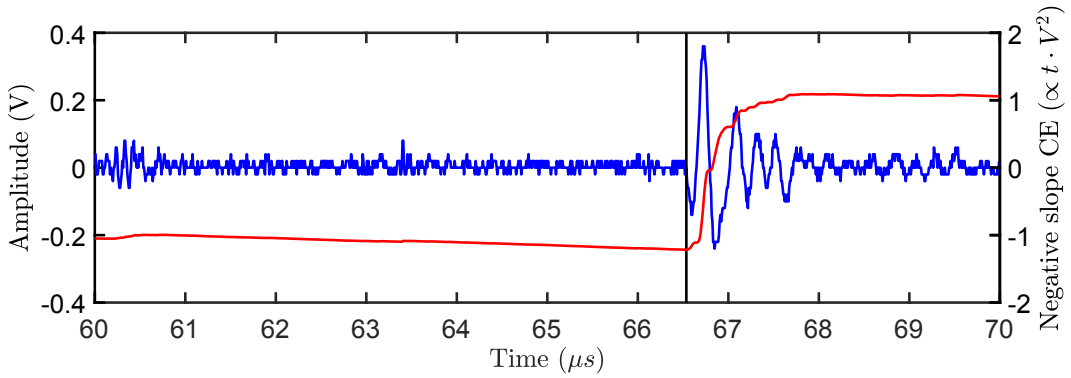

Figure 3.9: The vertical black line represents the relative ToF calculated through the minimum of the folded cumulative energy with negative slope, red line.

pulse onset and the second part is the pulse overlapped with the background noise. The onset of the pulsed signal is located at the point where the segment of the pulsed signal starts [13]. AIC represents the goodness of fit of a statistical model to a set of observations and it would give the exact time when the onset of the echo occurs [14]. The direct calculation of the AIC of the signal $s(n)$ can be computed by Equation (3.10). This algorithm sets the pulse onset through Equation (3.13) which represents the instant where the global minimum of Equation (3.10) takes place [4].

$$AIC(n) = n \cdot ln\left[\sigma^2(1,n)\right] + (N-n-1) \cdot ln\left[\sigma^2(n+1,N)\right] \tag{3.10}$$

where:

$$\sigma^2(1,n) = \frac{1}{n}\sum_{m=1}^{n}[s(m) - \overline{s}(1,n)]^2 \tag{3.11}$$

$$\sigma^2(n+1,N) = \frac{1}{N-n-1}\sum_{m=n+1}^{N}[s(m) - \overline{s}(n+1,N)]^2 \tag{3.12}$$

$$t' = \arg\min\left(AIC(n)\right) \tag{3.13}$$

Generally, the relative ToF is defined as the global minimum of the AIC function. The AIC function is very sensible and could have several local minima depending on the noise behind the pulse. This is why a time window definition is needed to delimit the local minimum which belongs to the onset of the signal [1]. The full AIC signal is shown in red in Figure 3.10, the blue signal is the original wave. Figure 3.11 shows the time window of the AIC function calculated over the original signal.

3.3.7 Maximum derivative of the time series cumulative kurtosis.

The kurtosis is a high order statistic parameter which is an indicator of the shape of a probability distribution. This method also considers that the acquired signal has

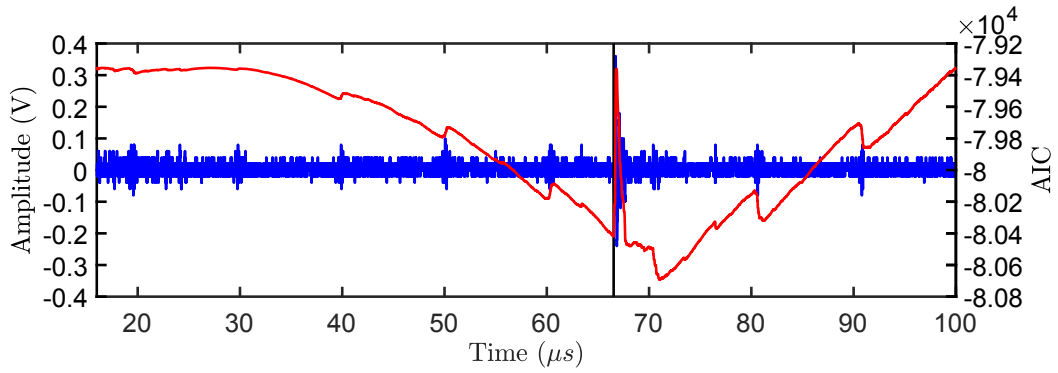

Figure 3.10: Shape of the AIC function in red for the original blue signal.

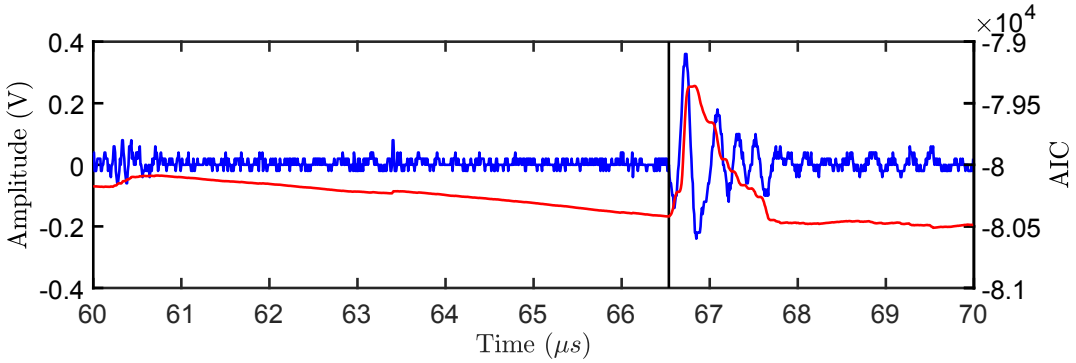

Figure 3.11: The black vertical line represents ToF calculated through the minimum of the red AIC function.

two parts, the first one belongs to background noise and the second part contains the pulsed signal. The background noise is a stationary process, the mean and variance are time invariant and higher-order statistics would be constant. Any new value belonging to a non-Gaussian distribution such as the inception of the pulse signal would induce an increment in the kurtosis, Equation (3.14). When more samples of the pulse arrive to the detector, the kurtosis increases as these new values are placed at the tails of the Gaussian distribution previously defined by the noise [14].

When the kurtosis is calculated at the onset of the pulsed signal, it increases suddenly, to decrease again when the pulse is extinguished. Equation (3.14) calculates the time series cumulative kurtosis. The relative ToF is defined as the instant where takes place the maximum derivative of the kurtosis, Equation (3.15). From now on, this algorithm will be referred as 'kurtosis 1'.

$$k(n) = \frac{\frac{1}{n}\sum_{m=1}^{n}[s(m) - \overline{s}(1,m)]^4}{\left(\frac{1}{n}\sum_{m=1}^{n}[s(m) - \overline{s}(1,m)]^2\right)^2} \tag{3.14}$$

$$t' = \arg\max\left(\frac{\partial k(n)}{\partial n}\right) \tag{3.15}$$

Table 3.1: Statistical parameters for two 1000-samples set containing noise and the onset of the echo.

	Mean (mV)	Std. dev. (mV)	Kurtosis
Noise	4	14.6	2.78
Onset	4.3	23.6	64.03

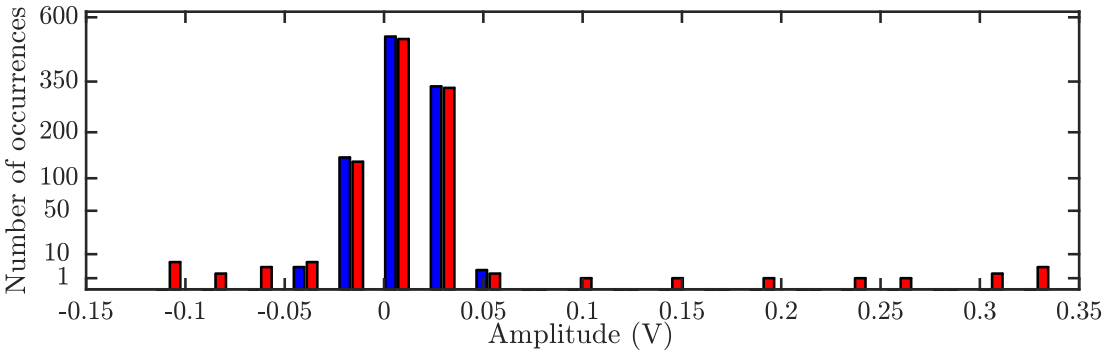

Figure 3.12: Histogram of two sets of 1000 samples from one of the measurements taken on a human thigh. The bars in blue are noise data while the bars in red correspond to noise and the onset of the echo signal. The vertical axis has been modified to show low numbers of occurrences.

Figure 3.12 is a clear example of what happens with the estimation of the kurtosis. The histogram represent the distribution of the numerical data of the analyzed signal that falls in certain amplitudes from a total of 1000 samples. The bars in blue correspond to the distribution of a portion of the total signal where there is only noise, see Figure 3.13. The bars in red conform the distribution of a part of the signal that selects the onset of the echo also refer to Figure 3.13. The amplitudes of some points in this sub-signal are ten times larger than the amplitude of noise so the tails of the distribution in the histogram are extended changing its shape and hence the kurtosis. Table 3.1 shows the mean, standard deviation and kurtosis of the two 1000-samples sets. Both cases have almost the same mean value, while the standard deviation and the kurtosis are larger in the case of the echo, as expected. The kurtosis for the noise is close to 3 so the shape of that distribution is very close to Gaussian, while in the case of the onset of the echo the kurtosis value is much larger, 64.03. Notice that the change in the kurtosis is more dramatic than the change in the standard deviation. As the energy of the signal is related to the standard deviation, it can be inferred that monitoring the changes in the kurtosis would be more effective in finding the relative ToF than any energy-based method.

The relative ToF can be determined calculating the maximum derivative of the cumulated kurtosis trying to find the suddenly increase of the kurtosis. Figure 3.14 shows the cumulative kurtosis in blue and its derivative in red. The derivative of the cumulative kurtosis, in red, and its maximum, vertical black line, is represented in Figure 3.15 where the original signal is displayed in blue.

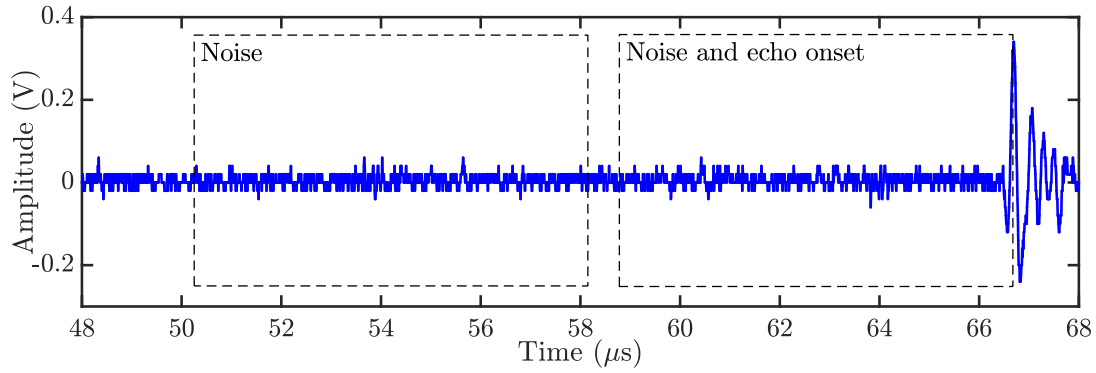

Figure 3.13: Plot of an echo where 1000 samples of noise and 1000 samples up to the onset of the echo are highlighted to show the performance of the kurtosis algorithm.

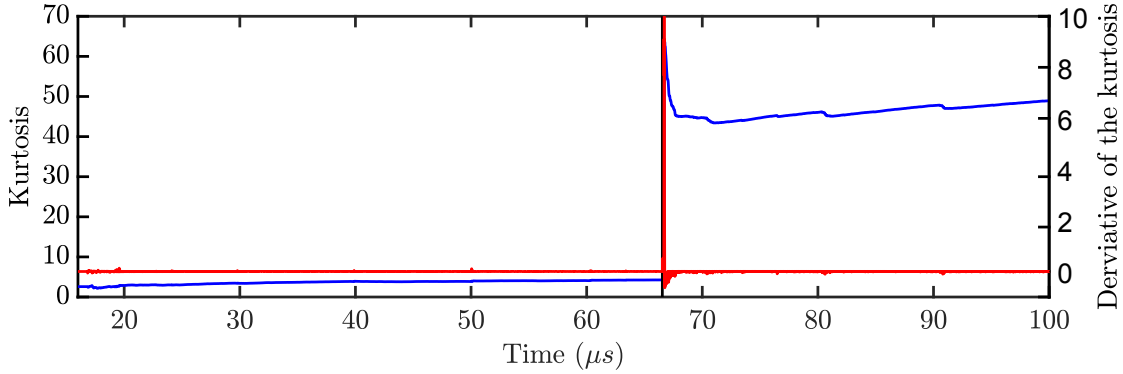

Figure 3.14: Shape of the cumulative kurtosis in blue and its derivative in red.

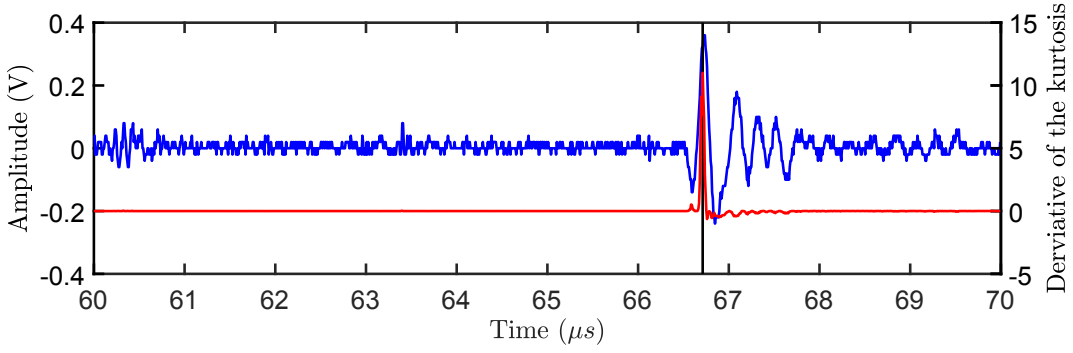

Figure 3.15: The black line represents the relative ToF estimation through maximum derivative of the cumulated kurtosis, in red, for the original signal in blue.

3.4 Time differences of arrival (TDoA)

The time delay denoted as TDoA is the time lapsed between two signals. In this section, a few methods to calculate this parameter are compiled and explained.

3.4.1 Difference of ToF

The introduction of this chapter explains how the TDoA can be calculated as the difference between two relative ToF using Equation (3.16).

$$t_{ij} = t_i - t_j \tag{3.16}$$

Therefore, using Equation (3.16) the TDoA can be calculated through every algorithm shown in Section 3.3.

3.4.2 Cross correlation

The classical method to calculate the time delay between two signals, s_i and s_j, is based on the application of cross correlation, R_{ij}, which is calculated through Equation (3.17). The TDoA is estimated as the shift where the maximum of $R_{ij}(n)$ takes place, see Equation (3.18).

$$R_{ij}(n) = \sum_{m=-N/2}^{N/2-1} s_i(m+n)s_j(m) \tag{3.17}$$

where N is the total number of samples.

$$t_{ij} = \arg\max\left(R_{ij}(n)\right) \tag{3.18}$$

This method has been extensively applied in many fields with good results, [15, 16, 17, 18]. However, the reflections due to multipath propagation and interferences due to reflections can yield larger peaks than the direct front wave. This means that the maximum of the correlation function would choose these peaks and would give a delayed picking of the signal. Using the preprocessing techniques presented in the generalized correlation method [19, 20], such as the Roth processor, the smoothed coherence transform (SCOT) and the phase transform (PHAT) would not help in obtaining good results since they are aimed at reducing the effect of white noise.

Figure 3.16 shows where the cross correlation algorithm would detect the onset of a signal. In this case, s_i is the pulse emitted by an ultrasonic sensor and s_j is the received signal. The output of the cross correlation gives directly the TDoA between s_i and s_j. Then, as s_i starts at 10 μs, R_{ij} has been manually shifted 10 μs to plot the cross correlation (red line) and the original signal s_j (blue line) in the same figure.

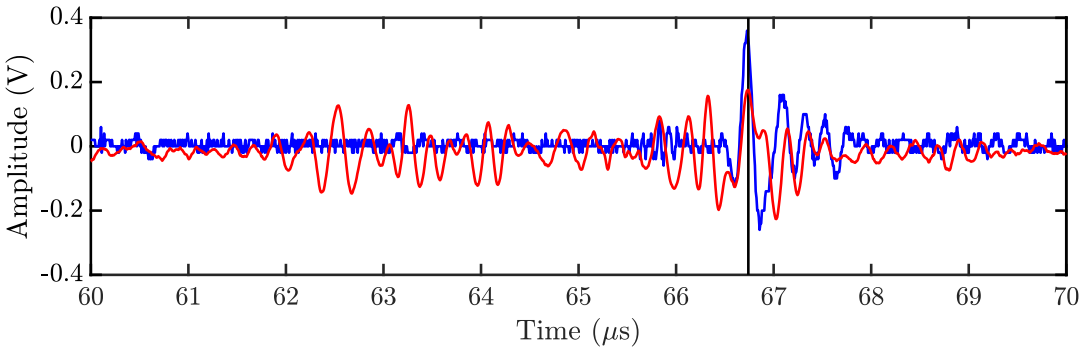

Figure 3.16: Detail of the cross correlation algorithm in the TDoA determination. The blue plot corresponds to the s_j signal and the red plot to the cross correlation.

3.4.3 Fourth-Order Cumulants

This method estimates the TDoA through four-order cumulates and its main advantage is that it is immune to Gaussian noise [21]. The next equations lets the user to implement the algorithm.

$$J_1(\tau) = \frac{|\hat{c}_4[s_i(n-\tau), s_i(n-\tau), s_j(n), s_j(n)]|}{\sqrt{[\hat{c}_4[s_i(n)]| \cdot |\hat{c}_4[s_j(n)]|}} \tag{3.19}$$

where $\hat{c}_4$ is the fourth-order cumulant and it is calculated through:

$$\hat{c}_4[s_i(n)] = \frac{1}{N}\sum_{n=1}^{N} s_i^4(n) - 3\left[\frac{1}{N}\sum_{n=1}^{N} s_i^2(n)\right]^2 \tag{3.20}$$

$$\begin{aligned}\hat{c}_4[s_i(n-\tau), s_i(n-\tau), s_j(n), s_j(n)] = \frac{1}{N}\sum_{n=-N_1}^{N_2} s_i^2(n-\tau)s_j^2(n) - \\ 2\left[\frac{1}{N}\sum_{n=-N_1}^{N_2} s_i^2(n-\tau)s_j^2(n)\right]^2 - \left[\frac{1}{N}\sum_{n=1}^{N} s_i^2(n)\right]\left[\frac{1}{N}\sum_{n=1}^{N} s_j^2(n)\right]\end{aligned} \tag{3.21}$$

where N denotes the length of the observed data, $N_1 = max(1, d+1)$ and $N_2 = min(N, N+d)$ to guarantee that the range goes from 1 to N. d is an auxiliary variable which ranges from the minimum to the maximum delay defined by the user in the search of the t_{ij}. The TDoA is estimated as the position where the maximum of Equation (3.19) takes place, Equation 3.22.

$$t_{ij} = \arg\max\left(J_1(\tau)\right) \tag{3.22}$$

Figure 3.17 shows how the red line, the result of the algorithm, is much smoother

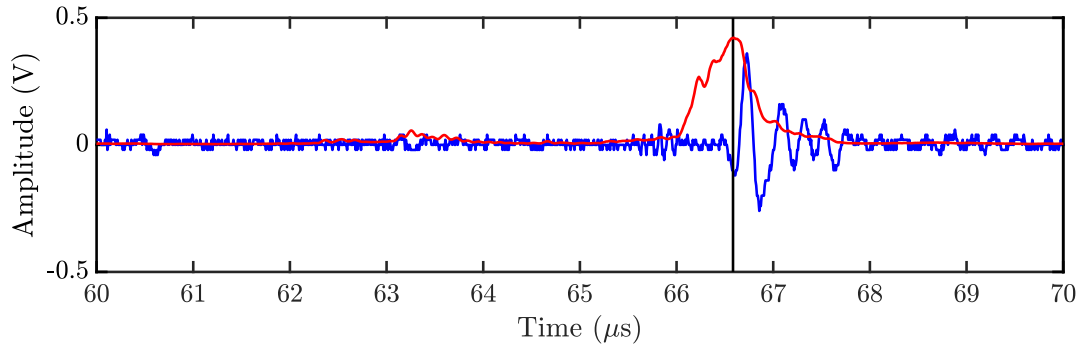

Figure 3.17: Detail of the statistics of high order algorithm in the TDoA determination. The blue plot corresponds to the s_j signal and the red plot to the statistics of high order signal.

than the cross correlation, shown in Subsection 3.4.2, due to the immunity of the algorithm to the Gaussian noise. As in the case of the cross correlation algorithm the signal s_i starts at 10 μs, $J_1(\tau)$ is manually shifted 10 μs to plot both lines in the same figure.

3.5 Proposed improvement in the kurtosis method

In this section, a variant of the kurtosis algorithm explained in Subsection 3.3.7 is presented. This modification is similar to the presented in Subsection 3.3.5 in the Hinkley criterion, used in the cumulated energy of the signal. It is added a negative slope line to highlight the bend of the cumulated kurtosis function as a local minimum before the maximum of the cumulative kurtosis. Equation (3.14) is, thus, modified to:

$$k_2(n) = k(n) - a \cdot n\frac{K}{n_K} \tag{3.23}$$

where, in this case, a is set equal to one, K is the maximum cumulative kurtosis and n_K is the sample where that maximum occurs. $k(n)$ is calculated through Equation (3.14). This modification gives a plot that decreases with a constant slope when the original signal is noise reaching a minimum in the onset of the pulse, Equation (3.24) before the maximum n_K. This algorithm will be named in the remaind of the thesis as 'kurtosis 2'.

$$t' = \arg\min\left(k_2(n)\right) \tag{3.24}$$

3.6 Time differences of arrival (TDoA) application in muscle depth estimation

This section is an extension of the publication "Ultrasonic bone localization algorithm based on time-series cumulative kurtosis", its full citation can be found in Subsection 7.3.1 in item 3.

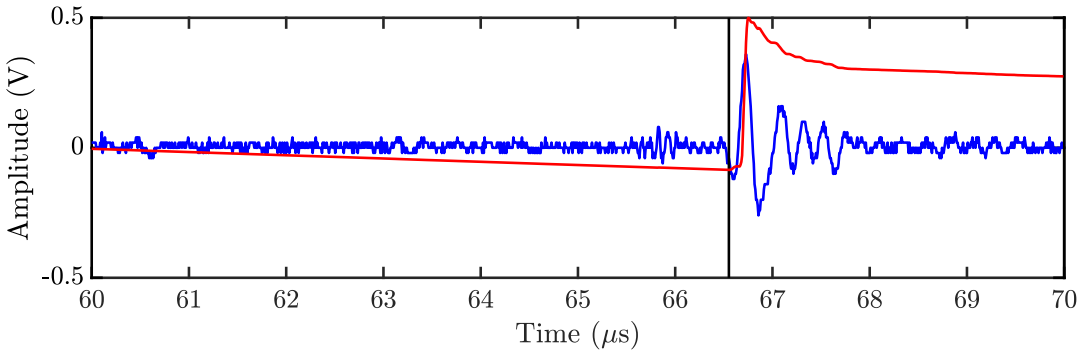

Figure 3.18: Relative ToF represented with a vertical line and calculated with the minimum time series cumulative kurtosis algorithm, red signal. The original signal in the time domain is represented by the blue signal.

The performance of eleven methods to determinate the TDoA is evaluated over ultrasonic pulses when they are applied to measure the muscle depth. The experiments are made using both simple setups used for calibration purposes and in real human tissues to test the performance of the algorithms. In this application, a 1D localization is undertaken estimating the TDoA and using Equation (3.2). The TDoA is calculated between the pulses emitted and the received echo.

3.6.1 Introduction

Accurate measurement of the dynamics of the musculoskeletal system is limited by the problem of measuring the position of the bones during dynamic and weight-bearing activities. Existing methods to measure motion in these conditions include optically-tracked markers [22] and wearable goniometric devices [23]. Both methods measure basically the skin position, and although sometimes it is possible to use them to mark patches of skin with very superficial bones, they are not generally able to give the necessary bone position accuracy [24]. For example, it would be very useful to be able to measure real-time position of the pelvis bones of subjects forced to stay in wheelchairs, in order to optimize the stance to avoid or minimize injuries; or, it could be devised an actuator able to automatically manage the tightness of a knee bracket responding to the bones movements in real-time. In those cases, the measurement of the position of markers on the skin can have relatively limited relationship with the underneath bone position.

One of the possible approaches to a wearable, non-invasive bone depth measurement is using US sensors in a similar way as they are used to detect failures in pipes and mechanical structures [6]. To perform the measurement, an ultrasonic sensor is rigidly associated to each one of the infrared markers used by the 3D tracking system, and a set of such compound sensors will be positioned around the limb for estimating the position of the bone, see Figure 3.19.

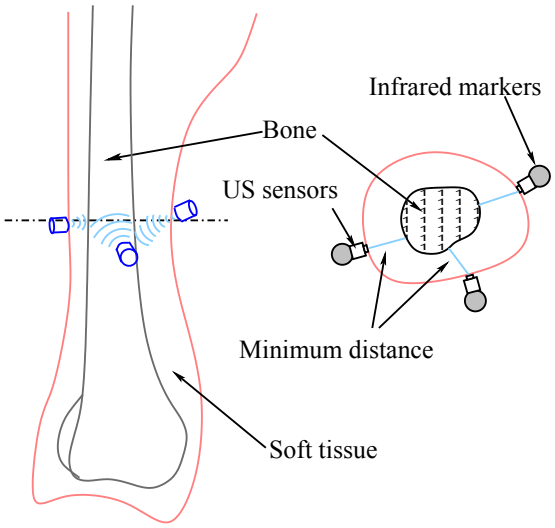

Figure 3.19: Triangulating a bone position by three coupled optical (IR) and US sensors.

Notice how, due to the movement of the muscle and fat tissue around the target bone, the angular orientation of the US sensor will be difficult to predict and estimate. The measurement strategy will be oriented to measure the smallest distance between the skin surface (where the US sensor is attached with an adhesive or an external restraint system) and the bone underneath.

The big difference in the acoustic impedance between soft tissues and bone tissues in human bodies will give a very strong echo to incident acoustic waves, smaller only than the echoes generated by a tissue/air interface, where the acoustic impedance difference is even higher. For example, at a frequency of 1 MHz, the acoustic impedance of bones is around $7.8 \cdot 10^6$ Rayls, while the different soft tissues (fat, blood, muscle) range from 1.35 to 1.75 MRayls [25]— so the echoes from the bone/soft tissue are bond to be quite stronger than the echoes caused by different tissues interfaces. The only difficult echoes could come by extremely porous cancellous bones [26], where the reflected pulses would be much weaker, but this case is not common in practical applications, so it does not seriously reduce the effectiveness of the method.

Even though the echoes are strong, the fact that there are multiple reflections involved, and lateral conduction in the bones [27], the received signal is not so sharp, and the detection of the significant point for the echo onset is not trivial; in Figure 3.20, the raw data from the echo of a human femur is shown. The effect of multipath reflections is minimized in the picking of the onset of the echo determining which is the first front wave arriving to the sensor. This is best done with methods based on the energy of the signal. The reflected waves from the periosteal surface of the bone are indeed very complex due to the non-planar and rough structure of the surface itself [28]; a detailed study of such reflections is needed when the objective is to image the bone geometry [29] and/or detecting additional information as density or elasticity [30]. In our application, we are interested in determining the depth (minimum path)

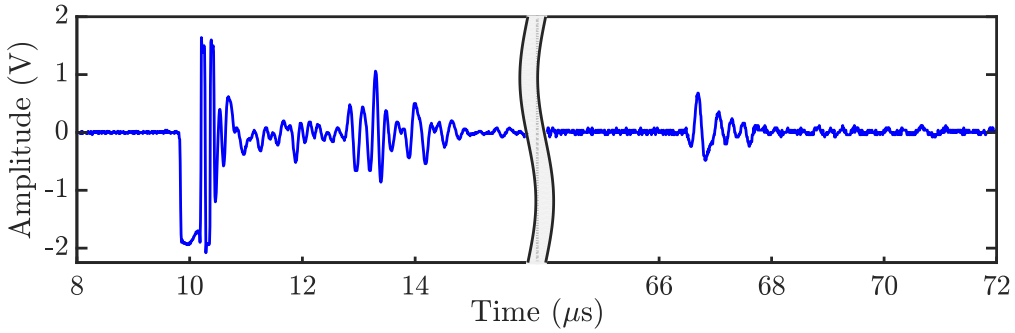

Figure 3.20: An example of echo from a bone measured in a human subject; the sensor was on the skin of the external part of the thigh. The ultrasonic pulse at 10 μs is the emitter pulse, and the pulse between 66 and 68 μs is the echo from the femur.

of the bone surface, with independence of the angle of incidence of the probe — which indeed shows a quite broad angle of emission which, in turn, simplifies the problem of the analysis of the echo.

Most studies involving US techniques are devoted to the measurement of the propagation of sound through bone. Mass and architecture of bones can be determined by the velocity or speed of sound and the attenuation of the US wave in frequency or broadband ultrasound attenuation (BUA) [31], [32]. The measurement of TDoA is almost restricted to the axial and circumferential propagation of the waves in bones to determine their geometry, elasticity and mineralization, [33]. The calculation of the relative ToF is done through simple techniques such as the time between the pulse and echo peaks or between the pulse and the first inflection point of the first echo without paying much attention to the SNR.

3.6.2 Instrumentation and measurements

In choosing the US signal frequency, a compromise must be done between the availability and price of the transceiver (which are cheaper and easier to find for low frequencies), and the resolution that the resulting wavelength in the soft tissue will enable. Working in the 2–10 MHz range, with a wavelength in soft tissues of about 0.75–0.15 mm, has been chosen as a good compromise.

The selected transducer is an Olympus V609-RB US bidirectional device, which costs around 300 USD; its nominal operating frequency (5 MHz) is well into the selected range. In the experiments, it was driven with an Olympus manually controlled ultrasonic pulser-receiver (5072PR) and the US signal was visualized and recorded using a Tektronix TDS 5104 digital storage oscilloscope (DSO). The DSO was set with a resolution of 8 ns and a time span of 100 μs. Figure 3.21 depicts the structure of the measurement setup.

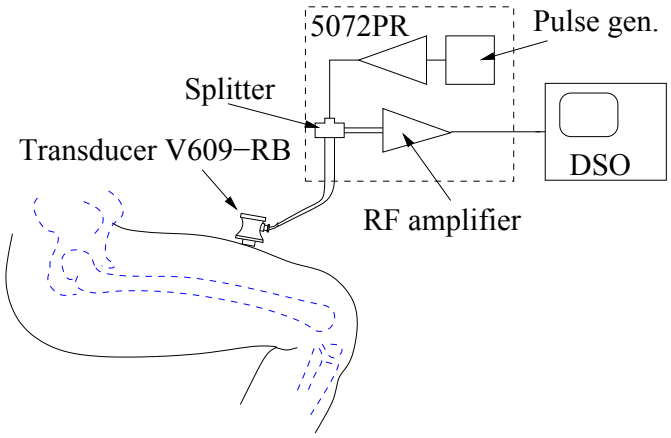

Figure 3.21: Setup of the measurement system shown when taking the measurement of bone depth of a femur bone in a human thigh.

3.6.3 Results

The test benchmark consisted on measurements conducted in different media, boundary conditions and positions of the US sensors which defined six test environments.

The algorithms were applied to sets of ten signals obtained in gel pads and a human thigh. The first two experiments are aimed at the evaluation of the algorithms in a controlled environment in which we have a homogeneous media of a known thickness. The experiment in human flesh represents a more realistic case in which different tissues can be found before reaching the bone and the thickness is unknown. Then, the first experiments help in the calibration of the method while the other experiment tests the algorithms with real measurements. In each configuration, the sensor is placed on the samples either vertically aligned, to have a direct reflection of the echo, or slanted, so the path of the echo is slightly different, see Figure 3.23. The purpose is to test the behavior of the measuring system and the algorithms in those cases where the sensor has drifted from its original position due to the movement of the subject. Ten consecutive measurements are taken in both positions and in all samples. Then, the average ToF is calculated and compared with the actual one in the case of the gel pads. This average would give a measurement of the accuracy of the results, whereas the standard deviation of the relative ToF would represent the repeatability of the algorithm.

3.6.3.1 Two gel pads with air interphase

Two pads 3 cm thick are placed one on the top of the other without any film gel in between, so that a thin air interphase will form and a reflection wave will be generated at the boundary between them. The pads are manufactured with a gel that has a transmission speed for US waves in this frequency range of about 1500 ms^{-1}. This means that the echo reaches the interphase in 20 μs and the reflected pulse hits the sensor in

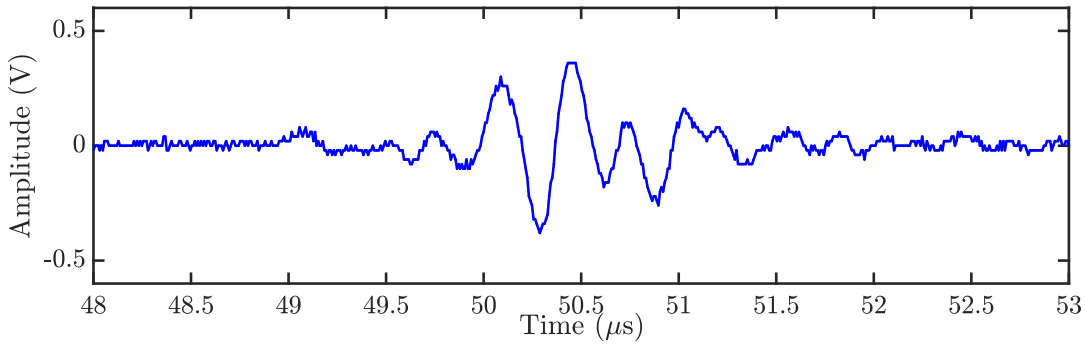

Figure 3.22: Echo in the air interphase when the sensor is slanted.

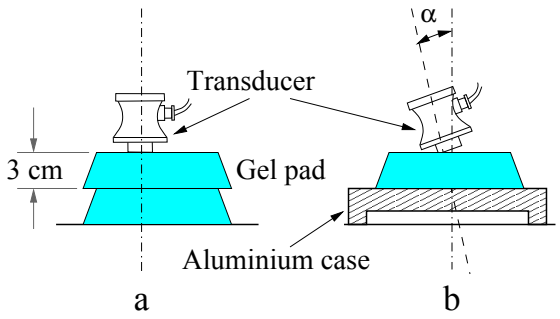

Figure 3.23: Experiment for the first set of data. The ToF measurement has been computed using several methods in the case of a couple of stacked gel pads (case *a*) with acoustic impedance similar to human soft tissues, and with a single gel pad positioned over a open metallic structure (*b*). In both cases the measurement were performed with the sensor vertically aligned and with the sensor slightly slanted.

40 μs, see Figure 3.23 case *a*. An example of an echo with the sensor slanted is shown in Figure 3.22.

Table 3.2 shows the results given by the algorithms for ten consecutive measurements in both positions: horizontal (or vertically aligned) and slanted. The most accurate algorithm would be the one with the closest average value to the actual thickness of the gel, 40 μs or 3 cm, and the best method, in terms of repeatability of the results, would be the one with the lowest standard deviation.

With the sensor vertically aligned, the most accurate methods are: the proposed in this thesis kurtosis 2 and the AIC with the same difference from the correct time, 40.02 μs and 39.98 μs, respectively. On the contrary, the best repeatability is given by the Hinkley method followed by kurtosis 2. When the sensor is slanted, the most accurate is again kurtosis 2, with 40.14 μs, while the lowest standard deviation corresponds to the maximum peak followed by kurtosis 2. The last column is the difference between the average in both positions. Ideally, this difference would be naught because the method should be as immune to the movement of the sensor as possible. The closest averages are achieved by the kurtosis 2 so overall, in this experiment, this method would be best option.

Table 3.2: TDoA measurements of the echo for the two gel pads configuration.

	Horizontal		Slanted		
	Mean	Std	Mean	Std	|Mean Diff.|
Max	40,21	0,195	40,39	0,225	0,173
Threshold	40,28	0,200	40,67	0,282	0,390
Threshold Slope	40,22	0,255	40,62	0,287	0,402
MDCE	40,12	0,182	40,49	0,262	0,370
Hinkley	40,04	0,138	39,55	0,349	0,481
AIC	39,98	0,168	39,32	0,274	0,662
Kurtosis 1	40,20	0,187	40,73	0,266	0,531
Kurtosis 2	40,02	0,161	40,14	0,260	**0,118**
Cross correlation	40,15	0,210	40,40	0,442	0,255
4-Order Cumulants	40,29	0,192	40,56	0,319	0,278

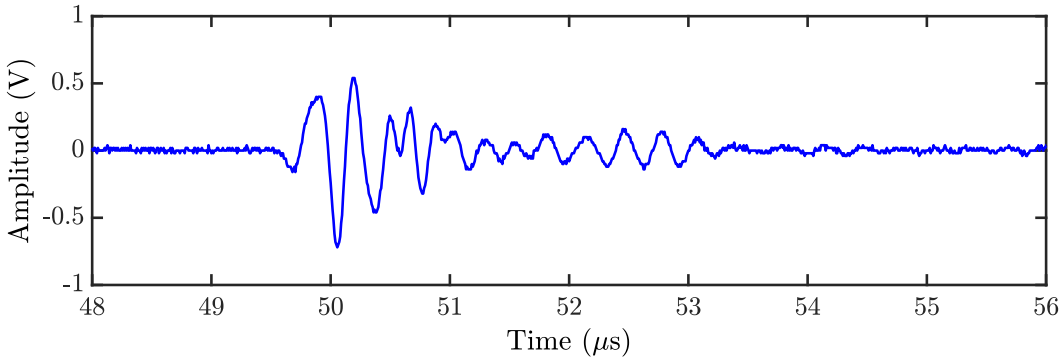

Figure 3.24: Echo in the gel-metal interphase when the sensor is slanted.

3.6.3.2 One gel pad with metallic interphase

This experiment uses only one gel pad with an aluminium plate at its base to simulate a different interphase where the echo is reflected, see Figure 3.23 case *b*. The signals are quite different from the first case due to the multipath echoes that originates with the multiple interfaces (where the shear waves in the metal propagate a lot faster than in the pad), see Figure 3.24.

The results of the algorithms are given in Table 3.3 where the most accurate is Hinkley (39.98 μs) followed by kurtosis 2 (39.95 μs) when the sensor is vertically aligned and kurtosis 2 (39.77 μs) when the sensor is slanted. In all cases, the kurtosis 2 has the lowest standard deviation which also gives the most similar averages in both positions (0.180 μs) and, again, turns to be the best option.

3.6.3.3 Human thigh

The results obtained in the calibration setups show that the algorithms are all of them reasonably accurate and precise in the measurements of the thickness of the gel pad, being the cumulative kurtosis the method with the best performance.

Table 3.3: TDoA measurements of the echo for one gel pad with aluminium base configuration.

	Horizontal		Slanted		
	Mean	Std	Mean	Std	| Mean Diff. |
Max	39,75	0,148	40,40	0,360	0,654
Threshold	40,08	0,107	40,39	0,361	0,312
Threshold Slope	40,05	0,118	40,35	0,370	0,303
MDCE	40,01	0,073	40,49	0,390	0,475
Hinkley	39,98	0,103	39,64	0,253	0,333
AIC	39,92	0,091	39,48	0,254	0,437
Kurtosis 1	40,06	0,119	40,55	0,443	0,496
Kurtosis 2	39,95	0,089	39,77	0,221	**0,180**
Cross correlation	40,11	0,283	40,41	0,410	0,300
4-Order Cumulants	40,05	0,092	40,62	0,409	0,574

Table 3.4: TDoA measurements of the echo in a human thigh. The best standard deviation results are underlined and marked in bold font.

Std	Set 1	Set 2	Set 3	Set 4	Set 5	Set 6	Set 7	Set 8	Set 9	Set 10
Max	1,823	1,677	1,283	1,368	1,540	1,413	0,899	0,754	0,532	0,736
Threshold	0,577	0,338	0,240	**0,229**	0,324	**0,244**	0,380	0,398	0,357	0,224
Threshold Slope	0,622	**0,326**	0,242	0,232	0,321	0,254	0,389	0,397	0,363	**0,225**
MDCE	1,578	1,768	0,819	0,774	1,325	1,508	1,297	0,573	1,262	1,644
Hinkley	0,606	0,413	0,334	0,331	0,448	0,267	0,494	0,356	0,415	0,240
AIC	2,627	0,454	0,392	3,940	**0,294**	0,286	0,505	0,415	0,416	0,307
Kurtosis 1	**0,461**	0,335	0,254	0,232	0,317	0,232	0,422	0,398	0,362	0,228
Kurtosis 2	0,740	0,425	**0,224**	0,256	0,434	0,265	**0,367**	**0,351**	**0,338**	0,289
Cross correlation	1,165	1,455	0,489	1,559	1,373	1,150	0,833	0,880	1,376	1,772
4-Order Cumulants	1,471	1,340	0,237	0,470	0,562	1,707	1,178	0,468	0,778	0,791

In the next experiment the objective was to measure the depth of the femur bone using a setup similar to the one shown in Figure 3.21. The depth of the bone is, in this case, unknown, so the important parameter to evaluate is the deviation of the results. A large set of measurements were carried out with the sensor in the same position but with different angles with respect the thigh surface, measurements 1 to 10 in Table 3.4 and Table 3.5. Subsequently, all of them consist of 10 measurements shifting the position and angle of the sensor. The lowest standard deviations are underlined and highlighted with bold fonts. The depth of the bone is determined with the average value corresponding to the method that gives the most stable results. Then, when the lowest standard deviation in the set of measurements number 3 corresponds to kurtosis 2 with a value of 0.224, the echo would be at 53.27 μs and the depth of the bone would be 4.00 cm. The overall results show that the lowest standard deviation is given by the kurtosis 2 in four cases out of ten. The threshold and the threshold with negative slope have also good performance in two out of ten occasions each. Then, considering that the kurtosis 2 also had an outstanding accuracy in the tests with the gels, the most reliable measurements of the bone-depth would be given by this method.

Table 3.5: The conclusions for the standard deviation are extrapolated to the average values and the better solutions are underlined and marked in bold font.

Mean	Set 1	Set 2	Set 3	Set 4	Set 5	Set 6	Set 7	Set 8	Set 9	Set 10
Max	49,83	49,68	49,47	51,54	51,31	50,29	50,67	52,35	50,77	51,64
Threshold	51,91	53,27	53,50	**53,22**	53,71	**53,14**	52,68	53,41	52,54	52,86
Threshold Slope	51,86	**53,25**	53,55	53,20	53,70	53,11	52,66	53,40	52,52	**52,85**
MDCE	50,79	52,14	52,92	52,60	51,85	51,69	51,82	53,27	51,74	51,51
Hinkley	51,20	52,92	53,15	52,75	53,27	52,54	52,23	52,99	51,83	52,27
AIC	50,03	52,77	52,94	51,35	**53,02**	52,52	52,07	52,96	51,76	52,12
Kurtosis 1	**52,06**	53,27	53,51	53,25	53,71	53,17	52,80	53,42	52,54	52,87
Kurtosis 2	51,36	53,12	**53,27**	53,00	53,45	52,55	**52,37**	**53,02**	**52,08**	52,42
Cross correlation	49,54	51,43	49,27	50,89	51,82	50,27	50,67	52,25	51,17	50,48
4-Order Cumulants	50,97	52,87	53,44	53,00	53,52	51,57	52,02	52,94	52,05	52,42

3.7 Time differences of arrival (TDoA) application in RF source localization in 3D

This section is an extract of the publication "Separation of Radio-Frequency Sources and Localization of Partial Discharges in Noisy Environments", its full citation can be found in Subsection 7.3.1 in item 1. In this section, the extract of the paper is extended with all the algorithms presented in this chapter to evaluate their performance when applied to RF sources localization.

3.7.1 Introduction

PD measurements can reveal multiple ageing mechanisms in HV infrastructures [34, 35, 36]. In the bibliography, many works related with on-line PD measurements can be found using ultrasonic sensors [37, 38] or antennas [39, 40]. In addition, these techniques allow to locate PD sources using arrays of at least four sensors, which is especially useful inside of oil-insulated power transformers and gas-insulated substations and air-insulated substations [41].

The algorithms used to locate RF emitters in 3D are enumerated, explained and compared in Section 4.3. These algorithms use the antennas/sensors position and the relative ToF or TDoA variables as inputs. In this section, the performance of the relative ToF or TDoA calculus is only analyzed in terms of accuracy and dispersion, the RF emitter localization is addressed in Section 4.3. The calculus of the time variables are compared with the theoretical value of these parameters which can be calculated using the antennas and emitter position and the speed propagation in the free space.

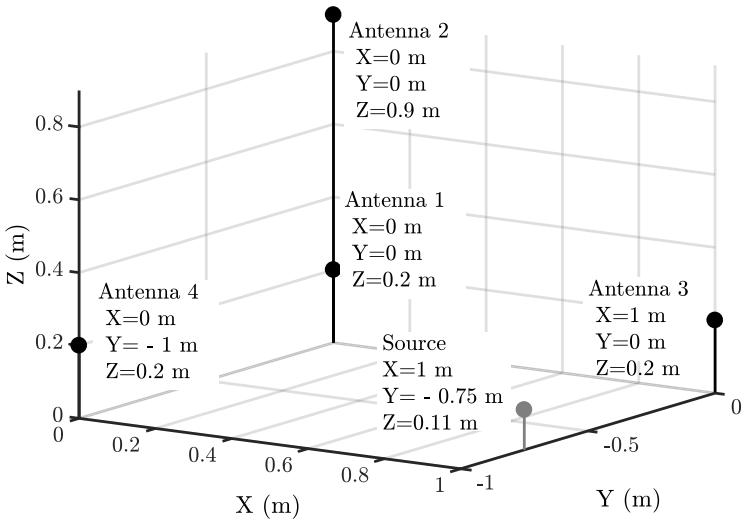

Figure 3.25: Antennas and PD emitter position.

3.7.2 Instrumentation and measurements

The main components of the setup in this section are four antennas to localize the RF emission of the PD pulses connected to a high-speed acquisition system, PD emitters connected to a HV transformer and several disturbance sources. The antennas are simple monopoles, 10 cm in length, with good receptivity in the frequency range of the PD [42]. They were placed at the four vertices of a tetrahedron with the base at 20 cm from the ground level, Figure 3.25, and connected to an oscilloscope through coaxial cables 5 m long. The oscilloscope bandwidth is 2.5 GHz and the sampling frequency was set to 5 GS/s so every sample was taken every 200 ps. The time window is 1 μs so the signals have 5000 samples.

The PD were generated placing a non-insulated wire loop connected to ground around the insulation of a 25 kV HV cable. When the cable is connected to a HV source, a Schleich BV 702210 transformer with a GLP1-e HV control module, there is a high electric field gradient ring around the cable that triggers surface PD for voltages above 3.5 kV. Figure 3.26 shows an example of the signals generated with this test object. It is very common to find these type of PD on contaminated surfaces of insulators of transmission lines and bushings in substations though the true nature of the discharge is not relevant for the results obtained in this section.

The activity of these discharges was previously confirmed in a PRPD pattern drawn with a commercial PD acquisition system. The shape and geometry of the objects provide a direct path to the antennas mainly through air. Under this assumption, the speed of propagation will be $c = 3 \cdot 10^8\ ms^{-1}$, so the space resolution between samples is $d_{min} = 200 \cdot 10^{-12} \cdot 3 \cdot 10^8 = 0.06$ m. Notice that there are many metallic structures around the setup, see Figure 3.27, so the multipath propagation of the signals due to reflections is very important and in some cases compromise the TDoA calculus.

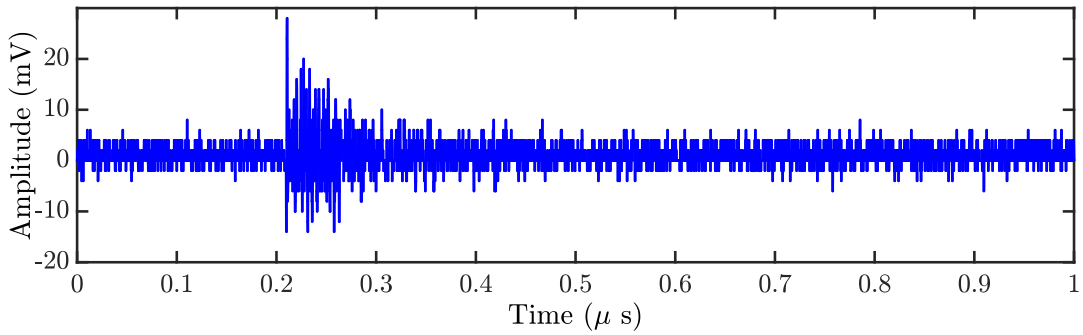

Figure 3.26: PD pulse acquired with monopole antennas 10 cm long.

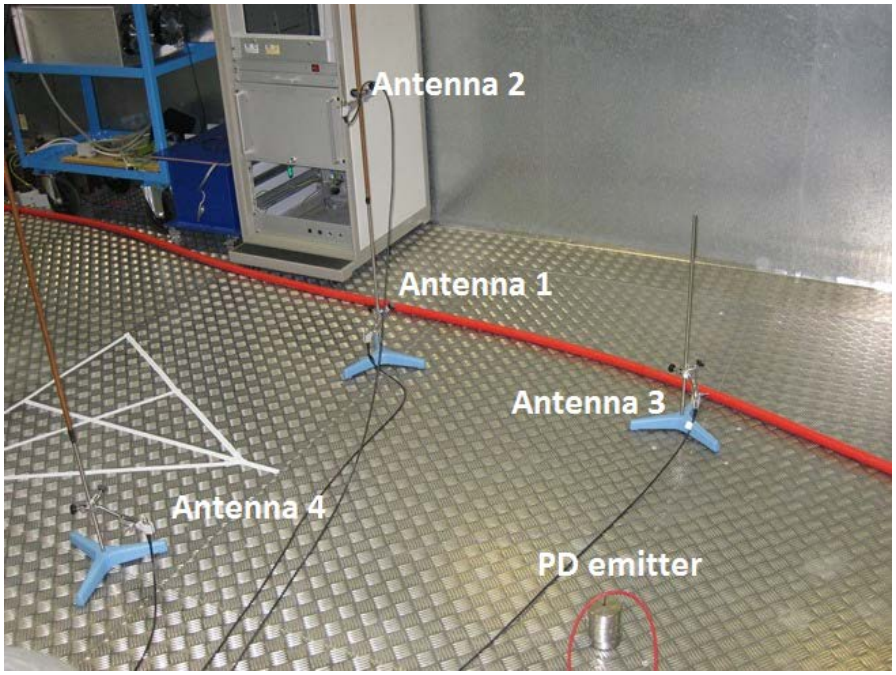

Figure 3.27: Setup in laboratory. Notice the abundance of metallic surfaces and structures around the antennas.

3.7.3 Results

The acquired signals are artificially oversampled by interpolating points using cubic splines between two real samples so the sampling time is reduced tenfold to 20 ps. This decision helps in the accuracy of the TDoA calculations giving errors that are below the actual sampling time.

To evaluate the results obtained by the algorithms, the estimated TDoA is compared with the theoretical value. It is calculated using the distances between the antennas and the source, D_i and D_j which are defined by Equation (3.3), and dividing by the light speed propagation, c, following Equation (3.25).

$$t_{ij} = \frac{1}{c}(D_i - D_j) \tag{3.25}$$

Table 3.6 summarizes the theoretical value TDoA and the mode values in samples, calculated by each algorithm after processing all signals. The best result of the algorithms are underlined and highlighted with bold numbers, the difference between the mode and the theoretical value is shown in the Table 3.7. The compactness of the TDoA represented by the standard deviation of the calculated TDoA can be observed in Table 3.8. The algorithms which yield low standard deviation will produce solutions close together so the localization should be quite exact. Then, these algorithms are the indicated ones to undertake the RF emitter localization.

In the calculus of the t_{21} the Threshold slope algorithm reports the best result with 0.042 samples of deviation from the theoretical value. In the t_{31} calculus Hinkley and kurtosis 2 report the best result 0.002 samples of error. The best algorithm to calculate the last TDoA between antenna 4 and 1 is kurtosis 2 with 0.042 samples of deviation from the theoretical value. Analyzing the three TDoA together it can be concluded that kurtosis 2 is the best algorithm in average. The kurtosis 2 algorithm obtains $0,096$ samples of deviation from the theoretical value which is the smallest error in the difference between the theoretical value and the mode of their TDoA estimation. Furthermore, its TDoA are very compact because its standard deviation is the third smaller. The Cross Correlation is the algorithm with the lowest deviation but it reports a very large error in the TDoA calculation and therefore it is not selected. Combining the great amount of TDoA calculated by kurtosis 2 close to the theoretical value together with its great compactness, an accurate localization of the PD source is expected.

Figure 3.28, Figure 3.29 and Figure 3.30 represent the histogram of the TDoA results for the algorithms: threshold corrected with slope, Hinkley with negative slope and the minimum time series cumulative kurtosis respectively. The abscissa axis represents the TDoA between two antennas in tens of samples considering that T_s = 20 ps. The ordinate axis is the number of events that give a certain TDoA. For the sake of clearness, the histograms only include those results that give TDoA relatively close to the mode,

Table 3.6: Theoretic value and mode of the TDoA calculated by each algorithm in PD source localization.

Mode	t_{21}	t_{31}	t_{41}
Theoretical	**3,76**	**-8,29**	**-3,64**
Max	68,0	-8,0	-3,0
Threshold	3,9	-8,0	-3,5
Threshold Slope	**3,8**	-8,5	-3,4
MDCE	43,0	-7,0	-3,0
Hinkley	4,0	**-8,3**	-3,3
AIC	4,0	-8,1	-3,1
Kurtosis 1	4,0	-8,4	-4,0
Kurtosis 2	4,0	**-8,3**	**-3,6**
Cross correlation	32,5	-7,5	-3,5
4-Order Cumulants	8,0	-7,5	-3,2

Table 3.7: Difference between the theoretic value of the TDoA and the mode calculated by each algorithm in PD source localization.

Diff Mode	t_{21}	t_{31}	t_{41}	Average
Max	64,242	0,298	0,642	21,727
Threshold	0,142	0,298	0,142	0,194
Threshold Slope	**0,042**	0,202	0,242	0,162
MDCE	39,242	1,298	0,642	13,727
Hinkley	0,242	**0,002**	0,342	0,196
AIC	0,242	0,198	0,542	0,327
Kurtosis 1	0,242	0,102	0,358	0,234
Kurtosis 2	0,242	**0,002**	**0,042**	**0,096**
Cross correlation	28,742	0,798	0,142	9,894
4-Order Cumulants	4,242	0,798	0,442	1,827

they do not show all the solutions. Nevertheless, the results far from the mode would never be considered to calculate the position of the source. The theoretical values of the TDoA are represented by red triangles which indicate the target in the TDoA calculus.

3.8 Conclusions

In this chapter it is shown that the algorithm used to determine the relative ToF or TDoA of the signals is significant to this purpose; several commonly used algorithm — Maximum value of the signal, threshold, threshold corrected with the slope, maximum derivative of the cumulative energy of the signal, Hinkley, AIC, kurtosis 1, cross correlation, four-order cumulants — a new algorithm based on the kurtosis is presented and labeled as kurtosis 2. All the algorithms have been compared in two applications; depth bone estimation and RF emitter localization.

In the first application, the analysis of the resulting data sets points yields that the overall best method is the kurtosis 2 proposed in this thesis, showing, on average,

Table 3.8: Standard deviation of the TDoA calculated by each algorithm in PD source localization.

Std	t_{21}	t_{31}	t_{41}	Average
Max	11,000	0,500	0,500	4,000
Threshold	0,550	0,300	0,262	0,371
Threshold Slope	1,300	1,250	0,450	1,000
MDCE	0,500	0,500	2,000	1,000
Hinkley	0,200	0,350	0,262	0,271
AIC	1,462	2,624	1,662	1,916
Kurtosis 1	0,550	0,350	0,400	0,433
Kurtosis 2	0,250	0,250	0,262	0,254
Cross correlation	0,200	0,100	0,100	0,133
4-Order Cumulants	3,850	0,050	0,050	1,317

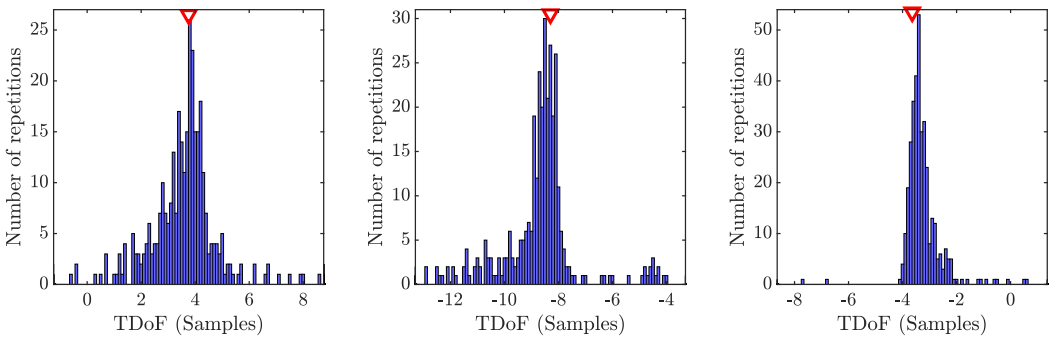

(a) t_{21} *(b)* t_{31} *(c)* t_{41}

Figure 3.28: TDoA calculated with the threshold corrected with slope algorithm in PD source localization.

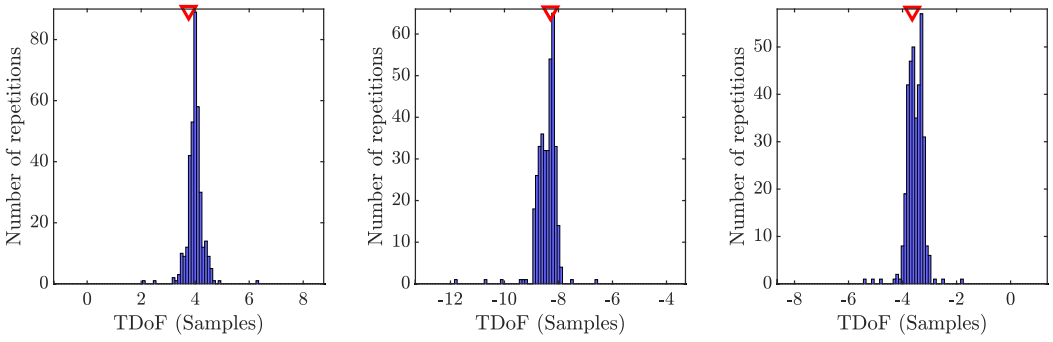

(a) t_{21} *(b)* t_{31} *(c)* t_{41}

Figure 3.29: TDoA calculated with Hinkley algorithm in PD source localization.

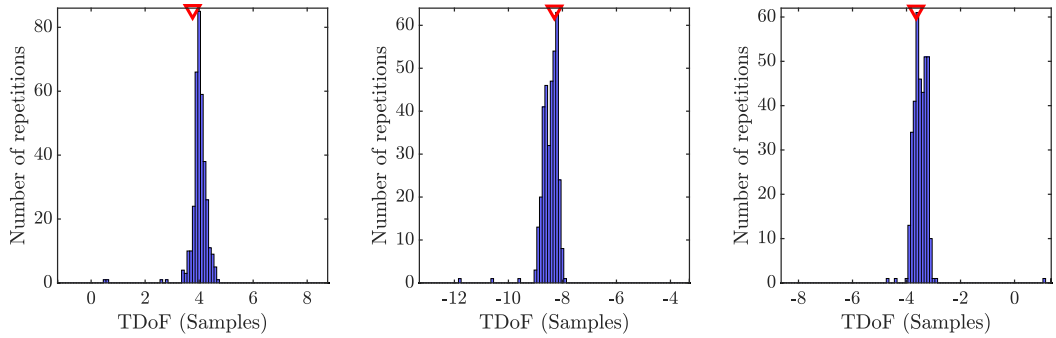

(a) t_{21} *(b)* t_{31} *(c)* t_{41}

Figure 3.30: TDoA calculated with the minimum time series cumulative kurtosis algorithm in PD source localization.

better repeatability (in the measurement where the depth of the interface where not known) and better accuracy (in the experiments where the nominal depth is known)when compared to the rest of the methods.

In the second application, the evaluation of the algorithms is undertaken by positioning the antennas and the RF emitter in known positions and comparing the theoretical TDoA values with the calculated values. The final RF emitter localization will be solved in Chapter 4 where several algorithms for 3D localization are shown. After comparing the calculated TDoA with the theoretical value it can be concluded that the best method is the proposed in this thesis, kurtosis 2 , showing, on average, the lowest deviation and, in many cases, the best accuracy.

In general, the algorithms which base their performance in the amplitude of the signals, such as maximum amplitude or cross correlation, report worse results than the algorithms which defines the onset as the beginning of the rise of the first front wave of the pulsed signal, as the Hinkley method or kurtosis 2. For the first kind of algorithms are substantially affected by the rise slope of the pulse in the other and the second kind of algorithms are insensible to this effect. Other situation which affects in the TDoA calculus is the reflections of the acquired signals. When the reflections provokes that the amplitude of the peaks after the first cycle are greater than the first one, the TDoA would have great undesired errors.

3.9 Bibliography

[1] H. Zhang, C. Thurber, and C. Rowe. "Automatic P-Wave Arrival Detection and Picking with Multiscale Wavelet Analysis for Single-Component Recordings". en. In: *Bulletin of the Seismological Society of America* 93.5 (Oct. 2003), pp. 1904–1912. ISSN: 0037-1106, 1943-3573. DOI: 10.1785/0120020241. URL: http://www.geology.wisc.edu/~hjzhang/Reviewed/Zhang.autopick.BSSA.03.pdf (cit. on pp. 53, 60).

[2] J. H. Kurz, C. U. Grosse, and H.-W. Reinhardt. "Strategies for reliable automatic onset time picking of acoustic emissions and of ultrasound signals in concrete". In: *Ultrasonics* 43.7 (June 2005), pp. 538–546. ISSN: 0041-624X. DOI: 10.1016/j.ultras.2004.12.005. URL: http://www.sciencedirect.com/science/article/pii/S0041624X04003166 (cit. on pp. 53, 59).

[3] G. Robles, J. M. Fresno, and J. M. Martínez-Tarifa. "Separation of Radio-Frequency Sources and Localization of Partial Discharges in Noisy Environments". en. In: *Sensors* 15.5 (Apr. 2015), pp. 9882–9898. DOI: 10.3390/s150509882. URL: http://www.mdpi.com/1424-8220/15/5/9882 (cit. on p. 53).

[4] P. Wagenaars, P. Wouters, P. van der Wielen, et al. "Accurate estimation of the time-of-arrival of partial discharge pulses in cable systems in service". In: *IEEE Transactions on Dielectrics and Electrical Insulation* 15.4 (Aug. 2008), pp. 1190–1199. ISSN: 1070-9878. DOI: 10.1109/TDEI.2008.4591242 (cit. on pp. 53, 59, 60).

[5] A. Lazaro, D. Girbau, and R. Villarino. "WAVELET-BASED BREAST TUMOR LOCALIZATION TECHNIQUE USING A UWB RADAR". en. In: *Progress In Electromagnetics Research* 98 (2009), pp. 75–95. ISSN: 1559-8985. DOI: 10.2528/PIER09100705. URL: http://www.jpier.org/PIER/pier.php?paper=09100705 (cit. on p. 53).

[6] R. Giannetti, A. Petrella, J. Bach, et al. "Feasibility study of in vivo bone depth measurement using high frequency ultrasound". In: *Instrumentation and Measurement Technology Conference (I2MTC), 2015 IEEE International*. May 2015, pp. 762–766. DOI: 10.1109/I2MTC.2015.7151364 (cit. on pp. 54, 67).

[7] F. Kreuger, M. Wezelenburg, A. Wiemer, et al. "Partial discharge. XVIII. Errors in the location of partial discharges in high voltage solid dielectric cables". In: *IEEE Electrical Insulation Magazine* 9.6 (Nov. 1993), pp. 15–22. ISSN: 0883-7554. DOI: 10.1109/57.245980 (cit. on pp. 54, 55).

[8] S. Björklund. *A survey and comparison of time-delay estimation methods in linear systems*. Citeseer, 2003. URL: http://citeseerx.ist.psu.edu/viewdoc/download?doi=10.1.1.452.765&rep=rep1&type=pdf (cit. on p. 55).

[9] L. Yang, M. Judd, and C. Bennoch. "Time delay estimation for UHF signals in PD location of transformers [power transformers]". In: *2004 Annual Report Conference on Electrical Insulation and Dielectric Phenomena, 2004. CEIDP '04.* Oct. 2004, pp. 414–417. DOI: 10.1109/CEIDP.2004.1364275 (cit. on p. 57).

[10] M. Judd, L. Yang, and I. Hunter. "Partial discharge monitoring of power transformers using UHF sensors. Part I: sensors and signal interpretation". In: *IEEE Electrical Insulation Magazine* 21.2 (Mar. 2005), pp. 5–14. ISSN: 0883-7554. DOI: 10.1109/MEI.2005.1412214 (cit. on p. 57).

[11] D. V. Hinkley. "Inference about the Change-Point from Cumulative Sum Tests". In: *Biometrika* 58.3 (1971), pp. 509–523. ISSN: 00063444. URL: http://www.jstor.org/stable/2334386 (cit. on p. 59).

[12] H. Akaike. "A new look at the statistical model identification". In: *IEEE Transactions on Automatic Control* 19.6 (Dec. 1974), pp. 716–723. ISSN: 0018-9286. DOI: 10.1109/TAC.1974.1100705 (cit. on p. 59).

[13] R. Sleeman and T. van Eck. "Robust automatic P-phase picking: an on-line implementation in the analysis of broadband seismogram recordings". In: *Physics of the Earth and Planetary Interiors* 113.1–4 (June 1999), pp. 265–275. ISSN: 0031-9201. DOI: 10.1016/S0031-9201(99)00007-2. URL: http://www.sciencedirect.com/science/article/pii/S0031920199000072 (cit. on p. 60).

[14] C. Saragiotis, L. Hadjileontiadis, and S. Panas. "PAI-S/K: A robust automatic seismic P phase arrival identification scheme". In: *IEEE Transactions on Geoscience and Remote Sensing* 40.6 (June 2002), pp. 1395–1404. ISSN: 0196-2892. DOI: 10.1109/TGRS.2002.800438 (cit. on pp. 60, 61).

[15] P. J. Moore, I. E. Portugues, and I. A. Glover. "Radiometric location of partial discharge sources on energized high-Voltage plant". In: *IEEE Transactions on Power Delivery* 20.3 (July 2005), pp. 2264–2272. ISSN: 0885-8977. DOI: 10.1109/TPWRD.2004.843397 (cit. on p. 64).

[16] Y.-C. Choi, J.-H. Park, and K.-S. Choi. "An impact source localization technique for a nuclear power plant by using sensors of different types". In: *ISA Transactions* 50.1 (Jan. 2011), pp. 111–118. ISSN: 0019-0578. DOI: 10.1016/j.isatra.2010.08.004. URL: http://www.sciencedirect.com/science/article/pii/S0019057810000728 (cit. on p. 64).

[17] S. Gezici. "A Survey on Wireless Position Estimation". en. In: *Wireless Personal Communications* 44.3 (Feb. 2008), pp. 263–282. ISSN: 0929-6212, 1572-834X. DOI: 10.1007/s11277-007-9375-z. URL: https://link.springer.com/article/10.1007/s11277-007-9375-z (cit. on p. 64).

[18] X. Lai and H. Torp. "Interpolation methods for time-delay estimation using cross-correlation method for blood velocity measurement". In: *IEEE Transactions on Ultrasonics, Ferroelectrics, and Frequency Control* 46.2 (Mar. 1999), pp. 277–290. ISSN: 0885-3010. DOI: 10.1109/58.753016 (cit. on p. 64).

[19] C. Knapp and G. Carter. "The generalized correlation method for estimation of time delay". In: *IEEE Transactions on Acoustics, Speech and Signal Processing* 24.4 (Aug. 1976), pp. 320–327. ISSN: 0096-3518. DOI: 10.1109/TASSP.1976.1162830 (cit. on p. 64).

[20] G. Carter. "Coherence and time delay estimation". In: *Proceedings of the IEEE* 75.2 (Feb. 1987), pp. 236–255. ISSN: 0018-9219. DOI: 10.1109/PROC.1987.13723 (cit. on p. 64).

[21] H. Hou, G. Sheng, and X. Jiang. "Robust Time Delay Estimation Method for Locating UHF Signals of Partial Discharge in Substation". In: *IEEE Transactions on Power Delivery* 28.3 (July 2013), pp. 1960–1968. ISSN: 0885-8977. DOI: 10.1109/TPWRD.2013.2262315 (cit. on p. 65).

[22] L. Chéze. "Comparison of different calculations of three-dimensional joint kinematics from video-based system data". In: *Journal of Biomechanics* 33.12 (Dec. 2000), pp. 1695–1699. ISSN: 0021-9290. DOI: 10.1016/S0021-9290(00)00146-9. URL: http://www.sciencedirect.com/science/article/pii/S0021929000001469 (cit. on p. 67).

[23] C. M. Myles, P. J. Rowe, C. R. C. Walker, et al. "Knee joint functional range of movement prior to and following total knee arthroplasty measured using flexible electrogoniometry". In: *Gait & Posture* 16.1 (Aug. 2002), pp. 46–54. ISSN: 0966-6362. DOI: 10.1016/S0966-6362(01)00198-9. URL: http://www.sciencedirect.com/science/article/pii/S0966636201001989 (cit. on p. 67).

[24] C. Reinschmidt, A. J. van den Bogert, et al. "Effect of skin movement on the analysis of skeletal knee joint motion during running". In: *Journal of Biomechanics* 30.7 (July 1997), pp. 729–732. ISSN: 0021-9290. DOI: 10.1016/S0021-9290(97)00001-8. URL: http://www.sciencedirect.com/science/article/pii/S0021929097000018 (cit. on p. 67).

[25] J. C. Ahn. "Ultrasound-guided Regional Anesthesia A Practical Approach to Peripheral Nerve Blocks and Perineural Catheters". In: *The Journal of the American Society of Anesthesiologists* 115.5 (Nov. 2011), pp. 1143–1143. ISSN: 0003-3022. DOI: 10.1097/ALN.0b013e318233789f. URL: http://anesthesiology.pubs.asahq.org/article.aspx?articleid=1934525 (cit. on p. 68).

[26] P. Laugier and G. Haïat. "Bone quantitative ultrasound". en. In: (2011). DOI: 10.1007/978-94-007-0017-8. URL: http://link.springer.com/10.1007/978-94-007-0017-8 (cit. on p. 68).

[27] P. Moilanen. "Ultrasonic guided waves in bone". In: *IEEE Transactions on Ultrasonics, Ferroelectrics, and Frequency Control* 55.6 (June 2008), pp. 1277–1286. ISSN: 0885-3010. DOI: 10.1109/TUFFC.2008.790 (cit. on p. 68).

[28] F. W. Mauldin, K. Owen, M. Tiouririne, et al. "The effects of transducer geometry on artifacts common to diagnostic bone imaging with conventional medical ultrasound". In: *IEEE Transactions on Ultrasonics, Ferroelectrics, and Frequency Control* 59.6 (June 2012), pp. 1101–1114. ISSN: 0885-3010. DOI: 10.1109/TUFFC.2012.2301 (cit. on p. 68).

[29] T.-S. Yeh, C.-H. Wu, W.-S. Chen, et al. "Serial Ultrasonography for Early Detection and Follow-up of Heterotopic Ossification in Stroke". In: *Journal of Medical Ultrasound* 20.2 (June 2012), pp. 119–124. ISSN: 0929-6441. DOI: 10.1016/j.

jmu.2012.04.009. URL: http://www.sciencedirect.com/science/article/pii/S0929644112000343 (cit. on p. 68).

[30] R. Zheng, L. H. Le, D. Hill, et al. "Estimation of bone quality on scoliotic subjects using ultrasound reflection imaging method - a preliminary study". In: *2015 IEEE International Ultrasonics Symposium (IUS)*. Oct. 2015, pp. 1–4. DOI: 10.1109/ULTSYM.2015.0218 (cit. on p. 68).

[31] T. Fuerst, C. C. Glüer, and H. K. Genant. "Quantitative ultrasound". In: *European Journal of Radiology* 20.3 (Sept. 1995), pp. 188–192. ISSN: 0720-048X. DOI: 10.1016/0720-048X(95)00650-F. URL: http://www.sciencedirect.com/science/article/pii/0720048X9500650F (cit. on p. 69).

[32] R. S. Siffert and J. J. Kaufman. "Ultrasonic bone assessment: "The time has come"". In: *Bone* 40.1 (Jan. 2007), pp. 5–8. ISSN: 8756-3282. DOI: 10.1016/j.bone.2006.07.018. URL: http://www.sciencedirect.com/science/article/pii/S8756328206006247 (cit. on p. 69).

[33] K. Rohde, D. Rohrbach, C. C. Glüer, et al. "Influence of porosity, pore size, and cortical thickness on the propagation of ultrasonic waves guided through the femoral neck cortex: a simulation study". In: *IEEE Transactions on Ultrasonics, Ferroelectrics, and Frequency Control* 61.2 (Feb. 2014), pp. 302–313. ISSN: 0885-3010. DOI: 10.1109/TUFFC.2014.6722615 (cit. on p. 69).

[34] "IEEE Guide for Partial Discharge Testing of Shielded Power Cable Systems in a Field Environment". In: *IEEE Std 400.3-2006* (Feb. 2007), pp. 1–44. DOI: 10.1109/IEEESTD.2007.305045 (cit. on p. 74).

[35] "IEEE Guide for the Measurement of Partial Discharges in AC Electric Machinery". In: *IEEE Std 1434-2014 (Revision of IEEE Std 1434-2000)* (Dec. 2014), pp. 1–89. DOI: 10.1109/IEEESTD.2014.6973042 (cit. on p. 74).

[36] R.-j. Liao, L.-j. Yang, J. Li, et al. "Aging condition assessment of transformer oil-paper insulation model based on partial discharge analysis". In: *IEEE Transactions on Dielectrics and Electrical Insulation* 18.1 (Feb. 2011), pp. 303–311. ISSN: 1070-9878. DOI: 10.1109/TDEI.2011.5704522 (cit. on p. 74).

[37] Q. Xie, S. Cheng, F. Lu, et al. "Location of partial discharge in transformer oil using circular array of ultrasonic sensors". In: *IEEE Transactions on Dielectrics and Electrical Insulation* 20.5 (Oct. 2013), pp. 1683–1690. ISSN: 1070-9878. DOI: 10.1109/TDEI.2013.6633698 (cit. on p. 74).

[38] J. Rubio-Serrano, M. Rojas-Moreno, J. Posada, et al. "Electro-acoustic detection, identification and location of partial discharge sources in oil-paper insulation systems". In: *IEEE Transactions on Dielectrics and Electrical Insulation* 19.5 (Oct. 2012), pp. 1569–1578. ISSN: 1070-9878. DOI: 10.1109/TDEI.2012.6311502 (cit. on p. 74).

[39] S. Coenen, S. Tenbohlen, S. Markalous, et al. "Sensitivity of UHF PD measurements in power transformers". In: *IEEE Transactions on Dielectrics and Electrical Insulation* 15.6 (Dec. 2008), pp. 1553–1558. ISSN: 1070-9878. DOI: 10.1109/TDEI.2008.4712657 (cit. on p. 74).

[40] C. Yao, P. Chen, C. Huang, et al. "Study on the Application of an Ultra-High-Frequency Fractal Antenna to Partial Discharge Detection in Switchgears". en. In: *Sensors* 13.12 (Dec. 2013), pp. 17362–17378. DOI: 10.3390/s131217362. URL: http://www.mdpi.com/1424-8220/13/12/17362 (cit. on p. 74).

[41] I. Portugues, P. Moore, I. Glover, et al. "RF-Based Partial Discharge Early Warning System for Air-Insulated Substations". In: *IEEE Transactions on Power Delivery* 24.1 (Jan. 2009), pp. 20–29. ISSN: 0885-8977. DOI: 10.1109/TPWRD.2008.2005464 (cit. on p. 74).

[42] G. Robles, M. Sánchez-Fernández, R. A. Sánchez, et al. "Antenna Parametrization for the Detection of Partial Discharges". In: *IEEE Transactions on Instrumentation and Measurement* 62.5 (May 2013), pp. 932–941. ISSN: 0018-9456. DOI: 10.1109/TIM.2012.2223332 (cit. on p. 75).

Chapter 4

Survey on the performance of source localization algorithms

4.1 Abstract

There exist different techniques to source location and they can be classified in multilateration, received signal strength (RSS) and proximity. The multilateration techniques rely their performance on the time variables presented in Chapter 3: ToF of the emission from the emitter to the sensor, TDoA of the emission between sensors and pToF of the emission to the sensors. The multilateration algorithms presented and compared in this thesis can be classified in iterative and non-iterative. Both standard least squares (SLS) and hyperbolic least squares (HLS) are iterative and based on Newton-Raphson to solve the non-linear equation system. The metaheuristic techniques GA and PSO are also studied. These optimization techniques estimate the source position as the optimum of an OF based on HLS, they are also iterative. Three non-iterative algorithms such as the hyperbolic positioning algorithms (HPA), maximum likelihood estimator (MLE) and Bancroft are also presented. A non-iterative combined algorithm

MLE-HLS based on MLE and HLS is proposed in this chapter. The algorithms performance is analyzed and compared in terms of accuracy in the localization of the position of the emitter and in terms of computational time. The analysis is made with different sensor layouts since the positions of the sensors affect in the localization; several source positions are also evaluated to make the comparison more robust. The analysis is made theoretically and including errors due to the effect of digitizing the time variables. Finally, the algorithms are compared and the most balanced, is the combined algorithm MLE-HLS, yielding better results than the other algorithms in terms of accuracy and outstanding results in computational time.

4.2 Introduction

In this chapter are merged and extended two publications "Survey on the performance of source localization algorithms" and "A Combined Algorithm Approach for PD Location Estimation Using RF Antennas". Their full citation are detailed in Subsection 7.3.1 in item 5 and in Subsection 7.3.2 in item 9 respectively.

There is a great interest in localizing radiative sources fast and accurately with passive receivers in many fields of work [1]. GPS is a widely used technique in many applications like navigation and location [2]. In sonar, radar and underwater radar, it is often of interest to determine the location of an object from its emissions [3, 4]. Indoor localization in wireless networks is addressed relying on a swarm-based approach [5]. Earthquake epicenter localization can also be handled with this approach [6, 7]. To locate defective assets in electrical facilities through the measurement of the electromagnetic field emitted by PD is another application [8, 9]. The relative position estimation among mobile objects or robots is also studied [10]. All of these applications use or can use the techniques presented in this chapter.

There exist different techniques in indoor positioning which also can be applied in outdoor localization. They can be classified in multilateration, RSS and proximity [11, 12]. The proximity algorithms rely upon a dense grid of antennas and, since the proposed study considers only four receivers, these algorithms are not studied. The RSS algorithms requires the analysis of the scene to collect its features [11] and the localization is done trough probabilistic methods, neural networks, SVM, etc. Finally, multilateration algorithms are easy to implement and there is a wide variety of them, thus the techniques analyzed in this chapter are based on multilateration.

The multilateration algorithms used to localize radiative sources can be classified into two categories: iterative and non-iterative. The iterative algorithms have different logics in the search. SLS and HLS undertake the search using the Newton-Raphson optimization technique [13, 14]. Other iterative algorithms base the search in metaheuristic techniques such as PSO [15, 16, 17] and GA [18]. In the second category, non-iterative algorithms are widely used in GPS where the emitters are satellites and

the target is to locate a sensor receiving the emissions. In this category, three algorithms are presented: HPA [19], MLE [3] and Bancroft algorithm [2].

Both iterative and non-iterative algorithms have advantages and disadvantages and they do not always achieve the actual position with confidence because in the first category, the algorithms not always converge and in the second the algorithms always yields two feasible solutions. The main disadvantages of the iterative algorithms are that these algorithms require an initialization setup and a definition of the initial parameters by the user. This affects the convergence of the algorithms, actually, the Newton's method would not converge in some analyzed points [20], consequently, it can provoke variations in the solution exactness and in the computational time. On the other hand, the non-iterative algorithms formulate different second degree polynomials and report directly two solutions, a positive and a negative root. In GPS, the root selection would be done in different ways such as solving the clock error of a single receiver [21], using pseudo-ranges [2] and others. Commonly, in emitter localization, both solutions are feasible though one root is closer than the other to the actual solution, and it is not immediate to determine which root is the closest [22].

In this thesis, a combined algorithm MLE-HLS is proposed to locate emitters solving the problem of determining the correct root. Then, it is compared with others algorithms in terms of localization accuracy and computational time.

The chapter is organized as follows: Section 4.3 provides an explanation and detailed formulation of all the algorithms used in the chapter and presents the new combined algorithm. The methodology to compare the algorithms is given in Section 4.4. The results of the algorithms comparison are shown in Section 4.5. Finally, the conclusions derived from the results are described in Section 4.6.

4.3 Localization techniques

For a better understanding of the algorithms, they have been divided in two categories: iterative and are non-iterative. Every multilateration algorithm has a different formulation but all of them are based on the fact that the distance travelled by the emissions is equal to the time spent in the flight multiplied by the speed propagation in the free space. The algorithms use different time variables which are described below. The ToF of the emission represents the time spent by the emission to travel from the emitter to the receiver. In some applications it is difficult to find the time when the emission departs. In such cases, it is preferable the use of the TDoA from the emitter to pair of receiver, and, then find the source with a system of non-linear equations. The pToF is another alternative which represents the ToF of the emission to any sensor with a fixed offset, pt_s, the offset represents time elapsed between the start of the clock, t_0, and the emission departure. Figure 4.1 represents the described variables, it is similar to Figure 3.1 but including the representation of TDoA.

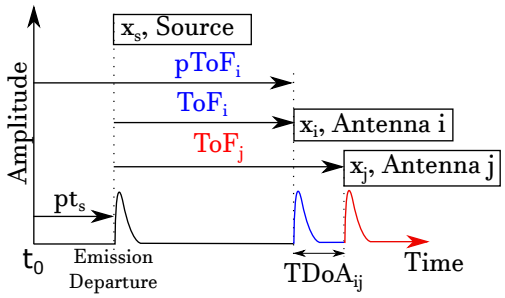

Figure 4.1: ToF, TDoA and pToF representation in an example of one dimension.

The spatial relationship between the time variables and the antennas and source position was previously described in Subsection 3.2. In this subsection the explanation is extended to the pToF variable which was not explained previously. The spatial relationship of the pToF is similar to the ToF but considering an offset. The pToF for i^{th} antenna is denoted as pt_i and $pt_i = t_i + pt_s$. pt_s is time offset elapsed between the instant when the acquisition starts, $t_0 = 0$, and the instant in which the emission departs.

All the algorithms need four sensors or antennas properly deployed with at least one of them allocated in a different plane than the other three for 3D localization [23].

4.3.1 Iterative algorithms

4.3.1.1 Standard Least Squares

The SLS algorithm estimates the emitter position $\mathbf{P_s}$ with $\hat{\mathbf{P}}_\mathbf{s} = (\hat{x}_s, \hat{y}_s, \hat{z}_s)$ minimizing the OF defined by Equation (4.1) using Newton-Raphson [13].

$$OF(\hat{x}_s, \hat{y}_s, \hat{z}_s, \hat{t}_1) = \sum_{i=1}^{N} (\hat{D}_i - \hat{t}_i \cdot c)^2 \tag{4.1}$$

where N is the number of antennas. Since t_i can not be measured because the emission departure instant is unknown then it is estimated through $\hat{t}_i = (\hat{t}_1 + t_{i1})$ where $\hat{t}_1$ is the estimated ToF of the emission from the emitter to the reference antenna, in this approach antenna 1. The TDoA between the reference antenna and the i^{th} antenna is represented by t_{i1}, with $t_{11} = 0$.

Applying partial derivatives in Equation (4.1) regarding the variables under study $(\hat{x}_s, \hat{y}_s, \hat{z}_s, \hat{t}_1)$ and setting them equal to zero, as defined in Equations (4.2).

$$\frac{\partial OF}{\partial \hat{x}_s} = 0, \ \frac{\partial OF}{\partial \hat{y}_s} = 0, \ \frac{\partial OF}{\partial \hat{z}_s} = 0, \ \frac{\partial OF}{\partial \hat{t}_1} = 0 \tag{4.2}$$

Equation (4.3) is obtained operating the partial derivative of OF with respect to $\hat{x}_s$.

$$\frac{\partial OF}{\partial \hat{x}_s} = \hat{x}_s - \frac{1}{N}\sum_{i=1}^{N}\left(x_i + \frac{(\hat{x}_s - x_i)(\hat{t}_1 + t_{i1})c}{\hat{D}_i}\right) = 0 \tag{4.3}$$

As this algorithm is iterative and searches the convergence, it can be assumed that $\hat{x}_s(l) \simeq \hat{x}_s(l-1)$. Then, Equation (4.3) can be modified to Equation (4.4) where the estimated source $\hat{x}_s$ coordinate in the l iteration, $\hat{x}_s(l)$, is defined as a function of the value $\hat{x}_s$ in the previous iteration $(l-1)$, denoted as $\hat{x}_s(l-1)$.

$$\hat{x}_s(l) = \frac{1}{N}\sum_{i=1}^{N}\left(x_i + \frac{(\hat{x}_s(l-1) - x_i)(\hat{t}_1(l-1) + t_{i1})c}{\hat{D}_i(l-1)}\right) \tag{4.4}$$

Equation (4.5) is obtained doing the same operation for every source coordinate $(\hat{x}_s, \hat{y}_s, \hat{z}_s)$ and grouping them in an unique vector $\hat{\mathbf{P}}_\mathbf{s}(l)$ representing the estimated source position of the source.

$$\hat{\mathbf{P}}_\mathbf{s}(l) = \frac{1}{N}\sum_{i=1}^{N}\left(\mathbf{P_i} + \frac{(\hat{\mathbf{P}}_\mathbf{s}(l-1) - \mathbf{P_i})(\hat{t}_1(l-1) + t_{i1})c}{\hat{D}_i(l-1)}\right) \tag{4.5}$$

The estimated ToF from the source to antenna 1, $\hat{t}_1$, is obtained as a function of $\hat{\mathbf{P}}_\mathbf{s}(l-1)$ embedded in $\hat{D}_i(l-1)$, from the last partial derivative in Equation (4.2):

$$\hat{t}_1(l) = \frac{1}{N}\sum_{i=1}^{N}\left(\frac{\hat{D}_i(l-1)}{c} - t_{i1}\right) \tag{4.6}$$

In the event that the algorithm converges before reaching the maximum iterations L, the algorithm stops. The convergency criterium is defined by Equation (4.7).

$$\begin{aligned}
\hat{x}_s(l) - \hat{x}_s(l-1) &< \epsilon_d \\
\hat{y}_s(l) - \hat{y}_s(l-1) &< \epsilon_d \\
\hat{z}_s(l) - \hat{z}_s(l-1) &< \epsilon_d \\
\hat{t}_1(l) - \hat{t}_1(l-1) &< \epsilon_t
\end{aligned} \tag{4.7}$$

In the simulations carried out in this chapter the maximum iteration, L, is fixed to 10^7, the distance error bound, ϵ_d, is set to 10^{-13} meters, the time error bound, ϵ_t, 10^{-13} seconds and the start point is defined as $\hat{\mathbf{P}}_\mathbf{s}(0) = (0,0,0)$ and $\hat{t}_1(0) = 0$. These conditions are defined trying to find the exact solution although it implies high computational time as demonstrated in reference [24].

4.3.1.2 Hyperbolic Least Squares

In this technique, the OF is similar to the one shown in Equation (4.1). The variation is in the time variable, in this case, it is the TDoA so the representations of the possible solutions of the equations are hyperbolas. Equation (4.8) can be obtained applying Equation (3.2) for the reference antenna to the other antennas and adding all of them [14].

$$OF(\hat{x}_s, \hat{y}_s, \hat{z}_s) = \sum_{i=2}^{N} \left(\hat{D}_i - \hat{D}_1 - t_{i1}c \right)^2 \tag{4.8}$$

This iterative algorithm also bases the calculation of the source position on Newton-Raphson. Again, the initial procedure is to calculate and to equal to zero the partial derivative of the OF, Equation (4.8), with respect to $(\hat{x}_s, \hat{y}_s, \hat{z}_s)$ as Equation (4.9) shows.

$$\frac{\partial OF}{\partial \hat{x}_s} = 0, \ \frac{\partial OF}{\partial \hat{y}_s} = 0, \ \frac{\partial OF}{\partial \hat{z}_s} = 0 \tag{4.9}$$

Operating and solving Equation (4.9) in the same way as in Section 4.3.1.1, three equations are obtained which can be expressed in only one, grouping $(\hat{x}_s, \hat{y}_s, \hat{z}_s)$ in $\hat{\mathbf{P}}_\mathbf{s}$:

$$\begin{aligned} \hat{\mathbf{P}}_\mathbf{s}(l) = \frac{1}{2(N-1)} \sum_{i=2}^{N} \Bigg(& \mathbf{P_i} + \mathbf{P_1} \\ & + (\hat{\mathbf{P}}_\mathbf{s}(l-1) - \mathbf{P_i}) \left(\frac{\hat{D}_1 + t_{i1}c}{\hat{D}_i} \right) \\ & + (\hat{\mathbf{P}}_\mathbf{s}(l-1) - \mathbf{P_1}) \left(\frac{\hat{D}_i - t_{i1}c}{\hat{D}_1} \right) \Bigg) \end{aligned} \tag{4.10}$$

Defining the initial value $\hat{\mathbf{P}}_\mathbf{s}(0) = (0, 0, 0)$, Equation (4.10) allows to find the source position iteratively. The solution is the intersection of the hyperbolas with foci defined by the antennas position and the measured TDoA. The initial conditions and the constraints of the simulations are the same as in Subsection 4.3.1.1. The convergency criterium is defined by the first three equations in (4.7).

4.3.1.3 Genetic Algorithm based on HLS

This technique can be used in many applications, in Chapter 2 it is used to separate different types of signals and, in this section, it is used in the localization of radiative sources. As mentioned previously, GA is a metaheuristic technique which uses darwinian evolution to find the optimum solution. This algorithm defines a population which evolutes throughout generations. The population consist of a number of members who represents a feasible solution to the problem. The population evolution is carried out with different operators as selection, crossover and mutation. Every member of the population has its own chromosome in the boolean domain forming a string

of 1 and 0. The minimum number of elements of the string, gens, of each variable has to be calculated through Equation (4.11).

$$Ng_{x_s} \geq \frac{\log\left(\frac{x_{s_{max}} - x_{s_{min}}}{\Delta x_s} + 1\right)}{\log(2)} \tag{4.11}$$

where Ng_{x_s} is the number of gens of the position of the source in the axis x, x_s; the maximum value of $\hat{x_s}$, is defined as $x_{s_{max}}$ and the minimum as $x_{s_{min}}$. The minimum step in the x_s digitalization is represented by Δx_s.

To evaluate the fitness of the members, their chromosomes have to be converted from the boolean to the decimal domain to obtain $(\hat{x_s}, \hat{y_s}, \hat{z_s})$ which represents one feasible solution of the problem. An example of the chromosome of one member of the population, in the boolean and decimal domains, is shown below. In this example, $(x_s, y_s, z_s)_{max} = 10$ m, $(x_s, y_s, z_s)_{min} = -10$ m, $Ng_{(x_s,y_s,z_s)} = 10$ bits and $\Delta x_s = \Delta y_s = \Delta z_s = 20/(2^{10} - 1) \simeq 0.02$ m. The starting point is the boolean domain:

$$(0110111011, 0000000000, 1111111111) = (\hat{x}_s, \hat{y}_s, \hat{z}_s)$$

the chromosome is converted to the decimal domain in the range of 0 to $2^{10} - 1$:

$$(886, 0, 1023)$$

Afterwards, the variables are fitted to the range under study. In this case, 0 corresponds to -10 m and 1023 corresponds to 10 m. In the example, the final result is:

$$(7.30, -10.00, 10.00) = (\hat{x}_s, \hat{y}_s, \hat{z}_s)$$

This algorithm uses a maximization of the OF, Equation (4.12), based on the HLS Equation (4.8). The OF allows to evaluate the fitness of each member and it is maximized through GA until the convergence criterium is reached.

$$OF(\hat{x}_s, \hat{y}_s, \hat{z}_s) = \frac{1}{1 + \sum_{i=1}^{N-1} \sum_{j=i+1}^{N} \left(\hat{D}_i - \hat{D}_j - t_{ij}c\right)^2} \tag{4.12}$$

The steps inside the algorithm are as follows:

1. To generate a random population and to evaluate their fitness.
2. To select the population's members according to their fitness to generate the next generation.
3. To apply crossover between the selected members and the rest of the population.
4. To apply mutation to the resulting individuals from the crossover.

5. To convert the boolean string to the decimal domain and evaluate the fitness using the OF, Equation (4.9).

6. If the number of generations does not reach the minimum specified by user, go to step 2. Otherwise, the solution is defined as the member that has the position with best fitness.

4.3.1.4 Particle Swarm Optimization based on HLS

This technique, as GA, can be used in many applications, in Chapter 2 it is used to separate different types of signals and in this section it is used in the localization of radiative sources. As mentioned previously, PSO is a metaheuristic technique which searches the optimum inspired in the way the birds or fish look for food. The particles are deployed in the solution space so each particle has three variables (x_s, y_s, z_s). The K particles change their position $\mathbf{P_k}$ in each iteration through:

$$\mathbf{P_k}(l) = \mathbf{P_k}(l-1) + \mathbf{v_k}(l) \tag{4.13}$$

The displacement or velocity of the k^{th} particle in the l-iteration, $\mathbf{v_k}(l)$, considers the particle velocity in the previous iteration, $\mathbf{v_k}(l-1)$, its personal best position, $\mathbf{P_{k,best}}(l-1)$, and the global best position of the swarm $\mathbf{P_{best}}(l-1)$, found at any time during the search.

$$\begin{aligned} \mathbf{v_k}(l) = \omega \mathbf{v_k}(l-1) \\ + C_1 \mathbf{U_1}(\mathbf{P_{k,best}}(l-1) - \mathbf{P_k}(l-1)) \\ + C_2 \mathbf{U_2}(\mathbf{P_{best}}(l-1) - \mathbf{P_k}(l-1)) \end{aligned} \tag{4.14}$$

where:

$$\mathbf{v_k}(l) = \begin{bmatrix} v_{k,x}(l) \\ v_{k,y}(l) \\ v_{k,z}(l) \end{bmatrix}, \mathbf{P_k}(l) = \begin{bmatrix} x_k(l) \\ y_k(l) \\ z_k(l) \end{bmatrix} \tag{4.15}$$

being $k = 1, 2, ..., K$ and $l = 1, 2, ..., L$. The particle inertia, ω, varies from 0.9 in the first iteration to 0.4 in the L iteration, [25]. This Provokes high movement of the particles in the beginning of the simulation to explore large regions and focus the search around the optimum moving the particles slowly at the end of the simulation. C_1 and C_2 allow to balance the influence of the personal best or global best position in the search. $\mathbf{U_1}$ and $\mathbf{U_2}$ are line matrices with three elements randomly distributed between 0 and 1 that randomizes the movement of the particles, and are generated in each iteration to introduce randomness in the search.

Every particle is evaluated in the minimization OF Equation (4.16), based on HLS

on Equation (4.8). It considers 6 TDoA when 4 antennas are used to obtain better accuracy in the localization [15].

$$OF(\hat{x}_s, \hat{y}_s, \hat{z}_s) = \sum_{i=1}^{N-1} \sum_{j=i+1}^{N} \left(\hat{D}_i - \hat{D}_j - t_{ij}c \right)^2 \tag{4.16}$$

The steps inside the algorithm are as follows:

1. K particles are spread in the space of solutions. Their initial velocity is set to 0 for all particles.
2. Each particle position is evaluated using Equation (4.16).
3. If some particle improves its local best, it is updated. If some particle improves the global best, it is also updated.
4. The velocity Equation (4.14) and the position Equation (4.13) are updated for each particle in the swarm.
5. If the maximum number of iterations L is reached or when all the particles are located close to the same point, the algorithm ends and the solution is the position of the $\mathbf{P_{best}}(L)$. Otherwise, go to step 2.

4.3.2 Non-iterative algorithms

4.3.2.1 Hyperbolic Positioning Algorithm

The HPA algorithm was developed by Ralph Bucher for GPS location using four fixed stations [19] and it also can be applied to any emitter localization. This algorithm uses the TDoA as HLS in Section 4.3.1.2.

The position of the source is defined as the intersection of four hyperbolas based on Equation (3.2):

$$\begin{aligned} D_{12} &= D_1 - D_2 = t_{12}c \\ D_{13} &= D_1 - D_3 = t_{13}c \\ D_{32} &= D_3 - D_2 = t_{32}c \\ D_{34} &= D_3 - D_4 = t_{34}c \end{aligned} \tag{4.17}$$

These equations are solved obtaining several intermediate variables with the final target of obtaining the source coordinates. The full formulation is developed in detail in 4.7. As a result of the equation system, the coordinates of source position (x_s, y_s, z_s) are defined through equations (4.71), (4.74) and (4.86) respectively. For each coordinate this algorithm reports two direct solutions, the positive and negative root.

4.3.2.2 Bancroft Algorithm

The Bancroft algorithm was developed by Stephen Bancroft also for GPS location [2]. This algorithm uses a different equation system to find the source position through the Lorenz inner product for four space arrays. The four space array for the antennas and the source is defined through Equations (4.18).

$$\mathbf{a_i} = \begin{bmatrix} x_i \\ y_i \\ z_i \\ c \cdot pt_i \end{bmatrix}, \quad \mathbf{a_s} = \begin{bmatrix} x_s \\ y_s \\ z_s \\ c \cdot pt_s \end{bmatrix} \tag{4.18}$$

where pt_i denotes the pToF measurements taken from each of the i^{th} antennas. In RF emitter localization, pt_i is the absolute ToF at the i^{th} antenna plus an additional offset pt_s. The source position is defined by (x_s, y_s, z_s) and pt_s is the elapsed time between the instant when the acquisitions starts and the instant when the emission departs. The Lorenz inner product of $\mathbf{a_i}$ and $\mathbf{a_s}$ can be calculated through:

$$\langle \mathbf{a_i}, \mathbf{a_s} \rangle = x_i x_s + y_i y_s + z_i z_s - c^2 \cdot pt_i \cdot pt_s \tag{4.19}$$

The Bancroft approach pivots around the variables defined above. The source position can be obtained following the operations detailed below.

$$\mathbf{A} = (\mathbf{a_1}\ , \mathbf{a_2}\ , \mathbf{a_3}\ , \mathbf{a_4})^T = \begin{bmatrix} x_1 & y_1 & z_1 & -c \cdot pt_1 \\ x_2 & y_2 & z_2 & -c \cdot pt_2 \\ x_3 & y_3 & z_3 & -c \cdot pt_3 \\ x_4 & y_4 & z_4 & -c \cdot pt_4 \end{bmatrix} \tag{4.20}$$

Computing the four space $\mathbf{u}$ and $\mathbf{v}$ vectors from

$$\begin{aligned} \mathbf{u} &= \mathbf{A}^{-1}\mathbf{i_0} \\ \mathbf{v} &= \mathbf{A}^{-1}\mathbf{r} \end{aligned} \tag{4.21}$$

where:

$$\mathbf{i_0} = \begin{bmatrix} 1 \\ 1 \\ 1 \\ 1 \end{bmatrix}, \mathbf{r} = \frac{1}{2} \begin{bmatrix} \langle \mathbf{a_1}, \mathbf{a_1} \rangle \\ \langle \mathbf{a_2}, \mathbf{a_2} \rangle \\ \langle \mathbf{a_3}, \mathbf{a_3} \rangle \\ \langle \mathbf{a_4}, \mathbf{a_4} \rangle \end{bmatrix} \tag{4.22}$$

together with the scalar coefficients E, F and G calculated with Equations (4.23).

$$\begin{aligned} E &= \langle \mathbf{u}, \mathbf{u} \rangle \\ F &= \langle \mathbf{u}, \mathbf{v} \rangle - 1 \\ G &= \langle \mathbf{v}, \mathbf{v} \rangle \end{aligned} \tag{4.23}$$

With the previous variables, the final Equation (4.24) can be defined as:

$$E\boldsymbol{\lambda}^2 + 2F\boldsymbol{\lambda} + G = 0 \tag{4.24}$$

As a result from Equation (4.24) two solutions $\boldsymbol{\lambda}^+$ positive root and $\boldsymbol{\lambda}^-$ negative root are obtained, so two possible source positions are calculated with Equation (4.25).

$$\mathbf{a_s}^+ = \boldsymbol{\lambda}^+\mathbf{u} + \mathbf{v} = \begin{bmatrix} x_s^+ \\ y_s^+ \\ z_s^+ \\ c \cdot pt_s^+ \end{bmatrix}, \quad \mathbf{a_s}^- = \boldsymbol{\lambda}^-\mathbf{u} + \mathbf{v} = \begin{bmatrix} x_s^- \\ y_s^- \\ z_s^- \\ c \cdot pt_s^- \end{bmatrix} \tag{4.25}$$

In GPS applications, the criterium to choose the correct root is based on clock synchronisation because only one solution fits. In source location, this criterium can not be applied because the time when the emission departs is unknown so both solutions would be, in principle, valid in the presented analysis.

4.3.2.3 Maximum Likelihood Estimator algorithm

MLE algorithm was developed by Chan and Ho also for GPS location and reports two explicit solutions [3]. Equation (3.3) is the initial equation and operating it is turned in:

$$D_i^2 = x_s^2 + y_s^2 + z_s^2 - 2x_s x_i - 2y_s y_i - 2z_s z_i + K_i \tag{4.26}$$

where:

$$K_i = x_i^2 + y_i^2 + z_i^2 \tag{4.27}$$

Considering antenna 1 as the reference, the TDoA for each pair of antennas can be represented by t_{i1} with $i = \{2, 3, 4\}$ representing the non reference antennas. Using the two first terms of the hyperbolic Equation (3.2) and operating, the equation (4.28) is obtained:

$$D_i = D_{i1} + D_1 \tag{4.28}$$

substituting (4.28) in (4.26):

$$\begin{aligned} &D_{i1}^2 + 2D_{i1}D_1 + D_1^2 \\ &= x_s^2 + y_s^2 + z_s^2 - 2x_s x_i - 2y_s y_i - 2z_s z_i + K_i \end{aligned} \tag{4.29}$$

subtracting (4.29) minus (4.26) considering $i = 1$:

$$\begin{aligned} D_{i1}^2 + 2D_{i1}D_1 &= -2x_s(x_i - x_1) \\ &- 2y_s(y_i - y_1) - 2z_s(z_i - z_1) + K_i - K_1 \end{aligned} \tag{4.30}$$

Equation (4.30) can be expressed in matrix form as shown in:

$$\begin{aligned} \begin{bmatrix} x_s \\ y_s \\ z_s \end{bmatrix} &= - \begin{bmatrix} x_2 - x_1 & y_2 - y_1 & z_2 - z_1 \\ x_3 - x_1 & y_3 - y_1 & z_3 - z_1 \\ x_4 - x_1 & y_4 - y_1 & z_4 - z_1 \end{bmatrix}^{-1} \\ &\times \left\{ \begin{bmatrix} D_{21} \\ D_{31} \\ D_{41} \end{bmatrix} D_1 + \frac{1}{2} \begin{bmatrix} D_{21}^2 - K_2 + K_1 \\ D_{31}^2 - K_3 + K_1 \\ D_{41}^2 - K_4 + K_1 \end{bmatrix} \right\} \end{aligned} \tag{4.31}$$

In the previous system, there are three equations and four unknown variables x_s, y_s, z_s, D_1. The fourth equation to solve the system is found in Equation (4.26). Substituting (x_s, y_s, z_s) from Equation (4.31) in Equation (4.26) at $i = 1$ a quadratic result in D_1 is obtained. Substituting the positive and negative roots of the D_1 back into Equation (4.31), two possible source positions are provided (x_s^+, y_s^+, z_s^+) positive root and (x_s^-, y_s^-, z_s^-) negative root.

4.3.2.4 Combined algorithm based on MLE and HLS (MLE-HLS)

A combined algorithm based on the MLE algorithm shown in Subsection 4.3.2.3 and the HLS algorithm shown in Subsection 4.3.1.2 is presented in the publication "A Combined Algorithm Approach for PD Location Estimation Using RF Antennas", which full citation can be found in Subsection 7.3.2 in item 9. The MLE algorithm reports two feasible solutions, one of them is closer to the actual source position than the other, and the desired solution is not always located in the position given by the positive root. With MLE-HLS, the solution selection is carried out with the OF based on HLS, Equation (4.16), because it has been already proved that reports great results in the PSO algorithm. Thus, from the solutions reported by the MLE algorithm explained in Subsection 4.3.2.3, the chosen solution is the one which returns the lowest value in (4.16) yielding the position closest to the source.

The MLE algorithm report results with high resolution, below micrometers but, there is no need to locate the sources with such resolution in this application. In the presented simulations, the solutions are rounded to millimeters before evaluating Equation (4.16).

4.4 Methodology

As mentioned in Section 4.3, the inputs to the localization algorithms are the antenna positions and the time variables ToF, TDoA or pToF depending on the algorithm. As the target of the chapter is to evaluate the algorithms through simulations, the time variables are calculated from the geometry instead of the measurements. The source position has to be previously defined to carry out the calculation of the time variables. Then, the ToF is defined as the distance between the source and the respective antenna and divided by the speed propagation, c. The TDoA between two antennas is the subtraction between their ToF. The pToF is calculated adding an offset to the ToF variables.

The simulations procedure has four steps, the first one is to set the four antennas and the source position. The second one is to calculate the exact ToF, TDoA and pToF for that geometric configuration. The third step is use those times to calculate back the source position with every algorithm using the antenna position and the time variables. The fourth step is to calculate the computational time spent and the errors of every algorithm in the source location.

The procedure described above is done in two cases; under exact values for the time variables and introducing a digitizing error. Under theoretical conditions the time variables are values with high resolution in decimal digits. In the other cases, the time variables are rounded to implement the effect of the digital acquisition and to analyze its effect in the localization. Simulating what happens in real applications when they are digitally collected in the discrete domain. Then, to emulate the digitizing error, the theoretic values of ToF, TDoA and pToF have to be rounded to the nearest sample, ie, using an acquisition system with sampling frequency f_s=10 Gs / s the time interval between the samples is the inverse $T_s = 1/f_s = 0.1$ ns multiplied by the speed of the light, c results in a maximum error of 3 cm. In this case, if the TDoA between two antennas multiplied by c is 1 m, digitalizing the discrete TDoA, with 3 cm of error, it will be 0.99 or 1.02 m. Interpolating the time variables the error magnitude can be reduced [8]. In the previous example, interpolating with 10 samples the sampling frequency increased to f_s=100 Gs/s, and T_s will be reduced to 0.01 ns, then, the error in distance would be 3 mm in Subsection 4.5.2.

In some cases, when the direct algorithms are executed under the digitizing error in the time variables, the localization can yield a solution with real and imaginary components. This is caused because the time round up introduces an error in the process which provokes square roots of negative values. In these cases, the imaginary term is omitted because the solution space (x_s, y_s, z_s) is in the real 3D space. In the iterative algorithms this problem does not exists because the search is done in the real 3D space and in the iterative algorithms process there are not chance to obtain any imaginary solution.

The simulations were carried out in a computer with processor Intel(R) Core(TM)

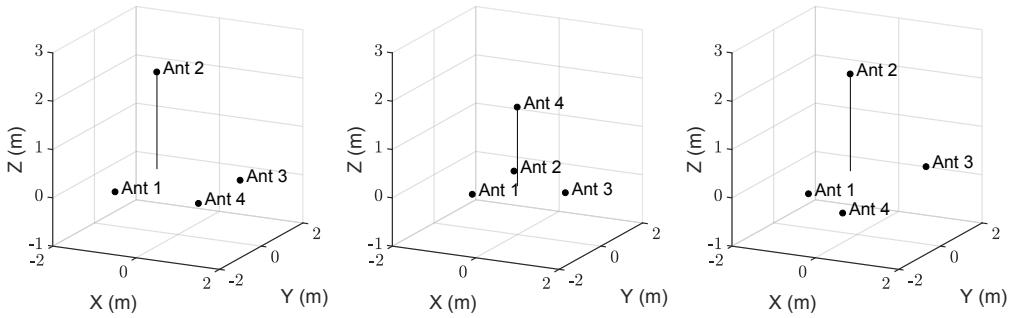

(a) Square *(b)* Pyramid *(c)* Trapezoidal

Figure 4.2: Antenna layouts used in the study. The antennas are represented by black dots.

Table 4.1: Antennas positions in meters for each configuration.

Layout		Ant 1	Ant 2	Ant 3	Ant 4
square	x	-1.00	-1.00	1.00	1.00
	y	-1.00	1.00	1.00	-1.00
	z	-1.00	1.00	-1.00	-1.00
pyramid	x	$-\frac{\sqrt{3}}{3}$	$-\frac{\sqrt{3}}{3}$	$2\frac{\sqrt{3}}{3}$	0.00
	y	-1.00	1.00	0.00	0.00
	z	$-\sqrt{\frac{2}{3}}$	$-\sqrt{\frac{2}{3}}$	$-\sqrt{\frac{2}{3}}$	$\sqrt{\frac{2}{3}}$
trapezoidal	x	-0.66	-0.66	0.66	0.66
	y	-1.00	1.00	2.00	-2.00
	z	-1.00	1.00	-1.00	-1.00

i7-3630QM CPU@2.40GHz 2.4GHz, the RAM memory 8.00 GB (7.89 GB usable), the Matlab version is R2016b. The priority of the Matlab process in the computer was *Real Time*.

The deviation in the source localization is analyzed in spherical coordinates, so $\hat{\mathbf{P}}_\mathbf{s} = (\hat{r}, \hat{\theta}, \hat{\varphi})$. This procedure permits to distinguish the errors in the distance estimation $(\hat{r})$ and the errors in the direction estimation $(\hat{\theta}, \hat{\varphi})$. The errors are calculated from the estimated source position $\hat{\mathbf{P}}_\mathbf{s}$ to the actual source position $\mathbf{P}_\mathbf{s} = (r, \theta, \varphi)$ through:

$$\begin{aligned} \Delta\hat{r} &= |\hat{r} - r| \\ \Delta\hat{\theta} &= |\hat{\theta} - \theta| \\ \Delta\hat{\varphi} &= |\hat{\varphi} - \varphi| \end{aligned} \tag{4.32}$$

The algorithms are evaluated under several conditions to make a sturdy comparison. They are applied in three widely used antennas layouts (square, pyramid and trapezoidal) see Figure 4.2. Different antenna layouts are analyzed since it was demonstrated that the receiver position affects in the source localization [23]. Table 4.1 shows the detailed coordinates of each antenna array configuration.

The source has been located at different positions in the space. These points are

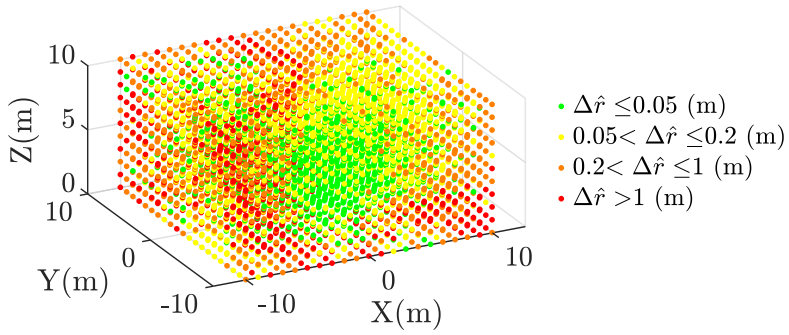

Figure 4.3: RF emitter positions analyzed with MLE-HLS algorithm in the real case, representing the radius error $\Delta\hat{r}$ by colors.

located every meter in each direction inside of $20 \times 20 \times 10$ meters centred in $(0, 0, 5)$ m. Figure 4.3 shows an example of all the possible positions of the source in that volume analyzing the accuracy in the estimated radius $\hat{r}$ by colors for the trapezoidal antennas configuration placed as in Figure 4.2(c). The resulting color graduation shows that as long as the source is close to the antennas the accuracy in $\hat{r}$ is high.

4.5 Results

In this section, all the results obtained from the simulations are generated following the procedure described in Section 4.4.

4.5.1 Theoretical conditions

The results of the simulations presented in this section are undertaken with theoretical conditions. This means that the ToF, TDoA and pToF used in the locations algorithms are the theoretical values with high resolution. The aim of these simulations is to test the performance of the algorithms when finding a solution to the OF.

4.5.1.1 Accuracy

Every algorithm is evaluated in the same source positions detailed in Section 4.4, see Figure 4.3. The accuracy in the variables: radius, elevation and azimuth for all the methods has been quantified in all positions with three antennas layouts. Figure 4.4 shows the percentage of points located within the radius errors defined by the legend by every algorithm in every antenna configuration. Table 4.2 displays the percentage of number of positions located with lower error than 1 cm in the radius calculus. The best algorithm, MLE-HLS yields 100% of points located with an error in radius calculation lower than 1 cm in every antenna layout. It is followed by PSO which localizes 90.8% of the points with an error lower than 1 cm. The positive root of the other non-iterative algorithms localizes 79-80% of the points with good accuracy. On the other

Table 4.2: Percentage of positions analyzed located with a radius error $\Delta\hat{r}$ lower than 1 cm under theoretical conditions for each algorithm and antenna array configuration.

$\Delta\hat{r} \leq 1\ cm$	**Square**	**Pyram**	**Trapez**	**Mean**
SLS	74.3%	50.2%	67.2%	**63.9%**
HLS	82.3%	81.4%	73.6%	**79.1%**
GA	0.2%	0.2%	0.1%	**0.2%**
PSO	90.7%	91.2%	90.4%	**90.8%**
HPA^+	79.0%	84.2%	81.5%	**81.6%**
HPA^-	12.8%	15.7%	18.2%	**15.5%**
$Bancroft^+$	83.9%	81.4%	73.7%	**79.7%**
$Bancroft^-$	18.6%	18.7%	26.4%	**21.2%**
MLE^+	83.9%	81.4%	73.7%	**79.7%**
MLE^-	18.6%	18.7%	26.4%	**21.2%**
MLE HLS	100.0%	100.0%	100.0%	**100.0%**

hand, the negative root reaches only 15-21%. The GA algorithm obtains very poor results compared with the others. It has been included in the comparison because it is used to locate emitters surrounded by the antennas, in the bibliography. In the analysis presented in this thesis, the emitter is usually outside of the volume defined by the antennas and it can compromise the accuracy of the localization, in the same way than SLS and HLS algorithms.

The percentage of number of points located within an error in elevation angle inside the error magnitude defined by the legend by every algorithm and every antenna array are shown in Figure 4.5. The percentage of number of positions located with an error lower than 1° in the elevation angle are indicated in Table 4.3. As a summary, the best algorithm is again MLE-HLS and reports 100 % of the analyzed positions with an error lower than 1° in the elevation angle in every antenna layout. The second best algorithm, PSO, locates 93.6 % of the points with high accuracy. The other algorithms are worse, they locate with high accuracy only 45-88 % of the points. The negative roots of the non-iterative algorithms report very poor results, they locate with high accuracy a mere 20-25 % of the points.

The same calculations are performed for the azimuth angle and the results are shown in Figure 4.6 and in Table 4.4. The percentage of positions located with an error lower than 1° in the azimuth angle for the best algorithm, is again 100 % for MLE-HLS. PSO is also the second best and the other algorithms are behind. In general, this variable is calculated with better accuracy in more points than the elevation angle.

4.5.1.2 Computational time

The computational time of each algorithm and antenna layout can be seen in Figure 4.7. Notice that the Y axis, time, is in logarithmic scale. The HPA algorithm is the fastest, needing only 13 μs to localize one position. MLE, MLE-HLS and Bancroft are

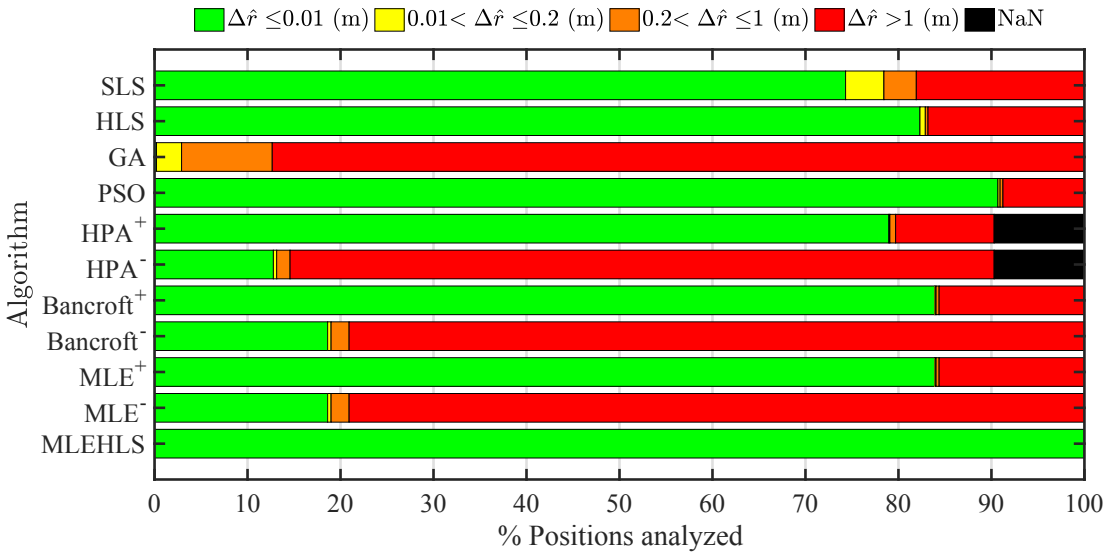

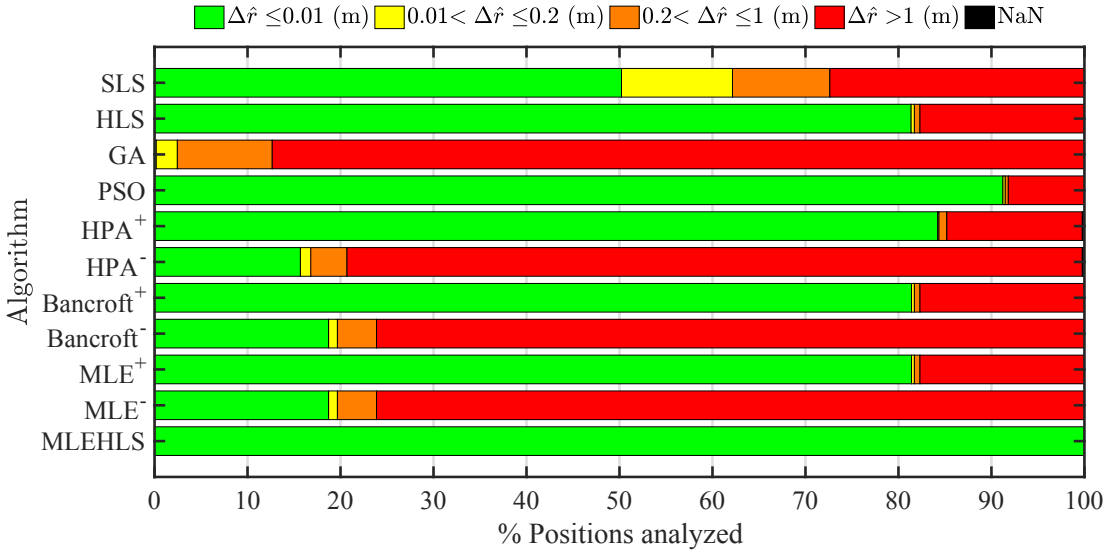

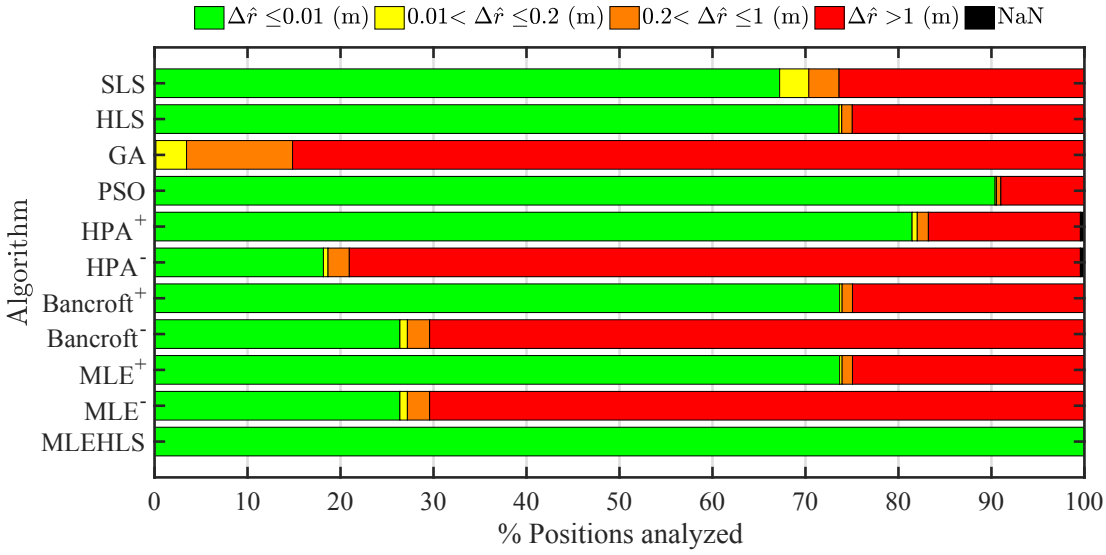

(c) Trapezoidal

Figure 4.4: Percentage of positions located within the errors in the radius $\Delta\hat{r}$ defined in the legend under theoretical conditions for each algorithm and antenna array configuration.

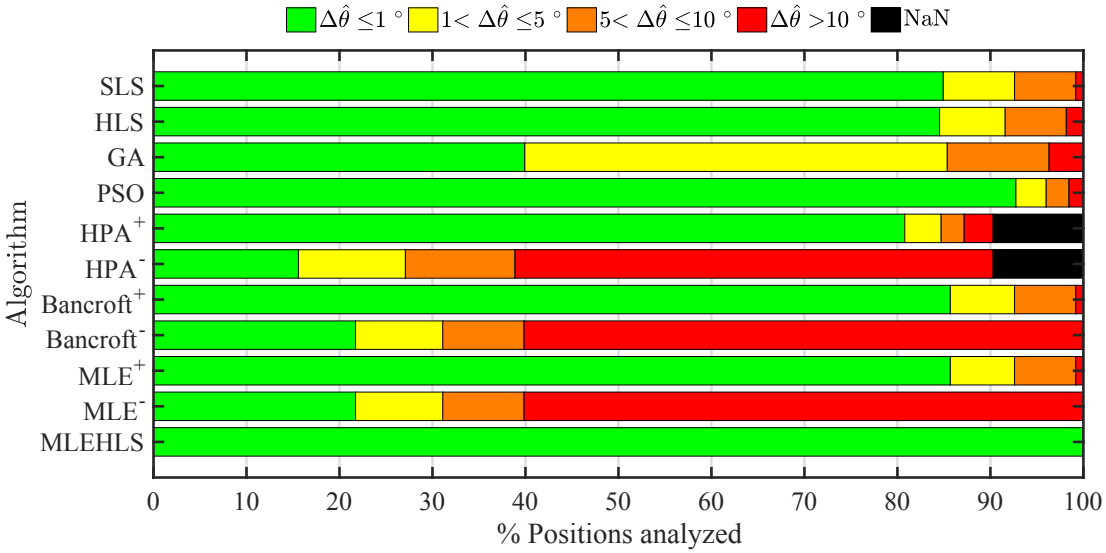

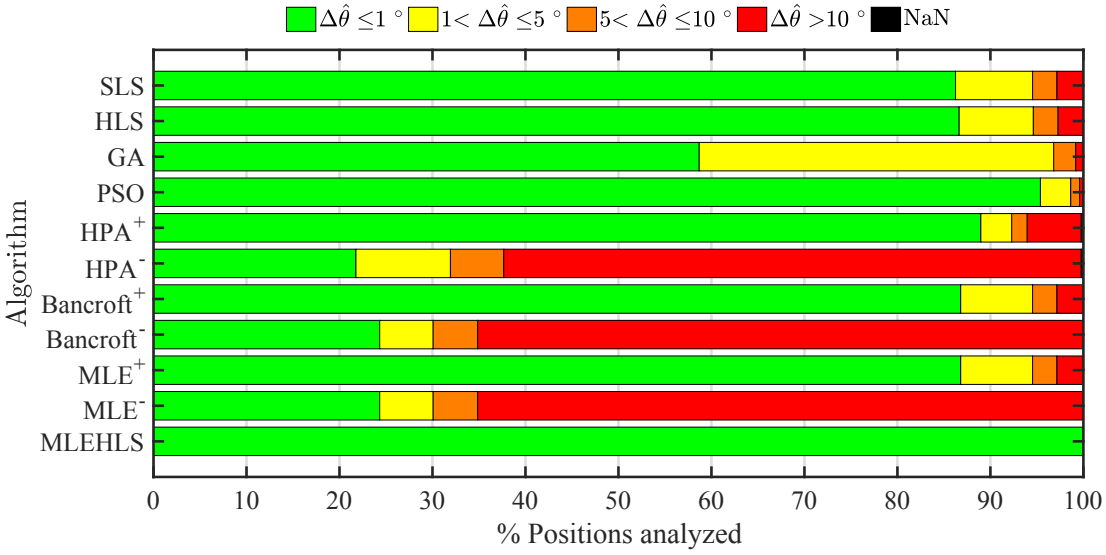

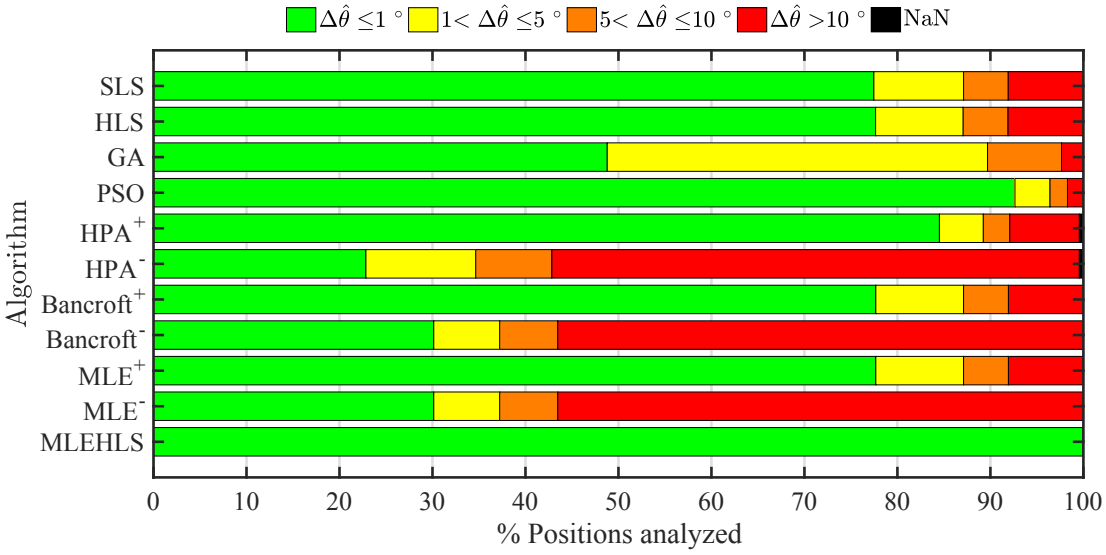

(c) Trapezoidal

Figure 4.5: Percentage of positions located within the errors in the Elevation angle $\Delta\hat{\theta}$ in distance defined in the legend under theoretical conditions for each algorithm and antenna array configuration.

Table 4.3: Percentage of positions analyzed located with an Elevation angle error $\Delta\hat{\theta}$ lower than 1° under theoretical conditions for each algorithm and antenna array configuration.

$\Delta\hat{\theta} \leq 1^\circ$	**Square**	**Pyram**	**Trapez**	**Mean**
SLS	84.9%	86.3%	77.5%	**82.9%**
HLS	84.5%	86.6%	77.7%	**82.9%**
GA	39.9%	58.7%	48.8%	**49.1%**
PSO	92.7%	95.4%	92.6%	**93.6%**
HPA^+	80.8%	89.0%	84.5%	**84.8%**
HPA^-	15.6%	21.8%	22.8%	**20.1%**
$Bancroft^+$	85.7%	86.8%	77.7%	**83.4%**
$Bancroft^-$	21.7%	24.3%	30.1%	**25.4%**
MLE^+	85.7%	86.8%	77.7%	**83.4%**
MLE^-	21.7%	24.3%	30.1%	**25.4%**
MLE HLS	100.0%	100.0%	100.0%	**100.0%**

Table 4.4: Percentage of positions analyzed located with an Azimuth angle error $\Delta\hat{\varphi}$ lower than 1° under theoretical conditions for each algorithm and antenna array configuration.

$\Delta\hat{\varphi} \leq 1^\circ$	**Square**	**Pyram**	**Trapez**	**Mean**
SLS	92.8%	92.8%	78.3%	**87.9%**
HLS	91.8%	92.6%	78.6%	**87.6%**
GA	64.7%	75.9%	55.0%	**65.2%**
PSO	96.3%	97.9%	92.8%	**95.7%**
HPA^+	83.8%	94.4%	84.9%	**87.7%**
HPA^-	30.0%	68.2%	24.3%	**40.8%**
$Bancroft^+$	93.0%	92.7%	78.7%	**88.2%**
$Bancroft^-$	33.7%	70.1%	31.1%	**45.0%**
MLE^+	93.0%	92.8%	78.7%	**88.2%**
MLE^-	33.7%	70.2%	31.1%	**45.0%**
MLE HLS	100.0%	100.0%	99.9%	**100.0%**

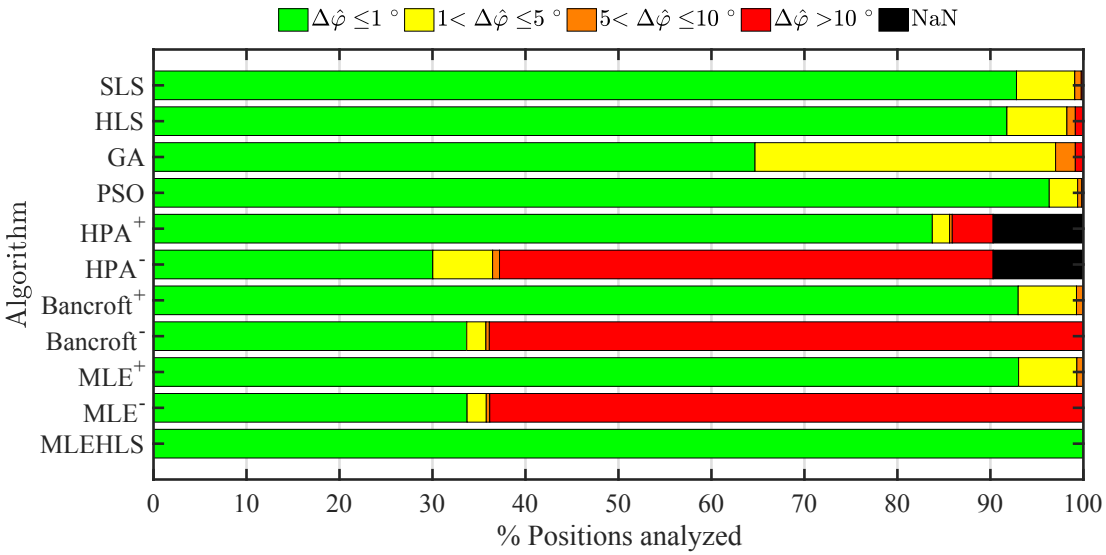

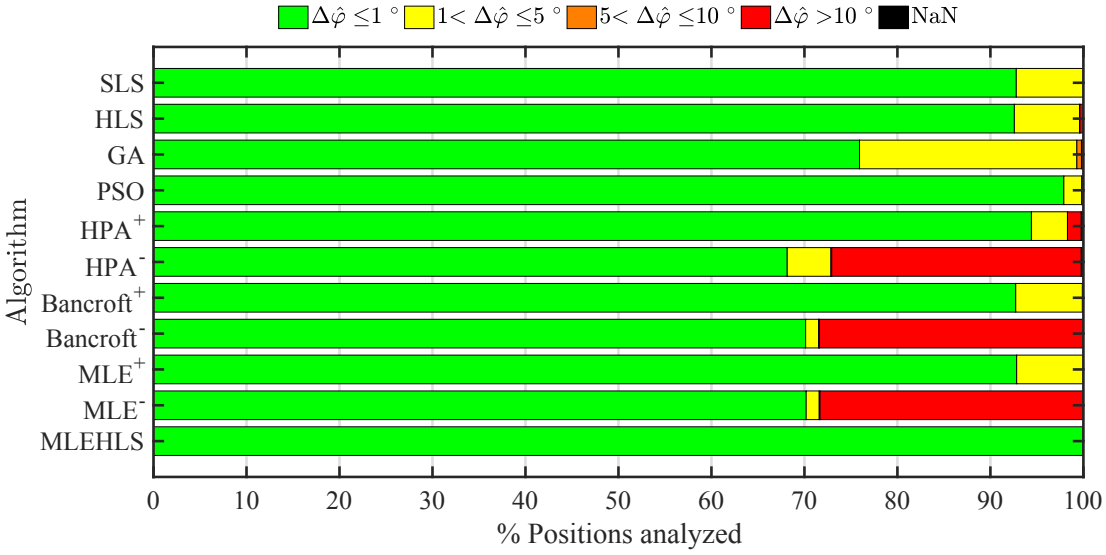

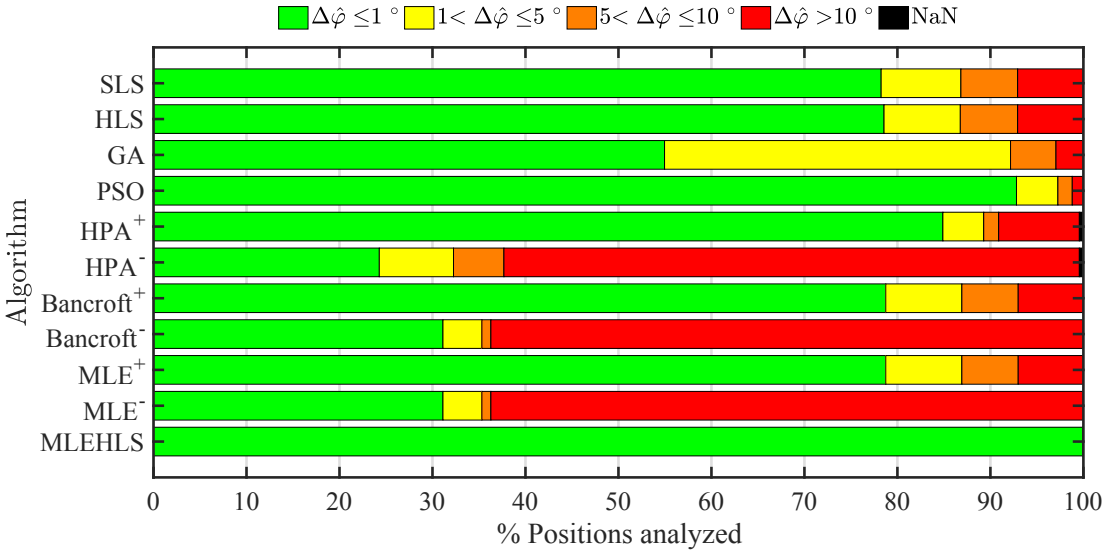

(c) Trapezoidal

Figure 4.6: Percentage of positions located within the errors in the Azimuth angle $\Delta\hat{\varphi}$ in distance defined in the legend under theoretical conditions for each algorithm and antenna array configuration.

Table 4.5: Summary of the mean computational time spent, in seconds, for each position analyzed in theoretical conditions by each algorithm.

Algorithm	Square	Pyram	Trapez	Mean
SLS	$7.8 \cdot 10^{-1}$	$1.3 \cdot 10^{0}$	$5.9 \cdot 10^{-1}$	$8.9 \cdot 10^{-1}$
HLS	$2.4 \cdot 10^{-1}$	$2.5 \cdot 10^{-1}$	$9.0 \cdot 10^{-1}$	$1.9 \cdot 10^{-1}$
GA	$2.3 \cdot 10^{-1}$	$2.3 \cdot 10^{-1}$	$2.4 \cdot 10^{-1}$	$2.3 \cdot 10^{-1}$
PSO	$3.3 \cdot 10^{-2}$	$3.4 \cdot 10^{-2}$	$3.2 \cdot 10^{-2}$	$3.3 \cdot 10^{-2}$
HPA	$1.6 \cdot 10^{-5}$	$1.2 \cdot 10^{-5}$	$1.2 \cdot 10^{-5}$	$1.3 \cdot 10^{-5}$
Bancroft	$2.0 \cdot 10^{-4}$	$1.8 \cdot 10^{-4}$	$1.8 \cdot 10^{-4}$	$1.9 \cdot 10^{-4}$
MLE	$9.1 \cdot 10^{-5}$	$8.1 \cdot 10^{-5}$	$8.1 \cdot 10^{-5}$	$8.4 \cdot 10^{-5}$
MLE-HLS	$1.9 \cdot 10^{-4}$	$1.5 \cdot 10^{-4}$	$1.5 \cdot 10^{-4}$	$1.6 \cdot 10^{-4}$

also fast needing 84-190 μs. The iterative algorithms are slower than the direct algorithms and they need 33-890 ms in average.

Most of the algorithms have a quite constant computational time except SLS and HLS algorithms which have high fluctuations. It is due to the fact that the number of iterations needed in each position is not the same. The initial position in their search is set equal to $(0, 0, 0)$ so, the algorithms have to translate the solutions closer to the actual position until the convergence is reached. When the source is placed near the initial position, the translation is sorter and the algorithms need less iterations, and therefore, less time to converge than when the source is farther. Table 4.5 shows the mean computational time for one source location.

4.5.2 Digitizing error in time variables

The results of the simulations presented in this section are carried out considering the digitizing error in the calculation of the time variables. The electromagnetic emissions have to be acquired by ADC equipment and in consequence, the acquired signals are discrete. This implies that the time variables used in the location algorithms are rounded to steps of 0.01 ns as explained in Section 4.4.

4.5.2.1 Accuracy

Under these conditions, the accuracy decreases compared with the theoretical case as expected. The radius is the most critical variable as Figure 4.8 and Table 4.6 indicate. The two best algorithms, MLE-HLS and PSO, localize $49 - 50\%$ of the analyzed points with an error lower than 20 cm in average which is acceptable when localizing inside an open-air substation for example. The pyramidal configuration of antennas gets the worst accuracy, 37 %, while for the square or trapezoidal configurations the best algorithms localize $61 - 65\%$ of the analyzed points with an error lower than 20 cm. Nevertheless, an average error lower than 20 cm is acceptable considering that the maximum distances from the source are as far as 10 m, Figure 4.3.

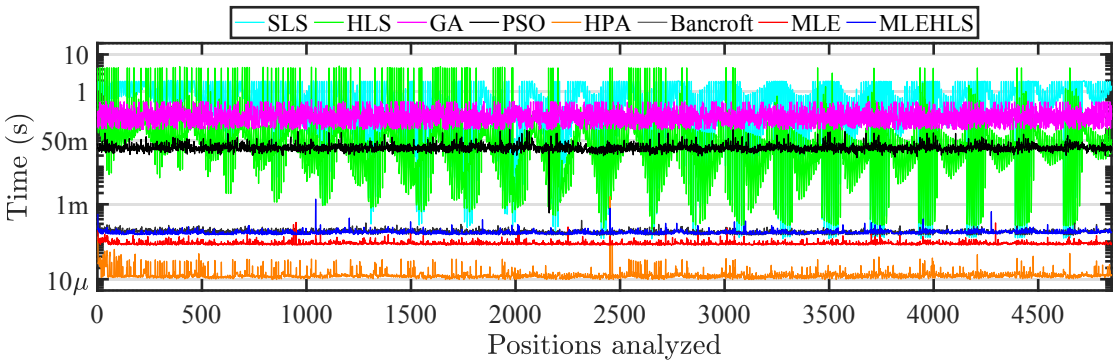

(a) Square

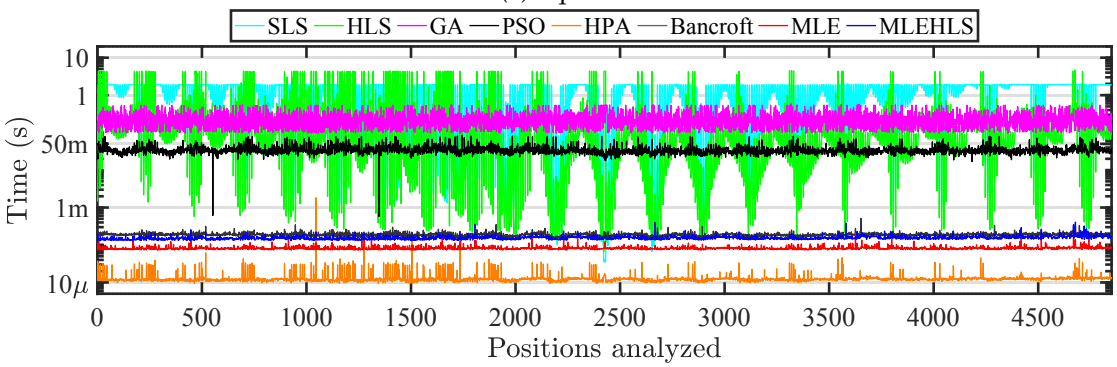

(b) Pyramid

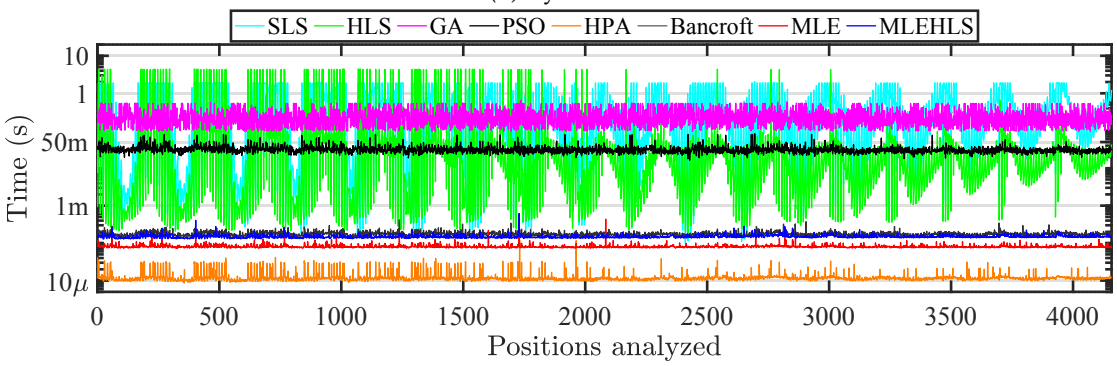

(c) Trapezoidal

Figure 4.7: Mean computational time spent for each position analyzed in theoretical conditions by each algorithm.

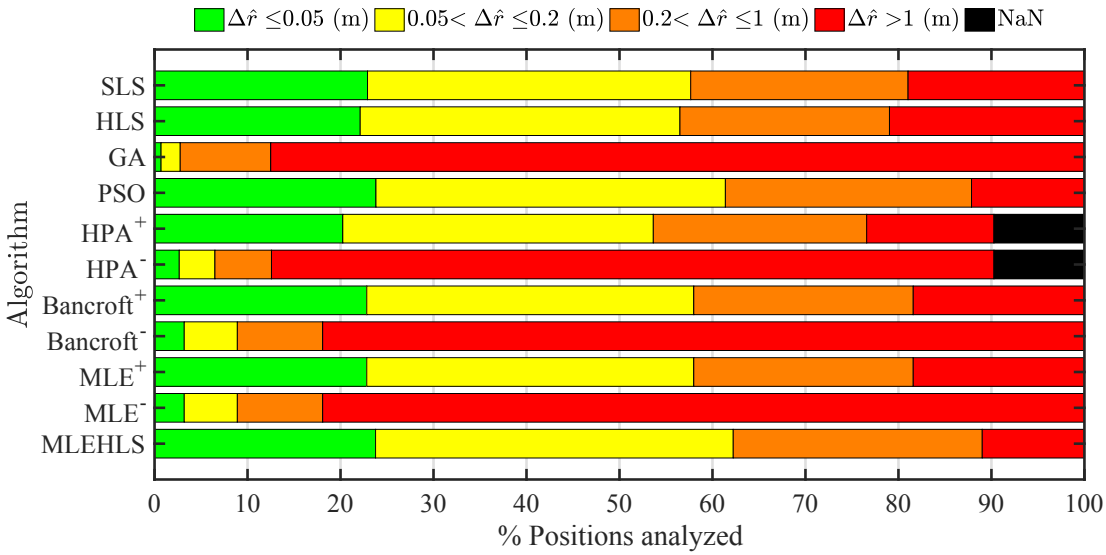

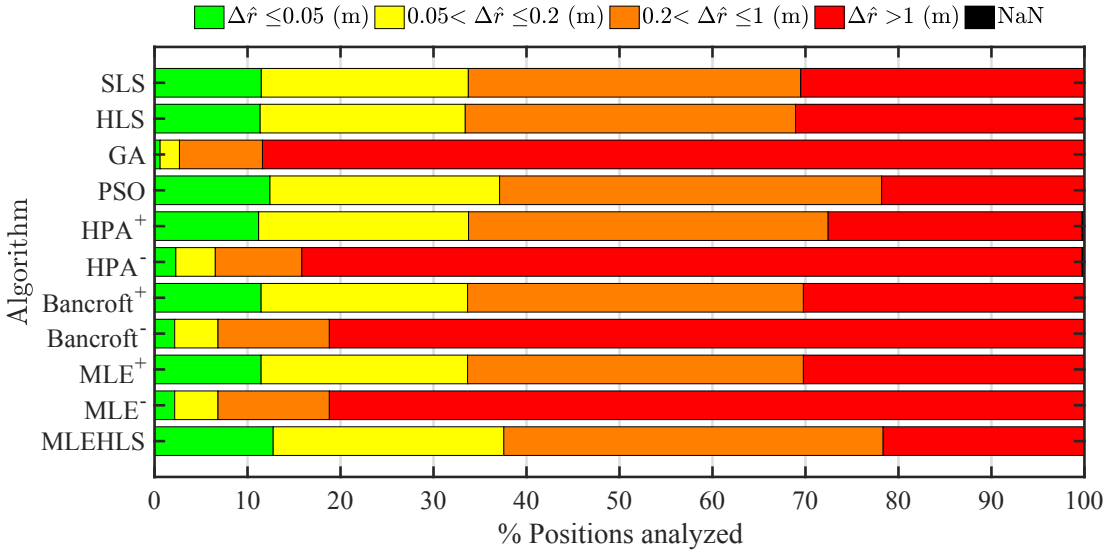

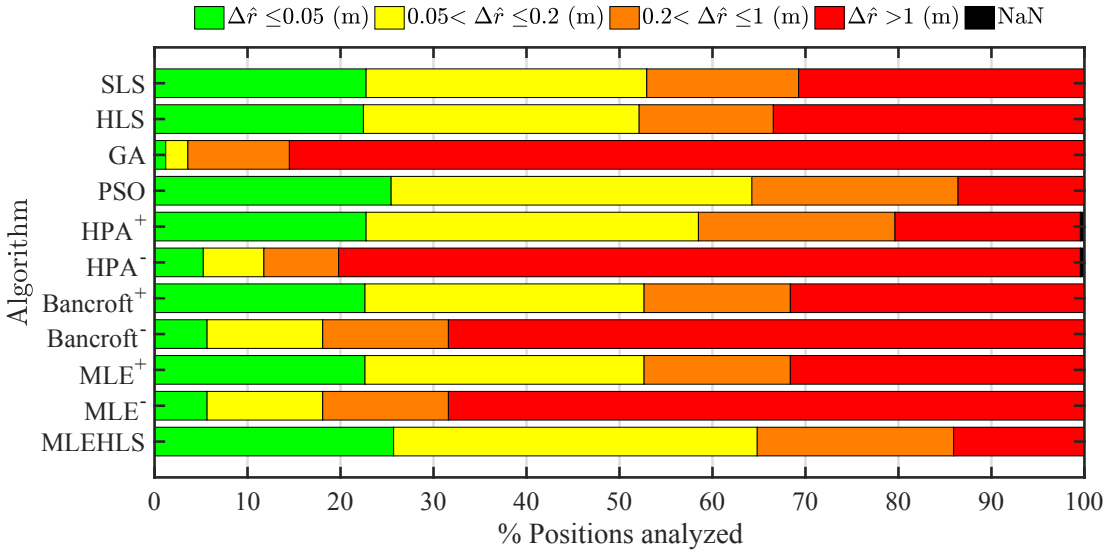

(c) Trapezoidal

Figure 4.8: Percentage of positions located within the errors in the radius $\Delta\hat{r}$ defined in the legend under digitizing error in time variables for each algorithm and antenna array configuration.

Table 4.6: Percentage of positions analyzed located with a radius error $\Delta\hat{r}$ lower than 20 cm under digitizing error in time variables for each algorithm and antenna array configuration.

$\Delta\hat{r} \leq 20\ cm$	**Square**	**Pyram**	**Trapez**	**Mean**
SLS	57.7%	33.7%	52.9%	**45.7%**
HLS	56.5%	33.4%	52.1%	**45.0%**
GA	2.8%	2.7%	3.6%	**2.7%**
PSO	61.4%	37.1%	64.2%	**49.2%**
HPA$^+$	53.6%	33.8%	58.5%	**43.7%**
HPA$^-$	6.5%	6.5%	11.8%	**6.5%**
Bancroft$^+$	58.0%	33.7%	52.6%	**45.8%**
Bancroft$^-$	8.9%	6.8%	18.1%	**7.9%**
MLE$^+$	58.0%	33.7%	52.6%	**45.8%**
MLE$^-$	8.9%	6.8%	18.1%	**7.9%**
MLE HLS	62.2%	37.6%	64.8%	**49.9%**

Table 4.7: Percentage of positions analyzed located with an Elevation angle error $\Delta\hat{\theta}$ lower than 1° under digitizing error in time variables for each algorithm and antenna array configuration.

$\Delta\hat{\theta} \leq 1^\circ$	**Square**	**Pyram**	**Trapez**	**Mean**
SLS	84.2%	86.0%	73.9%	**85.1%**
HLS	81.5%	84.7%	71.7%	**83.1%**
GA	39.8%	59.4%	45.5%	**49.6%**
PSO	92.2%	94.9%	91.1%	**93.6%**
HPA$^+$	79.8%	88.3%	83.8%	**84.0%**
HPA$^-$	14.5%	21.1%	23.6%	**17.8%**
Bancroft$^+$	84.3%	86.2%	74.0%	**85.3%**
Bancroft$^-$	20.9%	23.5%	33.9%	**22.2%**
MLE$^+$	84.3%	86.2%	74.0%	**85.3%**
MLE$^-$	20.9%	23.5%	33.9%	**22.2%**
MLE HLS	92.8%	94.9%	90.8%	**93.8%**

The elevation angle is calculated with good accuracy as seen in Figure 4.9. With the best two algorithms, MLE-HLS and PSO, the elevation angle is calculated with lower or equal error than 1° for 93% of the analyzed positions as shows Table 4.7. 97% of the points analyzed are calculated with an error in the azimuth angle lower or equal than 1°, see Figure 4.10 and Table 4.8. These facts imply that the bearing angle is solved with any of the antenna configuration, but determining the distance to the source accurately depends greatly on the algorithm and the antenna layout.

4.5.2.2 Computational time

The computational times spent in average by each algorithm for one position are displayed in Table 4.9. The times are very similar than those in the theoretical conditions for almost all the algorithms. In this case, only the HLS algorithm is slower

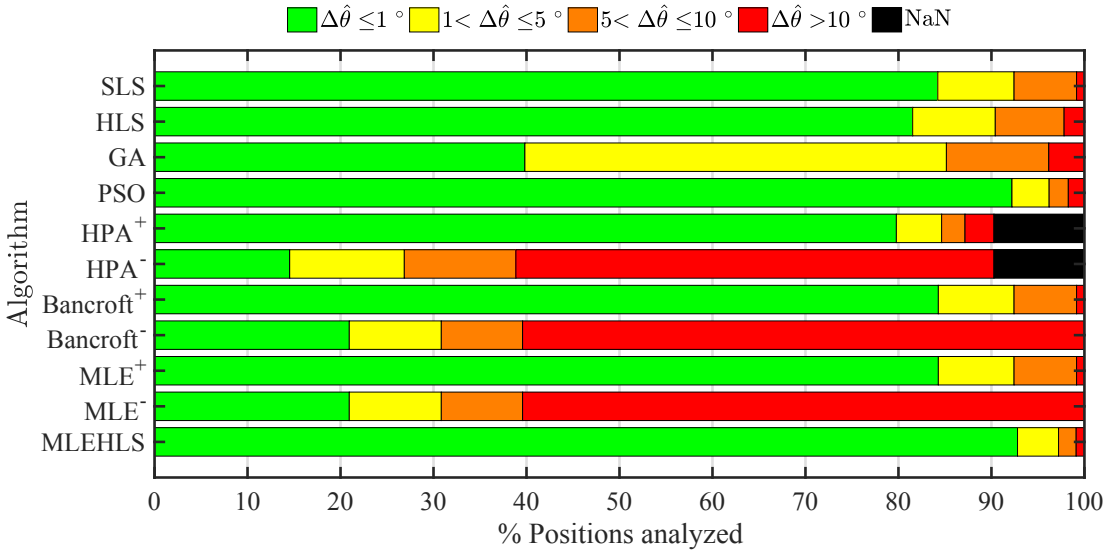

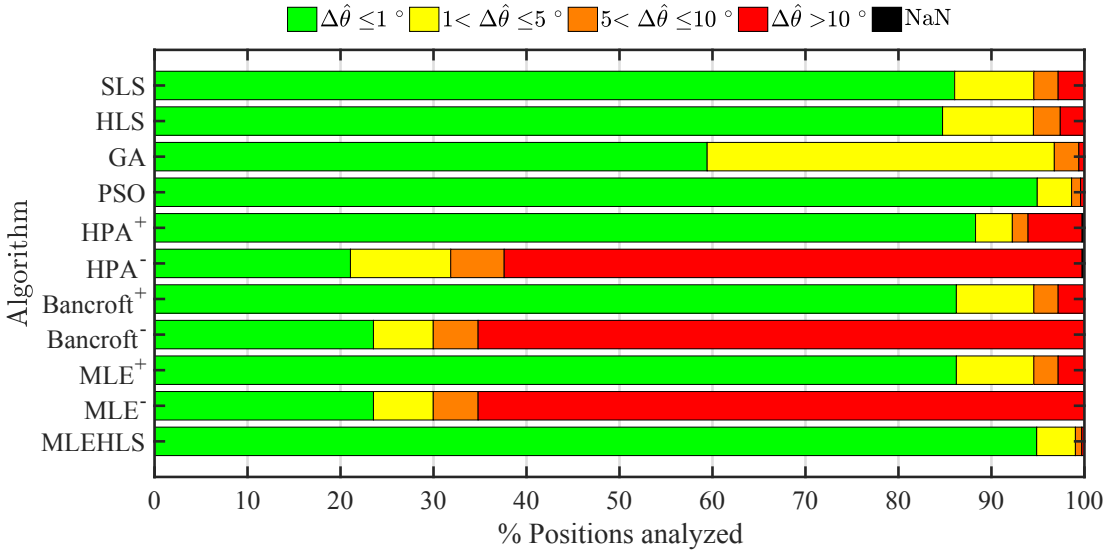

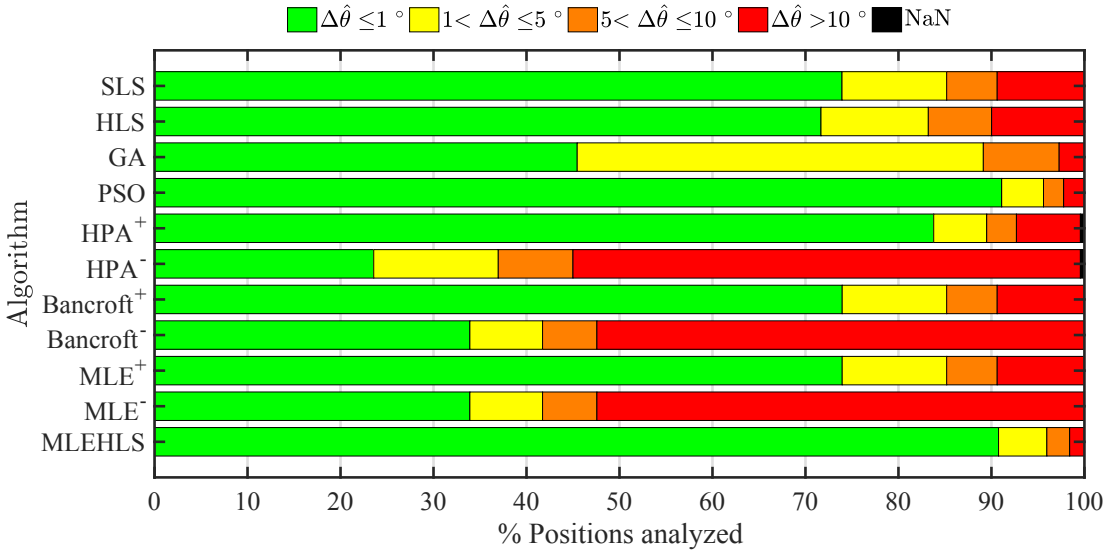

(c) Trapezoidal

Figure 4.9: Percentage of positions located within the errors in the Elevation angle $\Delta\hat{\theta}$ in distance defined in the legend under digitizing error in time variables for each algorithm and antenna array configuration.

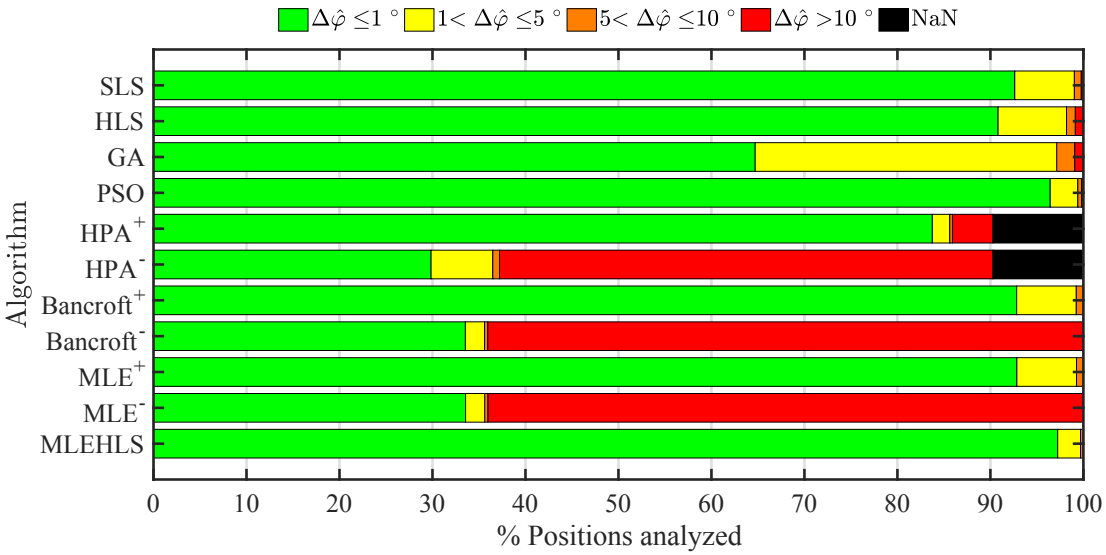

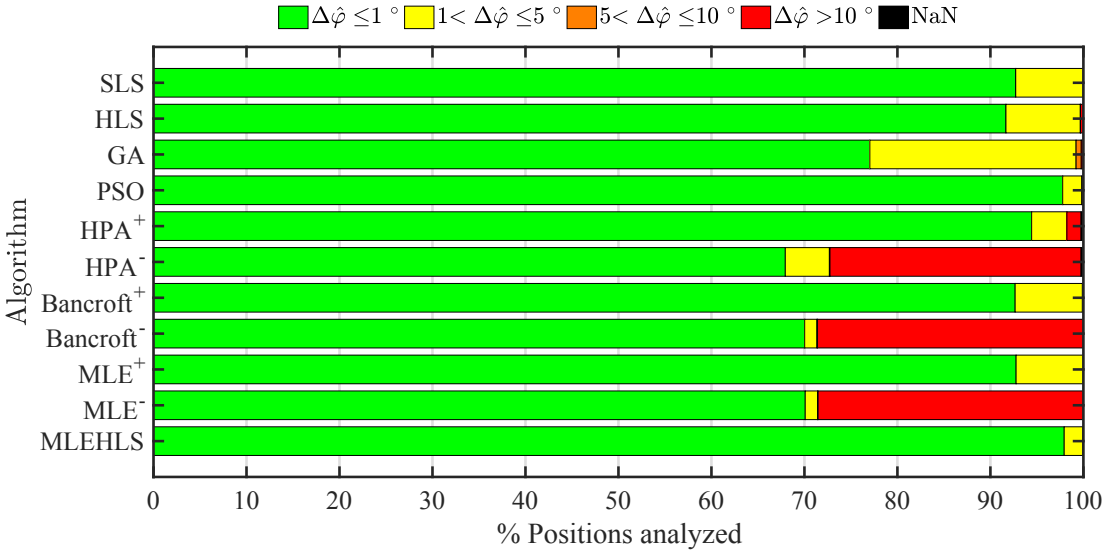

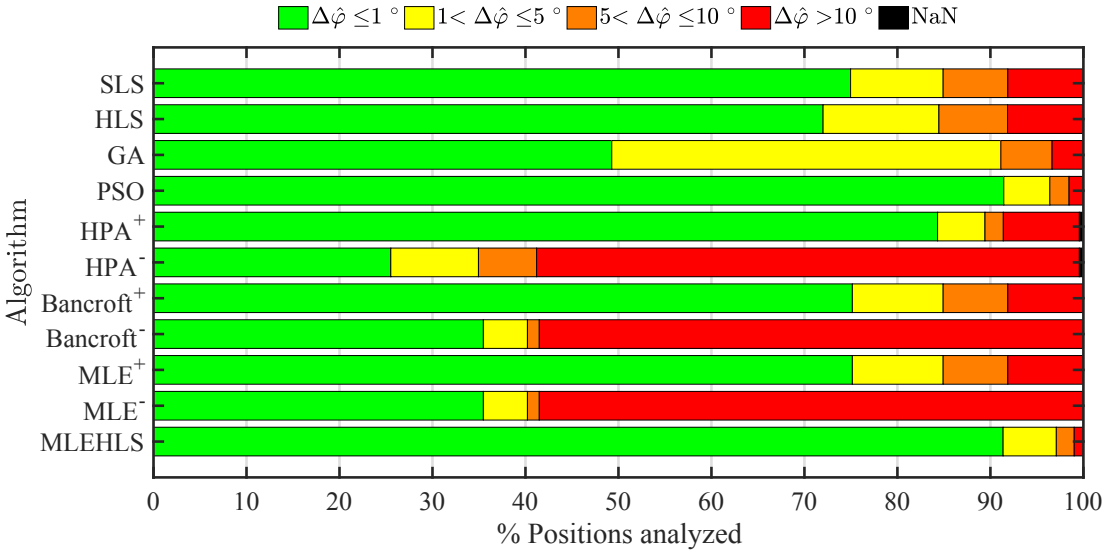

(c) Trapezoidal

Figure 4.10: Percentage of positions located within the errors in the Azimuth angle $\Delta\hat{\varphi}$ in distance defined in the legend under digitizing error in time variables for each algorithm and antenna array configuration.

Table 4.8: Percentage of positions analyzed located with an Azimuth angle error $\Delta\hat{\varphi}$ lower than 1° under digitizing error in time variables for each algorithm and antenna array configuration.

$\Delta\hat{\varphi} \leq 1^\circ$	**Square**	**Pyram**	**Trapez**	**Mean**
SLS	92.6%	92.7%	75.0%	**92.7%**
HLS	90.8%	91.7%	72.0%	**91.2%**
GA	64.7%	77.0%	49.3%	**70.9%**
PSO	96.4%	97.8%	91.4%	**97.1%**
HPA^+	83.8%	94.4%	84.3%	**89.1%**
HPA^-	29.8%	67.9%	25.5%	**48.9%**
$Bancroft^+$	92.8%	92.7%	75.2%	**92.7%**
$Bancroft^-$	33.5%	70.0%	35.5%	**51.8%**
MLE^+	92.8%	92.8%	75.2%	**92.8%**
MLE^-	33.6%	70.1%	35.5%	**51.8%**
MLE HLS	97.2%	97.9%	91.4%	**97.6%**

Table 4.9: Summary of the mean computational time spent, in seconds, for each position analyzed in digitizing error in time variables by each algorithm.

Algorithm	**Square**	**Pyram**	**Trapez**	**Mean**
SLS	$7.6 \cdot 10^{-1}$	$1.3 \cdot 10^{0}$	$5.6 \cdot 10^{-1}$	$8.7 \cdot 10^{-1}$
HLS	$2.2 \cdot 10^{-1}$	$3.2 \cdot 10^{-1}$	$2.1 \cdot 10^{-1}$	$2.5 \cdot 10^{-1}$
GA	$2.3 \cdot 10^{-1}$	$2.3 \cdot 10^{-1}$	$2.4 \cdot 10^{-1}$	$2.3 \cdot 10^{-1}$
PSO	$3.3 \cdot 10^{-2}$	$3.5 \cdot 10^{-2}$	$3.2 \cdot 10^{-2}$	$3.3 \cdot 10^{-2}$
HPA	$1.3 \cdot 10^{-5}$	$1.3 \cdot 10^{-5}$	$1.2 \cdot 10^{-5}$	$1.3 \cdot 10^{-5}$
Bancroft	$1.9 \cdot 10^{-4}$	$1.9 \cdot 10^{-4}$	$1.8 \cdot 10^{-4}$	$1.8 \cdot 10^{-4}$
MLE	$9.1 \cdot 10^{-5}$	$8.2 \cdot 10^{-5}$	$8.1 \cdot 10^{-5}$	$8.5 \cdot 10^{-5}$
MLE HLS	$1.8 \cdot 10^{-4}$	$1.6 \cdot 10^{-4}$	$1.5 \cdot 10^{-4}$	$1.6 \cdot 10^{-4}$

because the digitalization provokes situations where the algorithm does not converge or has more difficulties to converge.

4.6 Conclusions

The iterative algorithms (SLS, HLS, PSO and GA) require a definition of the initial parameters which can affect to the solution accuracy and in the computational time. Furthermore, PSO and GA include random variables which can provoke more uncertainty in the repeatability of the results. This situation provokes that these algorithms have a considerable disadvantage than the direct algorithms (HPA, Bancroft, MLE and MLE-HLS) which report direct solutions using only the antenna position and the time variables as inputs.

Analyzing the results presented in this chapter it can be concluded that every algorithm yields different results in terms of accuracy and computational time. The location accuracy by each algorithm, when the time variables are rounded, is poorer than under theoretical conditions. The average computational time by each algorithm is similar with theoretical or in digitizing error in time variables excepting HLS which is slower.

The accuracy has been analyzed for three variables; radius, elevation angle and azimuth angle. These variables represents the source position in spherical coordinates. The radius defines the distance of the source from the antenna array and the elevation and azimuth angles define the direction of the source. Analyzing the results, the distance is the most critical variable because the radius has the largest errors. On the other hand, the direction is calculated successfully by almost all algorithms in most of the analyzed points. In general, when the pyramidal antenna arrangement is analyzed, the radius estimation has larger errors than the square and trapezoidal ones. Conversely, the elevation and azimuth angle calculation have smaller errors for the pyramid arrangement.

The proposed MLE-HLS algorithm yields the best results. This algorithm uses the OF based in HLS, Equation (4.16), applied in PSO, to evaluate the fitness of the solutions. In PSO the search is in the 3D space where there are infinite solutions. The main idea of the combined algorithm is to evaluate two points uniquely, the outputs of the MLE algorithm, instead of all the solutions space. Since these points have high probability to be the actual position, the search is more efficient and more effective as it is shown in the presented results.

The MLE-HLS locations are almost exact under theoretical conditions but in digitizing error in time conditions the accuracy decreases. When introducing a digitizing error in the time variables, the MLE-HLS accuracy is approximately the same as with PSO. Analyzing the radius, MLE-HLS locates 49.9 % of the analyzed points with less error than 20 cm and PSO 49.2 %. Analyzing the elevation angle MLE-HLS calculates 93.8 % with an error lower than 1° and PSO 93.6 %. In the case of the azimuth angle the percentages are 97.6 % for MLE-HLS and 97.1 % for PSO. From these results, the accuracy of these algorithms with digitizing error in time variables is almost the same. The direction is estimated properly in most of the cases studied, around 93 %. On the other hand, the distance is poor; estimated in 50 % of the analyzed points.

The computational time for the iterative algorithms (SLS, HLS, PSO and GA) is longer than the direct algorithms (HPA, Bancroft, MLE and MLE-HLS), Table 4.5 and Table 4.9. Comparing the computational time in average of the most accurate algorithms, PSO and MLE-HLS, it can be seen that PSO with $3.3 \cdot 10^{-2}$ s in average is slower than MLE-HLS with $1.6 \cdot 10^{-4}$ s.

4.7 HPA detailed full formulation

The formulation of the HPA algorithm, presented in Subsection 4.3.2.1, is detailed in this appendix. Initially the distance, D_i, from the source to the antenna i, Equation (3.2), is defined for four antennas.

This algorithm takes four pairs of antennas to define four independent equations

to solve the unknown variables (x_s, y_s, z_s). Those equations, Equations (4.17), are presented in Subsection 4.3.2.1. Substituting Equation (3.2) in (4.17) are obtained Equations (4.33-4.36).

$$D_{12} = \sqrt{(x_1 - x_s)^2 + (y_1 - y_s)^2 + (z_1 - z_s)^2} - \sqrt{(x_2 - x_s)^2 + (y_2 - y_s)^2 + (z_2 - z_s)^2} \tag{4.33}$$

$$D_{13} = \sqrt{(x_1 - x_s)^2 + (y_1 - y_s)^2 + (z_1 - z_s)^2} - \sqrt{(x_3 - x_s)^2 + (y_3 - y_s)^2 + (z_3 - z_s)^2} \tag{4.34}$$

$$D_{32} = \sqrt{(x_3 - x_s)^2 + (y_3 - y_s)^2 + (z_3 - z_s)^2} - \sqrt{(x_2 - x_s)^2 + (y_2 - y_s)^2 + (z_2 - z_s)^2} \tag{4.35}$$

$$D_{34} = \sqrt{(x_3 - x_s)^2 + (y_3 - y_s)^2 + (z_3 - z_s)^2} - \sqrt{(x_4 - x_s)^2 + (y_4 - y_s)^2 + (z_4 - z_s)^2} \tag{4.36}$$

Moving one square root term to the other side of the equality are obtained the equations (4.37-4.40).

$$D_{12} - \sqrt{(x_1 - x_s)^2 + (y_1 - y_s)^2 + (z_1 - z_s)^2} = -\sqrt{(x_2 - x_s)^2 + (y_2 - y_s)^2 + (z_2 - z_s)^2} \tag{4.37}$$

$$D_{13} - \sqrt{(x_1 - x_s)^2 + (y_1 - y_s)^2 + (z_1 - z_s)^2} = -\sqrt{(x_3 - x_s)^2 + (y_3 - y_s)^2 + (z_3 - z_s)^2} \tag{4.38}$$

$$D_{32} - \sqrt{(x_3 - x_s)^2 + (y_3 - y_s)^2 + (z_3 - z_s)^2} = -\sqrt{(x_2 - x_s)^2 + (y_2 - y_s)^2 + (z_2 - z_s)^2} \tag{4.39}$$

$$D_{34} - \sqrt{(x_3 - x_s)^2 + (y_3 - y_s)^2 + (z_3 - z_s)^2} = -\sqrt{(x_4 - x_s)^2 + (y_4 - y_s)^2 + (z_4 - z_s)^2} \tag{4.40}$$

Squaring both sides of the equality and substituting Equation (3.2) by the squared roots the following set of the Equations (4.41-4.44) are produced.

$$D_{12}^2 - 2D_{12}D_1 + (x_1 - x_s)^2 + (y_1 - y_s)^2 + (z_1 - z_s)^2 = (x_2 - x_s)^2 + (y_2 - y_s)^2 + (z_2 - z_s)^2 \tag{4.41}$$

$$D_{13}^2 - 2D_{13}D_1 + (x_1 - x_s)^2 + (y_1 - y_s)^2 + (z_1 - z_s)^2 = (x_3 - x_s)^2 + (y_3 - y_s)^2 + (z_3 - z_s)^2 \tag{4.42}$$

$$D_{32}^2 - 2D_{32}D_3 + (x_3 - x_s)^2 + (y_3 - y_s)^2 + (z_3 - z_s)^2 = (x_2 - x_s)^2 + (y_2 - y_s)^2 + (z_2 - z_s)^2 \tag{4.43}$$

$$D_{34}^2 - 2D_{34}D_3 + (x_3 - x_s)^2 + (y_3 - y_s)^2 + (z_3 - z_s)^2 = (x_4 - x_s)^2 + (y_4 - y_s)^2 + (z_4 - z_s)^2 \tag{4.44}$$

Operating the squared terms modifies the previous equations in the Equations (4.45-4.48).

$$\begin{aligned} D_{12}^2 - 2D_{12}D_1 + x_1^2 - 2x_1x_s + x_s^2 + y_1^2 - 2y_1y_s + y_s^2 + z_1^2 - 2z_1^2z_s + z_s^2 = \\ x_2^2 - 2x_2x_s + x_s^2 + y_2^2 - 2y_2y_s + y_s^2 + z_2^2 - 2z_2z_s + z_s^2 \end{aligned} \tag{4.45}$$

$$\begin{aligned} D_{13}^2 - 2D_{13}D_1 + x_1^2 - 2x_1x_s + x_s^2 + y_1^2 - 2y_1y_s + y_s^2 + z_1^2 - 2z_1^2z_s + z_s^2 = \\ x_3^2 - 2x_3x_s + x_s^2 + y_3^2 - 2y_3y_s + y_s^2 + z_3^2 - 2z_3z_s + z_s^2 \end{aligned} \tag{4.46}$$

$$\begin{aligned} D_{32}^2 - 2D_{32}D_3 + x_3^2 - 2x_3x_s + x_s^2 + y_3^2 - 2y_3y_s + y_s^2 + z_3^2 - 2z_3^2z_s + z_s^2 = \\ x_2^2 - 2x_2x_s + x_s^2 + y_2^2 - 2y_2y_s + y_s^2 + z_2^2 - 2z_2z_s + z_s^2 \end{aligned} \tag{4.47}$$

$$\begin{aligned} D_{34}^2 - 2D_{34}D_3 + x_3^2 - 2x_3x_s + x_s^2 + y_3^2 - 2y_3y_s + y_s^2 + z_3^2 - 2z_3^2z_s + z_s^2 = \\ x_4^2 - 2x_4x_s + x_s^2 + y_4^2 - 2y_4y_s + y_s^2 + z_4^2 - 2z_4z_s + z_s^2 \end{aligned} \tag{4.48}$$

Eliminating the terms in both sides of the equation x_s^2, y_s^2 and z_s^2, reduces the previous Equations to (4.49-4.52).

$$\begin{aligned} D_{12}^2 - 2D_{12}D_1 + x_1^2 - 2x_1x_s + y_1^2 - 2y_1y_s + z_1^2 - 2z_1^2z_s = \\ x_2^2 - 2x_2x_s + y_2^2 - 2y_2y_s + z_2^2 - 2z_2z_s \end{aligned} \tag{4.49}$$

$$\begin{aligned} D_{13}^2 - 2D_{13}D_1 + x_1^2 - 2x_1x_s + y_1^2 - 2y_1y_s + z_1^2 - 2z_1^2z_s = \\ x_3^2 - 2x_3x_s + y_3^2 - 2y_3y_s + z_3^2 - 2z_3z_s \end{aligned} \tag{4.50}$$

$$\begin{aligned} D_{32}^2 - 2D_{32}D_3 + x_3^2 - 2x_3x_s + y_3^2 - 2y_3y_s + z_3^2 - 2z_3^2z_s = \\ x_2^2 - 2x_2x_s + y_2^2 - 2y_2y_s + z_2^2 - 2z_2z_s \end{aligned} \tag{4.51}$$

$$\begin{aligned} D_{34}^2 - 2D_{34}D_3 + x_3^2 - 2x_3x_s + y_3^2 - 2y_3y_s + z_3^2 - 2z_3^2z_s = \\ x_4^2 - 2x_4x_s + y_4^2 - 2y_4y_s + z_4^2 - 2z_4z_s \end{aligned} \tag{4.52}$$

Clearing D_1 and D_3 and combining similar terms generates Equations (4.53-4.56)

$$\begin{aligned} D_1 = \frac{1}{2D_{12}}\big(D_{12}^2 + x_1^2 - x_2^2 + y_1^2 - y_2^2 + z_1^2 - z_2^2 \\ + 2x_2x_s - 2x_1x_s + 2y_2y_s - 2y_1y_s + 2z_2z_s - 2z_1z_s\big) \end{aligned} \tag{4.53}$$

$$\begin{aligned} D_1 = \frac{1}{2D_{13}}\big(D_{13}^2 + x_1^2 - x_3^2 + y_1^2 - y_3^2 + z_1^2 - z_3^2 \\ + 2x_3x_s - 2x_1x_s + 2y_3y_s - 2y_1y_s + 2z_3z_s - 2z_1z_s\big) \end{aligned} \tag{4.54}$$

$$\begin{aligned} D_3 = \frac{1}{2D_{32}}\big(D_{32}^2 + x_3^2 - x_2^2 + y_3^2 - y_2^2 + z_3^2 - z_2^2 \\ + 2x_2x_s - 2x_3x_s + 2y_2y_s - 2y_3y_s + 2z_2z_s - 2z_3z_s\big) \end{aligned} \tag{4.55}$$

$$D_3 = \frac{1}{2D_{34}}\big(D_{34}^2 + x_3^2 - x_4^2 + y_3^2 - y_4^2 + z_3^2 - z_4^2 + 2x_4x_s - 2x_3x_s + 2y_4y_s - 2y_3y_s + 2z_4z_s - 2z_3z_s\big) \tag{4.56}$$

To reduce the number of terms in the set of Equations, the variables $(x_j - x_i)$ for x_{ji}, $(y_j - y_i)$ are substituted for y_{ji} and so on. This reductions creates:

$$D_1 = \frac{1}{2D_{12}}\left(D_{12}^2 + x_1^2 - x_2^2 + y_1^2 - y_2^2 + z_1^2 - z_2^2 + 2x_{21}x_s + 2y_{21}y_s + 2z_{21}z_s\right) \tag{4.57}$$

$$D_1 = \frac{1}{2D_{13}}\left(D_{13}^2 + x_1^2 - x_3^2 + y_1^2 - y_3^2 + z_1^2 - z_3^2 + 2x_{31}x_s + 2y_{31}y_s + 2z_{31}z_s\right) \tag{4.58}$$

$$D_3 = \frac{1}{2D_{23}}\left(D_{23}^2 + x_2^2 - x_3^2 + y_2^2 - y_3^2 + z_2^2 - z_3^2 + 2x_{32}x_s + 2y_{32}y_s + 2z_{32}z_s\right) \tag{4.59}$$

$$D_3 = \frac{1}{2D_{43}}\left(D_{43}^2 + x_4^2 - x_3^2 + y_4^2 - y_3^2 + z_4^2 - z_3^2 + 2x_{34}x_s + 2y_{34}y_s + 2z_{34}z_s\right) \tag{4.60}$$

The initial Equations (4.33-4.36) are now in an appropriate form: Equations (4.57-4.60) to define a plane Equation. To reach it, Equations (4.57 and 4.58) are equated to obtain Equations (4.61). Through the intermediate step shown in Equation (4.62), the plane equation in the form $y_s = Ax_s + Bz_s + C$ is obtained and defined by Equation (4.63).

$$\begin{aligned}&\frac{1}{2D_{12}}\left(D_{12}^2 + x_1^2 - x_2^2 + y_1^2 - y_2^2 + z_1^2 - z_2^2 + 2x_{21}x_s + 2y_{21}y_s + 2z_{21}z_s\right)\\ &= \frac{1}{2D_{13}}\left(D_{13}^2 + x_1^2 - x_3^2 + y_1^2 - y_3^2 + z_1^2 - z_3^2 + 2x_{31}x_s + 2y_{31}y_s + 2z_{31}z_s\right)\end{aligned} \tag{4.61}$$

$$\begin{aligned}&\frac{D_{13}}{2}\left(D_{12}^2 + x_1^2 - x_2^2 + y_1^2 - y_2^2 + z_1^2 - z_2^2\right)\\ &- \frac{D_{12}}{2}\left(D_{13}^2 + x_1^2 - x_3^2 + y_1^2 - y_3^2 + z_1^2 - z_3^2\right)\\ &= D_{12}\left(x_{31}x_s + y_{31}y_s + z_{31}z_s\right) - D_{13}\left(x_{21}x_s + y_{21}y_s + z_{21}z_s\right)\end{aligned} \tag{4.62}$$

$$\begin{aligned}&x_s\left(D_{12}x_{31} - D_{13}x_{21}\right) + y_s\left(D_{12}y_{31} - D_{13}y_{21}\right) + z_s\left(D_{12}z_{31} - D_{13}z_{21}\right)\\ &= \frac{D_{13}}{2}\left(D_{12}^2 + x_1^2 - x_2^2 + y_1^2 - y_2^2 + z_1^2 - z_2^2\right)\\ &- \frac{D_{12}}{2}\left(D_{13}^2 + x_1^2 - x_3^2 + y_1^2 - y_3^2 + z_1^2 - z_3^2\right)\end{aligned} \tag{4.63}$$

The plane equation defined by Equation (4.63) is now in the desired form $y_s = Ax_s + Bz_s + C$, where:

$$A = \frac{D_{13}x_{21} - D_{12}x_{31}}{D_{12}y_{31} - D_{13}y_{21}} \tag{4.64}$$

and

$$B = \frac{D_{13}z_{21} - D_{12}z_{31}}{D_{12}y_{31} - D_{13}y_{21}} \tag{4.65}$$

and

$$C = \frac{\begin{array}{c} D_{13}\left(D_{12}^2 + x_1^2 - x_2^2 + y_1^2 - y_2^2 + z_1^2 - z_2^2\right) \\ - D_{12}\left(D_{13}^2 + x_1^2 - x_3^2 + y_1^2 - y_3^2 + z_1^2 - z_3^2\right) \end{array}}{2(D_{12}y_{31} - D_{13}y_{21})} \tag{4.66}$$

In the same way, equating Equations (4.59 and 4.60) creates another plane Equation $y_s = Dx_s + Ez_s + F$, where:

$$D = \frac{D_{34}x_{23} - D_{32}x_{43}}{D_{32}y_{43} - D_{34}y_{23}} \tag{4.67}$$

and

$$E = \frac{D_{34}z_{23} - D_{32}z_{43}}{D_{32}y_{43} - D_{34}y_{23}} \tag{4.68}$$

and

$$F = \frac{\begin{array}{c} D_{34}\left(D_{32}^2 + x_3^2 - x_2^2 + y_3^2 - y_2^2 + z_3^2 - z_2^2\right) \\ - D_{32}\left(D_{34}^2 + x_3^2 - x_4^2 + y_3^2 - y_4^2 + z_3^2 - z_4^2\right) \end{array}}{2(D_{32}y_{43} - D_{34}y_{23})} \tag{4.69}$$

Equating both plane equations $y_s = Ax_s + Bz_s + C$ and $y_s = Dx_s + Ez_s + F$ generates a linear Equation for x_s as a function of z_s .

$$Ax_s + Bz_s + C = Dx_s + Ez_s + F \tag{4.70}$$

$$x_s = Gz_s + H \tag{4.71}$$

where

$$G = \frac{E - B}{A - D} \quad and \quad H = \frac{F - C}{A - D} \tag{4.72}$$

Replacing Equation (4.71) back into $y_s = Dx_s + Ez_s + F$ yields a linear Equation for y_s as a function of z_s.

$$y_s = A(Gz_s + H) + Bz_s + C \tag{4.73}$$

$$y_s = Iz_s + J \tag{4.74}$$

where

$$I = AG + B \quad and \quad J = AH + C \tag{4.75}$$

Substituting both Equations (4.71) and (4.74) back into Equation (4.58), the variable z_s can be calculated.

$$\begin{array}{c} 2D_{13}\sqrt{(x_1 - (Gz_s + H))^2 + (y_1 - (Iz_s + J))^2 + (z_1 - z_s)^2} = \\ \left(D_{13}^2 + x_1^2 - x_3^2 + y_1^2 - y_3^2 + z_1^2 - z_3^2\right. \\ \left. + 2x_{31}(Gz_s + H) + 2y_{31}(Iz_s + J) + 2z_{31}z_s\right) \end{array} \tag{4.76}$$

$$2D_{13}\sqrt{\begin{array}{c} (G^2z_s^2 - 2Gz_s(x_1 - H) + (x_1 - H)^2) \\ + (I^2z_s^2 - 2Iz_s(y_1 - J) + (y_1 - J)^2) + (z_s^2 + 2z_sz_1 + z_1^2) \end{array}} = Lz_s + K \tag{4.77}$$

where

$$K = D_{13}^2 + x_1^2 - x_3^2 + y_1^2 - y_3^2 + z_1^2 - z_3^2 + 2x_{31}H + 2y_{31}J \tag{4.78}$$

and

$$L = 2(x_{31}G + y_{31}I + z_{31}) \tag{4.79}$$

$$\begin{aligned} &4D_{13}^2\big(G^2z_s^2 + I^2z_s^2 + z_s^2 - 2Gz_s(x_1 - H) - 2Iz_s(y_1 - J) \\ &- 2z_1z_s + (x_1 - H)^2 + (y_1 - J)^2 + z_1^2\big) \\ &= L^2z_s^2 + 2KLz_s + K^2 \end{aligned} \tag{4.80}$$

$$\begin{aligned} &4D_{13}^2(G^2 + I^2 + 1)z_s^2 - 8D_{13}^2(G(x_1 - H) + I(y_1 - J) + z_1)z_s \\ &+ 4D_{13}^2((x_1 - H)^2 + (y_1 - J)^2 + z_1^2) = L^2z_s^2 + 2KLz_s + K^2 \end{aligned} \tag{4.81}$$

To obtain z_s, Equation (4.81) is reorganized into a binomial Equation.

$$Mz_s^2 - Nz_s + O = 0 \tag{4.82}$$

where

$$M = 4D_{13}^2(G^2 + I^2 + 1) - L^2 \tag{4.83}$$

and

$$N = 8D_{13}^2(G(x_1 - H) + I(y_1 - J) + z_1) + 2LK \tag{4.84}$$

and

$$O = 4D_{13}^2((x_1 - H)^2 + (y_1 - J)^2 + z_1^2) + K^2 \tag{4.85}$$

The z_s solutions can be obtained through:

$$z = \frac{N}{2M} \pm \sqrt{\left(\frac{N}{2M}\right)^2 - \frac{O}{M}} \tag{4.86}$$

Finally, to define the source coordinates, z_s can be substituted in both Equations (4.71) and (4.74) to solve for the coordinates x_s and y_s.

4.8 Bibliography

[1] T. S. Rappaport, J. H. Reed, and B. D. Woerner. "Position location using wireless communications on highways of the future". In: *IEEE Communications Magazine* 34.10 (Oct. 1996), pp. 33–41. ISSN: 0163-6804. DOI: 10.1109/35.544321 (cit. on p. 88).

[2] S. Bancroft. "An Algebraic Solution of the GPS Equations". In: *IEEE Transactions on Aerospace and Electronic Systems* AES-21.1 (Jan. 1985), pp. 56–59. ISSN: 0018-9251. DOI: 10.1109/TAES.1985.310538 (cit. on pp. 88, 89, 96).

[3] Y. T. Chan and K. C. Ho. "A simple and efficient estimator for hyperbolic location". In: *IEEE Transactions on Signal Processing* 42.8 (Aug. 1994), pp. 1905–1915. ISSN: 1053-587X. DOI: 10.1109/78.301830 (cit. on pp. 88, 89, 97).

[4] Y. Huang, J. Benesty, G. W. Elko, et al. "Real-time passive source localization: a practical linear-correction least-squares approach". In: *IEEE Transactions on Speech and Audio Processing* 9.8 (Nov. 2001), pp. 943–956. ISSN: 1063-6676. DOI: 10.1109/89.966097 (cit. on p. 88).

[5] S. Monica and G. Ferrari. "A swarm-based approach to real-time 3D indoor localization: Experimental performance analysis". In: *Applied Soft Computing* 43 (June 2016), pp. 489–497. ISSN: 1568-4946. DOI: 10.1016/j.asoc.2016.02.020. URL: http://www.sciencedirect.com/science/article/pii/S1568494616300710 (cit. on p. 88).

[6] L.-j. DONG and X.-b. LI. "Three-dimensional analytical solution of acoustic emission or microseismic source location under cube monitoring network". In: *Transactions of Nonferrous Metals Society of China* 22.12 (Dec. 2012), pp. 3087–3094. ISSN: 1003-6326. DOI: 10.1016/S1003-6326(11)61575-6. URL: http://www.sciencedirect.com/science/article/pii/S1003632611615756 (cit. on p. 88).

[7] J. H. Kurz. "New approaches for automatic threedimensional source localization of acoustic emissions Applications to concrete specimens". In: *Ultrasonics* 63 (Dec. 2015), pp. 155–162. ISSN: 0041-624X. DOI: 10.1016/j.ultras.2015.07.003. URL: http://www.sciencedirect.com/science/article/pii/S0041624X15001717 (cit. on p. 88).

[8] P. J. Moore, I. E. Portugues, and I. A. Glover. "Radiometric location of partial discharge sources on energized high-Voltage plant". In: *IEEE Transactions on Power Delivery* 20.3 (July 2005), pp. 2264–2272. ISSN: 0885-8977. DOI: 10.1109/TPWRD.2004.843397 (cit. on pp. 88, 99).

[9] S. M. Markalous, S. Tenbohlen, and K. Feser. "Detection and location of partial discharges in power transformers using acoustic and electromagnetic signals". In: *IEEE Transactions on Dielectrics and Electrical Insulation* 15.6 (Dec. 2008), pp. 1576–1583. ISSN: 1070-9878. DOI: 10.1109/TDEI.2008.4712660 (cit. on p. 88).

[10] C. D. Marziani, J. Urena, M. Mazo, et al. "Relative Positioning System Using Simultaneous Round Trip Time of Flight Measurements". In: *2006 IEEE Conference on Emerging Technologies and Factory Automation*. Sept. 2006, pp. 602–605. DOI: 10.1109/ETFA.2006.355244 (cit. on p. 88).

[11] H. Liu, H. Darabi, P. Banerjee, et al. "Survey of Wireless Indoor Positioning Techniques and Systems". In: *IEEE Transactions on Systems, Man, and Cybernetics, Part*

C (Applications and Reviews) 37.6 (Nov. 2007), pp. 1067–1080. ISSN: 1094-6977. DOI: 10.1109/TSMCC.2007.905750 (cit. on p. 88).

[12] L. Brás, N. B. Carvalho, P. Pinho, et al. "A Review of Antennas for Indoor Positioning Systems". en. In: *International Journal of Antennas and Propagation* 2012 (Dec. 2012), e953269. ISSN: 1687-5869. DOI: 10.1155/2012/953269. URL: https://www.hindawi.com/journals/ijap/2012/953269/abs/ (cit. on p. 88).

[13] Y. Lu, X. Tan, and X. Hu. "PD detection and localisation by acoustic measurements in an oil-filled transformer". In: *IEE Proceedings - Science, Measurement and Technology* 147.2 (Mar. 2000), pp. 81–85. ISSN: 1350-2344. DOI: 10.1049/ip-smt:20000223 (cit. on pp. 88, 90).

[14] L. Tang, Z. Wu, H. Li, et al. "Location of partial discharges in power transformers using computer-aided acoustic techniques". In: *Canadian Journal of Electrical and Computer Engineering* 21.2 (Apr. 1996), pp. 67–71. ISSN: 0840-8688. DOI: 10.1109/CJECE.1996.7102128 (cit. on pp. 88, 92).

[15] R. M. Harris and M. D. Judd. "Locating Partial Discharge Using Particle Swarm Optimisation". In: *Universities' Power Engineering Conference (UPEC), Proceedings of 2011 46th International*. Sept. 2011, pp. 1–6 (cit. on pp. 88, 95).

[16] S. Monica and G. Ferrari. "Swarm intelligent approaches to auto-localization of nodes in static UWB networks". In: *Applied Soft Computing* 25 (Dec. 2014), pp. 426–434. ISSN: 1568-4946. DOI: 10.1016/j.asoc.2014.07.025. URL: http://www.sciencedirect.com/science/article/pii/S1568494614004293 (cit. on p. 88).

[17] G. Robles, J. M. Fresno, and J. M. Martínez-Tarifa. "Separation of Radio-Frequency Sources and Localization of Partial Discharges in Noisy Environments". en. In: *Sensors* 15.5 (Apr. 2015), pp. 9882–9898. DOI: 10.3390/s150509882. URL: http://www.mdpi.com/1424-8220/15/5/9882 (cit. on p. 88).

[18] Z. Tang, C. Li, X. Cheng, et al. "Partial discharge location in power transformers using wideband RF detection". In: *IEEE Transactions on Dielectrics and Electrical Insulation* 13.6 (Dec. 2006), pp. 1193–1199. ISSN: 1070-9878. DOI: 10.1109/TDEI.2006.258190 (cit. on p. 88).

[19] R. Bucher and D. Misra. "A Synthesizable VHDL Model of the Exact Solution for Three-dimensional Hyperbolic Positioning System". In: *VLSI Design* 15.2 (2002), pp. 507–520. DOI: 10.1080/1065514021000012129. URL: http://dx.doi.org/10.1080/1065514021000012129 (cit. on pp. 89, 95).

[20] P. Miao, X. Li, H. Hou, et al. "Location Algorithm for Partial Discharge Based on Radio Frequency (RF) Antenna Array". In: *2012 Asia-Pacific Power and Energy Engineering Conference*. Mar. 2012, pp. 1–4. DOI: 10.1109/APPEEC.2012.6307662 (cit. on p. 89).

[21] M. Yang and K.-H. Chen. "Performance Assessment of a Noniterative Algorithm for Global Positioning System (GPS) Absolute Positioning". In: vol. 25. 2. 2001, pp. 102–106 (cit. on p. 89).

[22] O. El Mountassir, B. G. Stewart, A. J. Reid, et al. "Quantification of the performance of iterative and non-iterative computational methods of locating partial discharges using RF measurement techniques". In: *Electric Power Systems Research* 143 (Feb. 2017), pp. 110–120. ISSN: 0378-7796. DOI: 10.1016/j.epsr.2016.10.036. URL: http://www.sciencedirect.com/science/article/pii/S0378779616304333 (cit. on p. 89).

[23] G. Robles, J. M. Fresno, M. Sánchez-Fernández, et al. "Antenna Deployment for the Localization of Partial Discharges in Open-Air Substations". en. In: *Sensors* 16.4 (Apr. 2016), p. 541. DOI: 10.3390/s16040541. URL: http://www.mdpi.com/1424-8220/16/4/541 (cit. on pp. 90, 100).

[24] O. E. Mountassir, B. G. Stewart, S. G. McMeekin, et al. "Evaluation of an iterative method used for partial discharge RF location techniques". In: *2011 10th International Conference on Environment and Electrical Engineering (EEEIC)*. May 2011, pp. 1–4. DOI: 10.1109/EEEIC.2011.5874679 (cit. on p. 91).

[25] Y. Shi and R. C. Eberhart. "Parameter selection in particle swarm optimization". en. In: *Evolutionary Programming VII*. Springer, Berlin, Heidelberg, Mar. 1998, pp. 591–600. DOI: 10.1007/BFb0040810. URL: https://link.springer.com/chapter/10.1007/BFb0040810 (cit. on p. 94).

Chapter 5

Propagation of the TDoA errors in the localization of emitters

5.1 Abstract

The localization of emitters in the space can be done through the algorithms shown in Chapter 4. These algorithms require as inputs the position of the four antennas or sensors and the time variables of the electromagnetic pulses between antennas calculated with the algorithms explained in Chapter 3.

Small errors in the time variables estimation can lead to great displacements of the calculated position of the source. This chapter demonstrates that the antenna layout affects in localization of the source when this is done in the presence of systematic errors in the time variables. This demonstration is undertaken by simulation and experimental measurements in 2D and 3D. The localization algorithm used is PSO based on HLS,

the time variable used by this algorithm is the TDoA and in the experimental study, this variable is calculated with the Hinkley algorithm.

5.2 Introduction

In this chapter, both publications "Antenna Deployment for the Localization of Partial Discharges in Open-Air Substations" and "Spatial study of the uncertainties in the localization of partial discharges for different antenna layouts" are joined. Their full citation are detailed in Subsection 7.3.1 in item 2 and in Subsection 7.3.2 in item 8 respectively.

As mentioned in the previous chapters of the thesis, the location of a device, equipment or source is a well known issue in the literature [1] and it is typically based on a set of reference antennas receiving a signal or signals from where information can be extracted for location purposes. There are many works devoted to the localization of emitters as the localization of PD inside transformers and gas-insulated switchgear (GIS) substations based on TDoA. In most cases, the source is surrounded by antennas, so the location is straightforward and the accuracy is excellent. The difficulties appear when the source is outside the volume created by the four antennas; then, the uncertainty in the possible solutions is notably higher which is specially important when localizing PD sources in open-air substations. A simple example of the TDoA values with two antennas is represented in Figure 5.1. The lines represent the positions in (x, y) which have the same TDoA, for the sake of clarity, it is converted to meters, multiplying by the speed propagation, c. The plotted lines are discrete steps of 0.1 meters. In this Figure, it can be seen how in the region between the antennas, the lines are more compact and on the other hand, in positions far from the antennas the lines are more separated. For example, when the source is placed in the line $y = 0$ m and $x \geq 0.5$ m or $x \leq -0.5$ m the TDoA is the same 1 or -1, respectively and there is not resolution in x. On the other hand, when $|x| < 0.5$, there is high resolution in the TDoA and x can be defined. Therefore, the reason for the mismatch on performance given by the position of the emitter with respect to the antenna array is intrinsic to the hyperbolic solution that provides the TDoA. This fact provokes less dispersion in the hyperbolas when the source is inside of the region defined by the antennas than when the source is outside. This is demonstrated in Figure 5.2, where the theoretical t_{ij} and the deviation of ± 1 samples from t_{ij} due to possible errors multiplied by c is represented. The sampling frequency used in this Chapter is 5 GS/s and corresponds to a sampling time of 200 ps, so, one sample corresponds to 6 cm in distance. For each color the central line represents the theoretical value and the external lines represents the deviation of ± 1 sample, the theoretical t_{ij} always crosses the source position. Figure 5.2 shows that, when the source is surrounded by antennas, the grey area defined by the hyperbolas

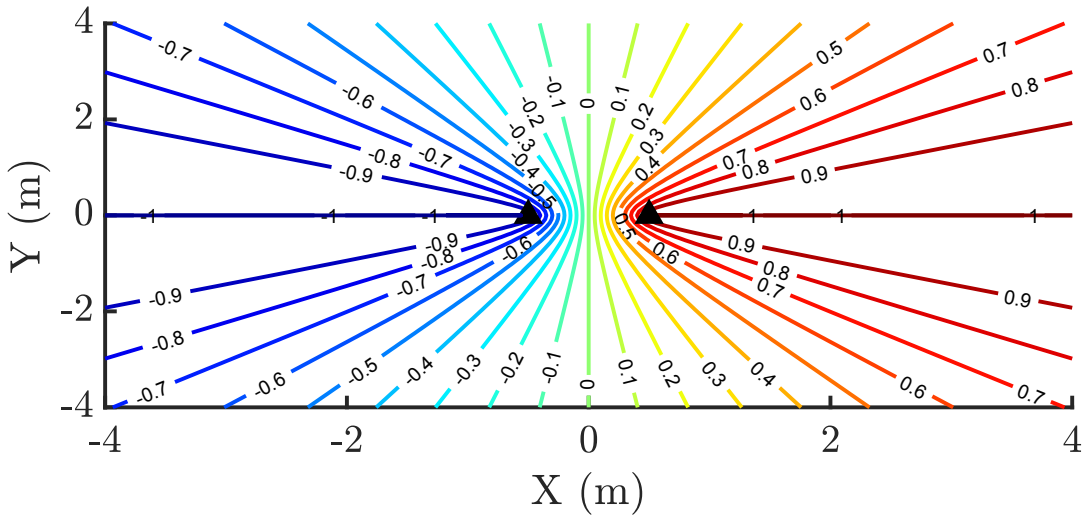

Figure 5.1: Hyperbolic lines represented in the XY plane defined by the TDoA between two antennas (black triangles) multiplied by the speed propagation, c. The $t_{12} \cdot c$ are discrete in steps of 0.1 meters.

which representing the deviation of $\pm$ 1 sample is smaller than when the source is out of the antennas layout.

The effect of the relative position of the receivers and the emitter is mentioned in an interesting paper by Moore et al. that studies the location performance of two antennas configurations forming a square and a pyramidal determining that the first one is the best option, [2]. There is also a mathematical study in [3] that concludes with some evident hints about how to place the antennas and test them in a square layout. Again, the square configuration is used in [4] and [5]. The authors in [5] included also a trapezoidal layout and tested the antenna deployments in a 400 kV substation obtaining experimental measurements of the statistical error. However, the sources were included inside the polygon of the antenna layout so their analysis is different from what the study presented in this Chapter.

In this work, several antenna layouts are compared forcing the PD source to be outside the polygon defined by the array. In 2D localization both realistic modelling of different antenna deployments that takes into account errors in the measurement of the TDoA and by experimental measurements are shown. The trapezoidal array improves the performance of a squared deployment, having better accuracy and less dispersion than other configurations. Since the simulations in 2D localization are validated with experimental measurements, the analysis in 3D localization is only undertaken by simulation due the complexity and quantity of the experimental measurements required.

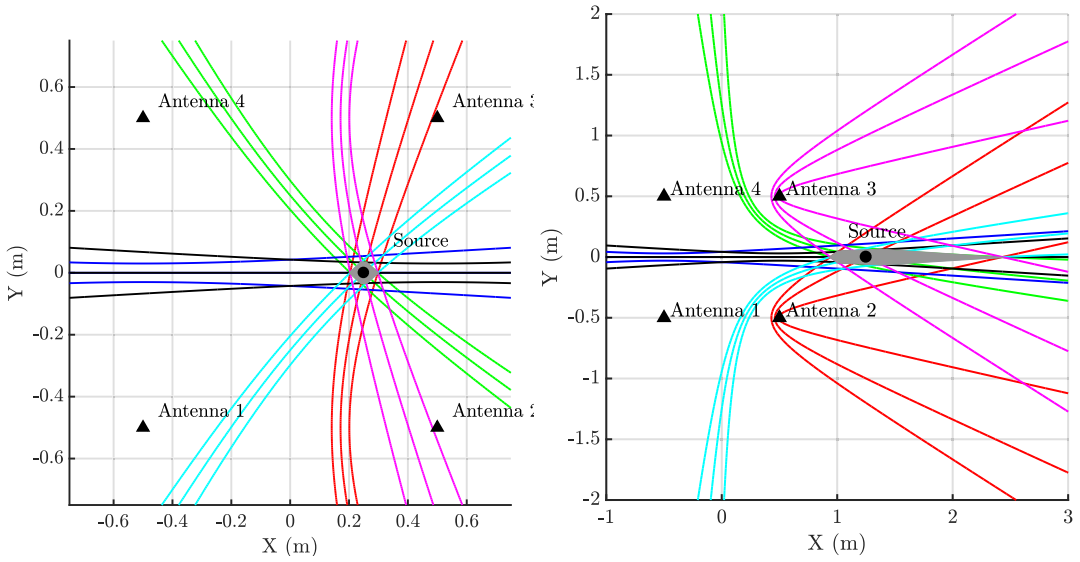

(a) Source inside the antennas layout *(b)* Source outside the antennas layout

Figure 5.2: Representation of the hyperbolas for each pair of antennas of the theoretical $TDoA \pm 1$ in samples.

5.3 Finding the RF source

The target is to locate the source position and it is done through PSO algorithm explained in Subsection 4.3.1.4. The inputs of the PSO algorithm are the antenna positions and the TDoA of the emission between antennas. The exactness in the determination of the TDoA is key to have an accurate position of the source, small variations in this variable can induce large misplacement, [2]. Chapter 3 shows an extensive analysis of algorithms to calculate the TDoA variables, the estimations undertaken in the experimental study of this chapter are done with Hinkley algorithm.

There are multiple factors that can lead to uncertainties or even errors in the TDoA. For example, the uncertainties produced by the intrinsically digital nature of the sampled signal and the system sampling rate, lead to a region in space inside which it would be impossible to locate the PD; while errors in the TDoA lead to wrong positioning. These factors have different origins that are classified in this thesis into three categories: due to the nature of the signal, due to the position of the antennas and due to the measuring procedure.

5.3.1 Uncertainties and errors in the TDoA due to the nature of the signal

To obtain the TDoA, it is necessary to extract information from the signals received in each antenna, i.e. we should be able, in the case of a PD, to identify the onset of the pulse. There are several aspects of the nature of the PD waveform that may affect negatively to this identification such as the rise slope of the PD wavefront, the presence

of noise and interferences in the propagation bandwidth and the propagation through multipaths.

In the absence of noise or any other perturbations, the sharpest rise slope a PD presents, the more precise will be to determine the onset of the pulse. The waveform of a PD depends on the type of insulation where it happens. The signal emitted by corona or surface PD, where the insulation interfaces are air or air-dielectric, will be different from PD inside the solid or liquid insulation because the wave has to pass through the dielectric before traveling through air to the detectors. Also, weather conditions such as temperature, humidity and pressure affect to PD inception voltages and hence the pulsed signal emitted during the discharge. Additionally, PD are intrinsically random signals, and therefore they need to be modeled as stochastic processes. The randomness comes from the fact that the charge involved in the discharge and the path followed by the electron avalanche change in every event [6]. For this reason, this phenomenon cannot be analyzed using only one PD event and the signal received in the antennas will not always have the same rise time or wavefront type.

In most propagation scenarios, and specifically for measurements in open-air substations, the PD pulse is contaminated by interferences in all RF spectrum such as FM radio, television broadcasting, mobile communications, WiFi, lighting, commutations, sparking and arcing. All these noise sources can ultimately degrade the SNR hindering the process of finding the onset of the pulse. These uncertainties in picking the initial time will add an error to the measurement of the TDoA. There are well-known algorithms to find the onset of a pulse such as cross correlation with or without preprocessor, first introduced in [7]; the detection of steep changes in the cumulative energy of the time signal [8]; or the modification of this method including a negative trend, [9, 10]; the AIC based on autoregressive processes; and, energy-based methods using high order statistics such as kurtosis and skewness, [11]. A benchmark of these algorithms can be found in Chapter 3, where how the depending on the algorithm used, in the TDoA calculus can differ from one algorithm to another.

Finally, the last significant source of uncertainty and errors is the lack of line-of-sight or the presence of obstacles that produce reflections in the signal. These reflections jeopardize the measurement of the ToF in Equation (3.1) given the fact that this formula assumes that the propagation is in free space. Then, if there are metallic structures between the source and the antenna, the signal received would be distorted, the wavefront rise-time would not be as fast as it should be and the effect of multipath reflections could hinder the obtention of the TDoA.

5.3.2 Errors in the TDoA due to the geometry and radiation characteristics of the antennas

Setting a reference system to place the antennas is essential to know the location of the source. The position of the antennas has to be measured carefully because small errors in the order of a few centimeters will be translated to a large dispersion in the results. Choosing an appropriate layout can reduce the uncertainty dramatically as demonstrated in the next sections.

Moreover, the antennas are not dimensionally negligible, so it is necessary to know their radiometric characteristics to place them correctly in a single point in space.

The radiation pattern of the antenna plays an important role in the localization process even when the antennas are omnidirectional. If the source is located below the ground plane of the antenna, the rise time of the received signal will be slower so all TDoA involving that antenna would be inducing an error to the measurement.

5.3.3 Uncertainties and errors in the TDoA due to measuring process

It should be borne in mind that the measurement of the TDoA underlays a digital processing of the PD signal that includes sampling. Taking into account that PD can have rise times well below hundreds of picoseconds, the signals have to be acquired with high-speed oscilloscopes or digitizers. Still in this scenario, the sampling time may eventually prompt uncertainty: there will be a region in space given by the sampling time T_s where we will be unable to determine the position of the source. The sampling frequency used in this Chapter is 5 GS/s, which corresponds to a sampling time of 200 ps as explained before. Differences in the TDoA below this time resolution will not be detected. Considering that the speed of propagation is the speed of light, the resolution in distance is 6 cm.

An additional error source in the detection of the signal onset may be present if the relation between the PD waveform bandwidth and the sampling frequency is not adequate. Digitalization implies missing information of the signal evolution between samples, which could be relevant if the sampling frequency is too low. As an example, we may be unable to pick the initial time if there is a significant change in the signal waveform between two consecutive samples.

It may be possible to mitigate artificially these shortcomings increasing the resolution with cubic splines interpolation, [2, 12], though the number of points introduced in the interpolation is limited.

Additionally, systematic errors in the digitizing process together with the uncertainty of the instrumentation, coaxial cable lengths and differences in the antennas properties can also modify the value of the TDoA.

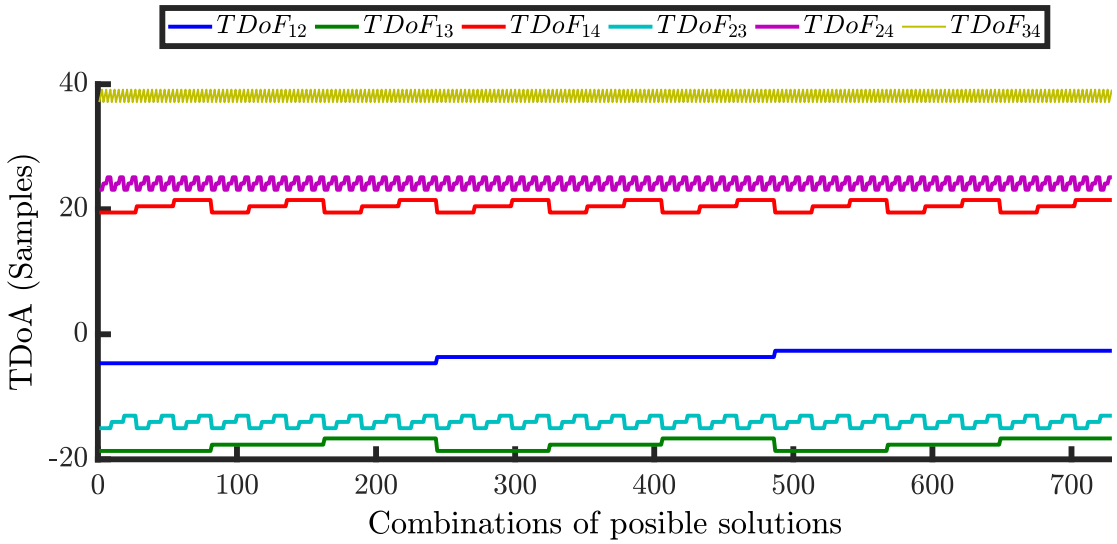

Figure 5.3: Possible TDoA combinations when the errors are introduced.

5.4 Antenna deployment, simulations and sensitivity to measurement errors in 2D localization

In this section, different antenna deployments are analyzed and each geometry performance is studied by simulation. It is assumed that there is a strong line-of-sight and that reflections are attenuated and delayed in such a way that they do not interfere in free-space assumption and all other error sources will be will be encompassed in a single error parameter given by the sampling time of the PD signal. Under these circumstances, the results will show that choosing an appropriate layout can reduce the uncertainty in the location of the source due to errors in the TDoA.

Finding analytically the sensitivity to the different measurement error sources in the TDoA applied to equation (4.16) to obtain all possible deviations in the source position is a difficult task. Moreover, though the source can be located with only three equations, there is a total of six TDoA that can be involved in the solution of the non-linear system. The proposed approach assumes an error of one time sample, $|\epsilon_{ij}| = T_s$, sequentially in all six TDoA. Then, there would three possible states for every TDoA: $t_{ij} - \epsilon_{ij}$, t_{ij}, and $t_{ij} + \epsilon_{ij}$ giving a total of $3^6 = 729$ possible solutions, see Figure 5.3. All possible errors in the range $\pm\epsilon_{ij}$ are not repeated and they explore all the locations of the source.

A common assumption when dealing with noise and errors is to assume that smaller errors are the most likely, a straightforward example of that is the Gaussian distribution, thus larger errors are not considered avoiding also the cluster of positions to be too vast and set far from the actual location losing it practical applicability.

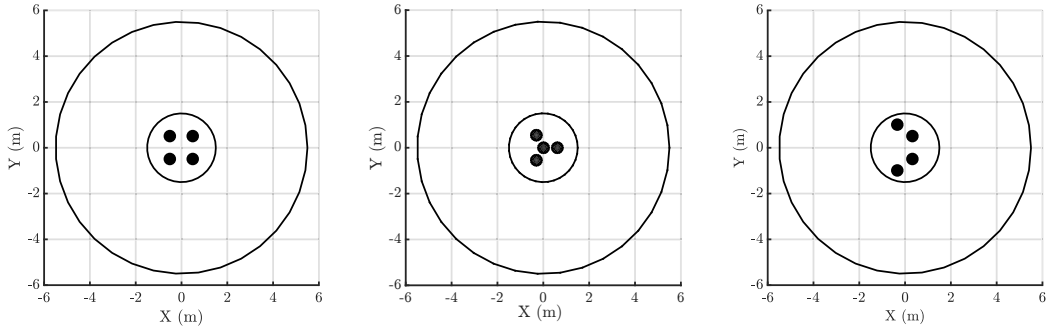

(a) Square array *(b)* Star array *(c)* Trapezoidal array

Figure 5.4: Three scenarios to test the performance of the antenna arrays. The radii of the circumferences are 1.5 m and 5.5 m.

Therefore, Equation (4.16) would be changed to Equation (5.1):

$$OF(\hat{x}_s, \hat{y}_s, \hat{z}_s) = \sum_{i=1}^{3} \sum_{j=i+1}^{4} \left(t'_{ij} \cdot c - \|\mathbf{P_i} - \hat{\mathbf{P}}_\mathbf{s}\| + \|\mathbf{P_j} - \hat{\mathbf{P}}_\mathbf{s}\| \right)^2 \tag{5.1}$$

where t'_{ij} is the t_{ij} including the error $\pm\epsilon_{ij}$ and $\hat{\mathbf{P}}_\mathbf{s} = (\hat{x}_s, \hat{y}_s, \hat{z}_s)$ is the position of the source with the error in the TDoA. The distance differences have been squared to consider only positive values in the OF. Equation (5.1) would be 0 for the correct estimation of $\hat{\mathbf{P}}_\mathbf{s}$. Notice that in 2D localization, the z component is set to zero for every antenna and the emitter.

The behavior of three different antenna deployments are tested for positions of the source on the circumferences around the antennas, see Figure 5.4. All formations are balanced so none of them is favoured in terms of their relative position to the source. This is ensured by keeping the area of the array constant to one square meter. In the case of the pyramidal arrangement, there is an antenna in the center that has also to be considered, so the total area is the area of the external equilateral triangle plus the areas of the three isosceles triangles formed by the perimetrical antennas and the central one.

In all scenarios the PSO algorithm is run every $10°$ along the circumferences to obtain all possible solutions when there is an error of $\pm\epsilon_{ij}$ in the TDoA. Then, the solutions are analyzed statistically calculating the distance of the mean value in each of the coordinates to the actual position of the source as a measure of the uncertainty in the localization; and the mean value of the distances of all possible solutions to the actual position, as a measure of the dispersion of the data. These parameters would determine whether there is a configuration that stands out from others in finding the source with higher accuracy and less dispersion due to errors in the measurement of the TDoA. All antennas are in the same plane because in this section the localization is in 2D, so the component z is neglected and the results are focused on the plane XY. To have an adequate resolution in the Z axis, at least one of the antennas should be placed in a different plane as shown Section 5.6.

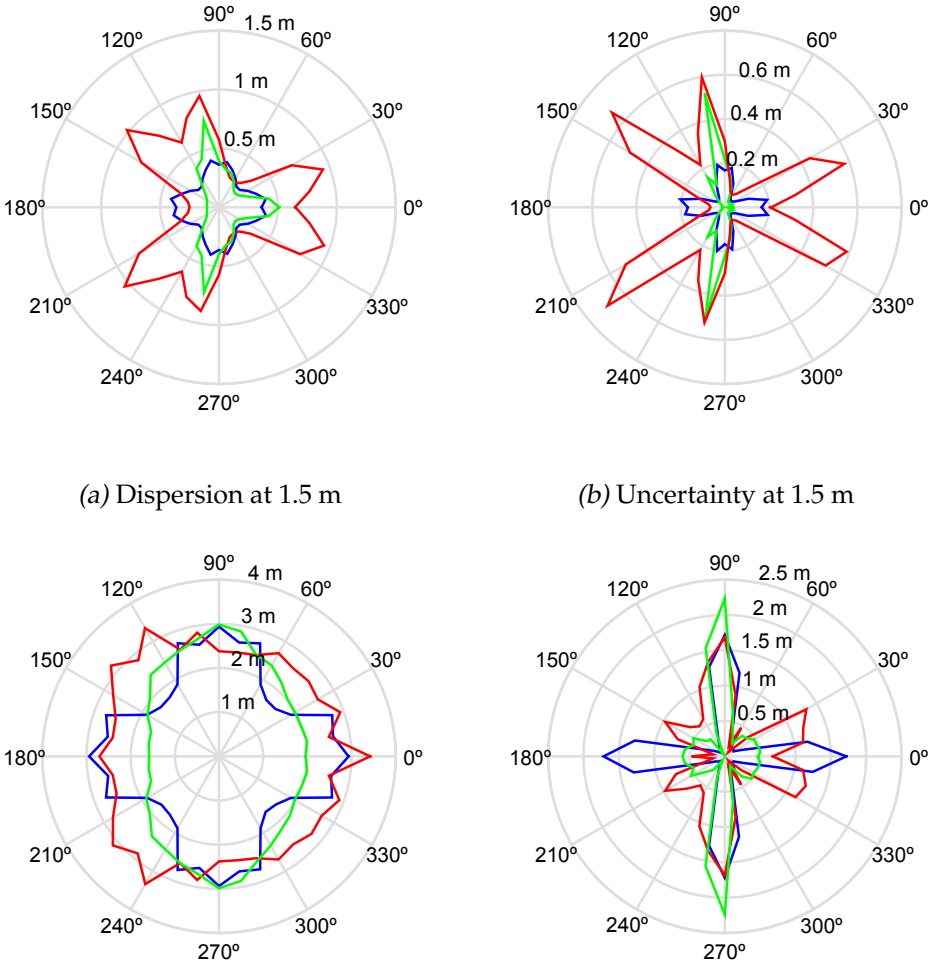

(a) Dispersion at 1.5 m

(b) Uncertainty at 1.5 m

(c) Dispersion at 5.5 m

(d) Uncertainty at 5.5 m

Figure 5.5: Simulation results for the three antenna layouts and the source located in circumferences with radii of 1.5 and 5.5 cm. The first column are the average dispersion of the solutions and the second column are the uncertainties of the average of the solutions. The layout in square is represented in blue, the pyramidal in red and the trapezoid in green.

Figure 5.5 shows the simulation results for dispersion and uncertainty measured in meters of all possible positions of the source when it is actually placed at 1.5 m and 5.5 m from the center of the layout. These polar plots are very helpful to find the directions in which the antennas have the best performance. The red line corresponds to the pyramidal formation. The preferable relative positions of the source in terms of dispersion of the results are $60°$, $180°$ and $300°$, plot 5.5 (a). This means that, when the TDoA have errors of $\pm\epsilon_{ij}$ samples, all possible positions of the source are less scattered in those angles. Additionally, plot 5.5 (b) shows the uncertainty as the mean of all possible positions with respect to the actual position of the source. The best performance of the pyramidal formation is again in the same directions as in the dispersion plot plus $0°$, $120°$ and $240°$. When the distance is increased to 5.5 m, the measure of the scatter tends to be uniform in all directions, plot 5.5 (c).

The blue line corresponds to the square array. In general, the performance of this formation is much better than the pyramidal's as long as the directions around $0°$, $90°$, $180°$ and $270°$ are avoided. This would mean that if the PD source is bearing for those angles, the square array would have problems in finding its position accurately and the possible positions would be scattered along those directions. Notice that the accuracy in finding the position of the source is very sharp between $15°$ and $75°$ and repeated in the rest of the quadrants, Figure 5.5 (b). When the source is located at 5.5 m, the arc of sharp accuracy is slightly extended, plot 5.5 (d).

Finally, the green plot corresponds to the trapezoidal arrangement. The scattering with the source at 1.5 m is similar to the formation in square in quadrants 1 and 4 and the performance is better from $120°$ to $240°$ in the second and third quadrants. There are two narrow circular sectors, though, where the square beats the trapezoid, $[90°, 120°]$ and $[240°, 270°]$. For longer distances, the behavior of the trapezoidal array is noticeable better when the parallel sides of the formation are perpendicular to the source position. However, the advantages of the trapezoid are better appreciated in the accuracy of the detection of the source. The differences between the actual position of the source and the average of the possible positions in the simulation is lower than 10 % (15 cm or 55 cm depending on the distance) for almost any bearing. Only for a narrow sector in $[90°, 100°]$ and $[260°, 270°]$, are the deviations important and similar to those of the pyramidal configuration, though still better than the squared one. A similar behaviour is observed when the source is located 5.5 m away.

5.5 Experimental study in 2D localization

The three antenna array layouts were tested in a laboratory, Figure 5.6. The antennas were monopoles 10 cm long which are omnidirectional and have good response in the range of frequencies where PDs emit [13]. All coaxial cables have the same length and are connected to an oscilloscope with four channels.

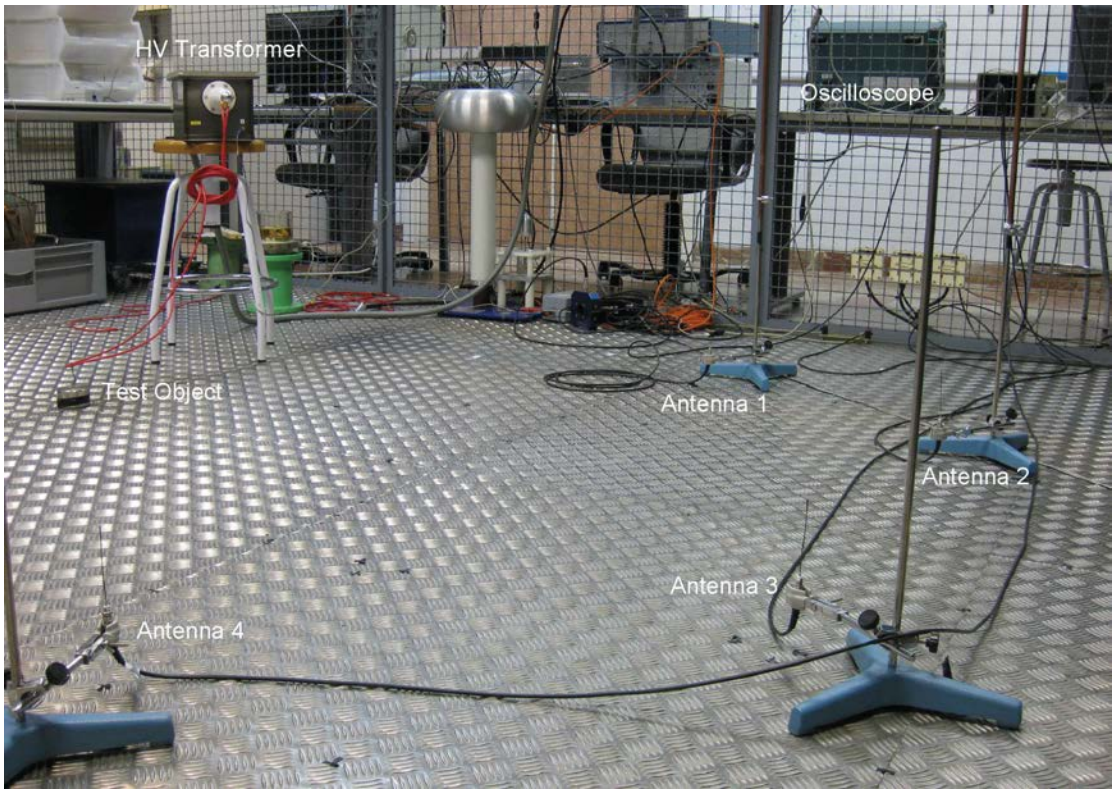

Figure 5.6: Antennal layout in the Laboratorio de Investigación y Ensayos en Alta Tensión (LINEALT) HV laboratory.

The PD source is created using a 25 kV HV cable connected to a voltage-controlled transformer. A copper wire is bent to form a ring around the HV cable and then, connected to ground. The resulting test object will have a high electric field divergence in that loop that will be able to create surface PD, [12].

All measurements consist of a set of 500 PDs. One of the key aspects to have an accurate TDoA is the choosing of an automatic picker to determine the onsets of the pulses and, with them, the time differences. In this Chapter, the TDoA are calculated using the cumulative energy method with negative trend or Hinkley criterion that has been proved to give accurate results, [12]. The TDoA are calculated for all the acquired signals to give a total of 500 sets of six TDoA. The location of the source is now estimated with the mode or the most repeated set of TDoA. It should be noted that we used the average position of all solutions in the simulation results for two reasons: any set of six TDoA can happen only once so the mode would not exist and the actual position of the source is known, so it is possible to calculate the exact deviation of all solutions with respect to the correct one through the average. Now, there are certain sets of TDoA that never happen due to imperfections in the antennas, the metallic holders that support the antennas and the metallic surfaces that surround the setup. This is translated into a distribution of frequencies of occurrence of the sets of TDoA that is not uniform as in the case of the simulation. Consequently, the mode is preferred to the average in a real experiment. As done in the simulation, all signals having a difference greater than $\pm\epsilon_{ij}$

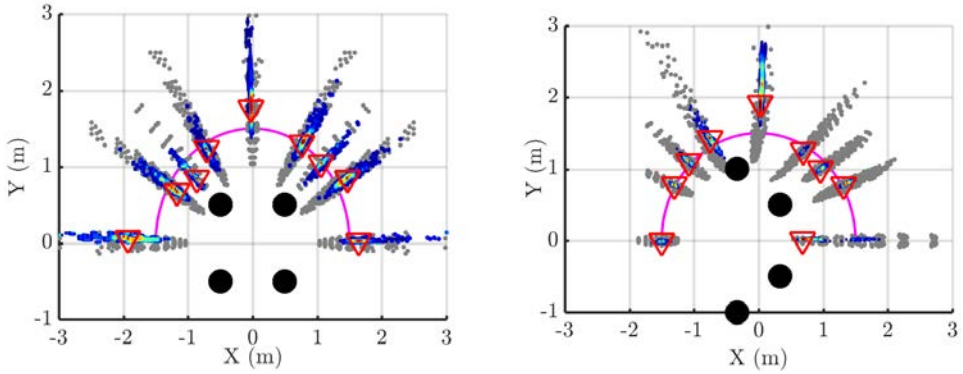

Figure 5.7: Simulated and experimental results for the squared (left) and trapezoidal (right) deployments.

referred to the mode are discarded. This is done to emulate the results presented in the previous section. The remaining sets of TDoA are used to locate the source minimizing Equation (5.1) using PSO.

Considering that the pyramidal array had a poor simulated performance, the experimental measurements were taken only for the formations in square and trapezoid. The PD source was placed in selected points on a semi-circumference around the antennas and the radius was set to 1.5 m due to room constraints in the laboratory. The results are shown in Figure 5.7 where the magenta line represents the positions of the source. The grey points are the outcome of the simulations when the TDoAs have errors of one sample; the points with colors ranging from dark blue to dark red correspond to the solutions given by the PSO for the TDoAs calculated from actual pulses. Dark blue points means that the concentration of solutions is low whereas dark red ones means that there are many solutions in that area, so the source would very likely be there. The triangles mark the mode of all experimental solutions which would be where the source is located based on those measurements.

Some conclusions can be drawn from Figure 5.7. First, all points obtained experimentally fall inside the cluster defined by the analysis done in Section 5.4 though they do not cover all possible solutions of the simulation. As explained before, this means that the deviations of the TDoA in the experimental measurements are not uniformly distributed and there are sets of TDoA that are repeated more than others. Second, the size of the clusters of the experimental outcome is noticeable smaller in the trapezoidal than in the square in all directions except in the interval $[90°, 120°]$ as expected from the simulations. This favors the use of this type of configuration because the position of the source is found with less uncertainty. Third, the accuracy of the trapezoidal formation given by the position triangles in Figure 5.7 is again better than in the square except in $0°$ and $90°$. This was expected in the latter direction, $90°$, as predicted by the simulations but in the bearing for $0°$ the trapezoidal should have placed the source in its exact point as suggested the green plot in Figure 5.5 (b). This can be explained examining in detail the possible solutions for this bearing: there are two clusters, one of them has

Table 5.1: Coordinates of the antennas positions for each layout in meters.

(m)		Antenna 1	Antenna 2	Antenna 3	Antenna 4
Square	x	-1.00	-1.00	1.00	1.00
	y	-1.00	1.00	-1.00	1.00
	z	-1.00	1.00	-1.00	-1.00
Pyramid	x	$-\frac{\sqrt{3}}{3}$	$-\frac{\sqrt{3}}{3}$	$2\frac{\sqrt{3}}{3}$	0.00
	y	-1.00	1.00	0.00	0.00
	z	-1	-1	-1	1
Cartesian	x	-1.00	-1.00	1.00	-1.00
	y	-1.00	1.00	1.00	1.00
	z	-1.00	-1.00	-1.00	1.00
Trapezoidal	x	0.66	-0.66	-0.66	0.66
	y	-2.00	-1.00	1.00	2.00
	z	-1.00	-1.00	1.00	-1.00

more probability of occurring so the mode (triangle) is placed on it. The other cluster in 0°, in blue colors, contains the correct set of TDoA of the real position of the source but, unfortunately, the PSO algorithm favors the wrong location.

5.6 Antenna deployment and simulations in 3D localization

As commented in the introduction, the presented simulations consider that the position of the source of PD is not known a priori, so the array of antennas is deployed in a certain region inside the substation and the source can fall outside the area defined by the antennas. This is the most adverse case because, if the source is inside that area, the accuracy in the localization is dramatically increased. A particular example of the simulation would be localizing PD sources inside transformers where the antennas can be placed at the vertices of the tank ensuring that the source is inside the array and its position is easier to find. Though the simulation could also consider this case, the most relevant situation is when the antennas do not surround the source.

The configurations of antenna arrangements tested in the simulations are shown in Figure 5.8. In the square arrangement (a), the antennas are placed in the vertices of a square and one of the antennas is elevated from the plane to have better resolution in the vertical axis. The layout in (b) has the antennas in a triangular pyramid so the behaviour is symmetric in four directions. The configuration in (c) has the antennas in the axis that define a cartesian coordinate system in 3D with the idea of having the best accuracy in the octant defined by the positive X and Z axes and the negative Y axis. Finally, the trapezoidal configuration is displayed in (d), in this layout the distribution of the antennas seems a paraboloid arrange trying to improve the exactness in the localization in some directions scarifying others less interesting. The detailed position of the antennas in each layout is shown in Table 5.1.

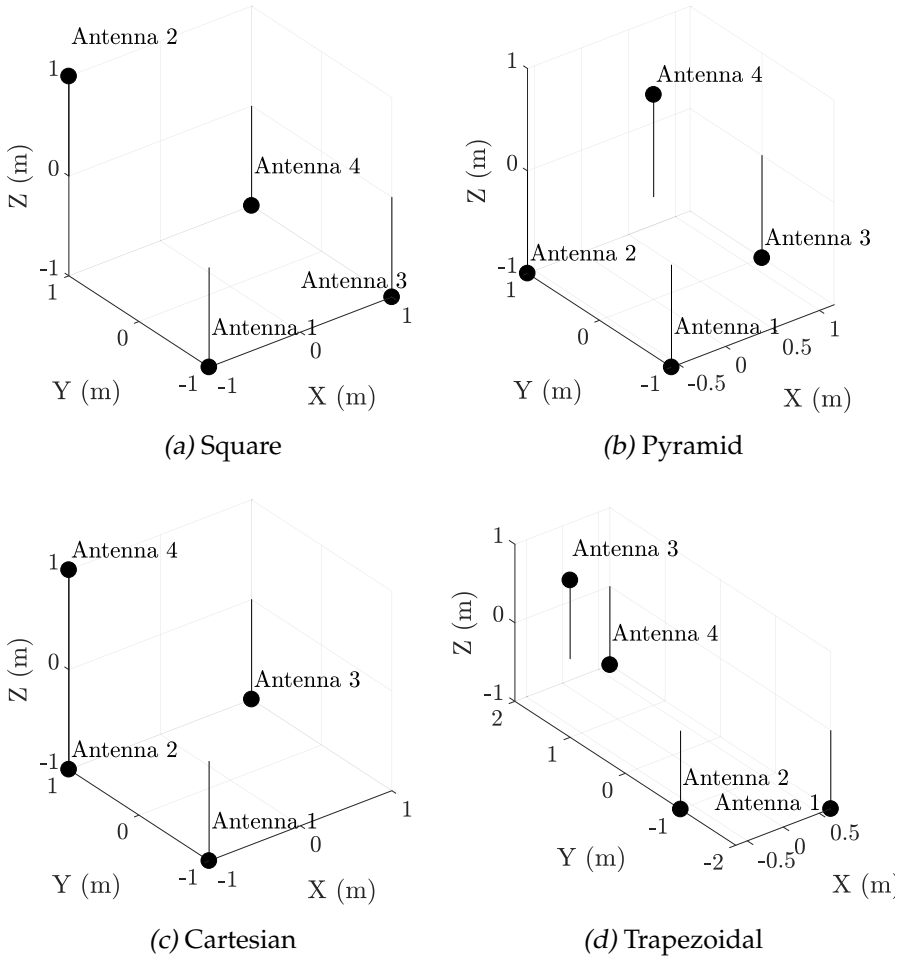

(a) Square *(b)* Pyramid

(c) Cartesian *(d)* Trapezoidal

Figure 5.8: Antenna configurations. (a) The antennas are in the vertices of a square and one of them has been elevated. (b) The antennas are placed at the vertices of a triangular pyramid. (c) The antennas are in the axes of a cartesian coordinate system in 3D. (d) The antennas are placed in a trapezoid isosceles in the XY plane with one antenna in different z.

For these configurations, the simulation will determine the accuracy in the calculation of the position of the source in all spatial directions introducing errors in the TDoA. All these possible errors will be encompassed in a maximum time error equal to the system sampling time T_s, which in the simulations is 200 picoseconds. As there are four antennas, there will be six TDoA available, and for each of them, three possible values will be added to the TDoA during the simulation: 0 (no error), and $\epsilon = \pm T_s$. The actual position of the source will be placed at 10 m from the origin of coordinates creating a sphere around the configurations of antennas so all azimuth, φ, and elevation, θ', angles will be covered. Starting from $\varphi = 0°$ and $\theta' = 0°$, the increment in azimuth is every $20°$ and the increment in elevation is every $10°$. Selecting a distance of 10 m would cover a large area inside a substation and ensures that the signal arriving to the antennas has a SNR sufficiently high to allow a clear detection of the signal. The six TDoA are calculated from the antennas to all the possible positions of the source and then modified according the error ϵ. Then, a localization algorithm based on PSO is run to minimize Equation (5.1) and to obtain the positions of the source when the TDoA have uncertainties. This results in a cloud of points for every position considered in the sphere. The expected location of the source, $\bar{\hat{\mathbf{P}}}_\mathbf{s}$, is determined as the mean of all possible values, and the uncertainty is the distance between the actual position to the expected position $e_k = \|\mathbf{P_s} - \bar{\hat{\mathbf{P}}}_\mathbf{s}\|$, where k denotes the position in the sphere for angles φ_k and θ'_k.

A summary of the simulation process would be:

1. Start with one of the four possible configurations of antennas.
2. Place the source at 10 m from the center of the array and set the azimuth and elevation angles, $\varphi_k = 0°$ and $\theta'_k = -90°$, respectively.
3. Calculate all six theoretical TDoA for the position of the source and modify them with an error $\epsilon = \pm\, T_s$ to consider all possible inaccuracies.
4. Use the modified TDoA in the PSO algorithm to calculate the erroneous positions of the source due to the inaccuracies in the measurement of those TDoA.
5. Calculate the mean point of the cloud of possible solutions and the distance, e_k, from that point to the actual position of the source.
6. Plot e_k in a sphere in the position determined by angles φ_k and θ'_k in a colormap scale code representing accuracy.
7. Repeat the process increasing k and increasing the elevation in $20°$, $\varphi_{k+1} = \varphi_k + 20°$
8. If $\varphi_{k+1} \leq 360°$ set $\theta'_{k+1} = \theta'_k$ and go to step 3. Otherwise, set $\varphi_{k+1} = 0°$ and increase the azimuth angle in $10°$ $\theta'_{k+1} = \theta'_k + 10°$ and go to step 3.
9. Repeat the process for another configuration of antennas.

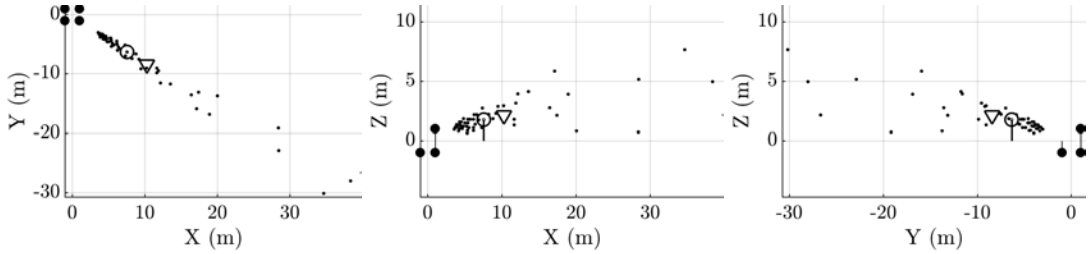

(a) XY view *(b)* XZ view *(c)* YZ view

Figure 5.9: Example of the cloud of points obtained when the source is placed at $r = 10$ m, $\varphi = -40°$ and $\theta' = 10°$ and the TDoA have uncertainties.

5.7 Sensitivity to measurement errors in 3D localization

Figure 5.9 is an example of the possible solutions obtained when the actual position of the source is placed at $r = 10$ m, $\varphi = -40°$ and $\theta' = 10°$ and the TDoA are modified with the uncertainty ϵ. The arrangement of the antennas is the square configuration defined in Figure 5.8. The three plots are the views in three different planes XY, XZ and YZ, to help in the comprehension of the spatial distribution of the antennas and solutions. The correct position of the source, $\mathbf{P_s}$, is marked with with a circle ($\odot$) and the mean of all possible solutions, $\bar{\hat{\mathbf{P}}}_\mathbf{s}$, with an inverted triangle ($\bigtriangledown$). The results show that the error in the Z axis is small while the errors in X and Y are approximately 2.5 m which are fairly high. Therefore, when the source of PD is in that direction, the accuracy will be low and the position might be misplaced so it should be avoided. Another interesting result derived from plot 5.9 (a) is that the cloud of points is clearly distributed along the line defined by any pair of antennas.

The total error, close to 3.6 m, is annotated in e_k for that direction. The process is repeated for all the points defined in the sphere as explained in Section 5.6 to obtain 18 directions in azimuth and 19 in elevation to yield a total of 342. A color graduation is defined as a function of the minimum and maximum values of e_k and that color is represented in a sphere with radius 10 m in the corresponding direction. The simulated results for every antenna layout are shown in Figure 5.10, Figure 5.11, Figure 5.12 and Figure 5.13 for the XY, XZ, YZ and 3D from $\varphi = -45°$ and $\theta' = 45°$ points of view respectively. In these figures, the results have been interpolated to have a smoother surface. The interpolation is done including 10 points with cubic-splines so the final resolution in azimuth would be $2°$ and $1°$ in elevation.

The four figures 5.10, 5.11, 5.12 and 5.13 have eight subfigures, the rows correspond to the different antenna layouts studied. The left column represent the uncertainty diagram for every antenna layout and the right column represent the antenna positions for each left diagram from the defined point of view. In the right figures, the ratio between the antennas position and the sphere is in a.u. to show clearly the antennas location and to identify the preferred direction of every layout.

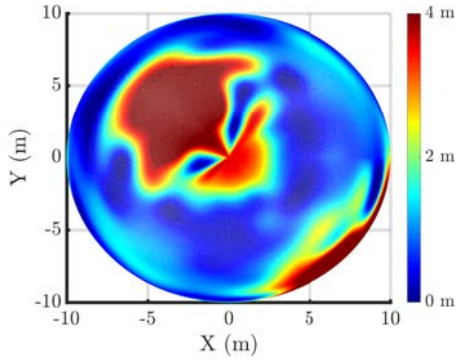

(a) Square uncertanity zenithal view

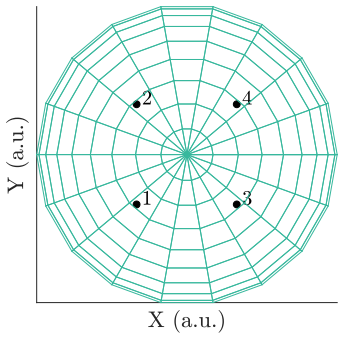

(b) Square layout zenithal view

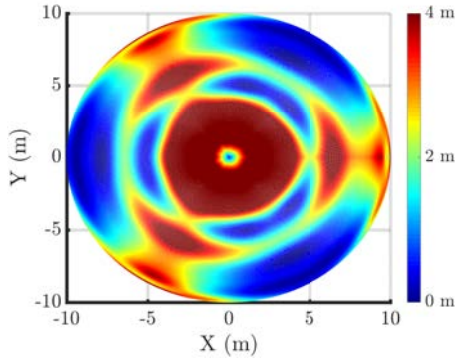

(c) Pyramid uncertanity zenithal view

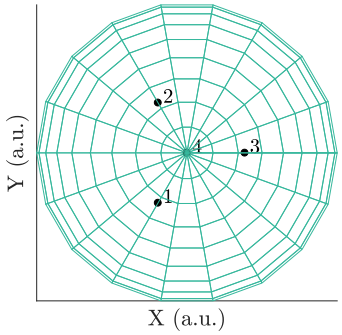

(d) Pyram. layout zenithal view

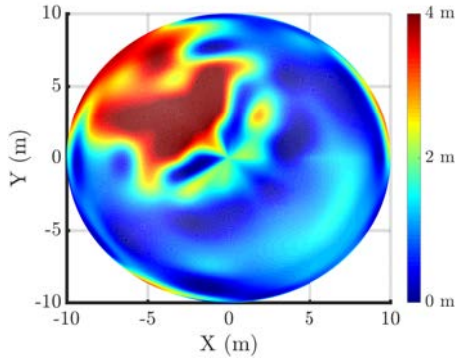

(e) Cartesian uncertanity zenithal view

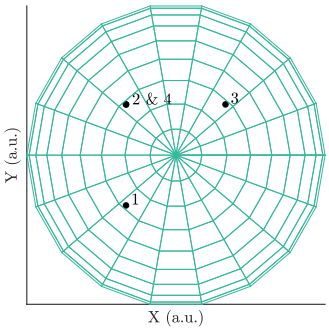

(f) Cartes. layout zenithal view

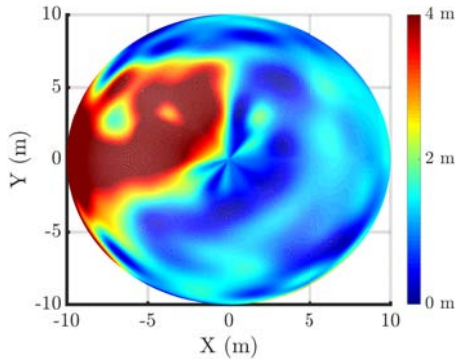

(g) Trapez. uncertanity zenithal view

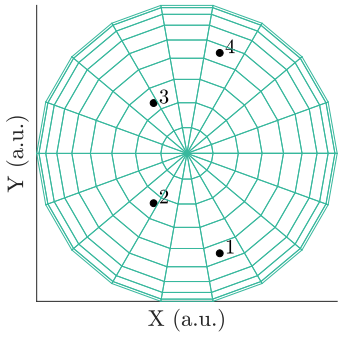

(h) Trapez. layout zenithal view

Figure 5.10: Uncertainties at a distance of 10 m from the source for all antennas layout from the zenithal point of view. In each row are shown the spheres which represents the uncertainty (left) and the antennas layout with the same point of view (right).

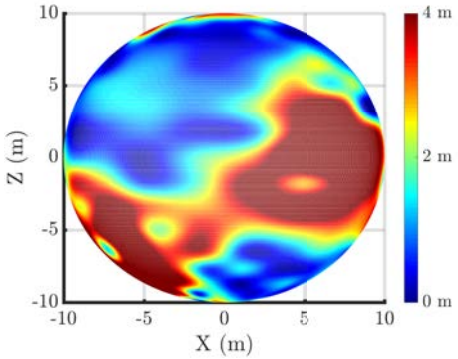

(a) Square uncertanity XZ view (m)

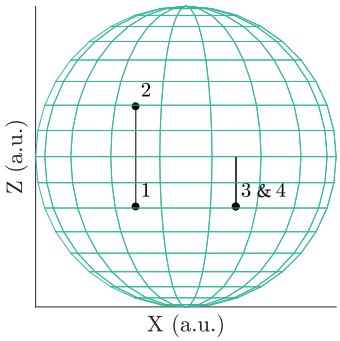

(b) Square layout XZ view (a.u)

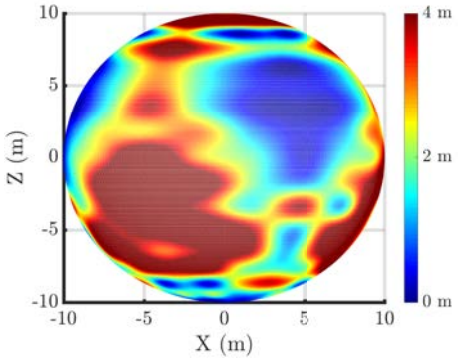

(c) Pyramid uncertanity XZ view (m)

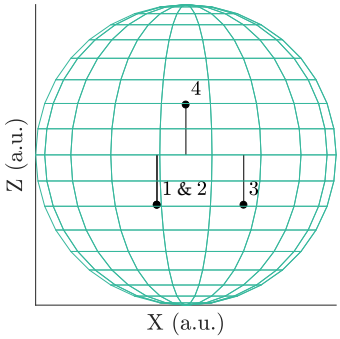

(d) Pyram. layout XZ view (a.u)

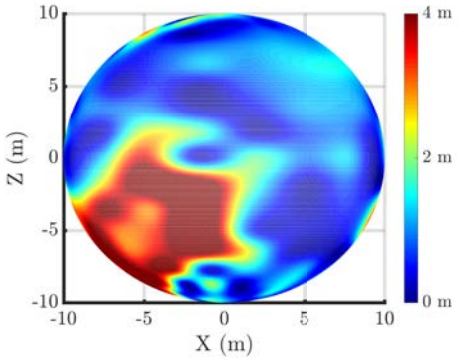

(e) Cartesian uncertanity XZ view (m)

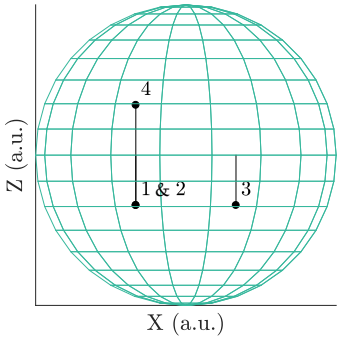

(f) Cartes. layout XZ view (a.u)

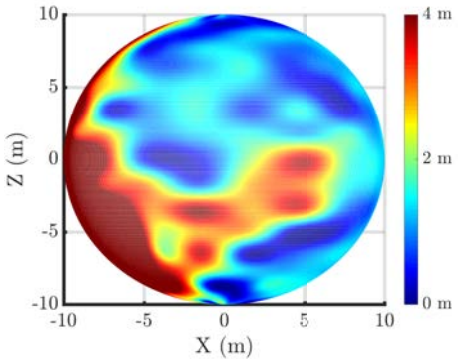

(g) Trapez. uncertanity XZ view (m)

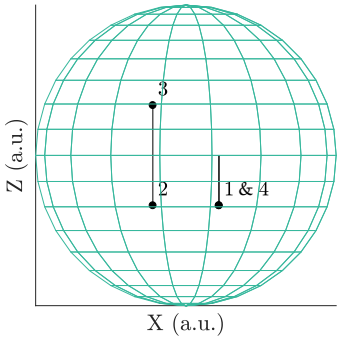

(h) Trapez. layout XZ view (a.u)

Figure 5.11: Uncertainties at a distance of 10 m from the source for all antennas layout from the XZ point of view. In each row are shown the spheres which represents the uncertainty (left) and the antennas layout with the same point of view (right).

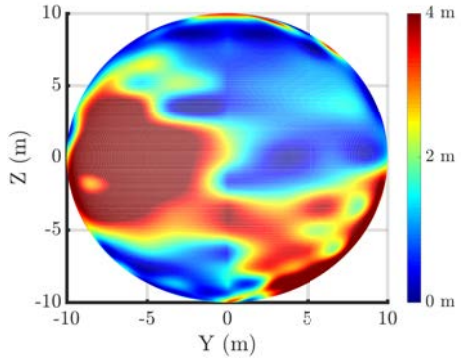

(a) Square uncertainty YZ view (m)

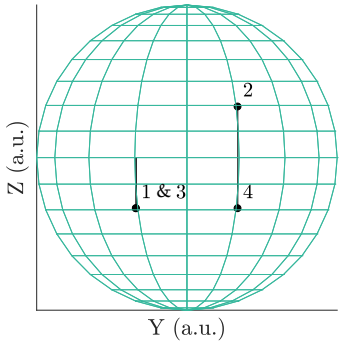

(b) Square layout YZ view (a.u)

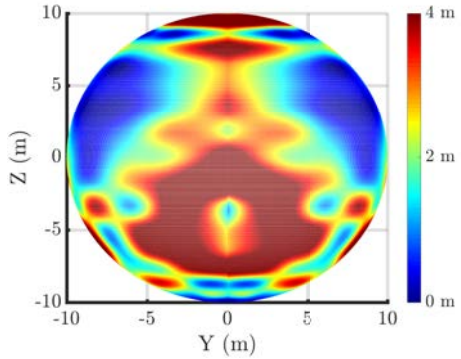

(c) Pyramid uncertanity YZ view (m)

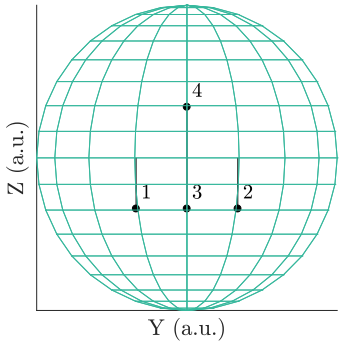

(d) Pyram. layout YZ view (a.u)

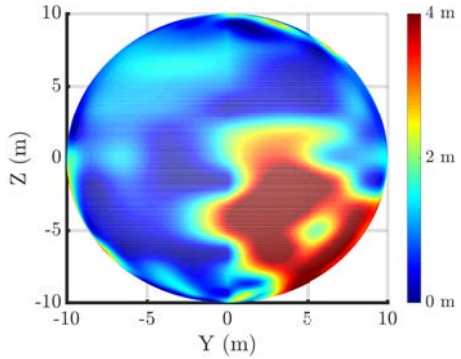

(e) Cartesian uncertanity YZ view (m)

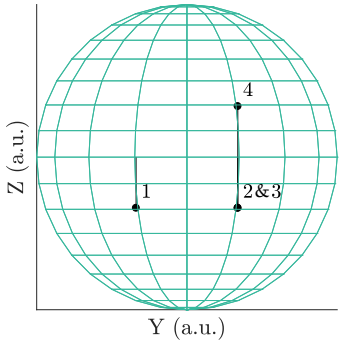

(f) Cartes. layout YZ view (a.u)

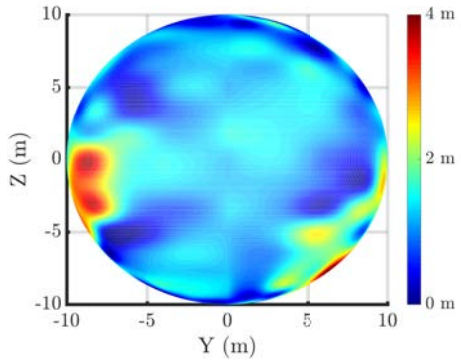

(g) Trapez. uncertanity YZ view (m)

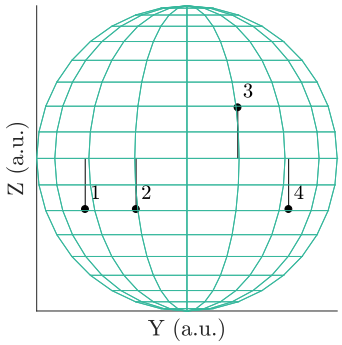

(h) Trapez. layout YZ view (a.u)

Figure 5.12: Uncertainties at a distance of 10 m from the source for all antennas layout from the YZ point of view. In each row are shown the spheres which represents the uncertainty (left) and the antennas layout with the same point of view (right).

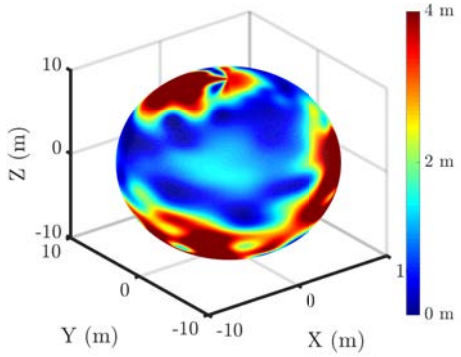

(a) Square uncertanity 3D view (m)

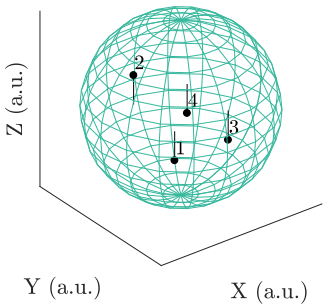

(b) Square layout 3D view (a.u)

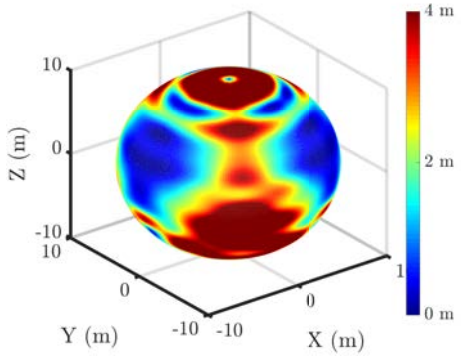

(c) Pyramid uncertanity 3D view (m)

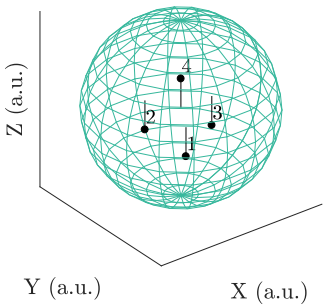

(d) Pyram. layout 3D view (a.u)

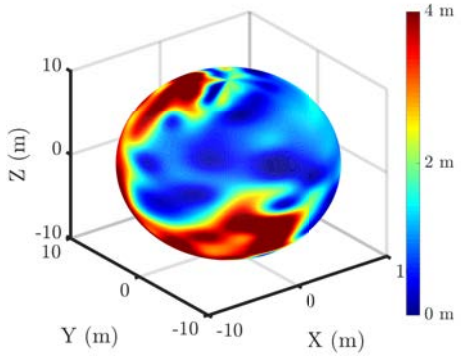

(e) Cartesian uncertanity 3D view (m)

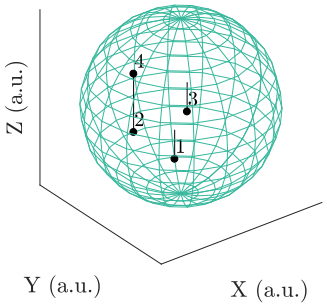

(f) Cartes. layout 3D view (a.u)

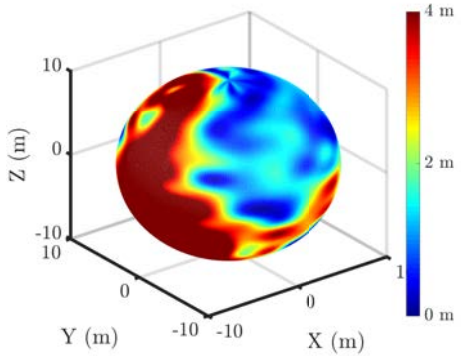

(g) Trapez. uncertanity 3D view (m)

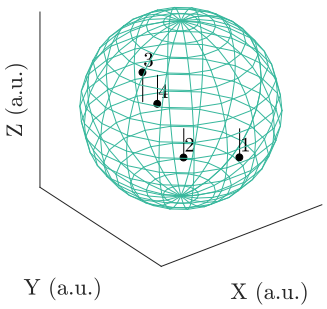

(h) Trapez. layout 3D view (a.u)

Figure 5.13: Uncertainties at a distance of 10 m from the source for all antennas layout from the 3D point of view. In each row are shown the spheres which represents the uncertainty (left) and the antennas layout with the same point of view (right).

In the uncertainty diagrams, left graphs, the reddish tones mean that the uncertainty e_k in that direction is high whereas blueish tones represent directions with low uncertainty. The range of uncertainties spans from 0 m to 4 m as shown in the scales on the right of the uncertainty diagrams. Under these considerations, it is clear to prove that the behaviour of the square, cartesian and trapezoidal arrays is very similar, favouring some directions in which the uncertainty is very low. In fact, there is a band at an elevation $\theta' = 0°$ to $\theta' = 80°$ where the blueish tones are predominant for almost all azimuths, see Figure 5.10. In that band, in the case of the square and cartesian configuration, azimuths around $\varphi = 135°$ have warm tones. In the case of the trapezoidal layout, azimuths around $170° - 190°$ have reddish regions where there are high uncertainty. Precisely, these zones where the uncertainty is larger correspond to the bearings defined by aligned antennas. Taking the first configuration, the pair of antennas 2-3 in $(-1, 1, 1)$ and $(1, -1, -1)$ define the space diagonal of the cube in ascending coordinates, Figure 5.10 (a). This is translated to two red zones in the surface of the sphere of uncertainties, one in the south hemisphere with all components in negative or $\varphi = -45°$ and $\theta' = -45°$, Figure 5.10 (a); and the other in the north hemisphere with all components in positive or $\varphi = 135°$ and $\theta' = 45°$, Figure 5.11 (a). This is also repeated in the cartesian configuration. For instance, the vertical direction defined by the antennas 2-4 in $(-1, 1, -1)$ and $(-1, 1, 1)$, define a zone of uncertainty in all bearings with azimuth $\varphi = 135°$ and almost all elevations, Figure 5.10 (c). The trapezoidal configuration has similar behaviour than cartesian and has large uncertainties with azimuth $\varphi = 180°$ and almost all elevations, Figure 5.10 (d). The pyramidal array of antennas is symmetric every $120°$ and this is also seen in the distribution of the uncertainties where the blueish tones are repeated precisely for this quantity, Figure 5.10 (b).Unfortunately, in the pyramid configuration, the concentration of lines defined by every pair of antennas is higher than in the other two cases so there are larger red zones in which the uncertainty is elevated and the source would be difficult find. These areas are in azimuths $\varphi = 0°$, $\varphi = -120°$ and $\varphi = 120°$ as derived from the relative position of the vertices of the pyramid. Additionally, there is a large uncertainty around the north pole of the sphere because the three edges of the pyramid converge in the top vertex. However, there is a blue zone for elevations close to $90°$ because there is not any vertical line passing through the top vertex that passes through another antenna, so the uncertainty there is very low.

5.8 Conclusions

Choosing an adequate layout of antennas can help in planar localization of PD sources. The results in Section 5.4 and Section 5.5 highlight that the dispersion and specially the accuracy in the estimations of the 2D location of the PD emitter show a strong dependence on the relative position of the source which respect to the antenna array.

Consequently, each configuration has its own optimal orientation for the localization of events. This Chapter also shows that the trapezoidal configuration can reduce the dispersion of the possible solutions of the source better than other configurations such as a square or a pyramidal. Additionally, the average value of all data in the components x and y is also closer to the actual position of the source in most of the directions considered. If the PD source is far from the antenna array, the performance of the trapezoidal configuration is also better which is very appropriate when measuring this type of events in open air substations.

In this chapter, new graphics are presented to determine what directions are the best to find the PD source with four antennas accurately in 3D. The uncertainties in presence of TDoA errors are plotted on the surface of a sphere following scales of color. The results show that the best direction is that those where the viewpoint towards the antenna layout does not find two or more antennas in its path. Therefore, the distribution of the antennas should favour some directions, i.e. blueish tones in the uncertainty spheres, where this constraint is fulfilled. In this sense, the most adequate layout from the cases studies in this chapter, would be the square formation with an elevated antenna followed very closely by the cartesian formation and the trapezoidal one.

When localizing PD inside a substation where the problematic asset is unknown and cannot be surrounded, the procedure would be to deploy an array of four antennas forming a square with one of the antennas in a different plane to have resolution in the vertical axis. The orientation of the square plays a significant role in terms of accuracy in the localization of the source. The array has to be rotated in such a way that the blue regions in the uncertainty spheres are aligned with the direction in which the PD source is suspected to be. This would minimize the uncertainty in localization due to unavoidable errors in the TDoA. As a general consideration in the antenna layouts, the lowest uncertainties are obtained in the bearings where the aperture of the antenna layouts is larger.

5.9 Bibliography

[1] L. Brás, N. B. Carvalho, P. Pinho, et al. “A Review of Antennas for Indoor Positioning Systems”. en. In: *International Journal of Antennas and Propagation* 2012 (Dec. 2012), e953269. ISSN: 1687-5869. DOI: 10.1155/2012/953269. URL: https://www.hindawi.com/journals/ijap/2012/953269/abs/ (cit. on p. 124).

[2] P. J. Moore, I. E. Portugues, and I. A. Glover. “Radiometric location of partial discharge sources on energized high-Voltage plant”. In: *IEEE Transactions on Power Delivery* 20.3 (July 2005), pp. 2264–2272. ISSN: 0885-8977. DOI: 10.1109/TPWRD.2004.843397 (cit. on pp. 125, 126, 128).

[3] J. He, M. Li, G. Chen, et al. “Error Analysis and Antenna Array Placement Optimization of Localization System for Partial Discharge in Substation”. In: *Przegląd*

Elektrotechniczny R. 90, nr 7 (2014). URL: http://yadda.icm.edu.pl/baztech/element/bwmeta1.element.baztech-c1157f2d-1b4a-4cd8-9f57-54e28632d71e (cit. on p. 125).

[4] H. Hou, G. Sheng, and X. Jiang. "Localization Algorithm for the PD Source in Substation Based on L-Shaped Antenna Array Signal Processing". In: *IEEE Transactions on Power Delivery* 30.1 (Feb. 2015), pp. 472–479. ISSN: 0885-8977. DOI: 10.1109/TPWRD.2014.2344014 (cit. on p. 125).

[5] B. G. Stewart, A. Nesbitt, and L. Hall. "Triangulation and 3D location estimation of RFI and Partial Discharge sources within a 400kV substation". In: *2009 IEEE Electrical Insulation Conference*. May 2009, pp. 164–168. DOI: 10.1109/EIC.2009.5166337 (cit. on p. 125).

[6] L. Niemeyer. "A generalized approach to partial discharge modeling". In: *IEEE Transactions on Dielectrics and Electrical Insulation* 2.4 (Aug. 1995), pp. 510–528. ISSN: 1070-9878. DOI: 10.1109/94.407017 (cit. on p. 127).

[7] C. Knapp and G. Carter. "The generalized correlation method for estimation of time delay". In: *IEEE Transactions on Acoustics, Speech and Signal Processing* 24.4 (Aug. 1976), pp. 320–327. ISSN: 0096-3518. DOI: 10.1109/TASSP.1976.1162830 (cit. on p. 127).

[8] M. Judd, L. Yang, and I. Hunter. "Partial discharge monitoring of power transformers using UHF sensors. Part I: sensors and signal interpretation". In: *IEEE Electrical Insulation Magazine* 21.2 (Mar. 2005), pp. 5–14. ISSN: 0883-7554. DOI: 10.1109/MEI.2005.1412214 (cit. on p. 127).

[9] J. H. Kurz, C. U. Grosse, and H.-W. Reinhardt. "Strategies for reliable automatic onset time picking of acoustic emissions and of ultrasound signals in concrete". In: *Ultrasonics* 43.7 (June 2005), pp. 538–546. ISSN: 0041-624X. DOI: 10.1016/j.ultras.2004.12.005. URL: http://www.sciencedirect.com/science/article/pii/S0041624X04003166 (cit. on p. 127).

[10] P. Wagenaars, P. Wouters, P. van der Wielen, et al. "Accurate estimation of the time-of-arrival of partial discharge pulses in cable systems in service". In: *IEEE Transactions on Dielectrics and Electrical Insulation* 15.4 (Aug. 2008), pp. 1190–1199. ISSN: 1070-9878. DOI: 10.1109/TDEI.2008.4591242 (cit. on p. 127).

[11] C. D. Saragiotis, L. J. Hadjileontiadis, I. T. Rekanos, et al. "Automatic P phase picking using maximum kurtosis and kappa;-statistics criteria". In: *IEEE Geoscience and Remote Sensing Letters* 1.3 (July 2004), pp. 147–151. ISSN: 1545-598X. DOI: 10.1109/LGRS.2004.828915 (cit. on p. 127).

[12] G. Robles, J. M. Fresno, and J. M. Martínez-Tarifa. "Separation of Radio-Frequency Sources and Localization of Partial Discharges in Noisy Environments". en. In: *Sensors* 15.5 (Apr. 2015), pp. 9882–9898. DOI: 10.3390/s150509882. URL: http://www.mdpi.com/1424-8220/15/5/9882 (cit. on pp. 128, 133).

[13] G. Robles, M. Sánchez-Fernández, R. A. Sánchez, et al. "Antenna Parametrization for the Detection of Partial Discharges". In: *IEEE Transactions on Instrumentation and Measurement* 62.5 (May 2013), pp. 932–941. ISSN: 0018-9456. DOI: 10.1109/TIM.2012.2223332 (cit. on p. 132).

Chapter 6

Montecarlo analysis of the error propagation in the antenna positioning in the localization of PD sources

6.1 Abstract

As mentioned previously in the thesis, according to the antenna arrangement and its relative position with respect the PD source, the pulsed PD emissions reach each antenna at different time instant. The TDoA between antennas together with the antennas position are the variables used to locate PD sources in space. How the errors in TDoA are propagated in the estimation of the source position is analyzed in Chapter 5. That study is done to compare the sensitivity to errors in the TDoAof the different antenna layouts and to identify which directions are more or less affected by errors in each arrangement.

After analyzing the sensibility to errors in the TDoA, this Chapter addresses a Montecarlo-analysis on how the systematic errors in the positioning of the antennas are propagated in the estimated location of the PD source. This effect is analyzed over three parameters: the direction and distance between the source and the antenna array and the magnitude of the positioning error. In the analysis of Chapter 5 the effect of the errors in TDoA is only analyzed considering the direction because the distance is set to 10 m. The analysis of the effect of the errors over the distance gives an idea on how the same error provokes larger shifts in the source localization as farther it is. For the error magnitude occurs the same, the greater error in the antenna positioning is the greater error in the localization. This study, as the one presented in Chapter 5, is carried out for the most widely used antenna layouts. Finally, general recommendations are suggested to deploy the antennas to locate accurately PD sources through its RF emission measurement even in the presence of errors.

6.2 Introduction

This Chapter is an adaptation of a paper pending of submission, it shows how the errors in the antenna positioning affect in the TDoA estimation and furthermore, in the PD source location. Even if the array is carefully deployed unknown and undesired errors will affect the propagation times. The consequence is that, when the acquired data are analyzed, the location is found to be shifted with respect the actual position. The study of propagation of the errors in the antenna positioning throughout all the process done in the localization is carried out by Montecarlo simulations due the complexity to reach a theoretic solution with a mathematical analysis. The PD source location is calculated by a combined algorithm MLE-HLS explained in Subsection 4.3.2.4, based on the merge of two algorithms, a GPS algorithm and another based on HLS. MLE-HLS algorithm yields similar results than PSO, presented in Subsection 4.3.1.4, but is considerably much faster. The location is carried out in spherical coordinates to analyze the radius, elevation and azimuth of the position of the source respect the position of the antennas. The propagated errors of these parameters are analyzed regarding the distance and direction of the PD source to the antennas array and with respect to the error magnitude of the antenna positioning. Some commonly used antenna layouts (cartesian, square, pyramidal and trapezoidal) are studied and, in each case, a statistical analysis is made to compare how the median error and the error deviation is affected by the positioning errors.

6.3 Location algorithm

The principle of localization is explained in Chapter 4 and Chapter 5. In this study, four antennas are used, then, three independent TDoAs, and, therefore, three independent non-linear equations can be obtained. An approach to find the solution of the non-linear equations and therefore the source, is based on the OF used in the PSO algorithm [1, 2]. The aim of these works is to find an estimation of the position $\hat{\mathbf{P}}_\mathbf{s}$ minimizing the HLS Equation (6.1)[1].

$$OF\left(\hat{x}_s, \hat{y}_s, \hat{z}_s\right) = \sum_{i=1}^{3} \sum_{j=i+1}^{4} \left(D'_{ij} - \|\mathbf{P_i} - \hat{\mathbf{P}}_\mathbf{s}\| + \|\mathbf{P_j} - \hat{\mathbf{P}}_\mathbf{s}\| \right)^2. \tag{6.1}$$

where D'_{ij} is the distance from the PD source to antenna i minus the distance from the PD source to antenna j. These variables are calculated as the product between the TDoAs and the speed propagation so they would consider any error introduced by an inaccurate antennas positioning.

A Montecarlo analysis is very time-consuming because requires the evaluation of many source positions, therefore, the time spent in the obtention of one solution is critical. PSO is certainly very accurate but it takes a long time to locate the PD source so, to reduce the total execution time, a combined algorithm approach presented in Subsection 4.3.2.4 is followed. This algorithm is presented in the publication "A Combined Algorithm Approach for PD Location Estimation Using RF Antennas", which full citation can be found in Subsection 7.3.2 in item 9. This combined algorithm is based on the GPS algorithm MLE [3] which reports two solutions. The criterium to chose the correct one is the solution which minimizes the HLS based Equation (6.1).

6.4 Antenna Layouts

There are a multiple possibilities to arrange the antennas and all of them affect the sensitivity to errors in the location of the source of PD [4]. This Chapter analyzes the same four antenna configurations as in Chapter 5 and they are shown in Figure 6.1 with exact position of each antenna for each configuration detailed in Table 6.1. The so-named cartesian layout is a recently proposed deployment that yields goods results [2]. The square configuration is the most widely used in other works [5, 6, 7]. The pyramidal formation has also been used in the bibliography [8] but its outcome is not as good as that obtained with the square configuration. The trapezoidal layout has been also used in [4, 9].

All the configurations studied have one of the antennas allocated out of the plane constituted by the other three antennas. This is necessary because with all antennas

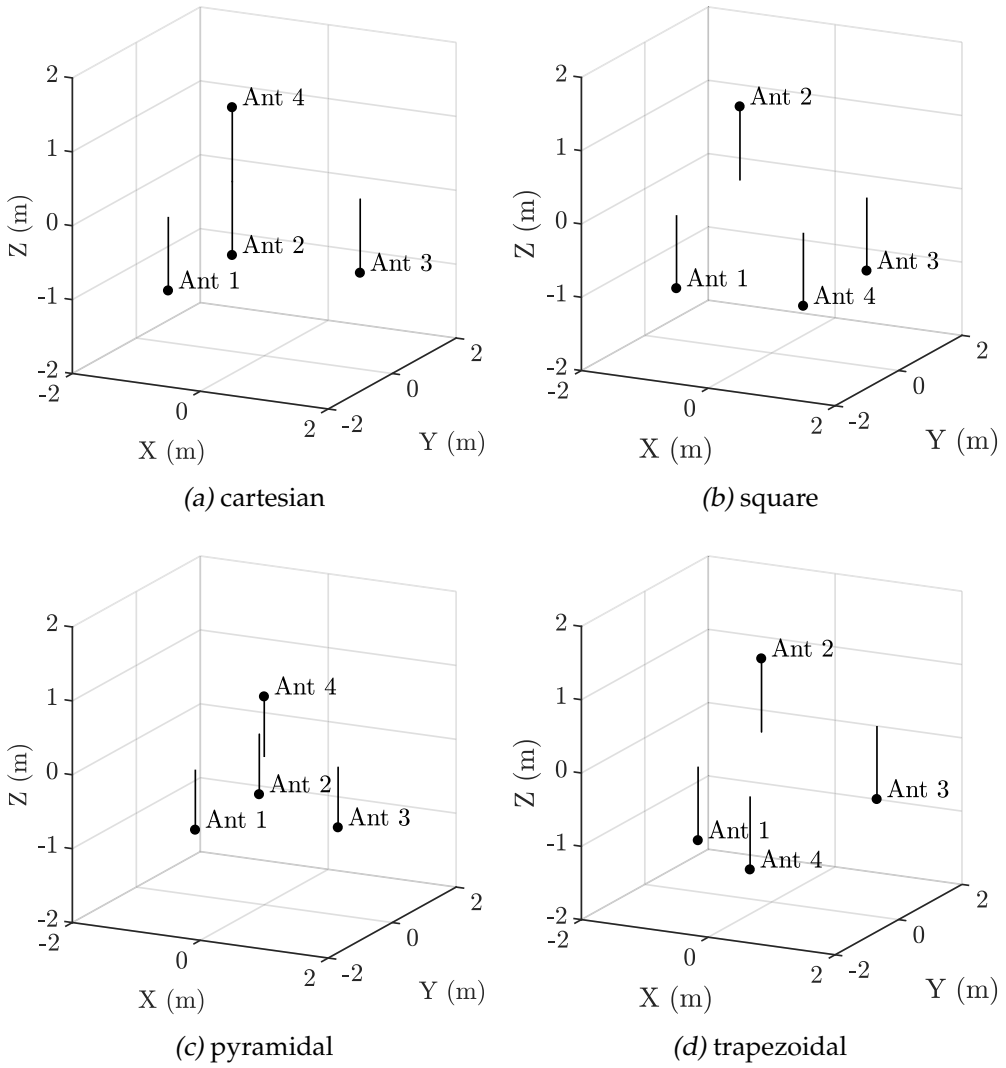

(a) cartesian *(b)* square

(c) pyramidal *(d)* trapezoidal

Figure 6.1: Antenna layouts used in the study. The antennas are represented by black dots.

located in the same plane, the position of the estimated source is undefined in the perpendicular direction. For instance, when antennas are placed as a square centered in $x = 0, y = 0$ in the XY plane and the source is placed in any point of the line $x = 0$ and $y = 0$, the emission will reach each antenna at the same time, rendering all TDoA to zero, independently of the value in the perpendicular axis z. Therefore, a deployment of the antennas in the same plane can only report planar localization estimating the position of the source as the intersection of the estimated directions in different positions [10]. Some authors have done a successful direction location in XY plane [11, 7]; for instance, Moore addresses a localization based on the estimation of the direction placing the antenna array in different positions and defining the PD source as the intersection of the calculated bearings but the location is also planar [11].

Table 6.1: Antenna positions for each analyzed layout.

(m)		Ant 1	Ant 2	Ant 3	Ant 4
cartesian	x	-1.00	-1.00	1.00	-1.00
	y	-1.00	1.00	1.00	1.00
	z	-1.00	-1.00	-1.00	1.00
square	x	-1.00	-1.00	1.00	1.00
	y	-1.00	1.00	1.00	-1.00
	z	-1.00	1.00	-1.00	-1.00
Pyramid	x	$-\frac{\sqrt{3}}{3}$	$-\frac{\sqrt{3}}{3}$	$2\frac{\sqrt{3}}{3}$	0.00
	y	-1.00	1.00	0.00	0.00
	z	$-\sqrt{\frac{2}{3}}$	$-\sqrt{\frac{2}{3}}$	$-\sqrt{\frac{2}{3}}$	$\sqrt{\frac{2}{3}}$
trapezoidal	x	-0.66	-0.66	0.66	0.66
	y	-1.00	1.00	2.00	-2.00
	z	-1.00	1.00	-1.00	-1.00

6.5 Error propagation and methodology

All measurements have associated errors and, when that measurement is used in a function to produce a result, the initial error is propagated through the function to the final outcome. Generally, in a function $g(x_1, x_2, ..., x_N)$ the theoretical propagation error of the variables $(x_1, x_2, ..., x_N)$ can be calculated through Equation (6.2) which represents the square of the quadratic sum of the partial derivatives of the function with respect to each variable x_n multiplied by its own uncertainty Δx_n.

$$\Delta x = \sqrt{\sum_{n=1}^{N} \left(\frac{\partial g}{\partial x_n} \Delta x_n \right)^2}. \tag{6.2}$$

The problem undertaken in this study, considering the uncertainty only in the antenna positioning, has twelve sources of error, one for each of the three coordinates in everyone of the four antennas. The analytic calculation of the propagated error in $(\hat{x}_s, \hat{y}_s, \hat{z}_s)$ in Equation (6.1) due the positioning of the antennas is complex and needs high computational efforts. Thus, the propagated error is evaluated and quantified through a Montecarlo analysis.

The procedure to obtain the results shown in Section 6.6 is divided in three steps. In the first one, a Gaussian error distribution in centimeters with zero mean and standard deviation ε, $N(0, \varepsilon^2)$, Equation (6.3), is added to the theoretical position of the antennas detailed in Table 6.1. The second step is the calculation of the TDoA (in seconds) between the position of the antennas with errors and the theoretical position of the source. The third step is to estimate the position of the source using the correct position of the antennas and the TDoA calculated in the step 2.

$$\begin{bmatrix} x_i' & y_i' & z_i' \end{bmatrix} = \begin{bmatrix} x_i & y_i & z_i \end{bmatrix} + \begin{bmatrix} \Delta_{x_i} & \Delta_{y_i} & \Delta_{z_i} \end{bmatrix} \tag{6.3}$$

The theoretical cartesian coordinates, (x_i, y_i, z_i), of i^{th} antenna $i = 1...4$, are modified including the positioning error defined by $\Delta_x, \Delta_y, \Delta_z$ where every Δ follows a $N(0, \varepsilon^2)$ Gaussian distribution yielding (x_i', y_i', z_i'). This is repeated 500 times to have a distribution of erroneous positions sufficiently high to have statistically reliable solutions.

Figure 6.2a shows an example of the x_1' variable (in meters) which already includes the error positioning Δ_x with a standard deviation of $\varepsilon = 1$ cm, in the coordinate x for antenna 1. Figure 6.2b shows the effect of the previous error in the TDoA (in nanoseconds) and, finally, Figure 6.2c shows the scattered points in the PD source location in presence of the previous errors.

The outcome of using 500 not so inaccurate positions of the antennas is a widely scattered cluster of possible positions for the source of PD.

6.6 Results and discussion

The analysis of the deviation of the shifted position of the source $(\hat{x}_s, \hat{y}_s, \hat{z}_s)$ respect the actual position (x_s, y_s, z_s) is better done in spherical coordinates since it easier to represent the error in distance and bearing from the actual source. Then, the source position is changed to (r, θ, φ) and all calculated possible positions to $(\hat{r}, \hat{\theta}, \hat{\varphi})$. The aim is to find out how the antenna arrays behave in all space directions and different distances in presence of antenna position uncertainties.

The first analysis is the one focused in the effect of the source direction. This analysis places the source at a fixed distance to the center of the array and in different bearings changing the elevation angle θ from $-90°$ to $90°$ and the azimuth φ from $0°$ to $360°$ both of them in steps of $1°$. This analysis covers the position of the source in spheres surrounding the antenna arrangement, thus, the results are presented in spherical graphs. The spheres are plotted in different color according the errors committed in the localization, the blue regions are insensitive to errors and the brown-red are very sensible to errors.

The second study is based on how the distance of the PD source to the antenna array affects in the source location error, it is expected that for greater distances, the error in the source location will be larger. The third study, it is based on how the magnitude of the uncertainty in the antennas positioning affects in the source location error. It is also expected that for large uncertainties in the antennas position, the error in the source location will be more considerable. These last two analyses are done for a preferred direction which was defined analyzing the spheres created in the firs analysis and choosing a direction low sensible to errors.

In every study, the errors $(\Delta\hat{r}, \Delta\hat{\theta}, \Delta\hat{\varphi})$ in the estimation of the variables $(\hat{r}, \hat{\theta}, \hat{\varphi})$ and the positive and negative deviation of the errors $(\pm\sigma_{\hat{r}}, \pm\sigma_{\hat{\theta}}, \pm\sigma_{\hat{\varphi}})$ are calculated.

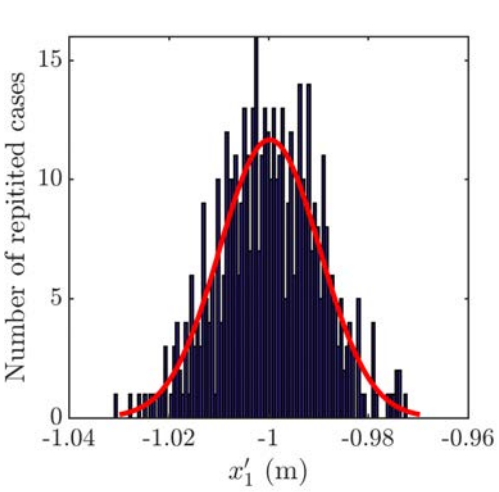

(a) Positioning errors, step 1

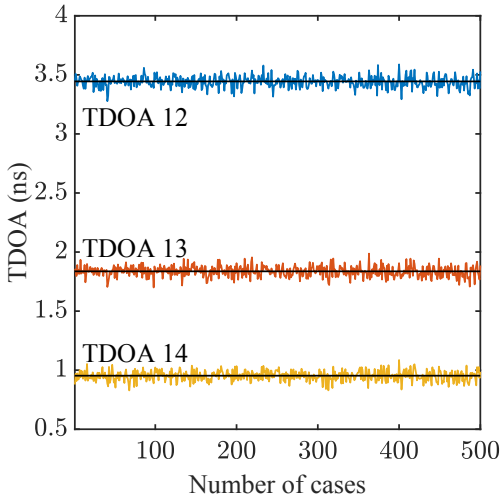

(b) TDoA, step 2

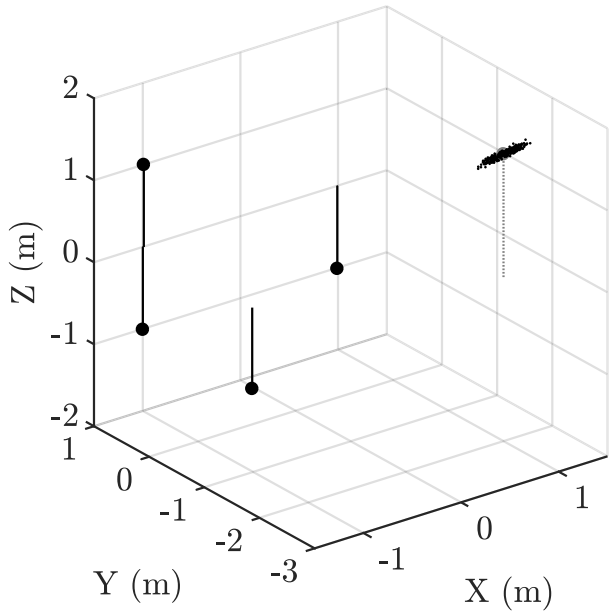

(c) Location, step 3

Figure 6.2: Effect of the errors in the three steps of the methodology of the study.

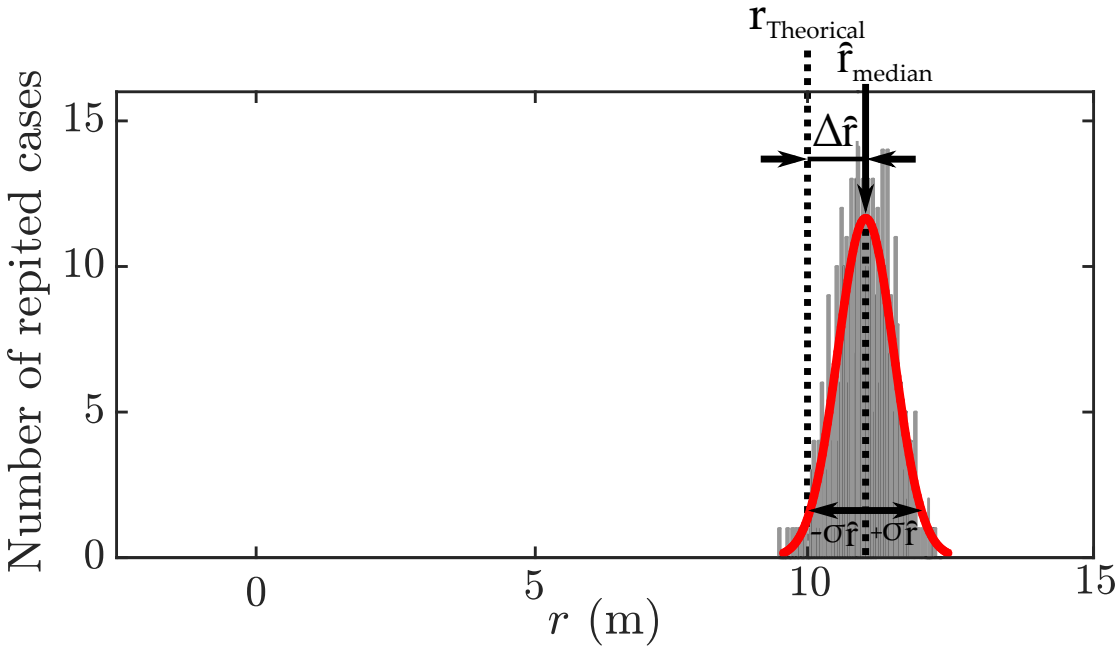

Figure 6.3: Graphic representation of the statistic variables analyzed in the study.

An example of the meaning of the variables is shown in Figure 6.3.

6.6.1 Analysis of errors in $\hat{r}$, distance estimation

This subsection analyzes the error and deviation in the distance of the calculated source $\hat{r}$ to the center of the antenna array in the presence of errors in the antenna positioning.

6.6.1.1 Directional analysis

The PD source positions are placed on a sphere with the center in the center of the antenna arrays and radius $r = 10$ m. The error introduced in the antennas positioning is the same for every array and follows a Gaussian distribution with zero mean and standard deviation $\varepsilon = 1$ cm. In Figures 6.4, 6.5, 6.6 and 6.7 the subfigures labeled with (a) and (b) represent the median error of the distances of the solutions in the cluster of possible positions to the center of the array, $\Delta\hat{r}$, and the graphics labeled with (c) and (d) represent the deviation of the error in the distances of the cluster to the center of the arrays with respect the median. Theoretically, the median $\Delta\hat{r}$ should be zero because the introduced errors are distributed as a Gaussian distribution with zero mean. However, the algorithms used to locate the source may not give an exact solution of the objective function as derived from the results represented in the next Figures.

The results are shown in Figure 6.4 for the antenna array forming a cartesian configuration, Figure 6.5 for a square configuration, Figure 6.6 for a pyramidal configuration

and Figure 6.7 for a trapezoidal configuration. These figures represent a sphere of radius 10 m with different hues corresponding to the median error or deviation of the median error for every bearing from the center of the antenna array; dark blue tones means low median error while dark red means high median error.

In general, every antenna arrangement shows that the median error is very close to zero in most directions but there are some dark red regions where $\Delta\hat{r}$ is shifted from zero so the algorithm is not converging to the exact solution. These critical directions represent rings around the directions formed by the antennas and the antennas array center, the rings can be interlaced among them. On the other side, the best directions are those which are far from any direction formed by the antennas and the antennas array center. The positive deviation in the median error $+\sigma_{\hat{r}}$, plots (c) and (d), is larger in the regions where $\Delta\hat{r}$ is shifted farther from zero. In the directions marked as blue in these plots, errors with a standard deviation of 1 cm in the positioning of the antennas can provoke deviations close to 1 m in the positioning of the PD source when this is 10 meters far.

A detailed analysis of the figures (c) and (d), finding which directions report lower $+\sigma_{\hat{r}}$, shows that cartesian array configuration has good behavior for elevations and azimuths $\theta \in (0°, 80°)$ and $\varphi \in (270°, 360°)$. The square layout has two narrow regions in $\theta \in (0°, 80°)$ and $\varphi \in (10°, 60°)$ and $\theta \in (0°, 80°)$ and $\varphi \in (190°, 260°)$. The pyramidal configuration has not any good directions compared with the other layouts because all antennas are uniformly distributed. The trapezoidal array has a very good region in the range $\theta \in (5°, 80°)$ and $\varphi \in (250°, 100°)$. These mentioned regions are the most noticeable regions but there are others as can be seen as a blue surfaces in the cited figures.

6.6.1.2 Distance analysis

This subsection analyzes the effect of the distance of the PD source to the center of the antenna array in the radius of the calculated position of the source, $\hat{r}$. For the sake of conciseness, the study is done choosing a direction for the cartesian configuration with $\theta = 10°$ and $\varphi = 330°$, and $\hat{r}$ is evaluated from $r = 0.5$ m to 15 m in steps of 0.5 m. In each case, the random error in the antennas positioning is applied 500 times to have a reliable statistical analysis, see Figure 6.8. As the source is located farther, the deviation of the median distance of the calculated source to the actual source position is larger. For instance, at a distance of $r = 9$ m, the median inaccuracy of the distance is $\Delta\hat{r} = 0.12$ m and the deviation of that inaccuracy is $+\sigma_{\hat{r}} = 1.10$ m and $-\sigma_{\hat{r}} = -1.03$ m.

6.6.1.3 Positioning error magnitude analysis

Finally, in this subsection the effect of the magnitude of the standard deviation in the positioning of the antennas, ε, on the median error of the distances of the solutions

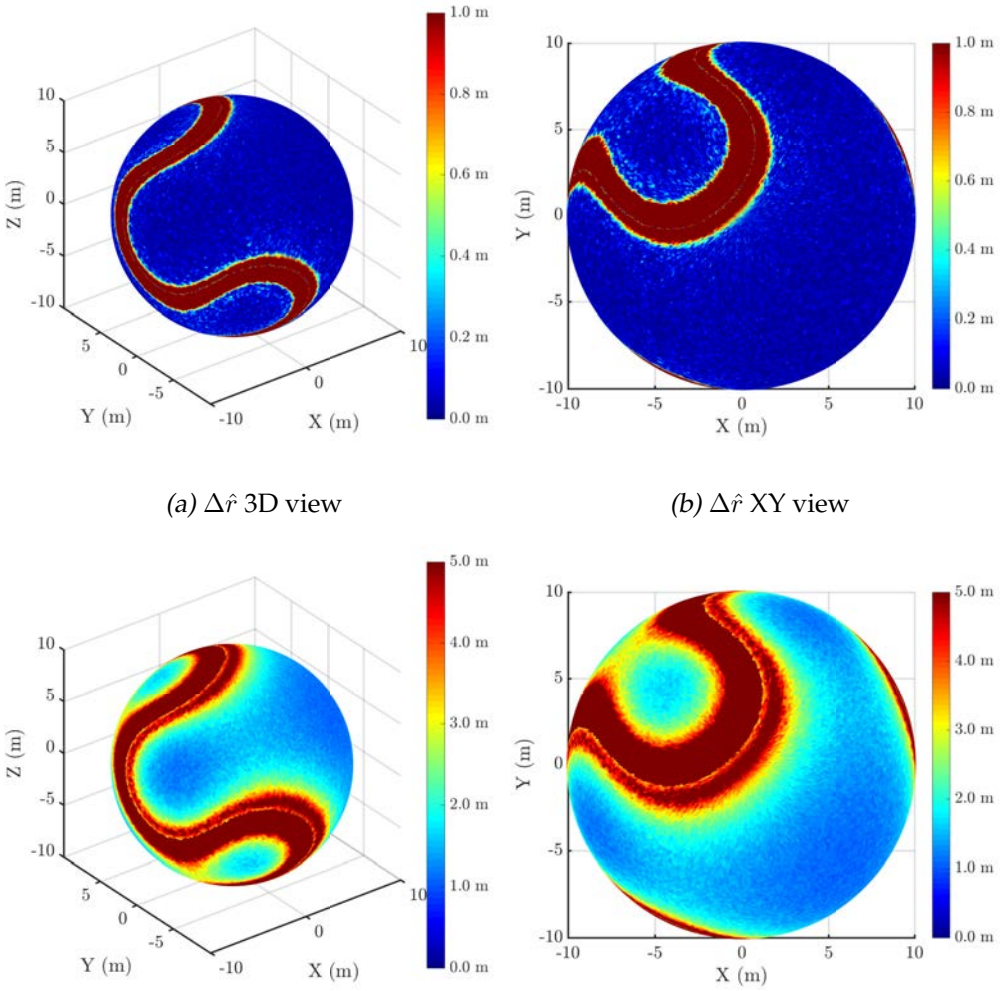

(a) $\Delta\hat{r}$ 3D view

(b) $\Delta\hat{r}$ XY view

(c) $+\sigma_{\hat{r}}$ 3D view

(d) $+\sigma_{\hat{r}}$ XY view

Figure 6.4: $\hat{r}$ median error $(\Delta\hat{r})$ and deviation $(+\sigma_{\hat{r}})$ with cartesian configuration over a sphere of radius 10 m and a standard deviation in the position of the antennas of $\varepsilon = 1$ cm.

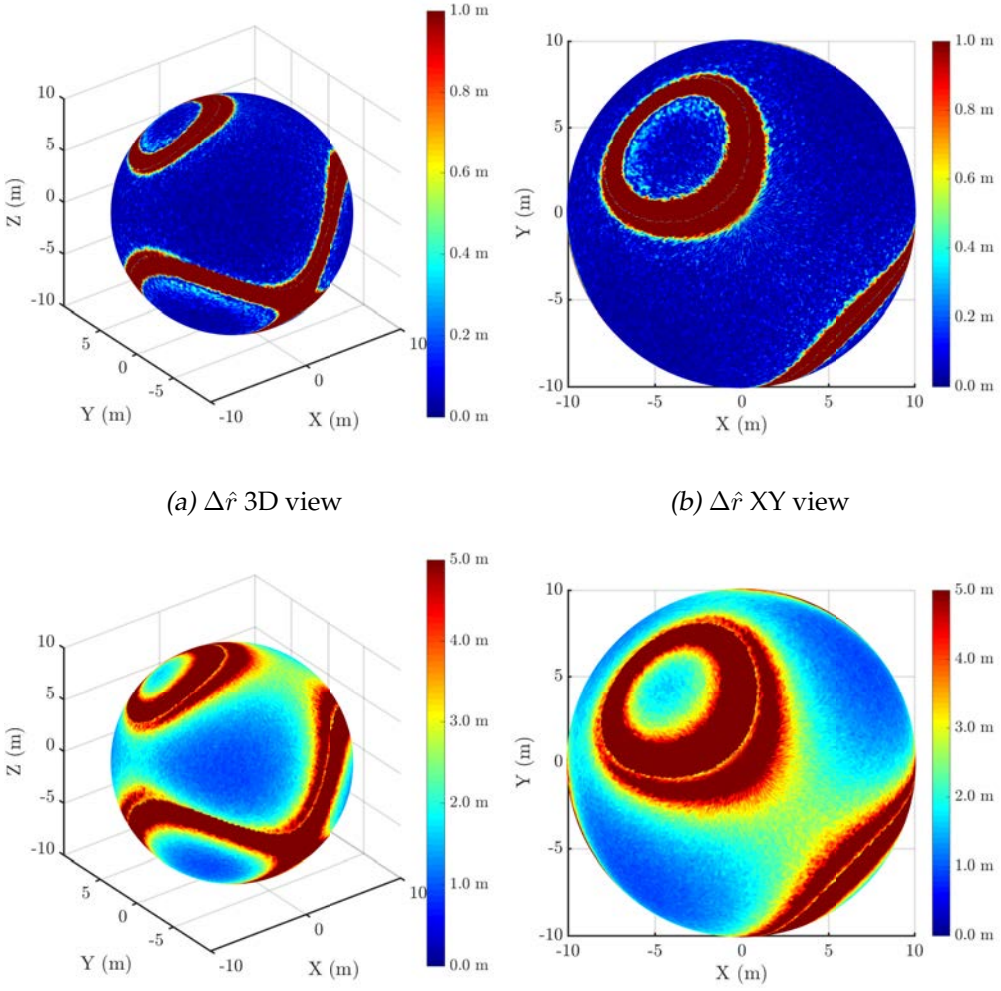

(a) $\Delta\hat{r}$ 3D view

(b) $\Delta\hat{r}$ XY view

(c) $+\sigma_{\hat{r}}$ 3D view

(d) $+\sigma_{\hat{r}}$ XY view

Figure 6.5: $\hat{r}$ median error $(\Delta\hat{r})$ and deviation $(+\sigma_{\hat{r}})$ with square configuration over a sphere of radius 10 m and a standard deviation in the position of the antennas of $\varepsilon = 1$ cm.

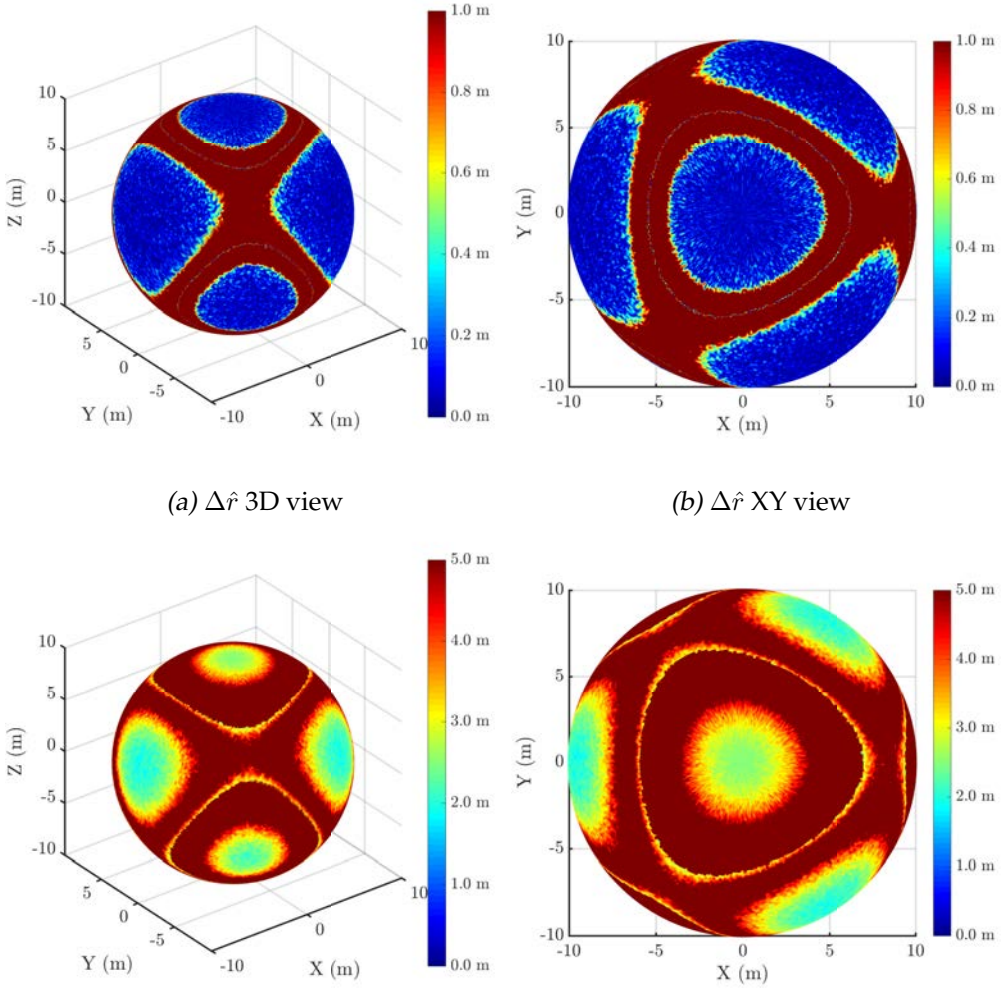

(a) $\Delta\hat{r}$ 3D view

(b) $\Delta\hat{r}$ XY view

(c) $+\sigma_{\hat{r}}$ 3D view

(d) $+\sigma_{\hat{r}}$ XY view

Figure 6.6: $\hat{r}$ median error $(\Delta\hat{r})$ and deviation $(+\sigma_{\hat{r}})$ with Pyramid configuration over a sphere of radius 10 m and a standard deviation in the position of the antennas of $\varepsilon = 1$ cm.

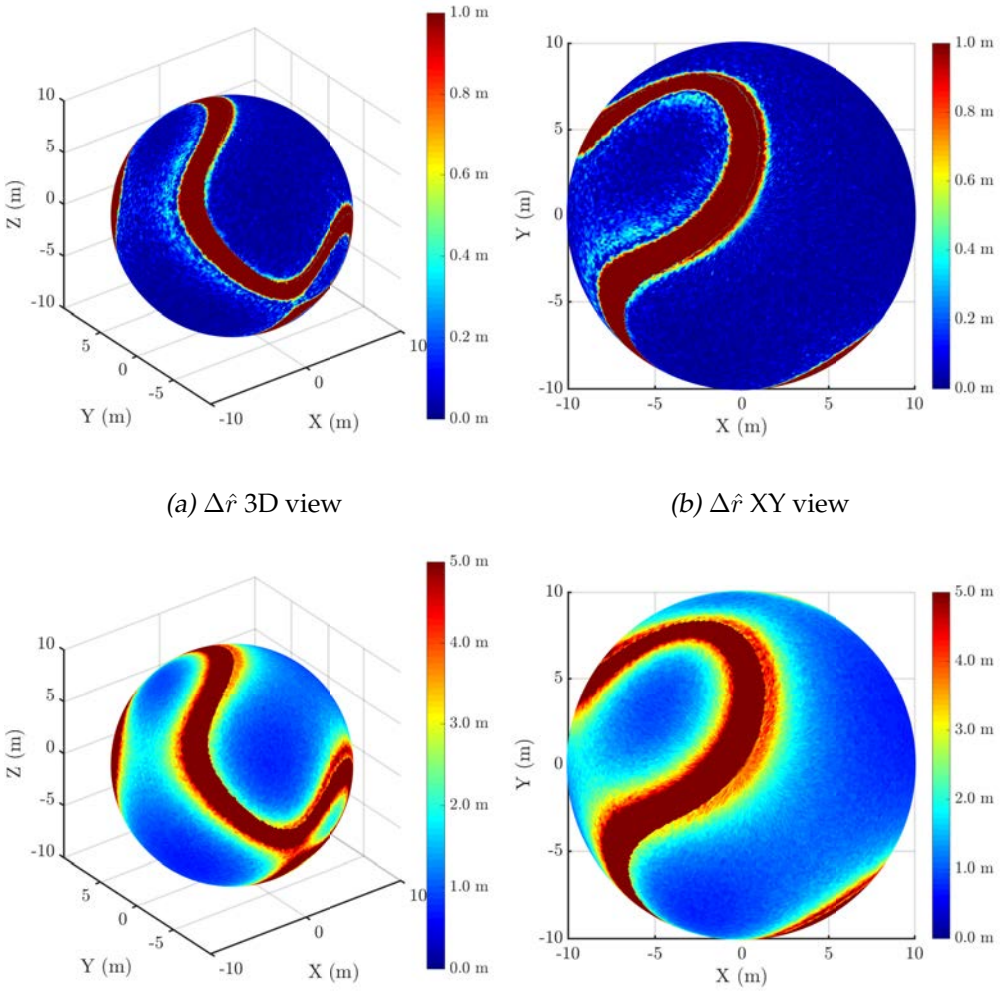

(a) $\Delta\hat{r}$ 3D view

(b) $\Delta\hat{r}$ XY view

(c) $+\sigma_{\hat{r}}$ 3D view

(d) $+\sigma_{\hat{r}}$ XY view

Figure 6.7: $\hat{r}$ median error $(\Delta\hat{r})$ and deviation $(+\sigma_{\hat{r}})$ with trapezoidal configuration over a sphere of radius 10 m and a standard deviation in the position of the antennas of $\varepsilon = 1$ cm.

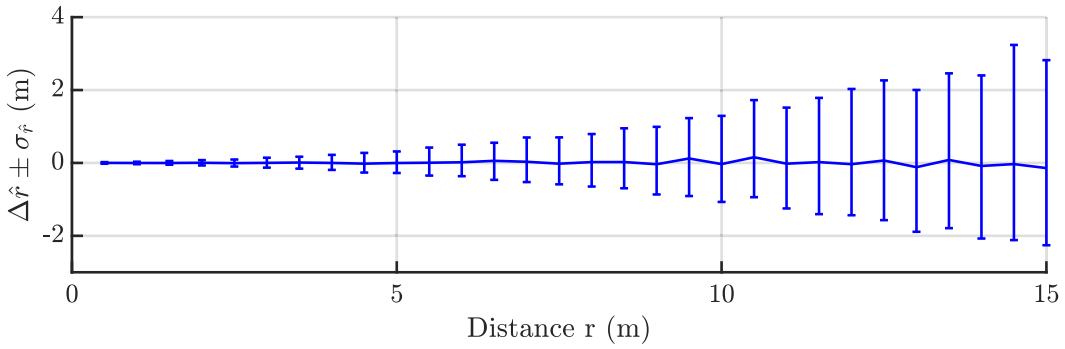

Figure 6.8: PD source distance influence in the radius error $(\Delta\hat{r} \pm \sigma_{\hat{r}})$ with a standard deviation in the position of the antennas of $\varepsilon = 1$ cm, for the cartesian configuration with $\theta = 10°$ and $\varphi = 330°$, and $\hat{r}$ is evaluated from $r = 0.5$ m to 15 m in steps of 0.5 m.

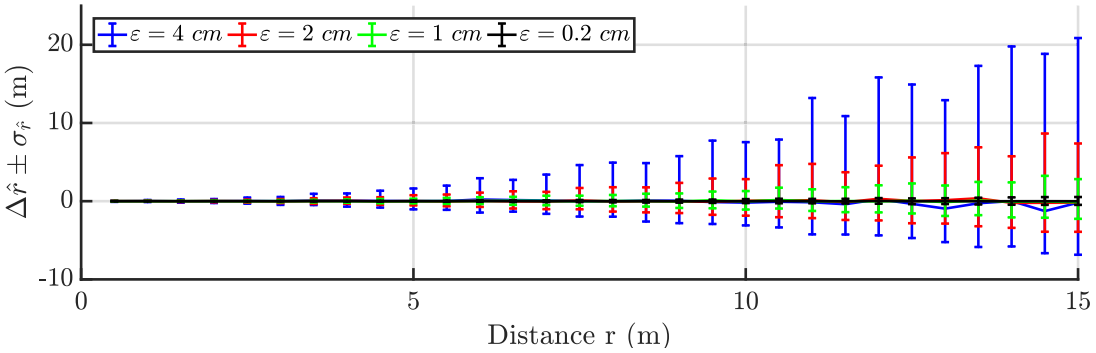

Figure 6.9: Influence in the distance error ($\Delta\hat{r} \pm \sigma_{\hat{r}}$) the standard deviation magnitude ε in the position of the antennas and the PD source distance. For the cartesian configuration with $\theta = 10°$ and $\varphi = 330°$, and $\hat{r}$ is evaluated from $r = 0.5$ m to 15 m in steps of 0.5 m.

Table 6.2: Positive and negative deviation of the propagated errors in the radius ($\pm\sigma_{\hat{r}}$) in meters regarding both the magnitude of the antenna positioning error and the distance of the source to the center of the antenna array.

(m)	$\varepsilon = 0.002$	$\varepsilon = 0.01$	$\varepsilon = 0.02$	$\varepsilon = 0.04$
$r = 0.5$	0.005 -0.004	0.021 -0.023	0.046 -0.047	0.090 -0.083
$r = 5$	0.062 -0.065	0.317 -0.273	0.752 -0.548	1.609 -1.060
$r = 10$	0.277 -0.227	1.323 -1.038	2.767 -1.904	7.735 -2.911
$r = 15$	0.542 -0.461	2.961 -2.116	7.563 -3.732	21.059 -6.654

in the cluster of possible positions to the center of the array, $\Delta\hat{r}$ is analyzed. Four error magnitudes are considered: $\varepsilon = \{0.2, 1, 2, 4\}$ cm, and, as in the previous subsection, the source is placed at distances from $r = 0.5$ m to 15 meters in steps of 0.5 m. Figure 6.9 shows the results. As expected, for large deviations in the position of the antennas, large errors, $\Delta\hat{r}$, in the position of the source are obtained. Moreover, the distribution of the dispersion of $\Delta\hat{r}$, $\sigma_{\hat{r}}$, is biased to positive values though the original distribution in the positioning error was Gaussian. Table 6.2 shows the propagated error in the radius increases with larger positioning errors and with farther source distances.

6.6.2 Analysis of errors in $\hat{\theta}$, elevation angle estimation

The analysis is also undertaken for errors in the elevation angle estimation, $\hat{\theta}$, of the location of the estimated position of the source of PD in presence of errors in the antennas positioning. This variable is the angle between the direction defined by the source position and the center of the array and plane $XY = 0$.

6.6.2.1 Directional analysis

The variability of $\hat{\theta}$ regarding the direction of the PD source with respect to the center of antenna array is analyzed in this subsection. The cases studied are the same as in Section 6.6.1. Graphics (a) and (b) in Figures 6.10, 6.11, 6.12 and 6.13 represent the median of $\Delta\hat{\theta}$, the difference between the elevation of the possible solutions to the position of the source and the elevation of the actual position, respectively. Graphics (c) and (d) represent the positive deviation of $\Delta\hat{\theta}$, $+\sigma_{\hat{\theta}}$. As in the radius analysis, the median $\Delta\hat{\theta}$ should be equal to zero because the distribution of the introduced errors is a Gaussian $(0, \varepsilon^2)$. Again, the deviation of $\Delta\hat{\theta}$ from 0 is due to the convergence of the algorithms to a solution close to the exact one.

The results are shown in Figure 6.10 for the cartesian configuration, Figure 6.11 for the square configuration, Figure 6.12 for the pyramidal one and Figure 6.13 for the trapezoidal one. As in the case of the distance, every configuration shows that $\Delta\hat{\theta}$ is very accurate for most bearings but there are some regions that should be avoided because the the median is slightly shifted from the actual value. The directions where the elevation has the poorest behaviour are those where the distance, $\hat{r}$, had also bad behaviour though $\Delta\hat{\theta}$ is low, under 5°. Furthermore, the poorest regions and their borders also have the worst dispersion of $\Delta\hat{\theta}$. Nevertheless, the deviations from the median are very small and the effect of the position of the antennas is almost negligible in a directional analysis involving the parameter Theta, especially in the case of the cartesian array.

6.6.2.2 Distance analysis

The study continues with the effect of the distance of the PD source to the center of the antenna array in the median of the differences of the elevations of the possible solutions and the elevation of the actual position of the source, $\Delta\hat{\theta}$. The analysis is made with the same set up than in Subsection 6.6.1.2. Figure 6.14 shows that, when the source is farther than 4 meters, the deviation $\pm\sigma_{\hat{\theta}}$ remains stable and it is independent of the distance to the array. Therefore, the distribution of the deviation is not biased to positive nor negative values. This is different from Figure 6.9 where there was a clear bias of the deviation of the distances to positive values although the distribution of the errors in the positioning was Gaussian. In the case of the elevation angle, the algorithms propagate the error in the position of the antennas to another Gaussian as long as the distance is sufficiently large compared to the size of the array, in this study 4 meters.

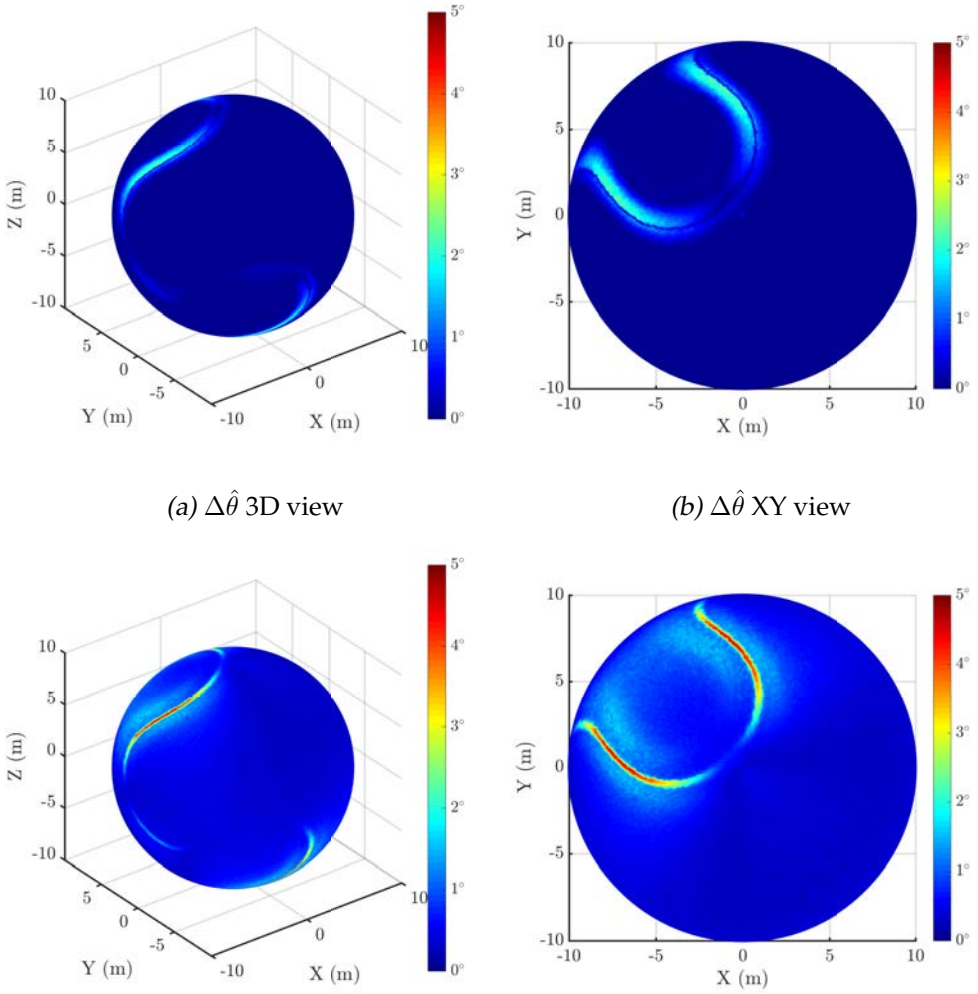

(a) $\Delta\hat{\theta}$ 3D view

(b) $\Delta\hat{\theta}$ XY view

(c) $+\sigma_{\hat{\theta}}$ 3D view

(d) $+\sigma_{\hat{\theta}}$ XY view

Figure 6.10: $\hat{\theta}$ median error $(\Delta\hat{\theta})$ and deviation $(+\sigma_{\hat{\theta}})$ with cartesian configuration over a sphere of radius 10 m and a standard deviation in the position of the antennas of $\varepsilon = 1$ cm.

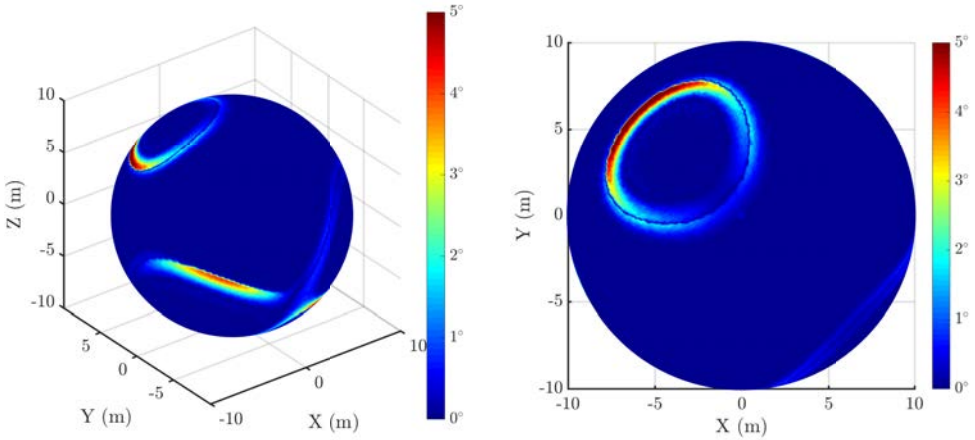

(a) $\Delta\hat{\theta}$ 3D view

(b) $\Delta\hat{\theta}$ XY view

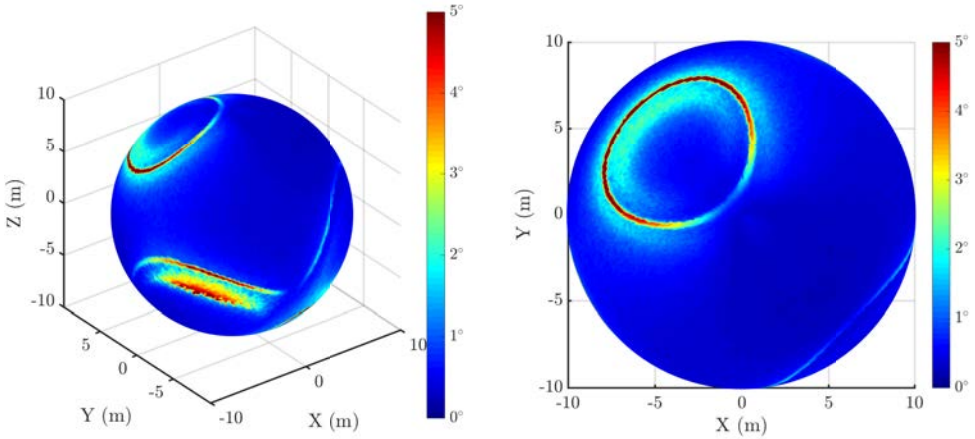

(c) $+\sigma_{\hat{\theta}}$ 3D view

(d) $+\sigma_{\hat{\theta}}$ XY view

Figure 6.11: $\hat{\theta}$ median error $(\Delta\hat{\theta})$ and deviation $(+\sigma_{\hat{\theta}})$ with square configuration over a sphere of radius 10 m and a standard deviation in the position of the antennas of $\varepsilon = 1$ cm.

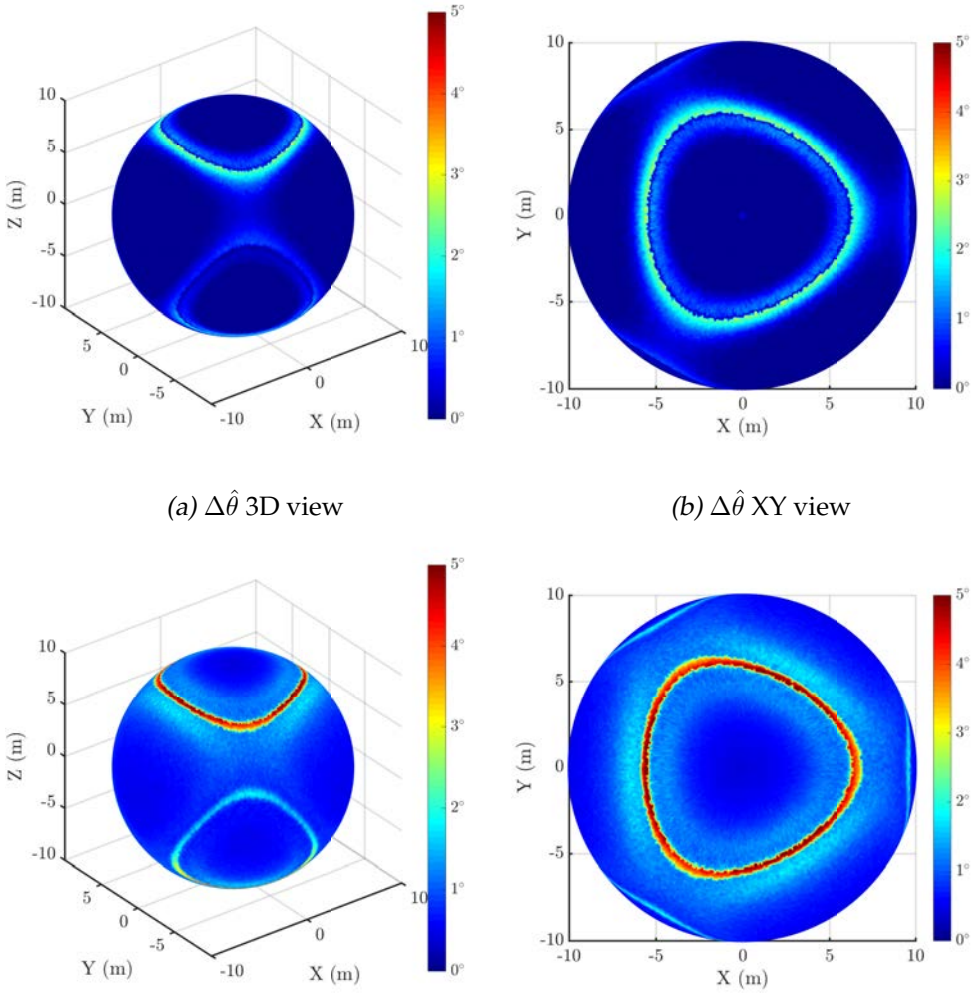

(a) $\Delta\hat{\theta}$ 3D view

(b) $\Delta\hat{\theta}$ XY view

(c) $+\sigma_{\hat{\theta}}$ 3D view

(d) $+\sigma_{\hat{\theta}}$ XY view

Figure 6.12: $\hat{\theta}$ median error $(\Delta\hat{\theta})$ and deviation $(+\sigma_{\hat{\theta}})$ with Pyramid configuration over a sphere of radius 10 m and a standard deviation in the position of the antennas of $\varepsilon = 1$ cm.

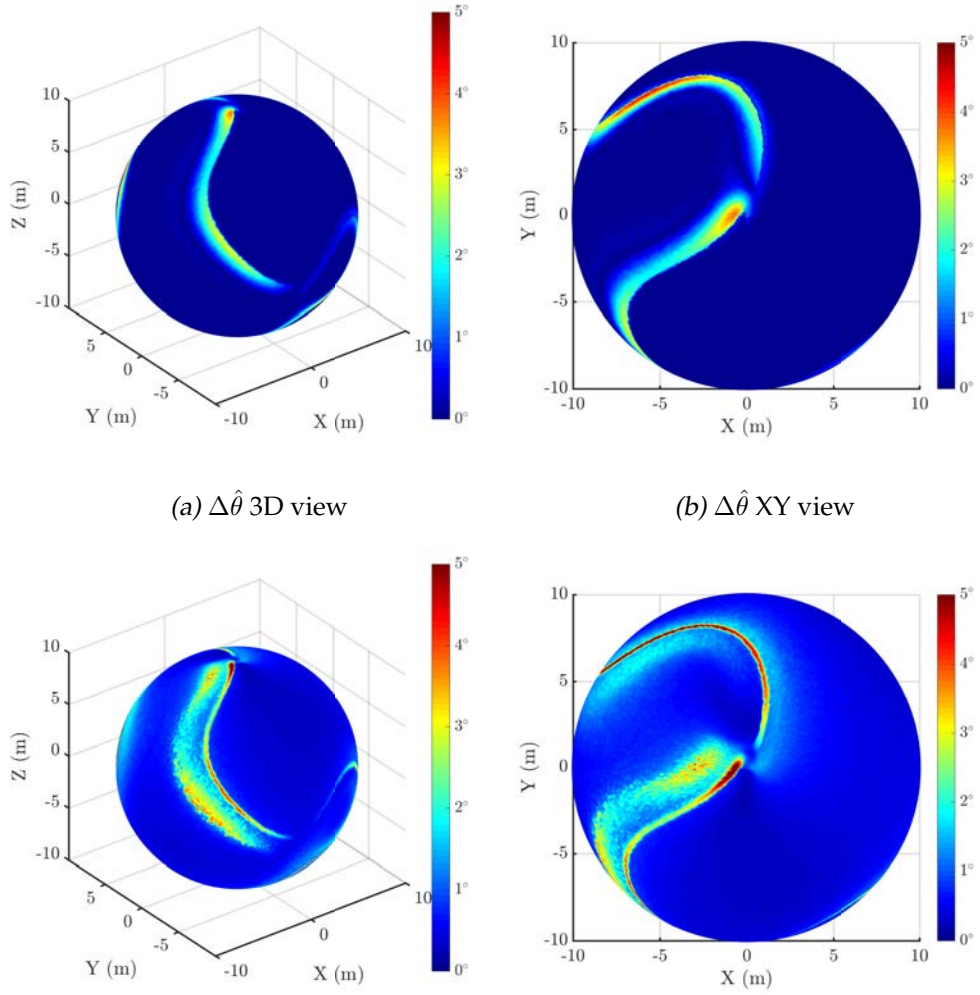

(a) $\Delta\hat{\theta}$ 3D view

(b) $\Delta\hat{\theta}$ XY view

(c) $+\sigma_{\hat{\theta}}$ 3D view

(d) $+\sigma_{\hat{\theta}}$ XY view

Figure 6.13: $\hat{\theta}$ median error $(\Delta\hat{\theta})$ and deviation $(+\sigma_{\hat{\theta}})$ with trapezoidal configuration over a sphere of radius 10 m and a standard deviation in the position of the antennas of $\varepsilon = 1$ cm.

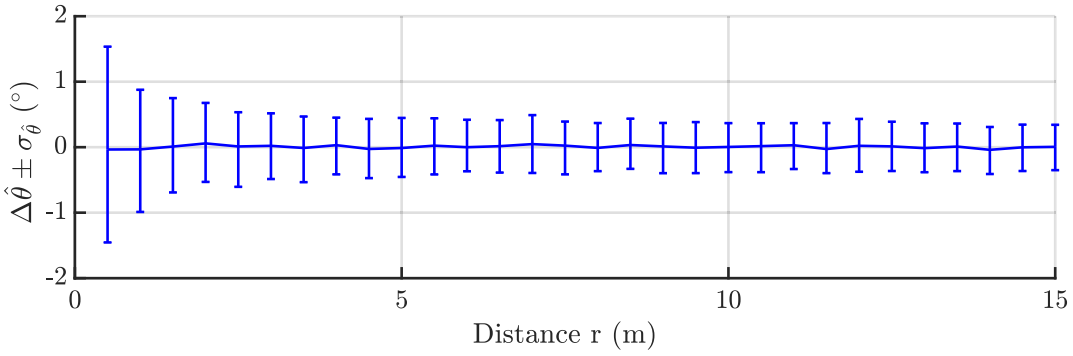

Figure 6.14: Influence of the distance to the position of the PD source in the error of the elevation angle, $\Delta\hat{\theta} \pm \sigma_{\hat{\theta}}$, with a standard deviation in the position of the antennas of $\varepsilon = 1$ cm. for the cartesian configuration with $\theta = 10°$ and $\varphi = 330°$, and $\hat{\theta}$ is evaluated from $r = 0.5$ m to 15 m in steps of 0.5 m.

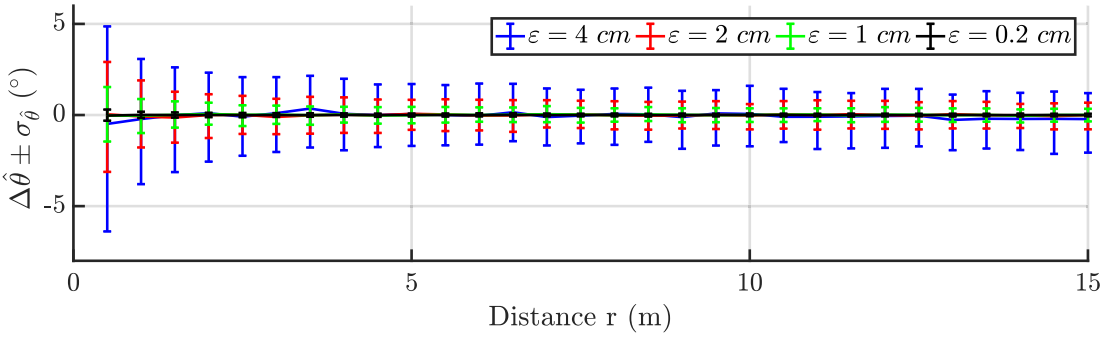

Figure 6.15: Influence in the elevation angle error $(\Delta\hat{\theta} \pm \sigma_{\hat{\theta}})$ the standard deviation magnitude ε in the position of the antennas and the PD source distance. For the cartesian configuration with $\theta = 10°$ and $\varphi = 330°$, and $\hat{\theta}$ is evaluated from $r = 0.5$ m to 15 m in steps of 0.5 m.

Table 6.3: Positive and negative deviation $(\pm\sigma_{\hat{\theta}})$ of the propagated errors in the elevation angle regarding both the magnitude of the antenna positioning error and the distance of the source from the antennas array.

$(\pm\sigma_{\hat{\theta}})$	$\varepsilon = 0.2cm$	$\varepsilon = 1cm$	$\varepsilon = 2cm$	$\varepsilon = 4cm$
$r = 0.5\ m$	$0.33°$ $-0.28°$	$1.57°$ $-1.42°$	$2.87°$ $-3.16°$	$5.35°$ $-5.90°$
$r = 5\ m$	$0.08°$ $-0.09°$	$0.46°$ $-0.44°$	$0.77°$ $-0.88°$	$1.64°$ $-1.75°$
$r = 10\ m$	$0.08°$ $-0.07°$	$0.36°$ $-0.38°$	$0.63°$ $-0.76°$	$1.54°$ $-1.77°$
$r = 15\ m$	$0.07°$ $-0.07°$	$0.34°$ $-0.36°$	$0.68°$ $-0.78°$	$1.43°$ $-1.84°$

6.6.2.3 Positioning error magnitude analysis

Finally, the effect of the magnitude of error in the positioning of the antennas, ε, in the median of the differences of the elevation angles $\Delta\hat{\theta}$. Again, four magnitude errors are analyzed $\varepsilon = \{0.2, 1, 2, 4\}$ cm. Figure 6.15 shows that as the positioning error is raised, the deviation of the median error in the elevation angle, $\Delta\hat{\theta}$ is larger. In any case when the source is farther than 4 meters, the $\pm\sigma_{\hat{\theta}}$ is almost constant, see Table 6.3. This result is interesting because it implies that when the distance to the array is sufficiently high, the error in the elevation angle remains constant and depends only on the uncertainty of the positions of the antennas, whereas, when the source is close to the array, the deviation of the possible solutions to its position is larger than the uncertainty of the positions of the antennas.

6.6.3 Analysis of errors in $\hat{\varphi}$, azimuth angle estimation

This subsection contains the analysis of the azimuth angle estimation, $\hat{\varphi}$, in PD source location with errors in positioning of the antennas. This angle represents the

Table 6.4: Positive and negative deviation of the propagated errors in the azimuth angle variable $(\pm\sigma_{\hat{\varphi}})$ in degrees regarding both the magnitude of the antenna positioning error and the distance of the source from the antennas array.

$(\pm\sigma_{\hat{\varphi}})$	$\varepsilon = 0.2cm$	$\varepsilon = 1cm$	$\varepsilon = 2cm$	$\varepsilon = 4cm$
$r = 0.5\ m$	$0.22°$ $-0.22°$	$1.26°$ $-0.94°$	$2.47°$ $-2.27°$	$5.17°$ $-5.18°$
$r = 5\ m$	$0.06°$ $-0.06°$	$0.30°$ $-0.33°$	$0.59°$ $-0.63°$	$1.61°$ $-1.27°$
$r = 10\ m$	$0.06°$ $-0.06°$	$0.31°$ $-0.30°$	$0.59°$ $-0.63°$	$1.40°$ $-1.24°$
$r = 15\ m$	$0.06°$ $-0.06°$	$0.30°$ $-0.27°$	$0.58°$ $-0.61°$	$1.37°$ $-1.31°$

orientation in the plane $XY = 0$.

6.6.3.1 Directional analysis

The study is repeated following the same steps as in the other two analyses. The results in Figure 6.16 are for the cartesian configuration, Figure 6.17 for the square array, Figure 6.18 for pyramidal arrangement and Figure 6.19 for the trapezoidal layout. Graphics (a) and (b) in these figures represent the median $\Delta\hat{\varphi}$ and the graphics (c) and (d) the positive $\Delta\hat{\varphi}$ deviation, $+\sigma_{\hat{\varphi}}$. The conclusions are similar to the other two cases: all configurations show accurate values for medians $\Delta\hat{\varphi}$ but there are some directions to avoid. The worst bearings have a median lower than $5°$ as in the case of the elevation angle. On the other hand, the deviation $\sigma_{\hat{\varphi}}$ is already considerable in the worst directions but close to the poles is greater since, at it would be expected, it is more difficult to determine the azimuth when the elevation is close to the maxima.

6.6.3.2 Distance analysis

The effect of the changing, r, the distance of the PD source to the center of the antenna array, in the median of the error of azimuth $\Delta\hat{\varphi}$ is similar to the previous distance analyses over $\Delta\hat{\theta}$. Figure 6.20 shows that the deviation of the median stable around $\pm 0.3°$ for distances larger that 4 m.

6.6.3.3 Positioning error magnitude analysis

Figure 6.21 shows the results when varying the magnitude of the error introduced in the positions of the antennas. The error in the azimuth angle raises as the error in the positioning is larger. When the source is farther than 4 meters to the center of the array, the deviation of the median is constant. Table 6.4 shows the magnitude of, $(\sigma_{\hat{\varphi}})$, the deviations in $\Delta\hat{\varphi}$.

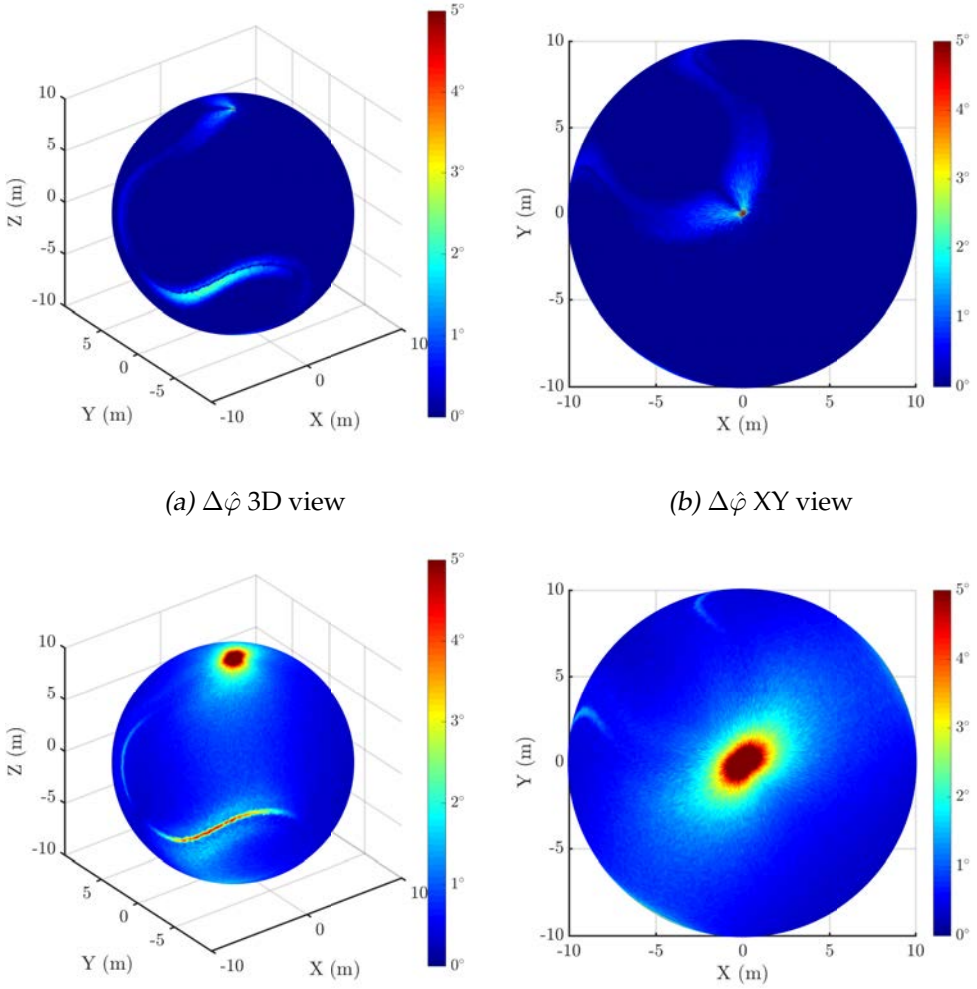

(a) $\Delta\hat{\varphi}$ 3D view

(b) $\Delta\hat{\varphi}$ XY view

(c) $+\sigma_{\hat{\varphi}}$ 3D view

(d) $+\sigma_{\hat{\varphi}}$ XY view

Figure 6.16: $\hat{\varphi}$ median error $(\Delta\hat{\varphi})$ and deviation $(+\sigma_{\hat{\varphi}})$ with cartesian configuration over a sphere of radius 10 m and a standard deviation in the position of the antennas of $\varepsilon = 1$ cm.

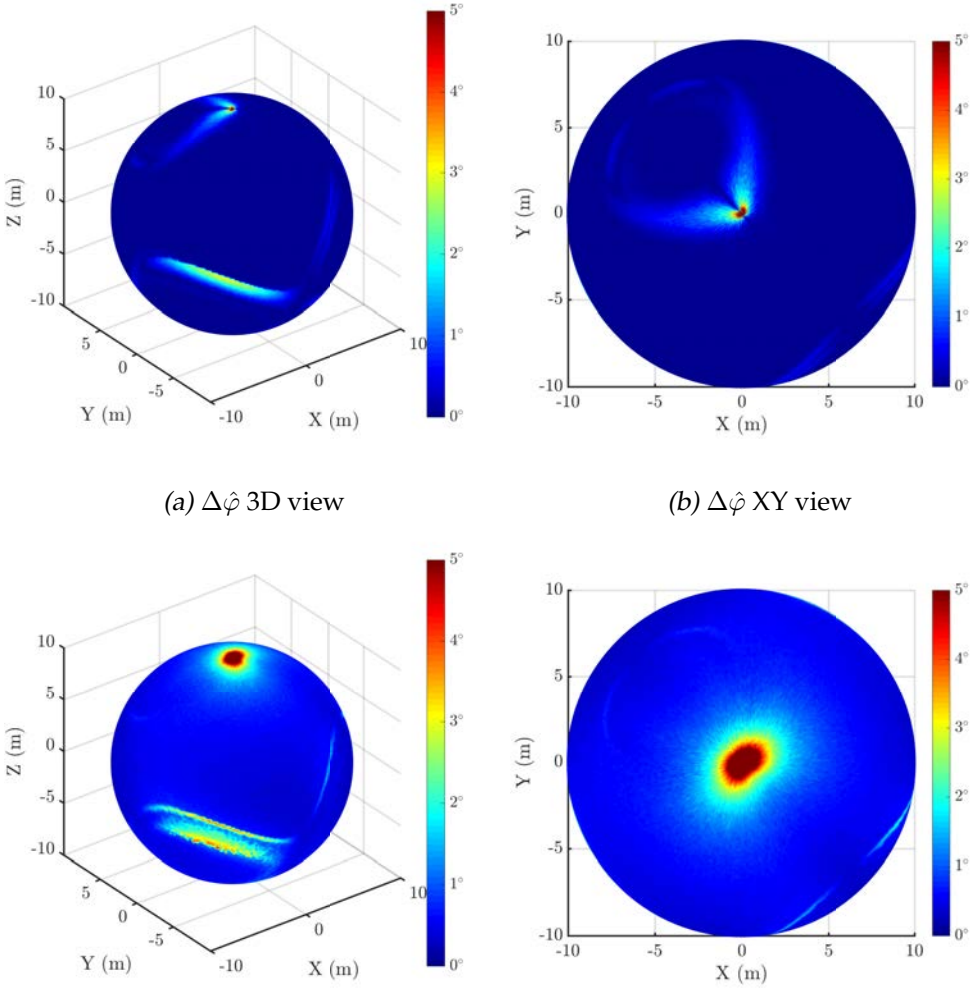

(a) $\Delta\hat{\varphi}$ 3D view

(b) $\Delta\hat{\varphi}$ XY view

(c) $+\sigma_{\hat{\varphi}}$ 3D view

(d) $+\sigma_{\hat{\varphi}}$ XY view

Figure 6.17: $\hat{\varphi}$ median error $(\Delta\hat{\varphi})$ and deviation $(+\sigma_{\hat{\varphi}})$ with square configuration over a sphere of radius 10 m and a standard deviation in the position of the antennas of $\varepsilon = 1$ cm.

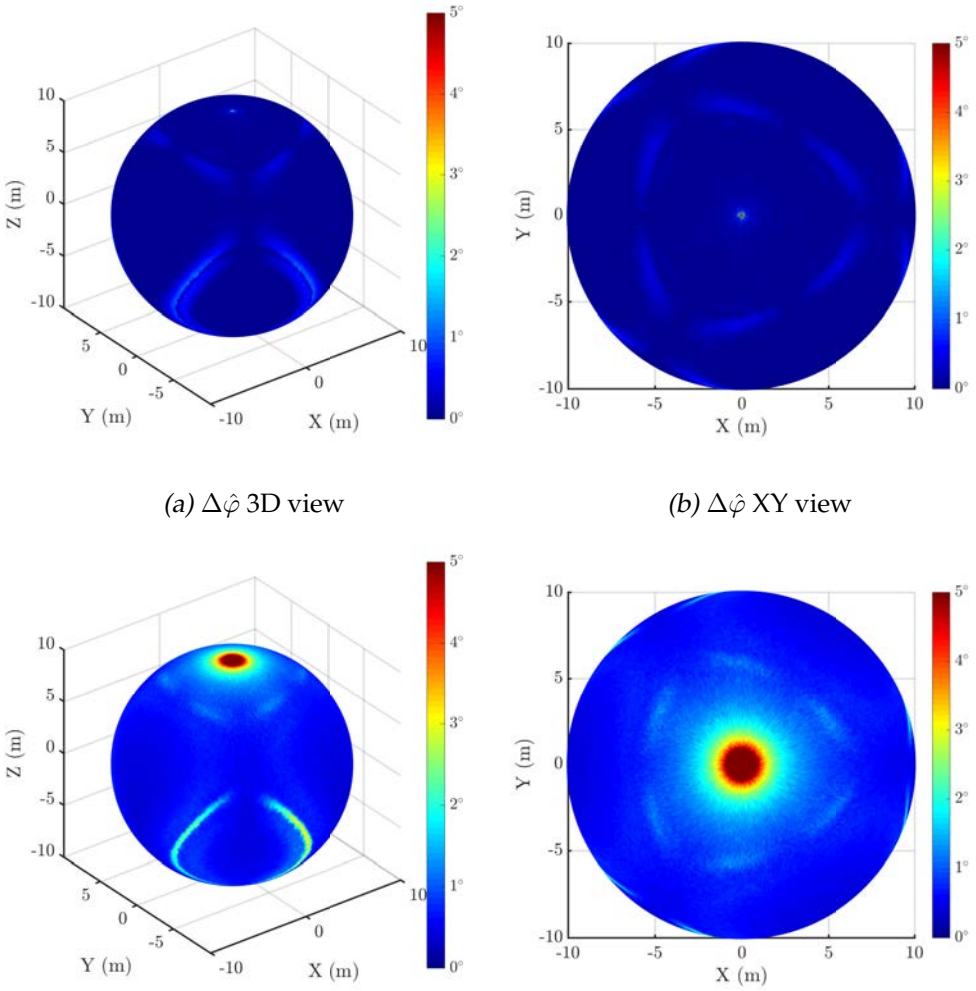

(a) $\Delta\hat{\varphi}$ 3D view

(b) $\Delta\hat{\varphi}$ XY view

(c) $+\sigma_{\hat{\varphi}}$ 3D view

(d) $+\sigma_{\hat{\varphi}}$ XY view

Figure 6.18: $\hat{\varphi}$ median error $(\Delta\hat{\varphi})$ and deviation $(+\sigma_{\hat{\varphi}})$ with Pyramid configuration over a sphere of radius 10 m and a standard deviation in the position of the antennas of $\varepsilon = 1$ cm.

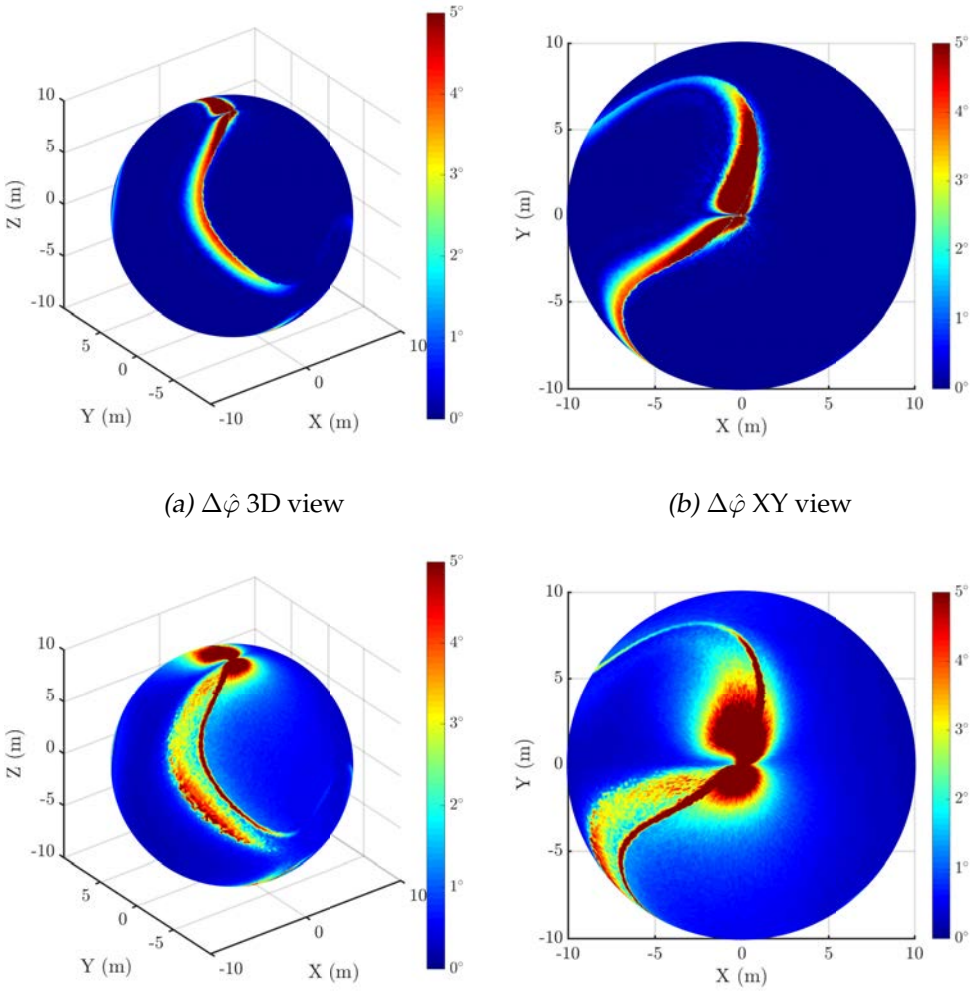

(a) $\Delta\hat{\varphi}$ 3D view

(b) $\Delta\hat{\varphi}$ XY view

(c) $+\sigma_{\hat{\varphi}}$ 3D view

(d) $+\sigma_{\hat{\varphi}}$ XY view

Figure 6.19: $\hat{\varphi}$ median error $(\Delta\hat{\varphi})$ and deviation $(+\sigma_{\hat{\varphi}})$ with trapezoidal configuration over a sphere of radius 10 m and a standard deviation in the position of the antennas of $\varepsilon = 1$ cm.

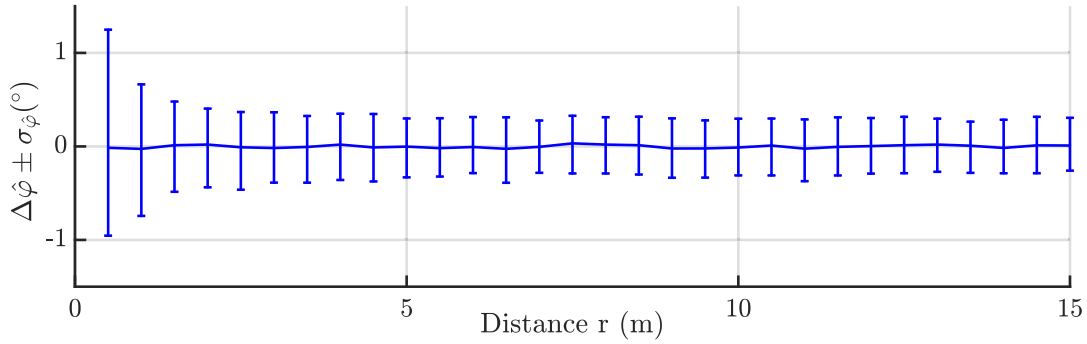

Figure 6.20: PD source distance influence in the azimuth angle error $(\Delta\hat{\varphi} \pm \sigma_{\hat{\varphi}})$ with a standard deviation in the position of the antennas of $\varepsilon = 1$ cm. for the cartesian configuration with $\theta = 10°$ and $\varphi = 330°$, and $\hat{\varphi}$ is evaluated from $r = 0.5$ m to 15 m in steps of 0.5 m.

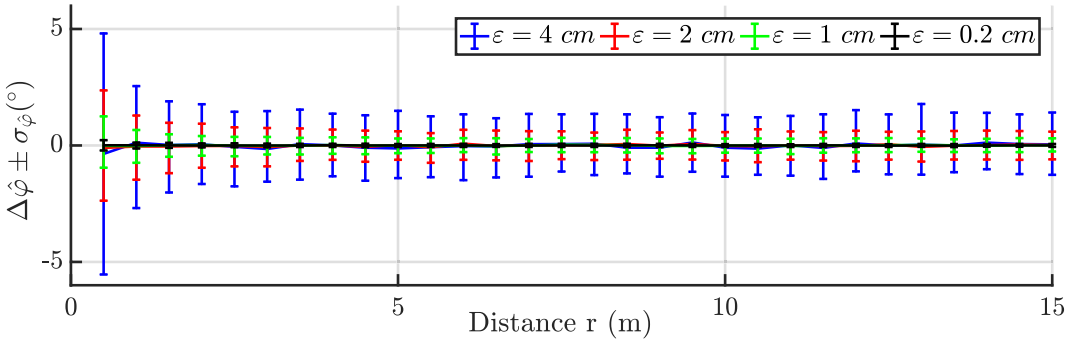

Figure 6.21: Influence in the azimuth angle error ($\Delta\hat{\varphi} \pm \sigma_{\hat{\varphi}}$) the standard deviation magnitude ε in the position of the antennas and the PD source distance. For the cartesian configuration with $\theta = 10°$ and $\varphi = 330°$, and $\hat{\varphi}$ is evaluated from $r = 0.5$ m to 15 m in steps of 0.5 m.

6.7 Conclusions

As a general advice, small errors in the positioning of the antennas can provoke large errors in the estimated position of the source, being the estimation of the distance, $\hat{r}$, the variable most affected by the errors. Then, it is of great interest be aware of the error committed in the antennas positioning to be able to estimate the error committed in the localization. The error in the distance estimation, $\Delta\hat{r}$, increases directly with the distance of the emitter. The most favorable case is when the PD source is surrounded by antennas, in this case, the errors in the localization and their deviations are very small. In the cases when the source is far from the antennas array, shift of few centimeters in the positioning of the antennas can be propagated in meters of error in the estimation of the distance of the source to the array. The elevation and azimuth errors and deviations are low in every case, this implies that the source direction can be calculated accurately, independently of the errors. It implies that when the distance to the array is sufficiently high, the error in the elevation angle remains constant and depends only on the uncertainty of the positions of the antennas.

The error in the radius estimation, $\Delta\hat{r}$, has a clear bias of the deviation of the distances to positive values. In the case of the elevation and azimuth angles, the algorithms propagate the error in the position of the antennas to a Gaussian distribution as long as the distance is sufficiently large compared to the size of the array, in this study 4 meters.

Applying the same errors to different antenna layouts, it can be seen that every configuration has some directions more or less sensible to errors. In general, it can be concluded that the preferred directions of any array are those where the antennas have more aperture. Comparing the preferred directions of each antenna array, it can be seen how some configurations have better behaviour than others. The trapezoidal and the cartesian have a good directions but the trapezoidal is less sensible to errors since it has larger antenna aperture than the cartesian.

In this paragraph are detailed some advices to deploy the antennas to locate PD sources. The positions of the antennas have to be measured with the maximum resolution possible to avoid uncertainties in the PD source location. The antennas have to be placed as close as possible to the PD source or even enclose it if it is possible. Although the greatest errors in the direction estimation $(\hat{\theta}, \hat{\varphi})$ take place in the positions with small r, the total localization error in meters is smaller in these regions because the lowest error in the distance estimation, $\hat{r}$, is there. To place antennas in the direction between the antenna array and the PD source has to be avoided. More over, the maximum aperture of the antenna array has to be oriented to the possible PD source position in order to reduce the influence of errors.

6.8 Bibliography

[1] R. M. Harris and M. D. Judd. "Locating Partial Discharge Using Particle Swarm Optimisation". In: *Universities' Power Engineering Conference (UPEC), Proceedings of 2011 46th International*. Sept. 2011, pp. 1–6 (cit. on p. 149).

[2] G. Robles, J. M. Fresno, and J. M. Martínez-Tarifa. "Separation of Radio-Frequency Sources and Localization of Partial Discharges in Noisy Environments". en. In: *Sensors* 15.5 (Apr. 2015), pp. 9882–9898. DOI: 10.3390/s150509882. URL: http://www.mdpi.com/1424-8220/15/5/9882 (cit. on p. 149).

[3] Y. T. Chan and K. C. Ho. "A simple and efficient estimator for hyperbolic location". In: *IEEE Transactions on Signal Processing* 42.8 (Aug. 1994), pp. 1905–1915. ISSN: 1053-587X. DOI: 10.1109/78.301830 (cit. on p. 149).

[4] G. Robles, J. M. Fresno, M. Sánchez-Fernández, et al. "Antenna Deployment for the Localization of Partial Discharges in Open-Air Substations". en. In: *Sensors* 16.4 (Apr. 2016), p. 541. DOI: 10.3390/s16040541. URL: http://www.mdpi.com/1424-8220/16/4/541 (cit. on p. 149).

[5] P. J. Moore, I. E. Portugues, and I. A. Glover. "Radiometric location of partial discharge sources on energized high-Voltage plant". In: *IEEE Transactions on Power Delivery* 20.3 (July 2005), pp. 2264–2272. ISSN: 0885-8977. DOI: 10.1109/TPWRD.2004.843397 (cit. on p. 149).

[6] H. Hou, G. Sheng, and X. Jiang. "Robust Time Delay Estimation Method for Locating UHF Signals of Partial Discharge in Substation". In: *IEEE Transactions on Power Delivery* 28.3 (July 2013), pp. 1960–1968. ISSN: 0885-8977. DOI: 10.1109/TPWRD.2013.2262315 (cit. on p. 149).

[7] J. Xu, M. Ma, and C. L. Law. "Cooperative angle-of-arrival position localization". In: *Measurement* 59 (Jan. 2015), pp. 302–313. ISSN: 0263-2241. DOI: 10.1016/j.measurement.2014.09.023. URL: http://www.sciencedirect.com/science/article/pii/S0263224114004035 (cit. on pp. 149, 150).

[8] A. Tungkanawanich, Z. I. Kawasaki, J. Abe, et al. "Location of partial discharge source on distribution line by measuring emitted pulse-train electromagnetic waves". In: 4 (2000), 2453–2458 vol.4. DOI: 10.1109/PESW.2000.847194 (cit. on p. 149).

[9] B. G. Stewart, A. Nesbitt, and L. Hall. "Triangulation and 3D location estimation of RFI and Partial Discharge sources within a 400kV substation". In: *2009 IEEE Electrical Insulation Conference*. May 2009, pp. 164–168. DOI: 10.1109/EIC.2009.5166337 (cit. on p. 149).

[10] H. Hou, G. Sheng, and X. Jiang. "Localization Algorithm for the PD Source in Substation Based on L-Shaped Antenna Array Signal Processing". In: *IEEE Transactions on Power Delivery* 30.1 (Feb. 2015), pp. 472–479. ISSN: 0885-8977. DOI: 10.1109/TPWRD.2014.2344014 (cit. on p. 150).

[11] P. J. Moore, I. E. Portugues, and I. A. Glover. "Partial discharge investigation of a power transformer using wireless wideband radio-frequency measurements". In: *IEEE Transactions on Power Delivery* 21.1 (Jan. 2006), pp. 528–530. ISSN: 0885-8977. DOI: 10.1109/TPWRD.2005.848438 (cit. on p. 150).

Chapter 7

Conclusions

In this chapter, the most relevant conclusions of the dissertation are highlighted. The original contributions of the thesis are also described and the publications yielded during the thesis are enumerated.

Notice that this thesis is an extended compilation of the publications enumerated in Subsection 7.3. Then, the conclusions and the contributions presented in this section are a collection of the conclusions and contributions presented in the papers and in the chapters of the thesis.

7.1 General conclusions

In the second chapter of this thesis, several optimization techniques are applied successfully to maximize the separation of signals through 2D PR maps. The optimization techniques select two intervals of frequency, PRL and PRH, where the spectral energy of the different kind of signals have different magnitudes. This fact permits to gather similar signals in clusters and separate the clusters in a PR map to select the signals of interest. This is a previous step to localize the position of pulsed sources even when they are active simultaneously. The maximization of the distances between the clusters is done without supervision, allowing the automatization of the separation and improving the results obtained when the intervals of frequency of interest are selected manually. The distances between clusters is quantified with the MD, because it considers the dispersion of the data inside the cluster. Then, the results obtained in the PR maps are compact clusters and clearly distanced. The PR method has been applied successfully to classify several types of signals yielding great results.

In Chapter 3, the used to determine the relative ToF or TDoA of the pulses is selected from the comparison of some several commonly used algorithms such as the maximum value of the signal, threshold, threshold corrected with the slope, maximum derivative of the cumulative energy of the signal, Hinkley criterium, AIC, Kurtosis 1, Cross correlation and four-order cumulants. A new algorithm, Kurtosis 2 is presented in Subsection 3.5 and when compared to the rest of the algorithms over different applications it can concluded that it is the one that gives the best results. Therefore, with the outcomes of the techniques presented in Chapter 2 and Chapter 3 it is possible to acquire signals with sensors, to select the signals of interest from noise, to determine the number of sources and to calculate the TDoA of those signals to setup an algorithm to locate their position which is done in Chapter 4.

In Chapter 4 two kinds of localization algorithms are compared; iterative algorithms such as (SLS, HLS, PSO and GA) and non-iterative algorithms such as (HPA, Bancroft and MLE). Since both iterative and non-iterative algorithms have different advantages and disadvantages, a new combined algorithm MLE-HLS is proposed in Subsection 4.3.2.4 trying to improve the previous algorithms avoiding their disadvantages. This new algorithm reports better results than the others, in terms of accuracy and time of execution.

Once the position of the source has been determined it is necessary to analyze the accuracy of the distance and the estimated direction of the source to the array. From the results derived in the thesis, the distance is the most critical variable because it has the largest errors. On the other hand, the direction is calculated successfully by all the algorithms in almost the major part of the possible positions of the source analyzed.

New error diagrams represented by spheres showing the sensitivity of different antennas layouts to TDoA errors and antenna positioning errors are presented in the next to Chapter 5 and Chapter 6. Using these diagrams the antenna layouts can be oriented to their preferred directions where the layout is less sensitive to inaccuracies, minimizing the error propagated in the localization.

Since the antennas deployment affects in the propagation of errors in the localization of the source, to choose an adequate layout of antennas can help in the exactness of the localization. In most of the cases, the direction of the source is properly estimated independently of the relative distance between the antennas and the emitter. On the other hand, in the source position estimation, the distance is the most critical variable. In many cases, the distance estimation has large errors, especially when the emitter is far from the receivers. Then, in the localization is recommended placing the antennas close to the emitter. The best scenario case is surround the emitter with the antennas.

7.2 Original contributions

The main original contributions of this thesis are:

- The automatization and optimization of the separation of different kinds of signals through spectrum characterization based on PR.
- A new algorithm to calculate the ToF based on high order statistics, named "Kurtosis 2". This algorithm yields better results than the previous.
- A wide comparison of the most common ToF calculus algorithms applied in several applications.
- A new combined algorithm to calculate the RF emitter position, based on two which already exist MLE and HLS.
- A wide comparison, in terms of exactness and computational time, of the most common used algorithms to locate RF emitters.
- New spherical diagrams of error which represents the directions where some antenna layout has better performance than others in presence of TDoA errors.
- Quantification of the antenna positioning error propagation in the source localization. In the results, the sensibility of the source distance and direction estimation can be seen in spheres.
- Quantification of the error propagation in the direction and distance of the source position estimation regarding the distance from the source to the antenna array.

7.3 Publications

The papers published throughout the thesis are sorted by date of publication and separated in two categories: journal paper and conference contributions.

7.3.1 Journal papers

1. G. Robles, J. M. Fresno, and J. M. Martínez-Tarifa, *"Separation of Radio-Frequency Sources and Localization of Partial Discharges in Noisy Environments,"* Sensors, vol. 15, no. 5, pp. 9882–9898, Apr. 2015.
2. G. Robles, J. M. Fresno, M. Sánchez-Fernández, and J. M. Martínez-Tarifa, *"Antenna Deployment for the Localization of Partial Discharges in Open-Air Substations,"* Sensors, vol. 16, no. 4, p. 541, Apr. 2016.

3. G. Robles, J. M. Fresno, and R. Giannetti, *"Ultrasonic bone localization algorithm based on time-series cumulative kurtosis,"* ISA Transactions, vol. 66, pp. 469–475, Jan. 2017.

4. J. M. Fresno, J. A. Ardila-Rey, J. M. Martínez-Tarifa, and G. Robles, *"Partial discharges and noise separation using spectral power ratios and genetic algorithms,"* IEEE Transactions on Dielectrics and Electrical Insulation, vol. 24, no. 1, pp. 31–38, Feb. 2017.

5. J. M. Fresno, G. Robles, B. G. Stewart, and J. M. Martinez-Tarifa, *"Survey on the performance of source localization algorithms,"* Sensors, 2017, vol. 17, no 11, p. 2666.

6. G. Robles, J. M. Fresno, J. A. Ardila-Rey, J. M. Martínez-Tarifa, and E. Parrado-Hernández *"Selective spectral characterization using particle swarm optimization,"* Engineering Applications of Artificial Intelligence, Submitted.

7.3.2 Conference papers

1. G. Robles, J. M. Fresno, M. Sánchez-Fernández, and J. M. Martínez-Tarifa, *"Antenna array layout for the localization of partial discharges in open-air substations,"* In Proceedings of the 2nd Int. Electron. Conf. Sens. Appl., 15–30 November 2015; Sciforum Electronic Conference Series, Vol. 2, 2015 , E008.

2. M. V. Rojas-Moreno, G. Robles, J. M. Martínez-Tarifa, and J. M. Fresno, *"Ensemble Empirical Mode Decomposition for the denoising of partial discharges measured in UHF"*, in 2016 IEEE International Conference on Dielectrics (ICD), 2016, vol. 2, pp. 963–966.

3. J. M. Martínez-Tarifa, J. A. Ardila-Rey, A. Prieto-Duque, J. M. Fresno, and G. Robles, *"Statistical analysis of RF signals emitted by partial discharges"*, in 2016 IEEE International Conference on Dielectrics (ICD), 2016, vol. 1, pp. 536–539.

4. J. M. Fresno, G. Robles, B. Stewart, and J. M. Martinez-Tarifa, *"The influence of antenna positioning errors on the radio-frequency localization of partial discharge sources"*, The 3rd International Electronic Conference on Sensors and Applications (ECSA 2016), 15–30 November 2016; Sciforum Electronic Conference Series, Vol. 3, 2016 , E003.

5. J. M. Fresno, G. Robles, B. G. Stewart, and J. M. Martinez-Tarifa, *"Effect of Uncertainties in Time Difference of Arrival (TDOA) measurements for PD Source Location Using RF Antennas"*, 10th Universities High Voltage Network Colloquium 2017.

6. J. M. Fresno, G. Robles, y J. M. Martinez-Tarifa, *"Localización de Fuentes de Descargas Parciales en Instalaciones Eléctricas"*, Workshop Monitorización de Líneas, Comité Nacional de España de CIGRE, Abril 2017.

7. J.M. Fresno, G. Robles, R. Giannetti,"*A survey of time-of-flight algorithms to determine bone positions in movement*", 2017 IEEE International Instrumentation and Measurement Technology Conference (I2MTC), Turin, 2017, pp. 1-6.

8. J. M. Fresno, G. Robles, B. G. Stewart, and J. M. Martinez-Tarifa,"*Spatial study of the uncertainties in the localization of partial discharges for different antenna layouts*" 2017 IEEE International Instrumentation and Measurement Technology Conference (I2MTC), Turin, 2017, pp. 1-6.

9. J. M. Fresno, G. Robles, B. G. Stewart, and J. M. Martinez-Tarifa, "*A Combined Algorithm Approach for PD Location Estimation Using RF Antennas*", 2017 IEEE Electrical Insulation Conference (EIC), Baltimore, MD, USA, 2017, pp. 384-387.

7.4 Financing sources

The financing sources received during the thesis are:

- Pre-doctoral research training scholarships - PIPF at Univerisdad Carlos III de Madrid, which consist of research training contracts. In the academic year 2014/2015.

- Mobility aids for researchers in foreign or national research centres. Supported by Univerisdad Carlos III de Madrid. Destination: University of Strathclyde. Glasgow, UK. Start date: 15/08/2016. End date: 16/12/2016 (4 months).

- Research project founded by the Spanish Government. Sensor inteligente para la localización e identificación de descargas parciales en el mantenimiento de activos eléctricos. Under contract DPI2015-66478-C2-1(MINECO/FEDER, UE). 2016-2018.

- Student Travel Award for the paper, "A survey of time-of-flight algorithms to determine bone positions in movement," to the attendance at I2MTC 2017 in Torino, Italy.

Acronyms

1D one dimension. v, xviii, 52–54, 67

2D two dimensions. vi, xiv, 2, 4, 5, 10, 14, 42, 123–146, 175

3D three dimensions. v, vi, xiii, xiv, xxi, 2, 5, 51–54, 67, 74, 80, 90, 99, 114, 123–146, 156–159, 162–165, 168–171

a.u. arbitrary units. 30, 138

AC alternating current. 35

AIC Akaike information criterion. xii, 4, 51, 59, 60, 71, 78, 127, 176

BUA broadband ultrasound attenuation. 69

DSO digital storage oscilloscope. 69

ED euclidean distance. xvii, 14

FM frequency modulation. xii, xvii, xviii, xxv, 3, 9, 31, 33, 34, 45, 127

GA genetic algorithms. xi, xvii, 4, 9, 18, 21, 28, 29, 33, 36, 40, 45, 87, 88, 92–94, 102, 113, 114, 176

GIS gas-insulated switchgear. 124

GPS global positioning systems. 5, 88, 89, 95–97, 148, 149

HLS hyperbolic least squares. xiii, xx, 4, 5, 87–89, 92–95, 98, 101, 102, 107, 110, 113, 114, 124, 148, 149, 176, 177

HPA hyperbolic positioning algorithms. xiii, 5, 87, 89, 95, 102, 113, 114, 176

HV high voltage. xxi, 2, 28, 30, 31, 36, 74, 75, 133

IEC international electrotechnical commission. 35

LINEALT Laboratorio de Investigación y Ensayos en Alta Tensión. xxi, 133

MD mahalanobis distance. xvii, 14, 15, 37, 45, 175

MLE maximum likelihood estimator. xiii, xx, 5, 87–89, 97, 98, 101, 102, 107, 110, 113, 114, 148, 149, 176, 177

OF objective function. xvii, xviii, 5, 15, 18, 20, 22, 27–30, 34, 36–38, 42, 45, 87, 90–95, 98, 101, 114, 130, 149

PD partial discharges. xii, xiv, xviii, xx, xxii–xxv, 2, 4, 5, 9, 35–41, 43, 44, 52, 53, 74–80, 88, 98, 124–129, 132–135, 138, 143, 144, 147–174

PHAT phase transform. 64

PR power ratio. v, xi, xii, xvii, xviii, 3, 4, 9, 10, 12–18, 28, 29, 33–38, 40–42, 45, 175, 177

PRH power ratio at high frequencies. 12–16, 18, 20, 27, 30, 33, 34, 37, 41, 175

PRL power ratio at low frequencies. 12–16, 18, 20, 27, 30, 33, 37, 41, 175

PRPD phase resolved partial discharge. xviii, 35, 38, 39, 41–43, 75

PSO particle swarm optimization. xi, xvii, 4, 9, 20, 22–24, 28, 29, 33, 36, 38, 40, 42, 45, 87, 88, 94, 98, 101, 102, 107, 110, 113, 114, 124, 126, 130, 134, 135, 137, 148, 149, 176

pToF pseudo time of flight. vi, xx, 1, 4, 87, 89, 90, 96, 99, 101

RF radio frequency. xiii, xiv, xx, 2–4, 28, 51, 53, 54, 74, 75, 77, 78, 80, 88, 96, 98, 101, 123, 126, 127, 148, 149, 177

RSS received signal strength. 1, 87, 88

SCOT smoothed coherence transform. 64

SLS standard least squares. 4, 87, 88, 90, 102, 107, 113, 114, 176

SNR signal-to-noise ratio. 10, 31, 34, 38, 55, 69, 127, 137

TDoA time differences of arrival. v, vi, xii–xiv, xvii–xxi, xxv, 1, 3–5, 28, 30–32, 42, 51–54, 64–67, 69, 72–75, 77–80, 87, 89, 90, 92, 95, 97, 99, 101, 123–153, 176, 177

ToA time of arrival. 52, 54

ToF time of flight. v, vi, xii, xviii–xx, 1, 3, 4, 31, 32, 51–64, 67, 69–71, 74, 78, 87, 89–91, 96, 99, 101, 127, 176, 177

UHF ultra high frequency. xii, xvii, xxv, 3, 9, 28–32, 45

US ultrasound. xix, 3, 67–70

VHF very high frequency. xii, xviii, xxv, 3, 9, 35–43, 45